

NANOTECHNOLOGY in ADVANCED DRUG DELIVERY

GUEST EDITORS: SANYOG JAIN, IJEOMA F. UCHEGBU, GURU BETAGERI,
AND GIORGIA PASTORIN





Nanotechnology in Advanced Drug Delivery

Journal of Drug Delivery

Nanotechnology in Advanced Drug Delivery

Guest Editors: Sanyog Jain, Ijeoma F. Uchegbu,
Guru Betageri, and Giorgia Pastorin



Copyright © 2011 Hindawi Publishing Corporation. All rights reserved.

This is a special issue published in volume 2011 of "Journal of Drug Delivery." All articles are open access articles distributed under the Creative Commons Attribution License, which permits unrestricted use, distribution, and reproduction in any medium, provided the original work is properly cited.

Editorial Board

Sophia Antimisiaris, Greece
Abdul Basit, UK
E. Batrakova, USA
Heather Benson, Australia
A. Bernkop-Schnürch, Austria
Guru V. Betageri, USA
María J. Blanco-Prieto, Spain
G. Buckton, UK
Yılmaz çapan, Turkey
Carla Caramella, Italy
Roberta Cavalli, Italy
Nevin çeleby, Turkey
Rita Cortesi, Italy
Alekhya K. Dash, USA
Martin J. D'Souza, USA
Jeanetta du Plessis, South Africa
N. D. Eddington, USA
A. Fadda, Italy
Jia You Fang, Taiwan
Sven Frøkjær, Denmark
Sanjay Garg, New Zealand
Andrea Gazzaniga, Italy

Richard A. Gemeinhart, USA
Lisbeth Illum, UK
Juan M. Irache, Spain
Bhaskara R. Jasti, USA
Hans E. Junginger, Thailand
Dae-Duk Kim, Republic of Korea
Yellela S.R. Krishnaiah, USA
Vinod Labhassetwar, USA
Claus S. Larsen, Denmark
Kang Choon Lee, USA
Lee-Yong Lim, Australia
Ram I. Mahato, USA
Philippe Maincent, France
Edith Mathiowitz, USA
Reza Mehvar, USA
Bozena Michniak-Kohn, USA
Tamara Minko, USA
Ambikanandan Misra, India
A. K. Mitra, USA
S. M. Moghimi, Denmark
A. Mullertz, Denmark
Steven H. Neau, USA

Ali Nokhodchi, UK
Abdelwahab Omri, Canada
R. Pignatello, Italy
Viness Pillay, South Africa
Morteza Rafiee-Tehrani, Iran
Michael Roberts, Australia
Patrick J. Sinko, USA
John Smart, UK
Quentin R. Smith, USA
Hartwig Steckel, Germany
Snow Stolnik-Trenkic, UK
K. Takayama, Japan
Hirofumi Takeuchi, Japan
Istvan Toth, Australia
Hasan Uludağ, Canada
Claudia Valenta, Austria
Jaleh Varshosaz, Iran
Subbu S. Venkatraman, Singapore
S. P. Vyas, India
Chi H. Wang, Singapore
Adrian Williams, UK
P. York, UK

Contents

Nanotechnology in Advanced Drug Delivery, Sanyog Jain, Ijeoma F. Uchegbu, Guru Betageri, and Giorgia Pastorin
Volume 2011, Article ID 343082, 2 pages

Tumor Suppressor Gene-Based Nanotherapy: From Test Tube to the Clinic, Manish Shanker, Jiankang Jin, Cynthia D. Branch, Shinya Miyamoto, Elizabeth A. Grimm, Jack A. Roth, and Rajagopal Ramesh
Volume 2011, Article ID 465845, 10 pages

An Overview on the Field of Micro- and Nanotechnologies for Synthetic Peptide-Based Vaccines, Aiala Salvador, Manoli Igartua, Rosa Maria Hernández, and José Luis Pedraz
Volume 2011, Article ID 181646, 18 pages

Enhanced Transport Capabilities via Nanotechnologies: Impacting Bioefficacy, Controlled Release Strategies, and Novel Chaperones, Thomai Panagiotou and Robert J. Fisher
Volume 2011, Article ID 902403, 14 pages

Preparation of DNA/Gold Nanoparticle Encapsulated in Calcium Phosphate, Tomoko Ito, Koyuki Ibe, Tomohiro Uchino, Hiroyuki Ohshima, and Makoto Otsuka
Volume 2011, Article ID 647631, 7 pages

Unveiling Stability Criteria of DNA-Carbon Nanotubes Constructs by Scanning Tunneling Microscopy and Computational Modeling, Svetlana Kilina, Dzmitry A. Yarotski, A. Alec Talin, Sergei Tretiak, Antoinette J. Taylor, and Alexander V. Balatsky
Volume 2011, Article ID 415621, 9 pages

Transplantation of Porcine Hepatocytes Cultured with Polylactic Acid-O-Carboxymethylated Chitosan Nanoparticles Promotes Liver Regeneration in Acute Liver Failure Rats, Zhong Chen, Renan Chang, Weijun Guan, Hongyu Cai, Fei Tang, Wencai Zhu, and Jiahui Chen
Volume 2011, Article ID 797503, 7 pages

Preparation of a Nanoscaled Poly(vinyl alcohol)/Hydroxyapatite/DNA Complex Using High Hydrostatic Pressure Technology for *In Vitro* and *In Vivo* Gene Delivery, Tsuyoshi Kimura, Yoichi Nibe, Seiichi Funamoto, Masahiro Okada, Tsutomu Furuzono, Tsutomu Ono, Hidekazu Yoshizawa, Toshiya Fujisato, Kwangwoo Nam, and Akio Kishida
Volume 2011, Article ID 962743, 8 pages

Nanoprodugs of NSAIDs: Preparation and Characterization of Flufenamic Acid Nanoprodugs, Bong-Seop Lee, Chi Woo Yoon, Arsen Osipov, Nuriel Moghavem, Daniel Nwachokor, Rina Amaty, Rebekah Na, Joe L. Pantoja, Michael D. Pham, Keith L. Black, and John S. Yu
Volume 2011, Article ID 980720, 13 pages

Encapsulation of Protein-Polysaccharide HIP Complex in Polymeric Nanoparticles, Ripal Gaudana, Varun Khurana, Ashwin Parenky, and Ashim K. Mitra
Volume 2011, Article ID 458128, 7 pages

High-Resolution Imaging of Dendrimers Used in Drug Delivery via Scanning Probe Microscopy, Lifang Shi, Christopher J. Fleming, Shawn L. Riechers, Nai-Ning Yin, Juntao Luo, Kit S. Lam, and Gang-yu Liu
Volume 2011, Article ID 254095, 12 pages



Poly(amidoamine)-Cholesterol Conjugate Nanoparticles Obtained by Electrospraying as Novel Tamoxifen Delivery System, R. Cavalli, A. Bisazza, R. Bussano, M. Trotta, A. Civra, D. Lembo, E. Ranucci, and P. Ferruti

Volume 2011, Article ID 587604, 9 pages

Editorial

Nanotechnology in Advanced Drug Delivery

Sanyog Jain,¹ Ijeoma F. Uchegbu,² Guru Betageri,³ and Giorgia Pastorin⁴

¹ Centre for Pharmaceutical Nanotechnology, Department of Pharmaceutics, National Institute of Pharmaceutical Education and Research (NIPER), Sector 67, Phase X, SAS Nagar (Mohali), Punjab 160062, India

² Department of Pharmaceutics, School of Pharmacy, University of London, 29 39 Brunswick Square, London WC1N 1AX, UK

³ Graduate College of Biomedical Sciences, Western University of Health Sciences, 309 E. Second Street, Pomona, CA 91766, USA

⁴ Department of Pharmacy, National University of Singapore, 3 Science Drive 2, Block S15, 05-PI-03, Singapore 117543

Correspondence should be addressed to Sanyog Jain, sanyogjain@nipер.ac.in

Received 24 August 2011; Accepted 24 August 2011

Copyright © 2011 Sanyog Jain et al. This is an open access article distributed under the Creative Commons Attribution License, which permits unrestricted use, distribution, and reproduction in any medium, provided the original work is properly cited.

Buzzing of nanotechnology in each and every aspect of science and technology has been booming at a tremendous rate now a day. Started its journey from inorganic chemistry, this field has now even reached to aeronautical research, and a special attention has been drawn in the medical and allied branches for exploitation of the nanotech for attending the limitations of the current scenario. Carrying foreword the success of nanotechnology in field of physical, chemical, and medical sciences, it has now started revolutionizing the drug delivery sciences. The specific advantages include superior pharmacodynamics, pharmacokinetics, reduced toxicity, and targeting capability. Vehicle in the delivery sciences being critical quality attribute needs special attention for tailor made design to rationalize the formulation development; which can be successfully achieved via nanotechnology. Additionally, unique size-dependent properties of nanosystems/nanodevices offers excellent opportunities for the development of novel “point-of-care” devices and therapeutic tools. Drugs incorporated in the nanocarriers, either physically entrapped or chemically tethered, have the potential to target physiological disorder zone sparing normal cells from collateral consequences.

Targeting several molecular mechanisms, for either treatment or prevention of difficult-to-treat diseases, for the design of the various nanotechnology-based drug delivery systems is one of prime focuses of the formulation scientist at the present juncture. Gene therapies and gene-based drug delivery using nanocarriers are booming especially in case of neoplastic extravasations. Various tumor suppressor genes are identified, isolated and successfully formulated for treatment of cancer. A remarkable number of such systems have

already made their pave and are under clinical trials, being expected very soon at the end user level. Besides treating these diseases, nanotechnology also offers its contributions in development of preventive measures such as vaccines. Various nanotechnological adjuvants have been evaluated for their capabilities to deliver vaccine subunits without compromising the immunogenicity for successful design and development of vaccine delivery systems. Furthermore, regeneration ability of the visceral organs such as liver has also been evaluated using nanocarriers, and the postulations are on their way stating the enhanced cytoactivity of the transplanted cells when cultured in nanocarriers.

The pharmacokinetic profile, especially transportation capabilities, of the drug substances have been greatly modified by incorporation in nanodrug delivery system. These include enhanced accommodation for targeting moieties such as chaperones and alteration in release rates comprising of controlled release and site-specific delivery by use of molecular engineering techniques. Additionally, encapsulation of the drug substances in various polymeric and inorganic composites has also been evaluated for their rationalizing the drug delivery systems. Such encapsulations are generally made for protecting the biologically active protein and peptide-based drug compounds from the detrimental effects of biological fluids. Newer nanoprodrug approaches have also been applied, which has posed enhanced therapeutic efficacy along with superior circulation time.

Emerging methodologies for formulation of nanodrug delivery systems include newer versions of the top-down and bottom-up approaches. Additionally allied technologies such as atomization and pressurization have come in to play

to facilitate the preparation of nanotechnological carriers. One such comprises a novel method of atomization, namely, electrohydrodynamic atomization used in electrospraying method. Pressurization techniques such as high hydrostatic pressure technology for encapsulation of genes into polymeric nanomaterials have recently been studied for their efficacy in delivering the biologically active compounds. These novel technologies offer advantages by eliminating the usage of toxic cationic polymers and chemical tethers further replacing them simple yet effective hydrogen bonding. Such advantages and simplifications of the process have already given their imminent revolutions in the field of drug delivery.

With these advancements in the novel nanocarriers and their applicability, the analytical tools are also not lagging behind. In order to cope up with this and stand aside, newer evaluation methodologies are already in move of their development. These include scanning probe microscopy, more specifically atomic force microscopy and scanning tunneling microscopy, which have great capabilities for molecular and submolecular characterizations.

Furthermore, various platform technologies at the nanoscale, often referred as nanoplatfroms, have been coming in to play and booming for widespread applications of these cutting edge technologies for its applicability at end users. Basically, the common ones in the race include the nanocrystals (nanopure, nanoedge, Dissocubes), nanomaterials (fullerenes, carbon nanotubes, and nanoparticles), nanomedicines, molecular self-assemblies (self-assembled monolayers, supramolecular assemblies and DNA nanotechnologies), nanoelectronics (*in silico* technologies), and so on to name a few. The extension and appliance will be the state-of-art for future research.

Finally, the common undeniable opinion highlighted in this issue is that, although it is too early to say whether these nanocarriers will wean the world from its current limitations, or monumentally backfire to cause harm, a deep understanding of the various mechanisms underneath the reported findings will favor great discoveries, even at the nanoscale.

In nutshell, efforts are extensively made for utilizing the nanotechnology concepts for advancements in the current drug delivery sciences and, further to this, the fruitfulness of the efforts has been achieved which is well reflected in this present issue.

Sanyog Jain
Ijeoma F. Uchegbu
Guru Betageri
Giorgia Pastorin

Review Article

Tumor Suppressor Gene-Based Nanotherapy: From Test Tube to the Clinic

**Manish Shanker,¹ Jiankang Jin,¹ Cynthia D. Branch,¹ Shinya Miyamoto,²
Elizabeth A. Grimm,³ Jack A. Roth,¹ and Rajagopal Ramesh^{1,2,4,5}**

¹Department of Thoracic and Cardiovascular Surgery, The University of Texas of MD Anderson Cancer Center, Houston, TX 77030, USA

²Department of Pathology, The University of Oklahoma Health Sciences Center, Oklahoma City, OK 73104, USA

³Department of Experimental Therapeutics, The University of Texas of MD Anderson Cancer Center, Houston, TX 77030, USA

⁴Peggy and Charles Stephenson Oklahoma Cancer Center, The University of Oklahoma Health Sciences Center, Oklahoma City, OK 73104, USA

⁵Graduate Program in Biological Sciences, The University of Oklahoma Health Sciences Center, Oklahoma City, OK 73104, USA

Correspondence should be addressed to Rajagopal Ramesh, rajagopal-ramesh@ouhsc.edu

Received 6 October 2010; Accepted 5 November 2010

Academic Editor: Sanyog Jain

Copyright © 2011 Manish Shanker et al. This is an open access article distributed under the Creative Commons Attribution License, which permits unrestricted use, distribution, and reproduction in any medium, provided the original work is properly cited.

Cancer is a major health problem in the world. Advances made in cancer therapy have improved the survival of patients in certain types of cancer. However, the overall five-year survival has not significantly improved in the majority of cancer types. Major challenges encountered in having effective cancer therapy are development of drug resistance by the tumor cells, nonspecific cytotoxicity, and inability to affect metastatic tumors by the chemodrugs. Overcoming these challenges requires development and testing of novel therapies. One attractive cancer therapeutic approach is cancer gene therapy. Several laboratories including the authors' laboratory have been investigating nonviral formulations for delivering therapeutic genes as a mode for effective cancer therapy. In this paper the authors will summarize their experience in the development and testing of a cationic lipid-based nanocarrier formulation and the results from their preclinical studies leading to a Phase I clinical trial for nonsmall cell lung cancer. Their nanocarrier formulation containing therapeutic genes such as tumor suppressor genes when administered intravenously effectively controls metastatic tumor growth. Additional Phase I clinical trials based on the results of their nanocarrier formulation have been initiated or proposed for treatment of cancer of the breast, ovary, pancreas, and metastatic melanoma, and will be discussed.

1. Introduction

Cancer is a major health problem in the world. In 2009, about 1,479,350 people living in the United States of America (USA), have been diagnosed with cancer [1]. About half of these cancer patients will die of the disease. The lifetime risk of developing cancer is predicted to be 1 in 2 for men and 1 in 3 for women [1]. Dissemination of scientific information and cancer awareness have reduced the incidence for certain cancer types while the incidence for other cancer types remain unchanged or increased. For example, reduced incidence of lung cancer in men due to cessation of smoking has been observed while the lung cancer incidence in women

is increasing. Similarly, ignoring the risks of exposure to ultraviolet rays and the potential for developing skin cancer has resulted in steady increase in the incidence of melanoma.

Effective cancer therapies developed in recent years have improved the survival of patients diagnosed with cancer. However, the overall five-year survival rate of cancer patients remain dismal and is less than 15% at least for solid tumors of epithelial origin [2]. Factors contributing to the poor survival rate despite having developed novel therapies include development of resistance to therapy by cancer cells, poor drug distribution and accumulation in the tumor, and nonspecific cytotoxicity to normal tissues thereby limiting the drug dosage. Thus, there is a tremendous effort in

developing new cancer therapeutics that are efficacious and safe with minimal cytotoxicity to normal tissues. Testing and demonstration of such new therapeutics in preclinical studies will ultimately lead to testing in humans as a cancer drug.

One therapeutic approach that has shown promise and safety is cancer gene therapy [3]. The gene therapy approach that has exploded and tested widely in the last decade is the use of tumor suppressor genes (TSG's). Cell division and cell growth are tightly controlled processes often regulated by TSG's. However, alterations such as mutations, deletions, and silencing at the DNA, RNA, or protein level of TSG result in dysregulation of the cell growth and transformation [4]. Retinoblastoma (Rb) and p53 TSG are classical examples whose function when lost or altered has been shown to initiate or contribute to cell transformation [5, 6]. Furthermore, p53 gene mutations are observed in a majority of human cancers, suggesting it is an important gatekeeper of the cell. Apart from Rb and p53, several other TSGs have been identified and shown to regulate diverse cellular processes and loss of their function affects normal cell activity. Based on these observations, it was hypothesized that restoration of normal TSG function will inhibit cell proliferation and growth leading to cell death. Thus TSG-based cancer therapy was conceived and initiated.

Early studies using viral vectors demonstrated that delivering TSG's resulted in tumor inhibition in animal models [3] (see Table 1). Translating these findings to the clinic demonstrated clinical and/or biological response to therapy. Stabilization of the disease (SD) was frequently observed in patients receiving therapy, and in few cases complete response to therapy as evidenced by tumors' regression [7–10]. Despite the encouraging clinical results observed in virus-based cancer gene therapy studies, this treatment strategy has limited application due to the elicitation of host-immune response by viral proteins [11–14]. Additionally, testing of virus-based cancer gene therapy for treatment for metastatic disease has not been proven to be successful so far.

To overcome the limitations encountered with virus-based cancer therapy, several laboratories including our own laboratory have been testing nonviral-gene-delivery vehicles for cancer gene therapy. The nonviral vectors are of different composition and formulations. They also vary in their size and geometry. A majority of these nonviral vectors are nanometer (nm) in size and often have a lipid component. According to the National Cancer Institute (NCI), any biological or synthetic material which in any one dimension is less than 1 micrometer (μm) is called a nanoparticle. Based on this definition, several nonviral vectors that are less than 1 μm in size are referred as nanoparticles, nanocarriers, nanosomes, and so forth.

An advantage of using nanoparticles as gene-delivery vehicles is that they can deliver therapeutic genes to *in situ* tumors that are disseminated inside the body [3, 15]. Studies have demonstrated nanoparticle-based gene-delivery results in antitumor activity in experimental preclinical tumor models. An added advantage of using nonviral nanocarrier systems, apart from the ease of manufacturing, is the avoidance of problems frequently encountered with adenovirus [15, 16].

In this paper, we will discuss our experiences with a lipid-based nanocarrier that was initially tested in the laboratory as a tumor suppressor gene-delivery vehicle and later tested in the clinic for the treatment of nonsmall cell lung cancer (NSCLC). Plans for applying our nanocarrier-based cancer gene therapy technology for treatment of other solid cancers will also be discussed.

2. Gene-Based Nanotherapy

2.1. Laboratory Studies. Our interest in testing lipid-based nanocarriers as gene-delivery vehicles arises from the following observations: (1) cancer is often metastasized in patients at the time of their initial diagnosis [1, 2]; (2) conventional therapies are ineffective in treating metastatic disease [17, 18]; (3) our own laboratory studies demonstrate that virus-based (retrovirus and adenovirus) tumor suppressor gene therapy for systemic therapy of metastatic cancer was ineffective; (4) preclinical studies demonstrated that nonviral vectors can deliver genes and drugs to localized and disseminated tumors [19–21].

Although several lipid-based nanocarriers were reported in the literature to be efficient gene-delivery vehicles, most of these studies were restricted to *in vitro* testing with few being tested *in vivo* [22–27]. Furthermore, only a limited number of nanocarriers has moved beyond the laboratory and has been tested in the clinic (see Table 2). The reasons for their inability to test several nanocarriers in the clinic are multifactorial and include inability to produce clinical grade nanocarriers in large quantities, inflammatory response [28–30], poor stability and short half-life of the nanocarrier *in vivo* [31, 32], interaction with serum proteins and aggregation [33, 34], poor uptake of the nanocarrier by the tumors, and rapid clearance by macrophage and the reticuloendothelial system (RES) [35].

Methods to overcome some of these limitations included PEGylation of the nanocarriers using polyethylene glycol (PEG). Pegylated nanocarriers demonstrated improved stability *in vivo*, reduced RES clearance, and increased accumulation in tumors resulting in enhanced antitumor activity [36–38]. Similarly, studies using neutral or negatively charged nanocarriers have reported effective delivery of oligonucleotides, siRNA, and chemotherapeutic drugs [39, 40]. Despite the advances made with neutral and anionic lipid-based nanocarriers, they have not been developed and tested widely as tumor-suppressor gene-delivery vehicles for cancer therapy.

In 1998, Templeton et al. [41] reported that cationic DOTAP:cholesterol (DOTAP:Chol) lipid nanocarrier efficiently delivered plasmid DNA to the lung when administered intravenously. Findings by Gaensler et al. [42] concurred that DOTAP:Chol lipid nanocarrier to be an efficient gene-delivery vehicle. Crook et al. [43] reported that inclusion of cholesterol was important and a key to achieving stabilization of the DOTAP:Chol-nanocarrier and efficient gene transfer. The key feature that makes this nanocarrier better than previously tested lipid-based nanocarriers is its stability and reduced interaction with blood proteins *in vivo*

TABLE 1: Tumor suppressor genes tested as cancer therapeutic in preclinical studies.

TSG	Cancer	Animal model	Therapeutic outcomes	Molecular events
E1A	Ovarian	Intraperitoneal tumor	Reduced abdominal tumor burden; increased animal survival	Apoptosis, reduced ascites, and cell cycle arrest
p53	Lung	Subcutaneous tumor; experimental lung metastasis	Tumor-growth inhibition; reduced extrapulmonary tumor nodules and increased animal survival	Cell cycle arrest, apoptosis, and antiangiogenesis
Fhit	Lung	Subcutaneous tumor; experimental lung metastasis	Tumor-growth inhibition; reduced extrapulmonary tumor nodules and increased animal survival	Cell cycle arrest and apoptosis
IL-24	Lung	Subcutaneous tumor; experimental lung metastasis	Tumor-growth inhibition; reduced extrapulmonary tumor nodules; increased animal survival	Cell cycle arrest, apoptosis, antiangiogenesis, and autophagy proimmune activity
Fus1	Lung	Subcutaneous tumor; experimental lung metastasis	Tumor-growth inhibition; reduced extrapulmonary tumor nodules; increased animal survival	Cell cycle arrest and apoptosis
BiKDD	Pancreas	Subcutaneous tumor; orthotopic tumor	Tumor-growth inhibition; reduced metastasis, increased animal survival	Apoptosis

which is contributed by the inclusion of cholesterol [41]. Another key feature that likely contributes to its effectiveness is that the lipid-nanocarrier, when mixed with DNA, forms unique bilamellar vase-like structures that keep the DNA intact from rapid degradation [41]. However, it is likely that additional factors that are unknown at the present time may contribute to its effectiveness.

Based on these reports, we initiated preclinical studies in our laboratory and tested whether DOTAP:Chol-lipid nanocarrier could efficiently deliver tumor suppressor genes when administered systemically and control metastatic lung tumors. Size fractionation studies showed our lipid nanocarrier was 200–400 nm in size and had a positive charge of 40 ± 2 mV [44, 45]. The nanocarriers are stable +4°C for over a period of one month when stored as empty nanocarriers and for at least 48 h when mixed with DNA. Although one may argue that our nanocarriers are large, results from our studies, as discussed below, support particle size of 200–400 nm to be optimal and to strike a balance between tumor uptake and macrophage clearance. Furthermore, we believe that the size of the nanocarrier will need to be varied and optimized depending on the disease to be treated and that the concept of one-size-fits-all disease treatments cannot be applied.

In vitro studies showed transfection efficiency mediated by the nanocarrier varied among cell types that correlated with transgene expression [44, 46, 47]. Transgene expression was observed to be detectable as early as 12 h after transfection and was detectable up to 72 h after transfection albeit expression levels decreased over time. The transfection efficiency and transgene expression were observed to be consistent in a given cell line even when different tumor

suppressor genes or marker genes were used. One factor that affected transfection efficiency and transgene expression was the size of plasmid contained in the nanocarrier. In general, a nanocarrier containing a plasmid that was 3–4 Kb in size produced higher transfection compared to nanocarrier containing a plasmid that was greater than 4 Kb in size. Furthermore, the DNA-containing nanocarrier was stable for at least 48 h when stored at +4°C and produced comparable transfection efficiency and transgene expression in tumor cells when compared to that produced by cells treated with a freshly prepared DNA-containing nanocarrier.

In vivo studies were initially focused on biodistribution and toxicity of the DNA-containing nanocarrier in immunocompetent mice. Biodistribution studies showed that the DNA-nanocarrier primarily localized to the lung when injected intravenously. However, over time the nanocarrier exited the lung and was detectable in other organs (liver, spleen, kidney etc). Toxicity studies demonstrated a dose-dependent response with LD10 being in the range of 55–70 µg of DNA in the lipid nanocarrier and depended on the backbone of the plasmid DNA. The therapeutic gene contributed very little to toxicity (unpublished data).

We next investigated the therapeutic effects of a TSG-containing nanocarrier on human lung tumor xenografts established in nude mice. Marker gene expression showed marked transgene expression when injected intratumorally into subcutaneous lung tumor xenografts [40]. Efficacy studies showed that a TSGs-containing (p53, Fhit, Fus1, TSG101, or IL-24) nanocarrier, when administered intratumorally, produced significant growth inhibition compared to tumor growth inhibition produced by nanocarrier treatment containing control plasmid DNA [44, 46, 47]. Growth inhibition,

TABLE 2: Synthetic nanocarriers tested for cancer gene therapy in human Phase I clinical trials.

Nanocarrier	Therapeutic gene	Cancer	Route of administration
DC (3 beta-[n-(N', N'-dimethylaminoethane)-carbamoyl]cholesterol): DOPE (dioleoylphosphatidylethanolamine)	E1A	Breast/ovarian	Intratumoral (it)/intraperitoneal (ip)
DC (3 beta-[n-(N', N'-dimethylaminoethane)-carbamoyl]cholesterol): Chol (cholesterol)	EGFR	Head & neck	Intratumoral
DOTAP (N-[1-(2, 3-dioleoyloxy)propyl]-N,N,N-trimethylammonium Chloride): DOPE (dioleoylphosphatidylethanolamine)	p53	Solid tumor	Intravenous (iv)
DOTAP (N-[1-(2, 3-dioleoyloxy)propyl]-N,N,N-trimethylammonium Chloride): Chol (cholesterol)	BiKDD	Pancreatic cancer	Intravenous (iv)
DOTAP (N-[1-(2, 3-dioleoyloxy)propyl]-N,N,N-trimethylammonium Chloride): Chol (cholesterol)	E1A	Breast/ovarian	Intravenous (iv)
DOTAP (N-[1-(2, 3-dioleoyloxy)propyl]-N,N,N-trimethylammonium Chloride): Chol (cholesterol)	Fus1	Lung	Intravenous (iv)
DOTMA (N-[1-(2,3-dioleoyloxy)propyl]-N,N,N-trimethylammonium Chloride): Chol (cholesterol)	IL-2	Head & neck	Intratumoral (it)

Source: www.cancertrials.gov.

produced by TSG-containing nanocarrier was independent of the tumor model, as comparable growth-inhibitory effects were observed in human H1299 lung tumor and murine UV2237 tumor xenografts established in nude mice and C3H mice, respectively [46]. Furthermore, repeated treatments showed greater tumor-growth inhibition that correlated with increased transgene expression when compared to growth-inhibitory effects produced by single treatments. Our study also showed that the therapeutic effect produced by p53 TSG-containing nanocarrier treatment was independent of the endogenous p53 status of the treated tumor. Additionally, the therapeutic effect produced using various TSGs was comparable, albeit differences existed among tumor types. These results provide evidence and support intratumoral treatments of localized tumors such as cancer of the head and neck that are unresectable with TSG-containing nanocarrier. It is envisioned that such localized intratumoral treatments with TSG-containing nanocarrier will reduce the tumor burden and make the tumor accessible to surgery and radiation therapy.

Since our objective and goal was to test the nanocarrier as a systemic gene-delivery vehicle for treatment of metastatic disease, we conducted *in vivo* studies using experimental tumor-metastasis models. Human H1299 (p53 null) and A549 (p53 wild-type) tumor cells were injected intravenously via tail vein to establish experimental lung metastasis in SCID/Beige and nude mice, respectively. Mice received daily intravenous treatments with a p53 TSG-containing nanocarrier for a total of six doses. At four weeks after the last treatment mice were euthanized, lungs were harvested and examined for the number of pulmonary nodules.

A significant reduction in the number of pulmonary tumor nodules were observed in mice receiving p53 TSG nanocarrier treatment compared to the number of pulmonary tumor nodules in mice receiving control DNA-containing nanocarrier treatment [44]. Histopathological examination of the lungs from mice receiving p53 TSG-containing nanocarrier treatment showed few tumors with evidence of tumor cells undergoing apoptotic cell death compared to the number of tumors in the lungs of control mice and very few tumor cells undergoing apoptosis.

Since the six-day treatment with p53 TSG-containing nanocarrier did not completely abolish pulmonary tumor growth we next determined whether these tumors will regrow and if they can be treated with a second cycle of treatment akin to that practiced in the clinic. For this purpose, mice bearing experimental lung tumors were divided into two groups. One group of mice ($n = 8$) received the initial six treatments with p53 TSG nanocarrier (day 1–6). A second group of mice ($n = 8$) received the initial six treatments with p53 TSG nanocarrier (day 1–6) and a second cycle of six treatments starting on day 30 (day 30–35). Mice ($n = 4$) from each group were euthanized on day 28 and on day 42. Lungs were harvested from the euthanized mice and the number of lung tumor nodules counted. Our results showed that a greater reduction in the number of pulmonary tumor nodules in the lungs of mice receiving two cycles of p53 TSG nanocarrier treatment compared to the reduction in tumor nodules in the lungs of mice receiving single cycle of p53 TSG nanocarrier treatment (unpublished data). Our results demonstrate repeated cycles of treatment are feasible and that they produced a greater therapeutic effect.

We next determined the therapeutic effects of p53 TSG-containing nanocarrier in disseminated tumor mouse model. Injection of H1299 lung tumor cells into SCID/Beige mice results in disseminated tumors in various organs [44]. Treating these mice with the p53 TSG nanocarrier intravenously resulted in prolonged animal survival compared to survival of control mice that were either untreated or treated with a control plasmid DNA-containing nanocarrier [44].

Effective gene-delivery mediated by the nanocarrier was not restricted to p53 TSG therapy or to lung tumor models. Delivery of Fhit and Fus1 TSGs, that are frequently lost in human lung cancer, produced therapeutic effects that were similar to the therapeutic effects observed with p53 [44, 47]. Furthermore, combination of Fus1-containing nanocarrier with chemotherapy was shown to produce additive to synergistic therapeutic effect [48]. Similarly, systemic therapy with IL-24-containing nanocarrier inhibited human lung tumor and murine fibrosarcoma growth established in nude mice and immunocompetent C3H mice, respectively [46]. In all of these studies repeated treatments resulted in additive increases in transgene expression in the tumors with minimal expression in normal tissues adjacent to the tumor [49], a finding that was in contrast to the report by Li et al. [50] who showed repeated treatments reduced transgene expression due to induction of treatment-related inflammatory response. The differences in the outcomes were due to difference in the animal models used. We demonstrated that mice bearing tumors produced immunosuppressive factors within the tumor microenvironment that altered the host immune pathology resulting in no inhibitory effects on transgene expression [51]. Additionally, nanocarrier tracking studies demonstrated tumors that were larger in size had more nanocarriers compared to tumors that were smaller in size [49]. The uptake of the nanocarriers involved tumor-mediated phagocytosis. Furthermore, the inflammatory response produced in the tumor-bearing mice was markedly reduced. On the contrary, if the mice did not bear any tumors then the nanocarrier was widely distributed in the lung, and induction of treatment-related inflammatory response and shutting down of transgene expression following repeated treatments was observed [44, 49, 52]. Thus, the outcomes of repeated nanocarrier treatment and transgene expression can be regulated by the host pathology and disease conditions and therefore need to be considered during drug development.

More recently, we have tested the systemic therapeutic effects of IL-24-containing nanocarrier treatments in a metastatic melanoma model. Nude mice injected with human melanoma (MeWo) tumor cells that are genetically modified to express the green fluorescent protein (GFP) produced tumors that metastasized to the lung, liver, brain, and several other organs and visible under bright light and fluorescent light (Figure 1). Mice injected with MeWo-GFP cells and bearing experimental metastasis were divided into the following groups: no treatment; treatment with IL-24 plasmid DNA; treatment with empty nanocarrier; treatment with IL-24-containing nanocarrier. Mice were treated twice a week (50 μ g DNA) until the study was terminated. Treatment of these mice having experimental

metastasis intravenously with IL-24-nanocarriers resulted in prolonged animal survival compared to survival of mice that received other treatments or no treatment (Figure 2). These studies showed systemic treatment with our nanocarrier delivers therapeutic genes and produces effective anticancer activity.

We next determined whether our nanocarrier can deliver TSGs to ovarian cancer when administered intraperitoneally (i.p.) and whether it was superior to adenovirus-mediated gene-delivery in producing a therapeutic effect. Nude mice were injected into the peritoneum with human ovarian MDAH2774 tumor cells. The mice rapidly form ascites with disease progression and at which time if untreated they will have to be euthanized. These i.p. tumor-bearing mice were divided into groups and treated as follows: treated with IL-24-containing nanocarrier, treated with adenovirus (Ad)-IL-24, treated with Ad-luciferase (Luc), or treated with phosphate buffered saline (PBS). Animals were monitored daily and animal survival recorded. As shown in Figure 3, mice receiving IL-24-containing nanocarrier showed a trend for increased survival compared to all other treatment groups. Our preliminary results showed nanocarrier-based therapy was more effective than adenovirus-based therapy in controlling tumor growth and progression for ovarian cancer. Finally, our studies demonstrate DOTAP:Chol-based nanocarrier is efficient in delivering therapeutics genes to local and metastatic tumor sites and can be administered via various routes resulting in enhanced therapeutic effects in preclinical models.

2.2. Clinical Studies. On the basis of our preclinical studies, a Phase I clinical trial for the systemic treatment of nonsmall cell lung cancer (NSCLC) has been initiated at the University of Texas MD Anderson Cancer Center, Houston, Texas, USA [53]. This trial which is a first of its kind aims at testing whether DOTAP:Chol. nanocarrier-containing a TSG, Fus1, can be administered intravenously in patients with recurrent/metastatic lung cancer previously treated with platinum-based chemotherapy. Fus1 is a TSG located on chromosome 3p21.3 [54, 55]. The rationale for selecting Fus1 for NSCLC therapy is because it is frequently lost or deleted in more than 60% of patients diagnosed with lung cancer [56]. Additionally, studies have shown that Fus1 effectively suppressed lung-tumor growth *in vivo* when used as monotherapy or in combination with other drugs [57–59]. The primary objective of this trial is to treat patients with an escalating dose (0.01–0.09 mg/Kg) of Fus1-containing nanocarrier at a three-week interval and determine the maximum tolerated dose (MTD). Up to date, 23 patients have been entered on the study trial and have received one or more Fus1-containing nanocarrier treatment. Preliminary results demonstrate Fus1 nanocarrier treatment is well tolerated with no major treatment-related toxicity [53]. Furthermore, MTD is yet to be determined, and the trial is open and continuing to accrue patients. The final results of the Fus1 nanocarrier treatment is expected to be available upon completion of the trial. The outcome of this trial will facilitate the design of future TSG-nanocarrier-based Phase I/II clinical trials for lung cancer.

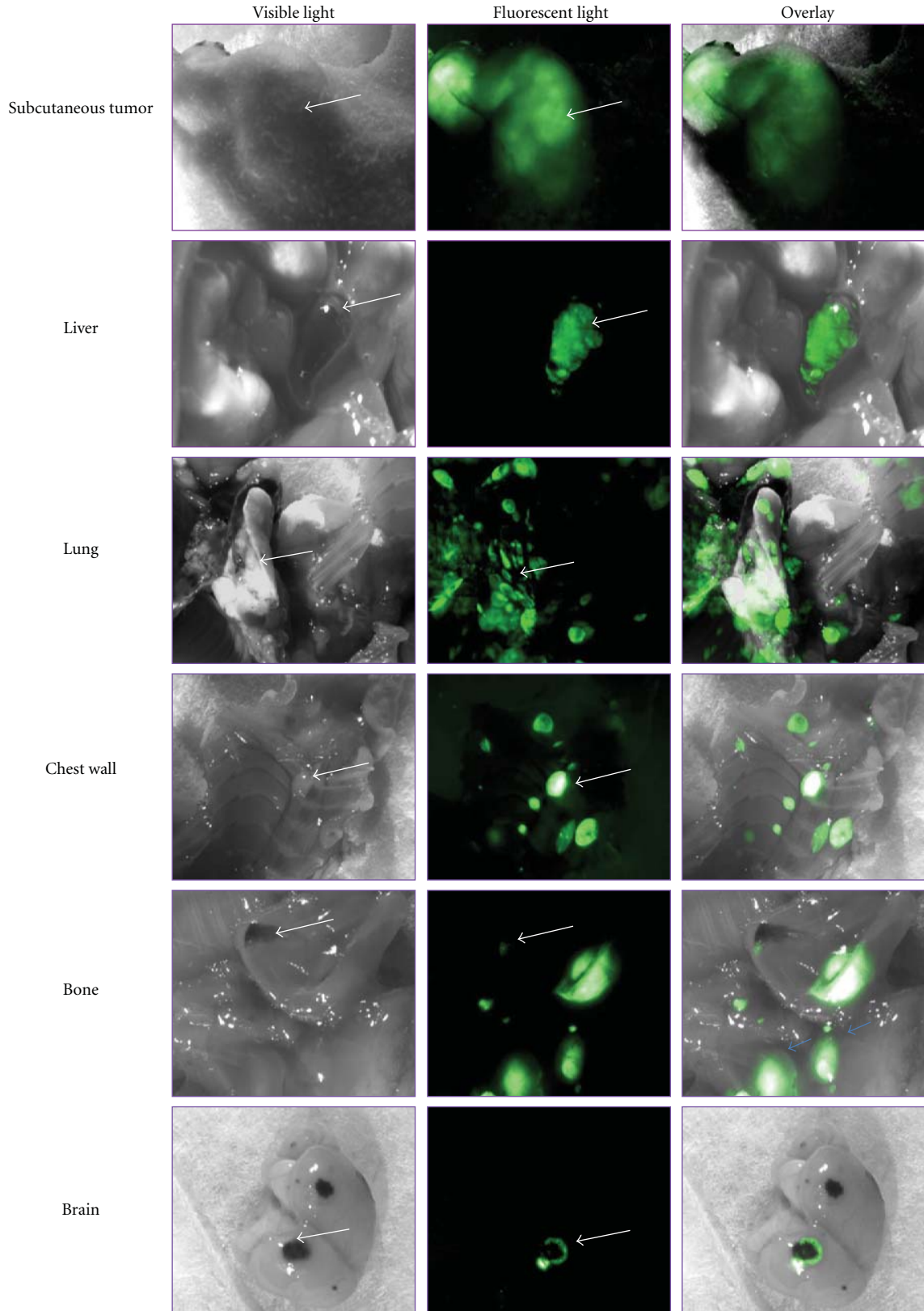


FIGURE 1: Detection of melanoma metastasis by fluorescent imaging. Human melanoma MeWo cell line was stably transfected and selected for GFP positive clones. The MeWo-GFP cells (5×10^6) were injected intravenously via tail vein in nude mice. Mice were euthanized after four to five weeks and observed under normal white light and under fluorescent light. Melanoma tumors were detectable under white light in various organs. However, an increased number of GFP-positive tumors (green fluorescence) were observed under fluorescence light in various organs indicating melanoma metastasis. Additionally, tumors not visible under white light were detected by fluorescence.

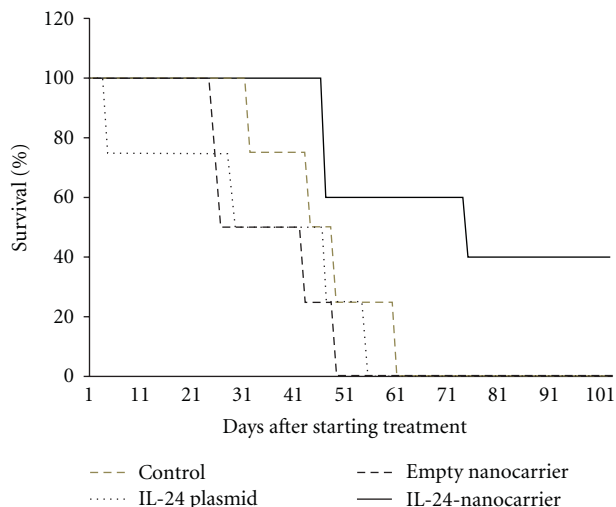


FIGURE 2: IL-24 nanotherapy improves animal survival. Nude mice were injected with MeWo-GFP. Ten days after tumor cell injection mice were divided into four groups: group received no treatment; group 2 received IL-24 plasmid DNA; group 3 received empty nanocarrier; group 4 received IL-24-containing nanocarrier (50 μg DNA). Treatment was twice a week and administered intravenously for six weeks. Mice were monitored for animal survival. Mice receiving IL-24-containing nanocarrier therapy showed increased survival compared to all other treatment groups.

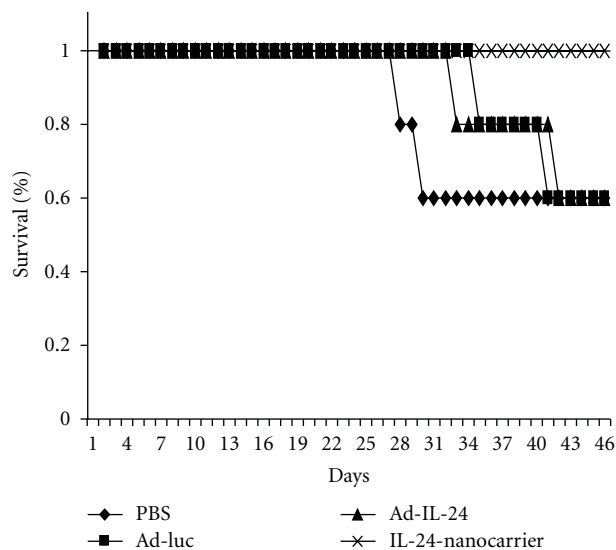


FIGURE 3: IL-24 nanotherapy for ovarian cancer. MDAH2774 (1 × 10⁶) cells were injected into the peritoneal cavity of nude mice. Mice were then divided into groups and treated with IL-24-containing nanocarrier intraperitoneally (i.p.). Mice that were treated with phosphate buffered saline (PBS), treated with adenovirus (Ad)-IL-24, or treated with Ad-luciferase (Luc) served as controls. An increase in animal survival was observed in mice that received IL-24-containing nanotherapy compared to all other treatment groups.

On the basis of our preclinical studies and the Fus1-containing nanocarrier Phase I clinical trial, two additional

Phase I clinical trials for the treatment of pancreatic cancer, ovarian, and breast cancer have been approved by the Food and Drug Administration (FDA) (see Table 2). These trials will be conducted at the MD Anderson Cancer Center, Houston, TX, USA. Both of these trials have objectives and endpoints similar to the Fus1 trial. The only difference is the therapeutic gene to be used for these cancer types is different and not Fus1. For pancreatic cancer, a proapoptotic gene called Bcl-2 interacting killer (Bik) gene (BikDD) will be used for therapy [60]. The uniqueness is that BikDD gene expression will be under the control of cholecystokinin type A receptor (CCKAR) that will be conditionally regulated by VP16-GAL4-WPRE integrated systemic amplifier (VISA). This system is tumor selective and high BikDD protein expression is expected to occur in cancer cells with minimal protein expression occurring in surrounding normal tissues, and thus eliminating unwanted cytotoxicity. The objective of the pancreatic cancer Phase I clinical trial is to determine the MTD and optimal biological active dose (OBAD) compared with the clinical response. The trial has not been completed, and the results from this trial are therefore pending.

In the Phase I clinical trial planned for breast cancer treatment, the therapeutic gene to be incorporated into the DOTAP:Chol. nanocarrier is the E1A tumor suppressor gene. E1A gene introduction into breast cancer cells induces cell cycle arrest and cell death both *in vitro* and *in vivo* [61]. Additionally, E1A has previously been tested in a Phase I clinical trial for treatment of breast and ovarian cancer patients. Although results from the early trial did not show any therapeutic benefits, it demonstrated E1A treatment was safe [62]. This trial, like the pancreatic trial, is currently open for patient accrual and not completed. Therefore, results from this trial will remain unknown for, at least, the next one to two years.

More recently plans for a Phase I clinical trial testing systemic IL-24 nanocarrier therapy for metastatic melanoma is underway. Preclinical efficacy and toxicity studies, that are prerequisites for submitting IL-24 nanocarrier as investigational new drug (IND), have been completed. The IL-24 nanocarrier phase I clinical trial is yet to receive approval from the Food and Drug Administration (FDA) and will be conducted at the MD Anderson Cancer Center, Houston, TX, USA.

It is evident from the number of Phase I clinical trials that have been initiated on the basis of our laboratory findings that the lipid-based DOTAP:Chol nanocarrier is useful for systemic delivery of cancer gene therapeutics. Successful translation of laboratory research to a clinic such as ours described above will lead to promising cancer treatment strategies and therapies. It is anticipated that additional laboratory research will be translated to the clinic in the next few years.

3. Conclusions

Since the inception and testing of gene-based therapies for cancer in the early 1990s, significant progress in the understanding of the biology of the disease and vector development has been made. Failure to control and/or

eradicate cancer using virus-based cancer gene therapy has led to advancement of the nonviral delivery field. Despite skepticism and unexpected gene therapy related deaths, progress has been made in the area of cancer gene therapy and will continue to be made. It is evident from the progress made in our own laboratory, by moving laboratory research to the clinic one could successfully translate future research for cancer therapy. Since combination therapies have often been reported to produce additive to synergistic therapeutic effect, it is not far from testing Fus1 nanocarrier in combination with conventional chemotherapies or molecularly targeted therapies. For example one could combine Fus1 nanocarrier with the epidermal growth factor receptor (EGFR) kinase-targeted inhibitors for treatment of lung cancer. Similarly, IL-24 nanocarrier therapy can be combined with Raf-targeted inhibitor (sorafenib) or alternatively with the chemotherapeutic Temozolomide for treatment of metastatic melanoma. Given the possibility of testing various combinations, it is critical that the ongoing Phase I clinical trials are successful so that future clinical trials incorporating combination therapies can be designed and tested.

With the advent of nanotechnology and its application to cancer medicine, novel nonviral vector-based nanocarriers that are multifunctional in their properties have been developed and are currently being tested in several laboratories around the world [24, 63–65]. It is thus not far from the near future that several Phase I clinical trials based on novel nanoformulations and properties will be initiated for testing drugs, genes, siRNA, aptamers, or molecular imaging agents for cancer diagnosis and therapy [27, 66, 67].

Acknowledgments

The authors thank all the laboratory members who have contributed to various aspects of the nanotherapy project. Grant funding received from the National Institutes of Health (NIH) R01 CA113450 and a Career Development Grant received from the Melanoma SPOR P50 CA093459 are acknowledged.

References

- [1] American Cancer Society, *Cancer Facts & Figures 2009*, American Cancer Society, Atlanta, Ga, USA, 2009.
- [2] R. T. Greenlee, T. Murray, S. Bolden, and P. A. Wingo, "Cancer statistics, 2000," *Ca: A Cancer Journal for Clinicians*, vol. 50, no. 1, pp. 7–33, 2000.
- [3] A. Mhashilkar, S. Chada, J. A. Roth, and R. Ramesh, "Gene therapy: therapeutic approaches and implications," *Biotechnology Advances*, vol. 19, no. 4, pp. 279–297, 2001.
- [4] C. J. Sherr, "Principles of tumor suppression," *Cell*, vol. 116, no. 2, pp. 235–246, 2004.
- [5] A. J. Levine and M. Oren, "The first 30 years of p53: growing ever more complex," *Nature Reviews Cancer*, vol. 9, no. 10, pp. 749–758, 2009.
- [6] D. Lohmann, "Retinoblastoma," *Advances in Experimental Medicine and Biology*, vol. 685, pp. 220–227, 2010.
- [7] J. A. Roth, D. Nguyen, D. D. Lawrence et al., "Retrovirus-mediated wild-type p53 gene transfer to tumors of patients with lung cancer," *Nature Medicine*, vol. 2, no. 9, pp. 985–991, 1996.
- [8] S. G. Swisher, J. A. Roth, J. Nemunaitis et al., "Adenovirus-mediated p53 gene transfer in advanced non-small-cell lung cancer," *Journal of the National Cancer Institute*, vol. 91, no. 9, pp. 763–771, 1999.
- [9] J. Nemunaitis, S. G. Swisher, T. Timmons et al., "Adenovirus-mediated p53 gene transfer in sequence with cisplatin to tumors of patients with non-small-cell lung cancer," *Journal of Clinical Oncology*, vol. 18, no. 3, pp. 609–622, 2000.
- [10] S. W. Zhang, S. W. Xiao, C. Q. Liu et al., "Treatment of head and neck squamous cell carcinoma by recombinant adenovirus-p53 combined with radiotherapy: a phase II clinical trial of 42 cases," *Zhonghua Yi Xue Za Zhi*, vol. 83, no. 23, pp. 2023–2028, 2003.
- [11] E. Marshall, "Gene therapy death prompts review of adenovirus vector," *Science*, vol. 286, no. 5448, pp. 2244–2245, 1999.
- [12] T. Kafri, D. Morgan, T. Krahl, N. Sarvetnick, L. Sherman, and I. Verma, "Cellular immune response to adenoviral vector infected cells does not require de novo viral gene expression: implications for gene therapy," *Proceedings of the National Academy of Sciences of the United States of America*, vol. 95, no. 19, pp. 11377–11382, 1998.
- [13] Y. Yang, H. C. J. Ertl, and J. M. Wilson, "MHC class I-restricted cytotoxic T lymphocytes to viral antigens destroy hepatocytes in mice infected with E1-deleted recombinant adenoviruses," *Immunity*, vol. 1, no. 5, pp. 433–442, 1994.
- [14] Y. Yang, J. Ku, Q. Su, H. C. J. Ertl, and J. M. Wilson, "Immune responses to viral antigens versus transgene product in the elimination of recombinant adenovirus-infected hepatocytes in vivo," *Gene Therapy*, vol. 3, no. 2, pp. 137–144, 1996.
- [15] T. Niidome and L. Huang, "Gene therapy progress and prospects: nonviral vectors," *Gene Therapy*, vol. 9, no. 24, pp. 1647–1652, 2002.
- [16] S. D. Li and L. Huang, "Gene therapy progress and prospects: non-viral gene therapy by systemic delivery," *Gene Therapy*, vol. 13, no. 18, pp. 1313–1319, 2006.
- [17] C. Huisman, E. F. Smit, G. Giaccone, and P. E. Postmus, "Second-line chemotherapy in relapsing or refractory non-small-cell lung cancer: a review," *Journal of Clinical Oncology*, vol. 18, no. 21, pp. 3722–3730, 2000.
- [18] Y. A. Hannun, "Apoptosis and the dilemma of cancer chemotherapy," *Blood*, vol. 89, no. 6, pp. 1845–1853, 1997.
- [19] M. V. Yezhelyev, X. Gao, Y. Xing, A. Al-Hajj, S. Nie, and R. M. O'Regan, "Emerging use of nanoparticles in diagnosis and treatment of breast cancer," *The Lancet Oncology*, vol. 7, no. 8, pp. 657–667, 2006.
- [20] L. Xu, C. C. Huang, W. Huang et al., "Systemic tumor-targeted gene delivery by anti-transferrin receptor scFv-immunoliposomes," *Molecular Cancer Therapeutics*, vol. 1, no. 5, pp. 337–346, 2002.
- [21] S. Sundaram, R. Trivedi, C. Durairaj, R. Ramesh, B. K. Ambati, and U. B. Kompella, "Targeted drug and gene delivery systems for lung cancer therapy," *Clinical Cancer Research*, vol. 15, no. 23, pp. 7299–7308, 2009.
- [22] C. Srinivasan and D. J. Burgess, "Optimization and characterization of anionic lipoplexes for gene delivery," *Journal of Controlled Release*, vol. 136, no. 1, pp. 62–70, 2009.
- [23] P. Sun, M. Zhong, X. Shi, and Z. Li, "Anionic LPD complexes for gene delivery to macrophage: preparation, characterization and transfection in vitro," *Journal of Drug Targeting*, vol. 16, no. 9, pp. 668–678, 2008.

- [24] A. M. Smith, S. Dave, S. Nie, L. True, and X. Gao, "Multicolor quantum dots for molecular diagnostics of cancer," *Expert Review of Molecular Diagnostics*, vol. 6, no. 2, pp. 231–244, 2006.
- [25] H. Devalapally, D. Shenoy, S. Little, R. Langer, and M. Amiji, "Poly(ethylene oxide)-modified poly(beta-amino ester) nanoparticles as a pH-sensitive system for tumor-targeted delivery of hydrophobic drugs: part 3. Therapeutic efficacy and safety studies in ovarian cancer xenograft model," *Cancer Chemotherapy and Pharmacology*, vol. 59, no. 4, pp. 477–484, 2007.
- [26] L. H. Reddy, K. Vivek, N. Bakshi, and R. S. R. Murthy, "Tamoxifen citrate loaded solid lipid nanoparticles (SLNTM): preparation, characterization, in vitro drug release, and pharmacokinetic evaluation," *Pharmaceutical Development and Technology*, vol. 11, no. 2, pp. 167–177, 2006.
- [27] O. C. Farokhzad, J. M. Karp, and R. Langer, "Nanoparticle-aptamer bioconjugates for cancer targeting," *Expert Opinion on Drug Delivery*, vol. 3, no. 3, pp. 311–324, 2006.
- [28] Y. Liu, L. C. Mounkes, H. D. Liggitt et al., "Factors influencing the efficiency of cationic liposome-mediated intravenous gene delivery," *Nature Biotechnology*, vol. 15, no. 2, pp. 167–173, 1997.
- [29] N. S. Yew, K. X. Wang, M. Przybylska et al., "Contribution of plasmid DNA to inflammation in the lung after administration of cationic lipid:pDNA complexes," *Human Gene Therapy*, vol. 10, no. 2, pp. 223–234, 1999.
- [30] B. D. Freimark, H. P. Blezinger, V. J. Florack et al., "Cationic lipids enhance cytokine and cell influx levels in the lung following administration of plasmid: cationic lipid complexes," *Journal of Immunology*, vol. 160, no. 9, pp. 4580–4586, 1998.
- [31] A. Pathak, S. Patnaik, and K. C. Gupta, "Recent trends in non-viral vector-mediated gene delivery," *Biotechnology Journal*, vol. 4, no. 11, pp. 1559–1572, 2009.
- [32] M. Ramezani, M. Khoshhamdam, A. Dehshahri, and B. Malaekhe-Nikouei, "The influence of size, lipid composition and bilayer fluidity of cationic liposomes on the transfection efficiency of nanolipoplexes," *Colloids and Surfaces B*, vol. 72, no. 1, pp. 1–5, 2009.
- [33] J. P. Yang and L. Huang, "Overcoming the inhibitory effect of serum on lipofection by increasing the charge ratio of cationic liposome to DNA," *Gene Therapy*, vol. 4, no. 9, pp. 950–960, 1997.
- [34] S. Li, W. C. Tseng, D. Beer Stolz, S. P. Wu, S. C. Watkins, and L. Huang, "Dynamic changes in the characteristics of cationic lipidic vectors after exposure to mouse serum: implications for intravenous lipofection," *Gene Therapy*, vol. 6, no. 4, pp. 585–594, 1999.
- [35] W. Li and F. C. Szoka, "Lipid-based nanoparticles for nucleic acid delivery," *Pharmaceutical Research*, vol. 24, no. 3, pp. 438–449, 2007.
- [36] V. P. Torchilin, "Polymer-coated long-circulating microparticulate pharmaceuticals," *Journal of Microencapsulation*, vol. 15, no. 1, pp. 1–19, 1998.
- [37] F. Szoka and D. Papahadjopoulos, "Comparative properties and methods of preparation of lipid vesicles (liposomes)," *Annual Review of Biophysics and Bioengineering*, vol. 9, pp. 467–508, 1980.
- [38] K. Iga, K. Ohkouchi, Y. Ogawa, and H. Toguchi, "Membrane modification by negatively charged stearyl-polyoxyethylene derivatives for thermosensitive liposomes: reduced liposomal aggregation and avoidance of reticuloendothelial system uptake," *Journal of Drug Targeting*, vol. 2, no. 3, pp. 259–267, 1994.
- [39] M. M. Mady, M. M. Ghannam, W. A. Khalil et al., "Efficient gene delivery with serum into human cancer cells using targeted anionic liposomes," *Journal of Drug Targeting*, vol. 12, no. 1, pp. 11–18, 2004.
- [40] E. Fattal, P. Couvreur, and C. Dubernet, "'Smart' delivery of antisense oligonucleotides by anionic pH-sensitive liposomes," *Advanced Drug Delivery Reviews*, vol. 56, no. 7, pp. 931–946, 2004.
- [41] N. S. Templeton, D. D. Lasic, P. M. Frederik, H. H. Strey, D. D. Roberts, and G. N. Pavlakis, "Improved DNA: liposome complexes for increased systemic delivery and gene expression," *Nature Biotechnology*, vol. 15, no. 7, pp. 647–652, 1997.
- [42] K. M. L. Gaensler, G. Tu, S. Bruch et al., "Fetal gene transfer by transuterine injection of cationic liposome-DNA complexes," *Nature Biotechnology*, vol. 17, no. 12, pp. 1188–1192, 1999.
- [43] K. Crook, B. J. Stevenson, M. Dubouchet, and D. J. Porteous, "Inclusion of cholesterol in DOTAP transfection complexes increases the delivery of DNA to cells in vitro in the presence of serum," *Gene Therapy*, vol. 5, no. 1, pp. 137–143, 1998.
- [44] R. Ramesh, T. Saeki, N. S. Templeton et al., "Successful treatment of primary and disseminated human lung cancers by systemic delivery of tumor suppressor genes using an improved liposome vector," *Molecular Therapy*, vol. 3, no. 3, pp. 337–350, 2001.
- [45] B. Gopalan, I. Ito, C. D. Branch, C. Stephens, J. A. Roth, and R. Ramesh, "Nanoparticle based systemic gene therapy for lung cancer: molecular mechanisms and strategies to suppress nanoparticle-mediated inflammatory response," *Technology in Cancer Research and Treatment*, vol. 3, no. 6, pp. 647–657, 2004.
- [46] R. Ramesh, I. Ito, Y. Saito et al., "Local and systemic inhibition of lung tumor growth after nanoparticle-mediated mda-7/IL-24 gene delivery," *DNA and Cell Biology*, vol. 23, no. 12, pp. 850–857, 2004.
- [47] I. Ito, L. Ji, F. Tanaka et al., "Liposomal vector mediated delivery of the 3p FUS1 gene demonstrates potent antitumor activity against human lung cancer in vivo," *Cancer Gene Therapy*, vol. 11, no. 11, pp. 733–739, 2004.
- [48] W. G. Deng, G. Wu, K. Ueda, K. Xu, J. A. Roth, and L. Ji, "Enhancement of antitumor activity of cisplatin in human lung cancer cells by tumor suppressor FUS1," *Cancer Gene Therapy*, vol. 15, no. 1, pp. 29–39, 2008.
- [49] I. Ito, G. Began, I. Mohiuddin et al., "Increased uptake of liposomal-DNA complexes by lung metastases following intravenous administration," *Molecular Therapy*, vol. 7, no. 3, pp. 409–418, 2003.
- [50] S. Li, S. P. Wu, M. Whitmore et al., "Effect of immune response on gene transfer to the lung via systemic administration of cationic lipidic vectors," *American Journal of Physiology*, vol. 276, no. 5, pp. L796–L804, 1999.
- [51] I. Ito, T. Saeki, I. Mohiuddin et al., "Persistent transgene expression following intravenous administration of a liposomal complex: role of interleukin-10-mediated immune suppression," *Molecular Therapy*, vol. 9, no. 3, pp. 318–327, 2004.
- [52] R. Ramesh, "Nanoparticle-mediated gene delivery to the lung," *Methods in Molecular Biology*, vol. 434, pp. 301–331, 2008.
- [53] C. Lu, D. J. Stewart, L. Ji et al., "A phase I trial of intravenous therapy with tumor suppressor Fus1-nanoparticles for recurrent/metastatic lung cancer," *Journal of Clinical Oncology*, vol. 27, abstract e19065, 2009.
- [54] M. I. Lerman and J. D. Minna, "The 630-kb lung cancer homozygous deletion region on human chromosome 3p21.3:

- identification and evaluation of the resident candidate tumor suppressor genes,” *Cancer Research*, vol. 60, no. 21, pp. 6116–6133, 2000.
- [55] E. R. Zabarovsky, M. I. Lerman, and J. D. Minna, “Tumor suppressor genes on chromosome 3p involved in the pathogenesis of lung and other cancers,” *Oncogene*, vol. 21, no. 45, pp. 6915–6935, 2002.
- [56] L. Prudkin, C. Behrens, D. D. Liu et al., “Loss and reduction of Fus1 protein expression is a frequent phenomenon in the pathogenesis of lung cancer,” *Clinical Cancer Research*, vol. 14, no. 1, pp. 41–47, 2008.
- [57] M. Kondo, L. Ji, C. Kamibayashi et al., “Overexpression of candidate tumor suppressor gene FUS1 isolated from the 3p21.3 homozygous deletion region leads to G1 arrest and growth inhibition of lung cancer cells,” *Oncogene*, vol. 20, no. 43, pp. 6258–6262, 2001.
- [58] L. Ji and J. A. Roth, “Tumor suppressor FUS1 signaling pathway,” *Journal of Thoracic Oncology*, vol. 3, no. 4, pp. 327–330, 2008.
- [59] L. Ji, M. Nishizaki, B. Gao et al., “Expression of several genes in the human chromosome 3p21.3 homozygous deletion region by an adenovirus vector results in tumor suppressor activities in vitro and in vivo,” *Cancer Research*, vol. 62, no. 9, pp. 2715–2720, 2002.
- [60] Y. P. Sher, T. F. Tzeng, S. F. Kan et al., “Cancer targeted gene therapy of BikDD inhibits orthotopic lung cancer growth and improves long-term survival,” *Oncogene*, vol. 28, no. 37, pp. 3286–3295, 2009.
- [61] M. C. Hung, G. N. Hortobagyi, and N. T. Ueno, “Development of clinical trial of E1A gene therapy targeting HER-2/neu-overexpressing breast and ovarian cancer,” *Advances in Experimental Medicine and Biology*, vol. 465, pp. 171–180, 2000.
- [62] G. N. Hortobagyi, N. T. Ueno, W. Xia et al., “Cationic liposome-mediated E1A gene transfer to human breast and ovarian cancer cells and its biologic effects: a phase I clinical trial,” *Journal of Clinical Oncology*, vol. 19, no. 14, pp. 3422–3433, 2001.
- [63] A. G. Cuenca, H. Jiang, S. N. Hochwald, M. Delano, W. G. Cance, and S. R. Grobmyer, “Emerging implications of nanotechnology on cancer diagnostics and therapeutics,” *Cancer*, vol. 107, no. 3, pp. 459–466, 2006.
- [64] T. Kubik, K. Bogunia-Kubik, and M. Sugisaka, “Nanotechnology on duty in medical applications,” *Current Pharmaceutical Biotechnology*, vol. 6, no. 1, pp. 17–33, 2005.
- [65] M. V. Yezhelyev, X. Gao, Y. Xing, A. Al-Hajj, S. Nie, and R. M. O’Regan, “Emerging use of nanoparticles in diagnosis and treatment of breast cancer,” *The Lancet Oncology*, vol. 7, no. 8, pp. 657–667, 2006.
- [66] E. Fattal, P. Couvreur, and C. Dubernet, ““Smart” delivery of antisense oligonucleotides by anionic pH-sensitive liposomes,” *Advanced Drug Delivery Reviews*, vol. 56, no. 7, pp. 931–946, 2004.
- [67] S. Y. Wu and N. A.J. McMillan, “Lipidic systems for in vivo siRNA delivery,” *The AAPS Journal*, vol. 11, no. 4, pp. 639–652, 2009.

Review Article

An Overview on the Field of Micro- and Nanotechnologies for Synthetic Peptide-Based Vaccines

Aiala Salvador,^{1,2} Manoli Igartua,^{1,2} Rosa Maria Hernández,^{1,2} and José Luis Pedraz^{1,2}

¹*NanoBioCel Group, Laboratory of Pharmaceutics, School of Pharmacy, University of the Basque Country, 01006 Vitoria, Spain*

²*Biomedical Research Networking Center in Bioengineering, Biomaterials and Nanomedicine (CIBER-BBN), 01006 Vitoria, Spain*

Correspondence should be addressed to José Luis Pedraz, joseluis.pedraz@ehu.es

Received 4 November 2010; Accepted 5 April 2011

Academic Editor: Sanyog Jain

Copyright © 2011 Aiala Salvador et al. This is an open access article distributed under the Creative Commons Attribution License, which permits unrestricted use, distribution, and reproduction in any medium, provided the original work is properly cited.

The development of synthetic peptide-based vaccines has many advantages in comparison with vaccines based on live attenuated organisms, inactivated or killed organism, or toxins. Peptide-based vaccines cannot revert to a virulent form, allow a better conservation, and are produced more easily and safely. However, they generate a weaker immune response than other vaccines, and the inclusion of adjuvants and/or the use of vaccine delivery systems is almost always needed. Among vaccine delivery systems, micro- and nanoparticulated ones are attractive, because their particulate nature can increase cross-presentation of the peptide. In addition, they can be passively or actively targeted to antigen presenting cells. Furthermore, particulate adjuvants are able to directly activate innate immune system *in vivo*. Here, we summarize micro- and nanoparticulated vaccine delivery systems used in the field of synthetic peptide-based vaccines as well as strategies to increase their immunogenicity.

1. Introduction

In recent years, there has been an increase in the development of vaccination technology, but the ideal vaccine has not already been found. In general terms, there are some criteria which a vaccine must satisfy; it must be capable of eliciting the appropriate immune response, and it should be safe, stable, and reproducible. There are other issues such as cost, number of administrations, or immunization route which may also have to be taken into account [1]. Traditional vaccines have been developed using live attenuated organisms (such as BCG—Bacillus Calmette-Guerin, measles, mumps, rubella, and varicella), killed or inactivated whole organisms (e.g., influenza) or inactivated toxins (including diphtheria and tetanus) [2]. Live vaccines have the advantage of producing both humoral and cellular immune responses and often require only one boost. However, these vaccines are environmentally labile and require refrigeration, making difficult the delivery of these therapeutic agents, especially in the developing countries. Furthermore, the use of attenuated pathogens can revert to a more active form, a danger particularly acute in immune-compromised individuals [3]. Killed or inactivated organisms generate a weaker immune response

and typically require multiple doses [4]. Hence, these types of vaccines generally require the addition of an adjuvant to be effective [5]. These disadvantages led to the development of subunit vaccines, including synthetic peptides as antigen, which consist of a specific part of the whole pathogen which has been demonstrated to stimulate an immune response. These vaccines are attractive, because they cannot revert to their virulent form and can be produced in bulk, safely and reproducibly. However, subunit vaccines have relatively low immunogenicity [6] which makes necessary the use of adjuvants and/or vaccine delivery systems. Besides, protein-based vaccines may be degraded by protease activity and have limited bioavailability, since they often cannot cross biological membranes [7, 8]. Finding the optimal combination between a given synthetic peptide and an adjuvant opens an unlimited clinical potential for these vaccines, because if adequate epitopes were identified for a certain disease, antigens could be synthesized on demand. For this reason, successful adjuvants need to be safe and well tolerated, simply produced and with inexpensive compounds, biodegradables, compatibles with many different antigens, and capable of function as a delivery system and immune potentiators [9]. Therefore, for licensing of new or newly formulated vaccines,

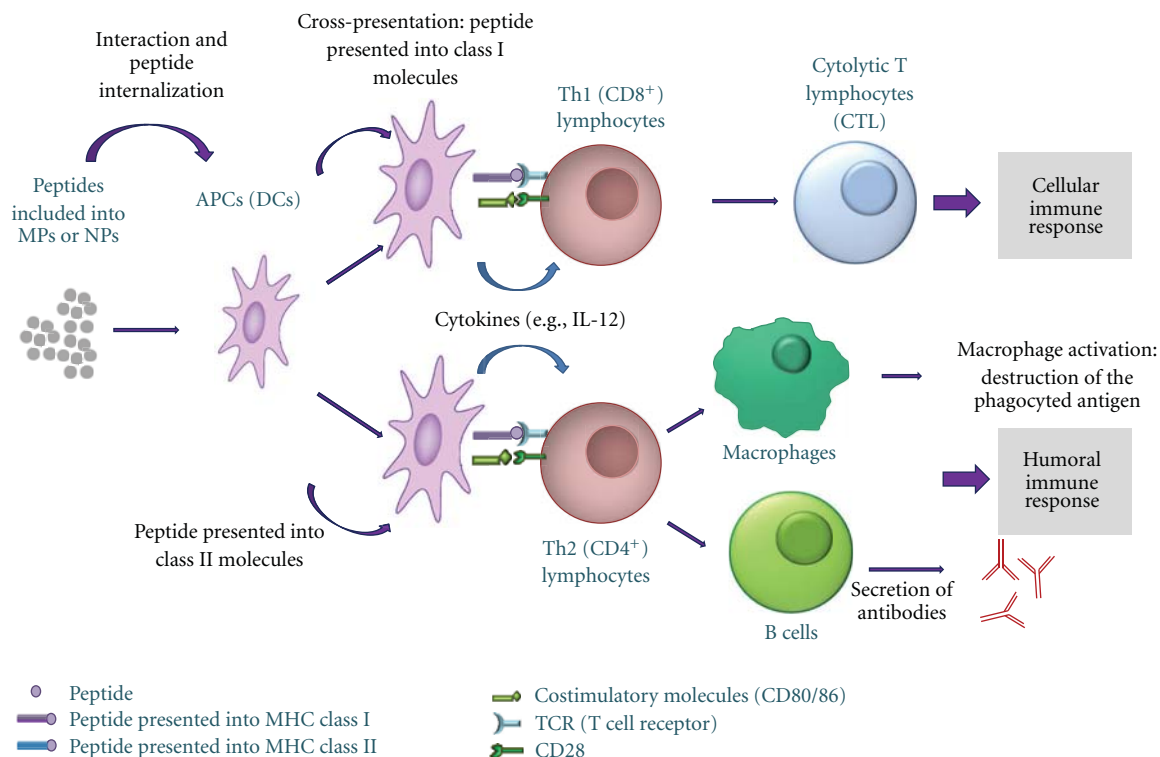


FIGURE 1: Schematic overview of the immune response developed after vaccination with micro- and nanoparticles entrapping antigenic peptides.

nonclinical and clinical data regarding safety and efficacy are required, next to pharmaceutical quality data. These data are needed on the active ingredients, as well as the adjuvants and delivery systems, and their combination in the final product [10]. In this regard, there is only one guideline specifically dedicated to peptides, *Guidance for Industry for the Submission of Chemistry, Manufacturing, and Controls Information for Synthetic Peptide Substances*, published in 1994 [11], which stipulates the lot release specifications (sufficient to ensure the identity, purity, and strength of the peptide and demonstrate lot-to-lot consistency).

The need of eliciting both humoral and cellular immune responses has limited the efficacy against certain pathogens, such as malaria and HIV [3]. Activating the cytolytic immune response (CTL) is needed in the case of intracellular pathogens or tumors, and it is mediated by CD8 T cells, CD4 Th1 cells and natural killer T cells. Dendritic cells (DCs) have several innate features that make them ideal targets for vaccination purposes. They can capture antigens that enter the body and move to the T cell areas of lymphoid organs to find the right clones and start the immune response [10]. In peripheral tissues, DCs are found in an immature stage specialized in capturing foreign antigens. In response to microbes, DCs undergo a process of maturation into antigen-presenting cells (APCs). Meanwhile, they migrate from the periphery to the draining lymph nodes, where they present antigens to the T lymphocytes. DCs can present peptides to the T cells in the context of major histocompatibility complex (MHC) classes I and II molecules and

also glycolipids and glycopeptides to T cells and NKT cells as well as polypeptides to B cells [12]. In order to achieve a CTL response, cytolytic cells must specifically recognize pathogen-derived antigens presented in MHC class I or in the CD1-lipid complex. Upon antigen recognition, immune cells release cytolytic agents that directly destroy infected cells and can induce inflammatory reactions which facilitate innate immune clearance and the development of some humoral response.

In order to generate CD8⁺ T cell immune responses cross-presentation have to occur, in which an exogenous antigen is presented into MHC I molecules in order to promote strong cytolytic and Th1 inflammatory bias [3]. Most protein-based vaccines do not develop cytolytic responses, because they are more readily processed into MHC class II molecules (which triggers humoral or antibody-dependent immune responses) [13]. For the development of a CTL response, antigens have to escape from the endosomal compartment into the cytosolic and endoplasmic reticular space, where the cross-presentation occurs [3]. Micro- and nanoparticle-based vaccine delivery systems can function as antigen carriers. Their particulate nature has some inherent ability to facilitate antigen cross-presentation [3], since they resemble pathogens particulate structure that looks like the biological situation. Particles *per se* are passively directed to the APCs and can increase the interaction between these cells and the antigen due to particles slow degradation [1]. Apart from the depot effect, particulate adjuvants can directly activate innate immunity *in vivo* [14]; that is, they work as

immunoadjuvants. Thus, modification of these systems to directly target APCs may be a good approach for improving their efficacy. Therefore, micro- and nanoparticulated delivery systems can lead good opportunities in the development of synthetic peptide-based vaccines (Figure 1).

When preparing micro- or nanodevices, there are some key formulation aspects such as chemical composition and manufacturing process, which affect the antigen loading capacity and release profile, product stability, efficacy, and safety [15]. For instance, the difference in size between micro- and nanoparticles may change the immune response achieved. The smaller the particle, the greater the proportion of drug located on its surface. This can lead to a substantial loss of payload or to a lower maximal drug loading for smaller particles [16], which finally may affect to the adjuvant activity. Moreover, the preparation process of micro- and nanoparticles can lead to stability problems due to the exposure to strong stress conditions (e.g., aqueous/organic interfaces, hydrophobic surfaces, and vigorous shaking) [17]. For this reason, peptide stability, once entrapped into the formulation, should be evaluated, since it is unlikely to develop a universal encapsulation approach appropriate to every peptide. For instance, in order to study the stability of the SPf66 peptide encapsulated into PLGA MPs, Carcaboso et al. [18] analyzed peptide integrity by polyacrylamide gel electrophoresis and showed no bands indicating partial degradation or aggregation of the protein.

Nowadays, there are no marketed vaccines composed of synthetic peptides. However, there are approved vaccines based on micro- and nanotechnologies. Alum is the most widely used adjuvant for human vaccines in the form of particulated aluminium salts (generally, $\text{Al}(\text{OH})_3$ and AlPO_4) [19]. As shown in Table 1, it is used in various vaccines, such as the combined vaccine containing antigens against diphtheria, tetanus, and pertussis [20] and against hepatitis B (Recombivax HB [21] or Engerix B [22, 23]). More recently, other particulate adjuvants have been licensed for human use. Emulsions like MF59 or AS03 are components of Fludax and Pandemrix, respectively [24, 25]. Other vaccines such as Epaxal [26] or Inflexal [27] include virosomes. Latest approved systems are composed of combination of adjuvants, such as AS04 (approved for human use in both Europe and USA), which comprises MPL (monophosphorilipid A) and alum and is used into Fendrix [28] or AS04 combined with virus like particles (VLPs) used into Cervarix [29, 30] and Gardasil [31].

This paper summarizes micro- and nanoparticulated delivery systems used in the development of synthetic peptide-based vaccines. We also discuss various strategies for improving their efficacy in developing an appropriate immune response (Table 2).

2. Micro- and Nanoparticulated Systems for Synthetic Peptide Vaccine Development

2.1. Alum. Aluminium salts (generally, $\text{Al}(\text{OH})_3$ and AlPO_4), often called alum, have been widely used in humans for more than 80 years, and, until recently, it has been the

only adjuvant approved for human use in the USA [32]. Currently, there are many vaccines containing alum, such as Recombivax HB or Engerix B. Alum adjuvancity is associated with enhanced antibody responses [19]. It has been shown that after OVA-alum administration Th2 effector response is generated, as T helper cells produced IL-4, IL-5, and IL-10 but little IFN- γ [33]. In addition, Li et al. demonstrated that alum enhances the production of IL-10, a Th2 cytokine, and inhibits that of IP-10 (IFN- γ -inducible protein), a chemokine specific for Th1 cells [34]. It has been shown that alum induces rapid cell recruitment at the injection site. Kool et al. demonstrated that after an intraperitoneal injection of alum, a local production of chemoattractants like CCL2 and CXCL1 was triggered, as well as a recruitment of neutrophils, eosinophils, monocytes, and subsequently DCs. This study also revealed that following intraperitoneal or intramuscular administration of alum, recruited monocytes migrate to the draining lymph nodes and differentiate into inflammatory DCs capable of priming T cells [33].

Several action mechanisms have been proposed in order to explain alum adjuvancity. Previously, it was thought that alum formed a depot by which the antigen was slowly released and which converted the antigen into a particulate form, facilitating phagocytosis by APCs [35]. Later, it has been shown that alum induces inflammatory responses that recruit and activate APCs which capture the antigen [34]. Recent data demonstrate that alum targets NOD-like receptor protein 3 (NLRP3 or NALP3) to mediate caspase-1 activation and IL-1 β release in lipopolysaccharide- (LPS-) primed macrophages [36]. NLRP3 interacts with Cardiacin and ASC (apoptosis-associated speck-like protein) to form a caspase-1-activating complex called inflammasome, which, in turn, mediates the activation of proIL-1 β , proIL-18, and proIL-33 into their active forms (Figure 2) [34]. However, *in vivo* data demonstrated that NLRP3 is dispensable for the adjuvant activity [36]. Nevertheless, other groups have reached conflicting conclusions. Eisenbarth et al. [37] and Li et al. [38] found an abrogation of the antibody responses to coadministered antigen in absence of NALP3 signaling, whereas Kool et al. [39] found only partial inhibition of the response. However, these results may be explained by the fact that different alum formulations were used in each study or different levels of TLR (Toll like receptor) agonist were used [40].

Other studies have suggested that NALP3 could be stimulated through indirect mechanisms. Kool et al. found that following alum administration, an increase in the endogenous danger signal uric acid happened. Neutralization of uric acid with uricase led to an inhibition of the inflammatory response induced by alum [33].

There are several investigators which study the immune response achieved after combining synthetic peptides with alum. For instance, a phase I clinical trial was conducted with the long synthetic peptide GLURP85-213 of *Plasmodium falciparum* combined with either alum or Montanide ISA as adjuvants [41]. Formulations were administered subcutaneously with 10, 30, or 100 μg peptide doses at days 0, 30, and 120. Although serious adverse events were not observed, adverse events were more prevalent in the Montanide ISA

TABLE 1: Examples of EMA- and/or FDA-approved vaccines based on micro- and nanoparticulated delivery systems. MF59 and AS03 are squalene- and tocopherol-based o/w emulsions, respectively. AS04 is composed of monophosphoril lipid A and alum. Virosomes are composed of viral-derived phospholipid bilayers, and virus-like particles (VLPs) are viral capsids lacking genetic material.

Vaccine	Delivery system	Indication	Reference
Recombivax	Alum	Hepatitis B	[17]
Engerix B	Alum	Hepatitis B	[18, 19]
Tripedia, Infanrix, DAPTACEL	Alum	Diphtheria, Tetanus and Pertussis	[16]
Fluad	MF59	Influenza/pandemic flu	[20]
Pandemrix	AS03	Pandemic flu	[21]
Fendrix	AS04	Hepatitis A	[24]
Epaxal	Virosomes	Hepatitis A	[22]
Inflexal	Virosomes	Influenza	[23]
Cervarix	AS04 + VLPs	Human papillomavirus	[25, 26]
Gardasil	VLPs + Alum	Human papillomavirus	[27]

TABLE 2: Schematic view of the mechanism of action and advantages of the different micro- and nanotechnologies for peptide-based vaccine delivery.

Type of technology	Role	Advantages
Alum	(i) Depot (ii) Activation of inflammasome and IL-1 β release	(i) Enhances antibody responses
Emulsions	(i) Promote antigen uptake by DCs (ii) Strong immunostimulatory activity	(i) Allows reduction of antigen dose (ii) Well tolerated (iii) Useful in children (iv) Mixed Th1/Th2 responses
Polymeric MPs and NPs	(i) Enhance IL-1 β secretion by DCs	(i) Biodegradable and biocompatible (ii) Release during long time periods (iii) Modulation of the delivery: continuous, by pulses, or triggered by several factors (pH, temperature, ionic strength, electric or magnetic fields) (iv) Elicit humoral and cellular immunity
Liposomes	(i) Passive targeting (ii) Tendency to interact with macrophages	(i) CD4 ⁺ , CD8 ⁺ and CTL immune responses (ii) Modulation of the immune response using different lipids
VLPs	(i) Taken up by APCs and MHC class I and II presentation	(i) Incorporation of peptides produced by recombination, or chemically coupling them once the VLP is formed (ii) Potent humoral and cellular immune responses
Virosomes	(i) Enter cells through receptor mediated endocytosis	(i) Membrane fusion properties of the virus are maintained (ii) Humoral and CTL responses (iii) Value for developing multivalent vaccines
ICOMs and ISCOMATRIX	(i) Antigen carrier (ii) Immunostimulation (because of the saponin)	(i) Potent humoral and cellular immune responses (ii) Reduction of the antigen dose (iii) Safe and well tolerated
Nanobeads	(i) Depends on the size: small ones elicit CD8 ⁺ immune response, whereas larger ones facilitate CD4 ⁺ responses	(i) Humoral and cellular immune responses

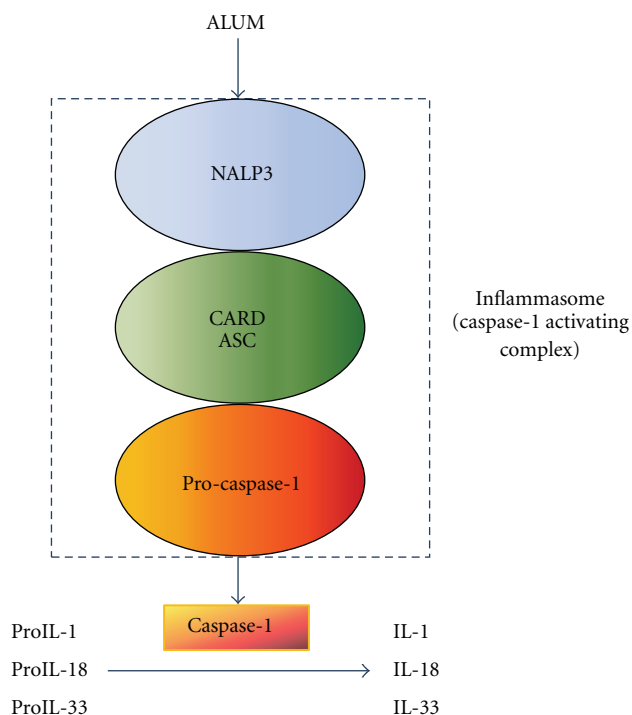


FIGURE 2: Scheme of the potential interaction of alum with the NALP3 inflammasome. Caspase-1 is activated, which in turn, promotes the activation of proinflammatory cytokines IL- β , IL-18, and IL-33. This process is abrogated by actin polymerization inhibitors, suggesting that activation of NALP3 requires phagocytosis.

group. On the other hand, both vaccines generated antibodies with capacity to mediate growth-inhibitory activity against *P. falciparum in vitro*.

However, nowadays, alum adjuvant is being replaced by other systems that improve the immune response achieved, and generally, it is used as a control or in combination with other adjuvants. For example, Raman et al. investigated the immunomodulatory effects of two types of CpG adjuvants intranasally administered with five synthetic peptide antigens of *Plasmodium vivax* in alum and microparticles. The addition of alum to CpG increased four-fold the antibody titers and triggered a predominance of IgG2a/2b isotypes. High titers against one of the peptides have a significant inhibitory effect on parasite development in the mosquito and the peptide-specific antisera reacted with the air-dried parasite antigens isolated from *P. vivax* patients [42].

2.2. Emulsions. Adjuvants composed of emulsions include oil in water (o/w) and water in oil (w/o) systems. There are two formulations approved for human use in Europe, MF59 and AS03. There is also another compound, Montanide, under phase III stage trials.

MF59, a squalene-based o/w emulsion is licensed for influenza vaccine (Fluad). Vaccines with MF59 are safe and have demonstrated a better immunogenicity than nonadjuvanted ones, even in the elderly [44] and childhood [45]. Evaluation of safety data of 64 clinical trials involving MF59

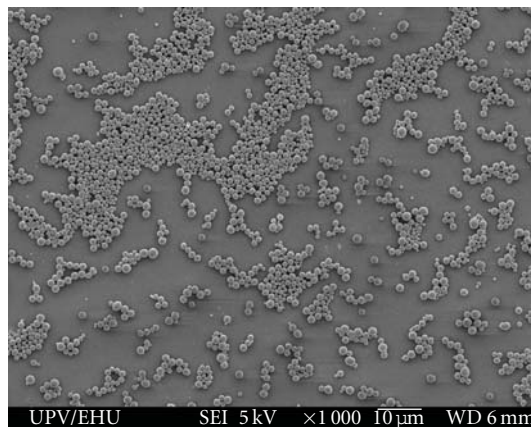


FIGURE 3: Scanning electron micrograph of PLGA microparticles ($\times 10,000$).

revealed that MF59 adjuvanted subjects had lower risks than nonadjuvanted ones of undergoing unsolicited adverse events. On the other hand, MF59 adjuvanted subjects had a higher risk of expected local (mild or moderate pain, injection-site warmth induration, and erythema) or systemic reactions (myalgia, headache, fatigue, and malaise) [46]. The effects of the exposure to MF59 during pregnancy have also been evaluated. Tsai et al. analysed the clinical trial database of Novartis Vaccine studies from 1991 to 2009 and found that distribution of pregnancy outcomes (normal, abnormal, or ending in the therapeutic abortion) was similar in subjects exposed to MF59 compared to non exposed ones at any time of pregnancy, specifically in early pregnancy [47]. Although these data are few to draw definitive conclusions, available observations, so far, indicate no signal of risk.

Despite the wide use of MF59, its mechanism of action is not well understood. Immunofluorescence analysis showed that MF59 promoted antigen uptake by DCs after intramuscular injection [48], which suggest that its adjuvancity is not mediated by a depot effect. A study comparing the adjuvant effect of MF59, alum and CpG, characterized the changes in the expression of genes after intramuscular injection in mice. MF59 was the stronger inducer of cytokines, cytokine receptors, adhesion molecules involved in leukocyte migration, and antigen presentation genes [49]. In this study, it was hypothesised that MF59 combines the antigen delivery function with strong immunostimulating activity. Moreover, it may also promote a sustained antigen-presentation triggering the recruitment of CD11b⁺ monocytes, which might differentiate in functional inflammatory DCs, expressing high levels of MHC class II, as previously described for alum [33].

AS03 is a tocopherol o/w emulsion-based adjuvant used in Pandemrix, an influenza pandemic vaccine. Clinical trials have demonstrated that AS03 adjuvanted vaccines are able to trigger an immune response comparable to that obtained with nonadjuvanted ones using a fourfold lower dose [50]. In addition, the vaccine is well tolerated, and solicited adverse events are transient and mainly mild to moderate in intensity.

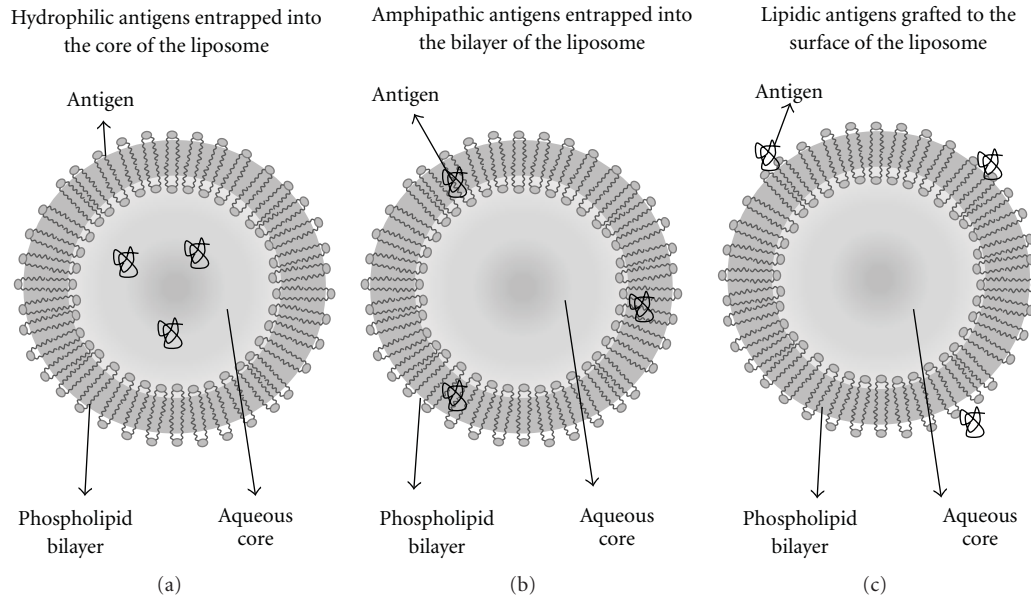


FIGURE 4: Scheme of liposomes structure. Antigens are differently incorporated based on their nature. Hydrophilic antigens can be encapsulated into the aqueous core; amphipathic antigens are integrated into the phospholipid bilayer, and lipidic antigens are adsorbed to the liposomes surface.

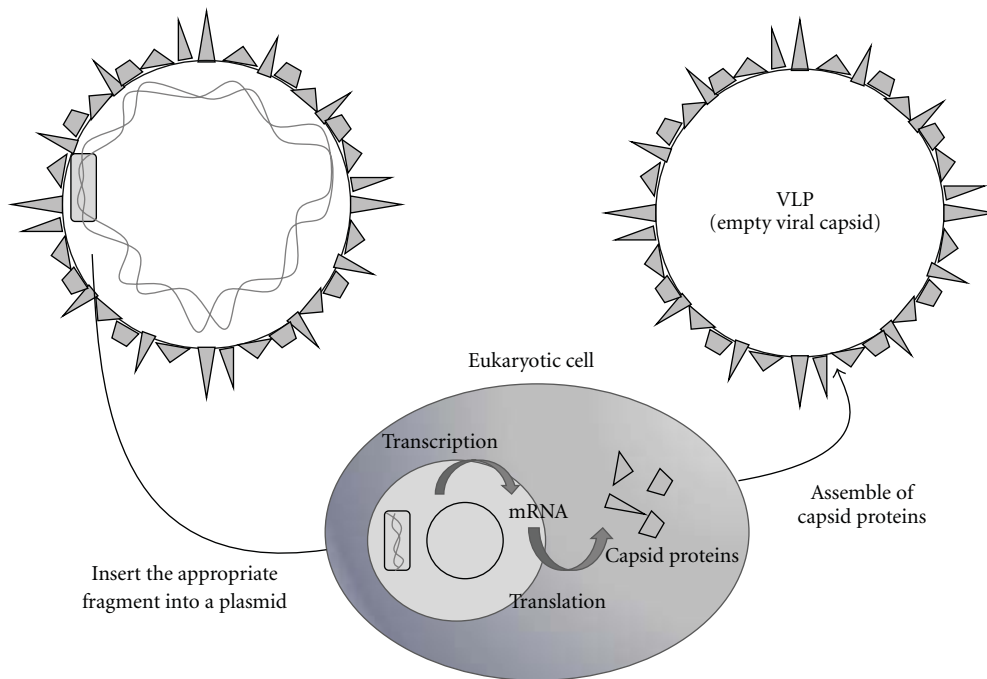


FIGURE 5: Preparation of VLPs. Viral genes encoding for the viral capsid proteins are inserted into a plasmid, which is transcribed and translated in a eukaryotic cell. Viral capsid proteins are synthesised and assemble spontaneously into VLPs.

Therefore, a high reduction in the dose of haemagglutinin can be achieved and can induce cross-clade immunity in humans, a prerequisite for an effective pre-pandemic vaccination strategy [51–53]. Moreover, a recent clinical trial suggests that Pandemrix used in children 6–35 months old is highly immunogenic and that overall reactogenicity profile is acceptable although reactions including fever tend to

increase after a second dose [54]. However, to our knowledge, no study has been published that combines the use of synthetic peptides and MF59 or AS03.

Montanide is a w/o emulsion-based adjuvant. Although it is not yet approved for human use, lot of clinical trials are undergoing against several diseases such as malaria, melanoma, or non-small cell lung cancer [55]. A study carried

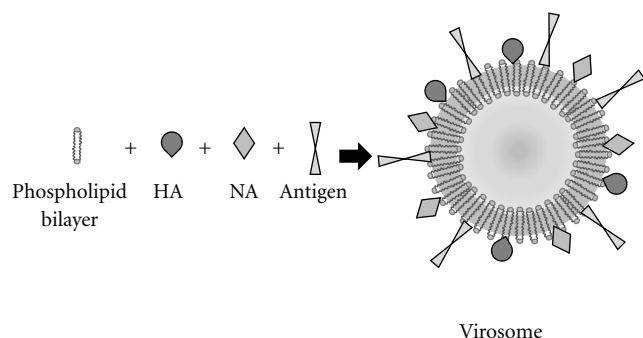


FIGURE 6: Composition of a virosome derived from influenza virus. The envelope of the virus is composed of a phospholipid bilayer and is similar to a liposome. This structure is used as a platform to which other viral components are incorporated. Influenza viruses are often used to prepare virosomes, which maintain the properties of viral haemagglutinin (HA) and neuraminidase (NA). Furthermore, other antigens can be incorporated into the system, allowing the vaccination against other microorganisms.

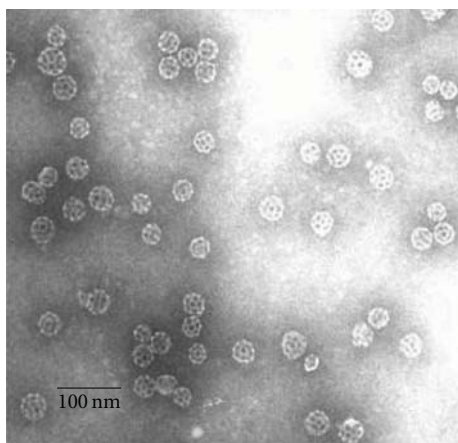


FIGURE 7: Electron micrograph of ISCOMATRIX adjuvant following negative staining. ISCOMATRIX adjuvant particles are typically rigid, hollow, spherical, and cage-like particles approximately 40 nm in diameter. Reproduced with permission from [43].

out in our laboratory, compared the immune response against the S3 malarial synthetic peptide using Montanide, poly-lactide-co-glycolide (PLGA) microparticles and aluminium hydroxide. Subcutaneously administered Montanide and microspheres resulted in effective adjuvants and revealed mixed Th1/Th2 immune responses [56]. However, in a previous study it was shown that Montanide was effective in eliciting antibodies against the 3D7 peptide but not against the FC27 peptide [57]. In addition, a recent clinical trial has been carried out to evaluate the safety, tolerability, and immunogenicity of mixtures of N, R, and C long synthetic peptides derived from the *P. vivax* circumsporozoite protein formulated in two types of Montanide (ISA 720 and ISA 51) [58]. However, the results of this study are not yet published.

2.3. Polymeric Micro- and Nanoparticles. Polymeric micro- and nanoparticle-based vaccine delivery systems have been

widely studied. The most commonly used polymers are poly(D,L-lactic-co-glycolic) acid (PLGA) and its derivatives (Figure 3), due to their inherent advantages over other systems. They are biodegradable and biocompatible, are able to release molecules during long periods of time (weeks or months), and they are easy to administer via injection [59] or orally [60]. In addition, PLGA has been approved for human use in sutures [61], bone implants [62], and screws [63] as well as in implants for sustained drug delivery [64]. Apart from PLGA, other polymers have also been used for vaccination purposes, such as alginate [65], chitin [66], albumin [67], sodium polyacrylate [68], chitosan [69], poly- ϵ -caprolactone [70], or poly(γ -glutamic acid) [71] as well as some polymer combinations [72, 73].

In these formulations, the antigen can be either entrapped or adsorbed on the surface of the particles. The delivery of the antigen can be slow and continuous, by pulses or it can be triggered by external or environmental factors such as changes in the pH [74], temperature [75], ionic strength [76], or electric and magnetic fields [77].

The particle size and size distribution are important factors to determine antigen release rate, as the total surface area for protein delivery depends on the particle size [78]. With regard to particle size, it has been shown that it can influence the type of immune response achieved. In fact, nano- and microparticles (NPs and MPs) do not have the same behaviour *in vivo*. Kanchan and Panda showed that HBsAg-loaded polylactide MPs (2–8 μm) elicited higher and long-lasting antibody titers and were not taken up by macrophages but were on their surface. In addition, MPs promoted IL-4 secretion and upregulation of MHC class II molecules and favoured Th2 immune response. On the other hand, NPs (200–600 nm) were efficiently phagocytized by macrophages and elicited lower antibody titers, but higher levels of IFN- γ production, upregulation of MHC class I molecules along with antibody isotypes favouring Th1-type immune response [79]. Moreover, Manolova et al. demonstrated that intradermally administered small-sized polystyrene particles (≤ 200 nm) were rapidly transported to the lymph nodes, where they were taken up by resident DCs. In contrast, large particles (500–2000 nm) depended on cellular transport by skin DCs [80]. Despite these differences, it is not clear which type of particle would be better for each particular case; therefore, particle size would be individually studied.

On the other hand, the administration route of particles may influence the immune response elicited. Mohanan et al. [81] have studied the bias of the immune response in mice when immunised by different routes, such as the subcutaneous, intradermal, intramuscular, and intralymphatic routes with ovalbumin-loaded liposomes, N-trimethyl-chitosan NPs and PLGA MPs, all with and without immune-response modifiers. This study has demonstrated that the IgG2a associated with Th1 immune response is sensitive to the route of administration, whereas IgG1 response associated with Th2 response was relatively insensitive to the administration route of particulate delivery systems.

Regarding to the mechanism of action, it has been shown that similarly to alum, PLGA microspheres enhance

IL-1 β secretion by DCs, in addition to trigger caspase-1 activation. These abilities require particle uptake by DCs and NALP3 activation [82]. Although the presence of a TLR agonist was required to induce IL-1 β release *in vitro*, injection of the particles in the absence of a TLR agonist induced IL-1 β production at the injection site, indicating that endogenous factors can synergize with particles to promote inflammasome activation. This study also showed that the enhancement of antigen-specific antibody production by microparticles was independent of NALP3, but it was needed in order to microspheres promote antigen-specific IL-6 production by T cells and recruitment and activation of CD11b⁺ Gr1⁻ cells. However, other studies showed that administration of LPS-modified PLGA microspheres loaded with antigen (ovalbumin), were preferentially internalized by DCs compared to nonmodified particles. In addition, these particles elicited potent humoral and cellular immunity against ovalbumin, and wild-type macrophages increased the release of IL-1 β , consistent with inflammasome activation [83]. These data highlight that there is still controversy with the mechanism of action of polymeric micro- and nanoparticles.

PLGA micro- and nanospheres can be used for systemic or mucosal immunization [84–86]. PLGA-based systems are able to be phagocytosed by DCs, even by the oral route [87] and enhance their immunostimulatory capacity [88], leading to the upregulation of maturation markers CD40 and CD80 and release of IL-6. It has been shown that Hp91 synthetic peptide (a peptide that can induce potent antigen-specific cytotoxic T-lymphocyte responses), both encapsulated or conjugated to the surface of PLGA nanoparticles, is able to activate both human and mouse DCs more potently than the free peptide [88].

PLGA microspheres have been extensively studied by our research group. Different synthetic peptides have been entrapped into these microspheres, such as malarial SPf66, and have been administered by subcutaneous, intradermal [89], oral [17], or nasal [90] routes in mice. Microencapsulated SPf66 induced a superior immune response than the one obtained with the administration of the peptide adjuvanted with alum and comparable with the response obtained with FCA. In addition, these particles have been administered to Aotus monkeys leading to high antibody levels and protection against *P. falciparum* challenge [91].

To our knowledge, only one clinical trial has been carried out using PLGA and synthetic peptides [92]. This phase I study evaluated the safety and immunogenicity of a synthetic HIV peptide (HIV-1 MN V3) administered intramuscularly with alum and a similar product encapsulated into PLGA microspheres administered by the oral route. However, the oral administration of this vaccine did not trigger significant humoral, cellular, or mucosal immune responses.

2.4. Liposomes. Liposomes are synthetic spheres comprised by phospholipid bilayers (Figure 4). According to their structure and size, liposomes can be classified into multilamellar vesicles (MLV), small unilamellar vesicles (SUV), intermediate unilamellar vesicles (IUV), or large unilamellar vesicles (LUV) [93]. For vaccine delivery, antigens can be

encapsulated into the aqueous core, integrated in the lipid bilayer or adsorbed on the surface [4].

The mechanism of action of liposomes is not well defined. Passive targeting, derived of their particulate nature, and tendency to interact with macrophages is likely to be an important factor, particularly for nontargeted liposomes [94]. Among the different lipids available, cationic ones have a better ability to initiate and potentiate the immune response. It has been shown that positive charge is an important factor for the retention of liposomes at the injection site. Neutral liposomes have been shown limited in their ability to mediate long-term antigen presentation to circulating antigen-specific T cells and to induce the Th1 and Th2 arms of the immune system, as compared to cationic liposomes. The neutral liposomes did, however, induce the production of IL-5 at levels comparable to cationic liposomes, indicating that they can induce weak Th2 response [95].

Liposomes composition may also affect the type of immune response achieved. The inclusion of a fusogenic lipid in the formulation (i.e., easily fuses with the lipid membranes), such as DOPE, leads to superior IgG2a response against OVA, indicative of directing towards a Th1 response [96].

Coupling antigens to the liposomal surface can lead to CD4⁺, CD8⁺ T, and CTL immune responses. CTL epitopes composed of synthetic peptides derived from severe acute respiratory syndrome (SARS) coronavirus (SARS-CoV) and coupled to the surface of liposomes were effective for peptide-specific CTL induction in mice. One of these peptides was also able to clearance vaccinia virus which expressed epitopes of SARS-CoV after a challenge, suggesting that surface-linked liposomal peptides might offer an effective CTL-based vaccine against this disease [97]. On the other hand, it has been demonstrated that even small amounts of antigen entrapped into liposomes can induce IgG2a antibodies, the bias towards Th1 is more pronounced when more antigen is entrapped [96].

Liposomes can also induce antigen-specific antitumor immunity. Liposomes grafted to synthetic peptides derived from DCs maturation signals, such as HMGB1 (high-mobility group box 1), are able to target macrophages and DCs *in vitro* and *in vivo*. Coupling these liposomes to tumor derived plasma membrane vesicles inhibited tumor growth and metastasis after a tumor challenge in mice [98].

2.5. Virus Like Particles and Virosomes. Virus like particles (VLPs) are obtained when viral structural proteins are produced in recombinant expression systems or even in cell-free systems [99, 100]. Recombinant viral structural proteins of several viruses can spontaneously assemble into VLPs in the absence of the viral genetic material and other viral proteins, which makes them non infectious (Figure 5). VLPs are able to incorporate peptide vaccines, either produced by recombination (genetically fused to the gene which encodes for the VLP), or chemically coupling peptides to the formed VLP [101, 102]. Pejavar-Gaddy et al. generated bovine papillomavirus (BPV) VLPs that were chemically

coupled to a synthetic derivative of MUC1 (human mucin-1) peptide [103]. This peptide is aberrantly expressed on a wide range of ductal adenocarcinomas and has been intensively studied as a candidate cancer vaccine antigen. MUC1-conjugated VLPs were subcutaneously administered to MUC1 transgenic mice, leading to a robust activation of bone marrow-derived DCs, which presented the antigen to MUC1-specific T cells. In addition, immunization of human MUC1 transgenic mice, where MUC1 is a selfantigen, with the VLP vaccine induced MUC1-specific CTL, delayed the growth of MUC1 transplanted tumors and elicited complete tumor rejection in some animals. This study and others [102, 104] demonstrate that VLP could be efficiently taken up by APCs, leading to both MHC class II and I presentation. In addition, VLPs are able to induce potent antiviral humoral and cellular immune responses [105–107].

Several vaccines based on VLPs are currently approved for human use (Gardasil and Cervarix), demonstrating that VLP provide an appropriate immunity against papillomavirus [27, 29, 108]. Moreover, other VLP-based vaccines are under development, including vaccines against influenza [109, 110], HIV [111], or Norwalk virus [112], and in clinical trials [113].

Virosomes are similar to virus-like particles, consisting of reconstituted viral envelopes lacking the viral genetic material. They are generated from virus by a detergent solubilization and reconstitution procedure [114]. The main difference with VLPs is that VLPs are self-assembled viral capsid proteins, while virosomes use the envelope phospholipid bilayers as a platform to which additional viral components or antigens are attached (Figure 6) [4]. Virosomes may be produced from a variety of enveloped viruses although the most used one is the influenza virus. In fact, virosomal approved vaccines (Inflexal and Epxal) are composed of influenza virosomes [24, 25]. Influenza virosomes possess membrane fusion properties very similar to the native virus, because they maintain the receptor-binding and membrane fusion activity of the viral haemagglutinin. Therefore, virosomes enter cells through receptor-mediated endocytosis, but this process does not result in the infection of cells, because virosomes lack the viral RNA [115].

Foreign macromolecules, including synthetic protein antigens, can be encapsulated in virosomes during the reconstitution process. These virosomes are able to induce a powerful class I MHC-restricted CTL response, mainly because they will deliver their content to the cell cytosol [116], which favours the cross-presentation. This makes virosomes possible to be used as a suitable delivery system in tumor immunotherapy [117].

On the other hand, a fraction of the particles will inevitably be degraded within the endosomal/lysosomal compartment. The resulting peptides will be able to associate with MHC II molecules, resulting in CD4⁺ response [116]. Development of antibody responses have been found upon administration of malarial synthetic antigens containing virosomes. In fact, IgG antibodies against UK-39 (a synthetic peptide derived from the circumsporozoite protein of *P. falciparum*) inhibited invasion of hepatocytes by *P. falciparum* sporozoites [118]. A second peptide (AMA49-C1) based on

domain III of apical membrane antigen 1 induced antibodies that inhibited blood-stage parasite growth *in vitro* [119]. Combination of both antigens into different virosomes did not affect negatively the anti-peptide antibody titers in mice or rabbits, demonstrating the value of this system for the development of multivalent vaccines [120]. In addition, a phase I clinical trial has been carried out in order to evaluate the safety and immunogenicity of two virosome-formulated *P. falciparum* derived synthetic peptide antigens (AMA 49-CPE and UK39) [121]. Both vaccines resulted safe, as no serious or severe adverse events were observed. In terms of immunogenicity, both formulations elicited already an antibody specific response in all volunteers with the appropriate dose.

2.6. ISCOMS and ISCOMATRIX. Immunostimulatory complexes (ISCOMs) are cage-like structures, approximately of 40 nm in diameter composed of antigen, cholesterol, phospholipid, and saponin, held together by hydrophobic interactions, so typically entrapped antigens are amphipathic. The most commonly used saponin is QuilA or its purified compounds [5, 122]. ISCOMATRIX has essentially the same structure as ISCOMs but lacks the antigen, which can be subsequently added (Figure 7). This fact provides ISCOMATRIX for more general applications as they are not limited to amphipathic antigens [4, 122]. Although numerous studies have been carried out with animal models [123–126], few clinical trials evaluating ISCOMs and ISCOMATRIX are currently in course [127].

ISCOMs are not immunogenic by themselves although other saponins different from QuilA are used [43, 128], but when the antigen is incorporated, they can trigger humoral, mucosal, and cellular immune responses [128]. Different results have been obtained when evaluating ISCOMs immunogenicity. For instance, Agrawal et al. [129] administered in the footpad of mice different HIV-1 derived synthetic peptides, with and without an immunoadjuvant, in liposomes or ISCOMs and compared to the administration of peptides with alum. In contrast to alum, both liposomes and ISCOMs induced a predominant Th1 like response. On the other hand, Pahar et al. [123] found that intrarectal immunization of macaques with two HIV-derived peptides (HIV-1_{env} and SIV_{gag}) incorporated into ISCOMs induced low level of immunity against simian-HIV. These differences may be due to the antigens used, differences in the administration route, dose, or schedule.

ISCOMATRIX adjuvant facilitates antigen delivery and presentation as well as immunomodulation to provide enhanced and accelerated immune responses. Moreover, it is capable of inducing broad and potent humoral and cellular immune responses including both CD4⁺ and CD8⁺T cell responses [130, 131]. The antibody response is often achieved with lower amounts of antigen than with other adjuvant systems [132]. Additionally, ISCOMATRIX adjuvant can be used in vaccines for induction of mucosal immune responses [133, 134]. In fact, protective ability of ISCOMATRIX adjuvanted vaccines has been reported [135], and they have been used in some veterinarian vaccines [136].

ISCOMATRIX adjuvants are also effective in the field of cancer treatment. NY-ESO-1 is a protein expressed in many cancers. This recombinant protein with ISCOMATRIX adjuvant has been evaluated in a clinical trial [137] demonstrating that the vaccine is safe and highly immunogenic. Recently, Ebert et al. have studied the effects of a NY-ESO-1 peptide synthetic derivate (NY-ESO-1_{60–72}/HLA-B7 tetramer) with ISCOMATRIX in humans. They have found that this vaccine formulation allows DCs to cross-present the NY-ESO-1_{60–72} epitope efficiently and generates a potent T cell response.

Regarding to safety concerns, Anderson et al. have pooled and analyzed the safety data obtained from a number of vaccine development programs comprising ISCOMATRIX. Overall, the ISCOMATRIX vaccines were found to be safe and well tolerated, with no vaccine-related deaths or serious adverse events. Reactogenicity at the injection site was found to be the most frequent adverse event compared with subjects who received placebo or active comparator; however, this reactogenicity was generally mild, self-limiting, and of short duration. Until the end of the study, ISCOMATRIX vaccines have not been associated with events suggestive of autoimmune or allergic disorders nor events of anaphylaxis [138].

Recently, cationic immune stimulating complexes have been developed (PLUSCOMs). In contrast to ISCOMs, PLUSCOMs are able to incorporate hydrophilic peptides adsorbed onto their surfaces by ionic interactions. In addition, they are as effective as classic ISCOMs in inducing antigen-specific CD8⁺ T cell responses [139].

2.7. Nanobeads. The use of nanobeads as vaccine carrier/adjuvant systems implies the coupling of solid inert beads, generally made of carboxylated polystyrene, with an antigen [5]. Beads of 40–50 nm are better internalized by DCs than higher ones and induce CD8⁺ type immune response, whereas larger beads facilitate CD4⁺ response [140]. Other studies carried out *in vivo* were in accordance to this finding. Particles in this size range could elicit antibody and cell immunity in mice, as well as provide protection after a tumor challenge [9, 141]. Later, these findings were also confirmed in sheep [142, 143]. For instance, administration of multiple synthetic peptides derived from foot-and-mouth disease virus conjugated separately to individual nanobeads or conjugated as a mixture, were able to induce significant cell-mediated and humoral immune responses in sheep administered intradermally [143].

3. Current Approaches to Improve the Immunogenicity of Particulated Systems

The development of successful vaccines implies the production of an appropriate immune response against a given pathogen. This approach concerns immunological, biotechnological, and pharmaceutical aspects, as the interaction between DCs and T lymphocytes, selection of appropriate antigens and adjuvants, and the production of a stable end product must be taken into account [15]. In some cases, vaccine delivery systems have been sufficient to

induce a long lasting protective immunity. However, poorly immunogenic antigens, such as synthetic peptides, are often unable to induce a protective immunity when incorporated into delivery systems alone and require the incorporation of immune potentiating molecules [8]. Immune potentiators activate innate immune receptors of APCs (named pathogen recognition receptors—PRRs), which recognize pathogen associated molecular patterns (PAMPs). Among PRRs, signalling receptors act as primary sensor of pathogens and damage, and finally trigger both effector and adaptive immune responses. These receptors can be located on the plasma membrane, in different internal compartments, or in membranes from intracellular vesicles, or can be cytosolic proteins [144]. Three families of signalling receptors have been identified: TLRs, NLRs, and RLRs. Members of TLR family recognize bacteria, viruses, fungi and protozoa; NLRs detect bacteria and RLRs are antiviral. It is likely that interaction between these families provides synergistic or cooperative signalling [145]. In addition, other PRRs (humoral proteins and endocytic receptors) have a critical role in activating antigen presentation [144, 146].

The activation of PRRs by immune potentiators induces the secretion of proinflammatory cytokines and type I interferon, the upregulation of costimulatory molecules and MHC class II molecules. In addition, PRRs also trigger the migration of APCs from the injection site to the T cell areas of the draining lymph nodes. All these processes are needed for activation of naive T cells and the development of both humoral and cellular immune responses [147]. Thus, formulation of vaccines that target PRRs is an interesting approach in order to improve their immune response.

Traditionally, antigens have been formulated into their soluble form plus an immune potentiating molecule [148, 149] or were entrapped into delivery systems alone [89, 150]. Current tendency is to combine more than one adjuvant into the same vaccine formulation in order to achieve the desired immune response.

3.1. Combination of Adjuvants with Different Action Mechanism. It has been shown that combination of adjuvants can increase the immune response. For this reason, most of the novel vaccine formulations comprise a combination of adjuvants.

The most common combination of adjuvants with different action mechanism is the use of a vaccine delivery system which contains the antigen and an immune potentiating adjuvant. For instance, combination of PLGA nanoparticles coencapsulating the poorly immunogenic melanoma antigen, tyrosinase-related protein 2 (TRP2), along with Toll-like receptor 4 ligand (TLR4) (7-acyl lipid A) led to a therapeutic antitumor effect against melanoma after the subcutaneous administration to mice [151].

Although they do not contain synthetic peptides, some of the licensed vaccines are comprised of a mixture of adjuvants, such as Gardasil (composed of VLPs and alum), Fendrix (comprising AS04, approved for human use in Europe and USA), or Cervarix (which includes AS04 and VLPs). These vaccines present a high immunogenicity and are safe [26, 152].

3.2. *Targeting Antigens to Dendritic Cells.* Vaccine delivery systems can incorporate ligands in order to specifically target APCs receptors. It has been shown that ligand grafting can enhance the uptake of microparticles by immune cells. Brandhonneur et al. [153] studied the uptake of different ligand-grafted PLGA microspheres by alveolar macrophages of pigs *ex vivo*. Three different ligands were used: WGA (lectin weat germ agglutinin, which interacts with lectin receptors), a RGD (arginine-glycine-aspartate) containing peptide (interacting on integrins), and a carbohydrate moiety (mannose-PEG₃-NH₂, interacting on mannose receptor). A much higher uptake was observed for mannose-, WGA-, and RGD-grafted microspheres, mainly because of the specific mechanism of phagocytosis. When other ligands were grafted to the microspheres (peptides like BSA—bovine serum albumin or RAD—arginine-alanine-aspartame), the uptake was not significantly different from ungrafted microspheres, due to the nonspecific mechanism of uptake, given the lack of receptors for BSA and RAD into macrophages.

Among PRR ligands, TLR ligands have been widely studied. TLR activation leads to upregulation of CD40, CD80, CD86, and CD70 costimulatory molecules in the surface of APCs, as well as release of Th1 cytokines such as IL-1, IL-2, IL-6, and TNF. In addition, some ligands are able to trigger cross-presentation. Therefore, TLRs facilitate coordination between innate and adaptive immunities by activating B and T cells as well as memory responses [154]. It has been shown that antigens and TLR ligands can generate more potent immune responses when coencapsulated into the same particle [155]. This can be understood taking into account that endosomal organelles of DCs express some TLRs, in addition to possess machinery to process captured antigens and present them into MHC molecules. Consequently, simultaneous delivery of antigen and TLR-ligands into the cytosol may lead to a better DC activation and subsequent development of immune response.

There exist at least 13 members of TLRs, which recognize different microbial components. For instance, TLR2 recognize bacterial lipoproteins and lipopeptides in cooperation with TLR1 or TLR6 [156], TLR4 binds LPS [157], TLR3 recognizes double stranded RNA [158], TLR5 attaches to flagellin [159], TLR7 and TLR8 recognize single-stranded viral RNA [160] and synthetic imidazoquinolines [161], and TLR9 recognizes DNA rich in nonmethylated CpG (cytosine-phosphorothioate-guanine) [162].

One of the most widely used immunopotentiating adjuvants are those which interact with TLR9, either CpGs present into bacterial or viral DNA or synthetic CpG oligodeoxynucleotides (CpG ODN) [163]. Vaccination with liposomes containing synthetic peptides derived from lymphocytic choriomeningitis virus (LCMV) and CpG motifs by intramuscular route, resulted in the efficient induction of antiviral CD8⁺ T cell responses and complete protection against not only LCMV but also against a highly virulent mutant strain. Moreover, the intranasal administration induced mucosal immunity able to protect mice from the virus challenge, even using a low dose [164].

Other frequently used TLR ligands are those directed to TLR3. Poly(inosinic-cytidilic) acid, that is, poly(I:C), is

a synthetic analogue of double-stranded RNA which exerts its function via TLR3 [165]. Poly(I:C) induces maturation of DCs [166], is a potent IFN inducer and can activate monocytes and NK cells to produce proinflammatory cytokines and chemokines [167]. Furthermore, poly(I:C) is able to enhance specific antitumor immunity against synthetic peptide-based vaccines by inducing CTL response [168], mainly because it allows cross-priming [169]. It has been shown that fluorescent-BSA-loaded PLGA microparticles including poly(I:C) are effectively phagocytized by DCs *ex vivo* and induce a maturation similar to that achieved with a cytokine cocktail or higher concentrations of soluble poly(I:C) [170]. Besides, murine splenic DCs pulsed with polyketal-OVA-poly(I:C) microparticles induce higher percentage of IFN- γ -producing CD8⁺ T cells than DCs treated with polyketal-OVA particles or soluble OVA/poly(I:C) [171].

In addition to targeting TLRs, other delivery systems have been prepared which target other DC receptors. These carriers incorporate antibodies or molecules that specifically interact with receptors such as DC-SIGN [172] or DEC-205 [173] and have the ability to trigger the phagocytosis of entrapping synthetic peptides by DCs and promote their maturation.

4. Conclusion

Vaccination with subunit vaccines comprised of synthetic proteins and peptides is not always successful, because they can be degraded by proteases, possess limited bioavailability, and present relatively low immunogenicity. Delivery systems are able to overcome these problems, since they protect proteins from degradation and increase their bioavailability allowing the cross of biological membranes. With regard to immune response, delivery systems can improve and/or modulate the response achieved with soluble peptides alone. Although it has been proposed that they exert their adjuvancy by generating a depot effect at the injection site, currently, other action mechanism have been found which better explain the modulation or improvement of the immune response. Carriers can be passively directed and subsequently endocytized by APCs and deliver the antigen to the cytosol or intracellular organelles. In addition, they can interact with protein complexes, such as inflammasome, to activate immune response. Furthermore, they can incorporate other immunostimulatory molecules which may improve or modulate the immune response in order to develop not only humoral but also cellular immunity.

Delivery systems also possess other advantages; they are safe, stable, and reproducible. Besides, they can be administered by several routes, which offer the possibility of developing both mucosal and systemic immune responses.

All these features have led to the approval of some of these systems to clinical use, such as VLPs, virosomes, or traditional alum. Although these adjuvants are able to trigger appropriate immune responses against certain pathogens, the future in this field will be focused on the development of combined vaccines to better design the induction of an appropriate immune response.

Abbreviations

APCs:	Antigen-presenting cells
ASC:	Apoptosis-associated speck-like protein
BCG:	Bacillus Calmette-Guerin
BPV:	Bovine papillomavirus
BSA:	Bovine serum albumin
CoV:	Coronavirus
CpG:	Cytosine-phosphorothioate-guanine
CTL:	Cytolytic immune response
DCs:	Dendritic cells
HBsAg:	Hepatitis B surface antigen
HIV:	Human immunodeficiency virus
HMGB1:	High-mobility group box 1
IFN:	Interferon
IL:	Interleukin
IP:	Inducible protein
ISCOMs:	Immunostimulatory complexes
IUV:	Intermediate unilamellar vesicles
LCMV:	Lymphocytic choriomeningitis virus
LUV:	Large unilamellar vesicles
MHC:	Major histocompatibility complex
MLV:	Multilamellar vesicles
MPL:	Monophosphoril lipid A
MPs:	Microparticles
MUC1:	Human mucin-1
NKT cells:	Natural killer T cells
NLR:	Nod-like receptor
NLRP3 or NALP3:	NOD-like receptor protein 3
NPs:	Nanoparticles
o/w:	Oil in water
OVA:	Ovalbumin
PAMPs:	Pathogen associated molecular patterns
PLGA:	Poly(D,L-lactic-co-glycolic) acid
PLUSCOMs:	Cationic immune stimulating complexes
Poly(I:C):	Poly(inosinic-cytidilic) acid
PRRs:	Pathogen recognition receptors
RAD:	arginine-alanine-aspartame
RGD:	arginine-glycine-aspartate
RLR:	Rig-like receptor
RNA:	Ribonucleic acid
SARS:	Severe acute respiratory syndrome
SUV:	Small unilamellar vesicles
TLR:	Toll like receptor
TRP2:	Tyrosinase-related protein 2
VLPs:	Virus like particles
w/o:	Water in oil
WGA:	Lectin weat germ agglutinin.

Acknowledgments

This project was partially supported by the “Ministerio de Ciencia e Innovación” (SAF2007-66115) and FEDER funds. A. Salvador thanks the “Universidad del País Vasco” for the Fellowship Grant.

References

- [1] Y. Perrie, A. R. Mohammed, D. J. Kirby, S. E. McNeil, and V. W. Bramwell, “Vaccine adjuvant systems: enhancing the efficacy of sub-unit protein antigens,” *International Journal of Pharmaceutics*, vol. 364, no. 2, pp. 272–280, 2008.
- [2] FDA, United States Food and Drug Administration, “Complete list of vaccines licensed for immunization and distribution in the US,” 2010, <http://www.fda.gov/BiologicsBloodVaccines/Vaccines/ApprovedProducts/ucm093833.htm>.
- [3] M. Look, A. Bandyopadhyay, J. S. Blum, and T. M. Fahmy, “Application of nanotechnologies for improved immune response against infectious diseases in the developing world,” *Advanced Drug Delivery Reviews*, vol. 62, no. 4-5, pp. 378–393, 2010.
- [4] L. J. Peek, C. R. Middaugh, and C. Berkland, “Nanotechnology in vaccine delivery,” *Advanced Drug Delivery Reviews*, vol. 60, no. 8, pp. 915–928, 2008.
- [5] J. C. Aguilar and E. G. Rodríguez, “Vaccine adjuvants revisited,” *Vaccine*, vol. 25, no. 19, pp. 3752–3762, 2007.
- [6] V. W. Bramwell, J. E. Eyles, and H. O. Alpar, “Particulate delivery systems for biodefense subunit vaccines,” *Advanced Drug Delivery Reviews*, vol. 57, no. 9, pp. 1247–1265, 2005.
- [7] S. Chadwick, C. Kriegel, and M. Amiji, “Nanotechnology solutions for mucosal immunization,” *Advanced Drug Delivery Reviews*, vol. 62, no. 4-5, pp. 394–407, 2010.
- [8] N. Azad and Y. Rojanasakul, “Nanobiotechnology in drug delivery,” *American Journal of Drug Delivery*, vol. 4, no. 2, pp. 79–88, 2006.
- [9] D. T. O’Hagan and E. De Gregorio, “The path to a successful vaccine adjuvant—the long and winding road,” *Drug Discovery Today*, vol. 14, no. 11-12, pp. 541–551, 2009.
- [10] R. Steinman, “Dendritic cells and vaccines,” *Baylor University Medical Center Proceedings*, vol. 21, no. 1, pp. 3–8, 2008.
- [11] Center for Drug Evaluation and Research (CDER) and Center for Biologics Evaluation and Research (CBER), 1994, http://www.seoho.biz/GMP_Quick_Search/Data/1.%20FDA%20Documents/1.6.29.pdf.
- [12] P. Blanco, A. K. Palucka, V. Pascual, and J. Banchereau, “Dendritic cells and cytokines in human inflammatory and autoimmune diseases,” *Cytokine and Growth Factor Reviews*, vol. 19, no. 1, pp. 41–52, 2008.
- [13] K. C. McCullough and A. Summerfield, “Targeting the porcine immune system-particulate vaccines in the 21st century,” *Developmental and Comparative Immunology*, vol. 33, no. 3, pp. 394–409, 2009.
- [14] E. De Gregorio, U. D’Oro, and A. Wack, “Immunology of TLR-independent vaccine adjuvants,” *Current Opinion in Immunology*, vol. 21, no. 3, pp. 339–345, 2009.
- [15] M. G. Carstens, “Opportunities and challenges in vaccine delivery,” *European Journal of Pharmaceutical Sciences*, vol. 36, no. 4-5, pp. 605–608, 2009.
- [16] D. S. Kohane, “Microparticles and nanoparticles for drug delivery,” *Biotechnology and Bioengineering*, vol. 96, no. 2, pp. 203–209, 2007.
- [17] A. Schoubben, P. Blasi, S. Giovagnoli, L. Perioli, C. Rossi, and M. Ricci, “Novel composite microparticles for protein stabilization and delivery,” *European Journal of Pharmaceutical Sciences*, vol. 36, no. 2-3, pp. 226–234, 2009.
- [18] A. M. Carcaboso, R. M. Hernández, M. Igartua et al., “Immune response after oral administration of the encapsulated malaria synthetic peptide SPf66,” *International Journal of Pharmaceutics*, vol. 260, no. 2, pp. 273–282, 2003.

- [19] E. Tritto, F. Mosca, and E. De Gregorio, "Mechanism of action of licensed vaccine adjuvants," *Vaccine*, vol. 27, no. 25–26, pp. 3331–3334, 2009.
- [20] FDA United States Food and Drug Administration, "Vaccines licensed for immunization and distribution in the US with supporting documents," 2010, <http://www.fda.gov/BiologicsBloodVaccines/Vaccines/ApprovedProducts/ucm093830.htm>.
- [21] P. Van Damme, G. Minervini, C. L. Liss et al., "Safety, tolerability and immunogenicity of a recombinant hepatitis B vaccine manufactured by a modified process in healthy young adults," *Human Vaccines*, vol. 5, no. 2, pp. 92–97, 2009.
- [22] S. Thoelen, N. De Clercq, and N. Tornieporth, "A prophylactic hepatitis B vaccine with a novel adjuvant system," *Vaccine*, vol. 19, no. 17–19, pp. 2400–2403, 2001.
- [23] M. W. Tregnaghi, R. Voelker, E. Santos-Lima, and B. Zambrano, "Immunogenicity and safety of a novel yeast *Hansenula polymorpha*-derived recombinant hepatitis B candidate vaccine in healthy adolescents and adults aged 10–45 years," *Vaccine*, vol. 28, no. 20, pp. 3595–3601, 2010.
- [24] F. R. Vogel, C. Caillet, I. C. Kusters, and J. Haensler, "Emulsion-based adjuvants for influenza vaccines," *Expert Review of Vaccines*, vol. 8, no. 4, pp. 483–492, 2009.
- [25] T. Jones, "GSK's novel split-virus adjuvanted vaccines for the prevention of the H5N1 strain of avian influenza infection," *Current Opinion in Molecular Therapeutics*, vol. 11, no. 3, pp. 337–345, 2009.
- [26] P. A. Bovier, "Epaxal®: a virosomal vaccine to prevent hepatitis A infection," *Expert Review of Vaccines*, vol. 7, no. 8, pp. 1141–1150, 2008.
- [27] C. Herzog, K. Hartmann, V. Künzi et al., "Eleven years of Inflexal® V-a virosomal adjuvanted influenza vaccine," *Vaccine*, vol. 27, no. 33, pp. 4381–4387, 2009.
- [28] M. Kundi, "New hepatitis B vaccine formulated with an improved adjuvant system," *Expert Review of Vaccines*, vol. 6, no. 2, pp. 133–140, 2007.
- [29] (CDC) Centers of Disease Control and Prevention, "FDA licensure of bivalent human papillomavirus vaccine (HPV2, Cervarix) for use in females and updated HPV vaccination recommendations from the Advisory Committee on Immunization Practices (ACIP)," *Morbidity and Mortality Weekly Report*, vol. 59, no. 20, pp. 626–629, 2010.
- [30] T. W. Dubensky Jr. and S. G. Reed, "Adjuvants for cancer vaccines," *Seminars in Immunology*, vol. 22, no. 3, pp. 155–161, 2010.
- [31] P. Bonanni, C. Cohet, S. K. Kjaer et al., "A summary of the post-licensure surveillance initiatives for GARDASIL/SILGARD," *Vaccine*, vol. 28, no. 30, pp. 4719–4730, 2010.
- [32] M. L. Mbow, E. De Gregorio, N. M. Valiante, and R. Rappuoli, "New adjuvants for human vaccines," *Current Opinion in Immunology*, vol. 22, no. 3, pp. 411–416, 2010.
- [33] M. Kool, T. Soullié, M. Van Nimwegen et al., "Alum adjuvant boosts adaptive immunity by inducing uric acid and activating inflammatory dendritic cells," *Journal of Experimental Medicine*, vol. 205, no. 4, pp. 869–882, 2008.
- [34] H. Li, S. Nookala, and F. Re, "Aluminum hydroxide adjuvants activate caspase-1 and induce IL-1 β and IL-18 release," *Journal of Immunology*, vol. 178, no. 8, pp. 5271–5276, 2007.
- [35] J. W. Mannhalter, H. O. Neychev, G. J. Zlabinger, R. Ahmad, and M. M. Eibl, "Modulation of the human immune response by the non-toxic and non-pyrogenic adjuvant aluminium hydroxide: effect on antigen uptake and antigen presentation," *Clinical and Experimental Immunology*, vol. 61, no. 1, pp. 143–151, 1985.
- [36] L. Franchi and G. Núñez, "The Nlrp3 inflammasome is critical for aluminum hydroxide-mediated IL-1 β secretion but dispensable for adjuvant activity," *European Journal of Immunology*, vol. 38, no. 8, pp. 2085–2089, 2008.
- [37] S. C. Eisenbarth, O. R. Colegio, W. O'Connor, F. S. Suterwala, and R. A. Flavell, "Crucial role for the Nalp3 inflammasome in the immunostimulatory properties of aluminium adjuvants," *Nature*, vol. 453, no. 7198, pp. 1122–1126, 2008.
- [38] H. Li, S. B. Willingham, J. P. Y. Ting, and F. Re, "Cutting edge: inflammasome activation by alum and alum's adjuvant effect are mediated by NLRP3," *Journal of Immunology*, vol. 181, no. 1, pp. 17–21, 2008.
- [39] M. Kool, V. Pétrilli, T. De Smedt et al., "Cutting edge: alum adjuvant stimulates inflammatory dendritic cells through activation of the NALP3 inflammasome," *Journal of Immunology*, vol. 181, no. 6, pp. 3755–3759, 2008.
- [40] B. N. Lambrecht, M. Kool, M. A. Willart, and H. Hammad, "Mechanism of action of clinically approved adjuvants," *Current Opinion in Immunology*, vol. 21, no. 1, pp. 23–29, 2009.
- [41] C. C. Hermsen, D. F. Verhage, D. S. C. Telgt et al., "Glutamate-rich protein (GLURP) induces antibodies that inhibit in vitro growth of *Plasmodium falciparum* in a phase 1 malaria vaccine trial," *Vaccine*, vol. 25, no. 15, pp. 2930–2940, 2007.
- [42] V. S. Raman, A. Bhatia, A. Picone et al., "Applying TLR synergy in immunotherapy: implications in cutaneous leishmaniasis," *Journal of Immunology*, vol. 185, no. 3, pp. 1701–1710, 2010.
- [43] A. M. Daines, B. W. Greatrex, C. M. Hayman et al., "Mannosylated saponins based on oleanolic and glycyrrhizic acids. Towards synthetic colloidal antigen delivery systems," *Bioorganic and Medicinal Chemistry*, vol. 17, no. 14, pp. 5207–5218, 2009.
- [44] D. Sindoni, V. La Fauci, R. Squeri et al., "Comparison between a conventional subunit vaccine and the MF59-adjuvanted subunit influenza vaccine in the elderly: an evaluation of the safety, tolerability and immunogenicity," *Journal of Preventive Medicine and Hygiene*, vol. 50, no. 2, pp. 121–126, 2009.
- [45] T. Vesikari, N. Groth, A. Karvonen, A. Borkowski, and M. Pellegrini, "MF59-adjuvanted influenza vaccine (FLUAD) in children: safety and immunogenicity following a second year seasonal vaccination," *Vaccine*, vol. 27, no. 45, pp. 6291–6295, 2009.
- [46] M. Pellegrini, U. Nicolay, K. Lindert, N. Groth, and G. Della Cioppa, "MF59-adjuvanted versus non-adjuvanted influenza vaccines: integrated analysis from a large safety database," *Vaccine*, vol. 27, no. 49, pp. 6959–6965, 2009.
- [47] T. Tsai, M. H. Kyaw, D. Novicki, P. Nacci, S. Rai, and R. Clemens, "Exposure to MF59-adjuvanted influenza vaccines during pregnancy—a retrospective analysis," *Vaccine*, vol. 28, no. 7, pp. 1877–1880, 2010.
- [48] M. Dupuis, T. J. Murphy, D. Higgins et al., "Dendritic cells internalize vaccine adjuvant after intramuscular injection," *Cellular Immunology*, vol. 186, no. 1, pp. 18–27, 1998.
- [49] F. Mosca, E. Tritto, A. Muzzi et al., "Molecular and cellular signatures of human vaccine adjuvants," *Proceedings of the National Academy of Sciences of the United States of America*, vol. 105, no. 30, pp. 10501–10506, 2008.
- [50] F. Roman, T. Vaman, B. Gerlach, A. Markendorf, P. Gillard, and J. M. Devaster, "Immunogenicity and safety in adults of one dose of influenza A H1N1v 2009 vaccine formulated

- with and without AS03-adjuvant: preliminary report of an observer-blind, randomised trial,” *Vaccine*, vol. 28, no. 7, pp. 1740–1745, 2010.
- [51] D. W. S. Chu, S. J. Hwang, F. S. Lim et al., “Immunogenicity and tolerability of an AS03-adjuvanted prepandemic influenza vaccine: a phase III study in a large population of Asian adults,” *Vaccine*, vol. 27, no. 52, pp. 7428–7435, 2009.
- [52] J. M. Langley, L. Frenette, L. Ferguson et al., “Safety and cross-reactive immunogenicity of candidate AS03-adjuvanted prepandemic H5N1 influenza vaccines: a randomized controlled phase 1/2 trial in adults,” *Journal of Infectious Diseases*, vol. 201, no. 11, pp. 1644–1653, 2010.
- [53] I. Leroux-Roels, F. Roman, S. Forgue et al., “Priming with AS03-adjuvanted H5N1 influenza vaccine improves the kinetics, magnitude and durability of the immune response after a heterologous booster vaccination: an open non-randomised extension of a double-blind randomised primary study,” *Vaccine*, vol. 28, no. 3, pp. 849–857, 2010.
- [54] A. Carmona, F. Omeñaca, J. C. Tejedor et al., “Immunogenicity and safety of AS03-adjuvanted 2009 influenza A H1N1 vaccine in children 6–35 months,” *Vaccine*, vol. 28, no. 36, pp. 5837–5844, 2010.
- [55] Clinicaltrials.gov, “Studies with search of: montanide,” 2010, <http://www.clinicaltrials.gov/ct2/results?term=montanide>.
- [56] E. Mata, M. Igartua, R. M. Hernández, J. E. Rosas, M. E. Patarroyo, and J. L. Pedraz, “Comparison of the adjuvanticity of two different delivery systems on the induction of humoral and cellular responses to synthetic peptides,” *Drug Delivery*, vol. 17, no. 7, pp. 490–499, 2010.
- [57] E. Mata, A. M. Carcaboso, R. M. Hernández, M. Igartua, G. Corradin, and J. L. Pedraz, “Adjuvant activity of polymer microparticles and Montanide ISA 720 on immune responses to Plasmodium falciparum MSP2 long synthetic peptides in mice,” *Vaccine*, vol. 25, no. 5, pp. 877–885, 2007.
- [58] Clinicaltrials.gov, “Safety and immunogenicity study of Plasmodium vivax derived synthetic peptides formulated in two adjuvants (fase1B),” 2010, <http://www.clinicaltrials.gov/ct2/show/NCT01081847?term=Montanide+AND+synthetic+peptides&rank=1>.
- [59] R. C. Mundargi, V. R. Babu, V. Rangaswamy, P. Patel, and T. M. Aminabhavi, “Nano/micro technologies for delivering macromolecular therapeutics using poly(D,L-lactide-co-glycolide) and its derivatives,” *Journal of Controlled Release*, vol. 125, no. 3, pp. 193–209, 2008.
- [60] M. Garinot, V. Fiévez, V. Pourcelle et al., “PEGylated PLGA-based nanoparticles targeting M cells for oral vaccination,” *Journal of Controlled Release*, vol. 120, no. 3, pp. 195–204, 2007.
- [61] S. Madduri, K. Feldman, T. Tervoort, M. Papaloizos, and B. Gander, “Collagen nerve conduits releasing the neurotrophic factors GDNF and NGF” *Journal of Controlled Release*, vol. 143, no. 2, pp. 168–174, 2010.
- [62] F. Wang, Y. L. Song, C. X. Li et al., “Sustained release of insulin-like growth factor-1 from poly(lactide-co-glycolide) microspheres improves osseointegration of dental implants in type 2 diabetic rats,” *European Journal of Pharmacology*, vol. 640, no. 1–3, pp. 226–232, 2010.
- [63] N. J. Cotton, M. J. Egan, and J. E. Brunelle, “Composites of poly(DL-lactide-co-glycolide) and calcium carbonate: in vitro evaluation for use in orthopedic applications,” *Journal of Biomedical Materials Research A*, vol. 85, no. 1, pp. 195–205, 2008.
- [64] S. H. Ranganath, Y. Fu, D. Y. Arifin et al., “The use of submicron/nanoscale PLGA implants to deliver paclitaxel with enhanced pharmacokinetics and therapeutic efficacy in intracranial glioblastoma in mice,” *Biomaterials*, vol. 31, no. 19, pp. 5199–5207, 2010.
- [65] O. Froy, N. Chapnik, and A. Nussinovitch, “Defensin carriers for better mucosal immunity in the digestive system,” *International Journal of Pharmaceutics*, vol. 393, no. 1–2, pp. 263–267, 2010.
- [66] B. J. G. Baaten, B. Clarke, P. Strong, and S. Hou, “Nasal mucosal administration of chitin microparticles boosts innate immunity against influenza A virus in the local pulmonary tissue,” *Vaccine*, vol. 28, no. 25, pp. 4130–4137, 2010.
- [67] G. W. Bumgarner, R. Shashidharamurthy, S. Nagarajan, M. J. D’Souza, and P. Selvaraj, “Surface engineering of microparticles by novel protein transfer for targeted antigen/drug delivery,” *Journal of Controlled Release*, vol. 137, no. 2, pp. 90–97, 2009.
- [68] R. Vialle, L. Dupuis, S. Deville, F. Bertrand, J. Gaucheron, and J. Aucouturier, “Microgel particulate adjuvant: characterisation and mechanisms of action,” *Procedia in Vaccinology*, vol. 2, no. 1, pp. 10–14, 2010.
- [69] B. Slütter, P. C. Soema, Z. Ding, R. Verheul, W. Hennink, and W. Jiskoot, “Conjugation of ovalbumin to trimethyl chitosan improves immunogenicity of the antigen,” *Journal of Controlled Release*, vol. 143, no. 2, pp. 207–214, 2010.
- [70] R. Da Costa Martins, J. M. Irache, J. M. Blasco et al., “Evaluation of particulate acellular vaccines against Brucella ovis infection in rams,” *Vaccine*, vol. 28, no. 17, pp. 3038–3046, 2010.
- [71] T. Uto, T. Akagi, T. Hamasaki, M. Akashi, and M. Baba, “Modulation of innate and adaptive immunity by biodegradable nanoparticles,” *Immunology Letters*, vol. 125, no. 1, pp. 46–52, 2009.
- [72] Y. Yang, Y. Kuang, Y. Liu et al., “Immunogenicity of multiple-epitope antigen gene of HCV carried by novel biodegradable polymers,” *Comparative Immunology, Microbiology and Infectious Diseases*, vol. 34, no. 1, pp. 65–72, 2010.
- [73] A. Caputo, A. Castaldello, E. Brocca-Cofano et al., “Induction of humoral and enhanced cellular immune responses by novel core-shell nanosphere- and microsphere-based vaccine formulations following systemic and mucosal administration,” *Vaccine*, vol. 27, no. 27, pp. 3605–3615, 2009.
- [74] A. Makhlof, Y. Tozuka, and H. Takeuchi, “pH-sensitive nanospheres for colon-specific drug delivery in experimentally induced colitis rat model,” *European Journal of Pharmaceutics and Biopharmaceutics*, vol. 72, no. 1, pp. 1–8, 2009.
- [75] Y. Tang and J. Singh, “Biodegradable and biocompatible thermosensitive polymer based injectable implant for controlled release of protein,” *International Journal of Pharmaceutics*, vol. 365, no. 1–2, pp. 34–43, 2009.
- [76] A. Yang, L. Yang, W. Liu, Z. Li, H. Xu, and X. Yang, “Tumor necrosis factor alpha blocking peptide loaded PEG-PLGA nanoparticles: preparation and in vitro evaluation,” *International Journal of Pharmaceutics*, vol. 331, no. 1, pp. 123–132, 2007.
- [77] N. Butoescu, C. A. Seemayer, M. Foti, O. Jordan, and E. Doelker, “Dexamethasone-containing PLGA superparamagnetic microparticles as carriers for the local treatment of arthritis,” *Biomaterials*, vol. 30, no. 9, pp. 1772–1780, 2009.
- [78] M. Ye, S. Kim, and K. Park, “Issues in long-term protein delivery using biodegradable microparticles,” *Journal of Controlled Release*, vol. 143, no. 2, pp. 241–260, 2010.

- [79] V. Kanchan and A. K. Panda, "Interactions of antigen-loaded polylactide particles with macrophages and their correlation with the immune response," *Biomaterials*, vol. 28, no. 35, pp. 5344–5357, 2007.
- [80] V. Manolova, A. Flace, M. Bauer, K. Schwarz, P. Saudan, and M. F. Bachmann, "Nanoparticles target distinct dendritic cell populations according to their size," *European Journal of Immunology*, vol. 38, no. 5, pp. 1404–1413, 2008.
- [81] D. Mohanan, B. Slütter, M. Henriksen-Lacey et al., "Administration routes affect the quality of immune responses: a cross-sectional evaluation of particulate antigen-delivery systems," *Journal of Controlled Release*, vol. 147, no. 3, pp. 342–349, 2010.
- [82] F. A. Sharp, D. Ruane, B. Claass et al., "Uptake of particulate vaccine adjuvants by dendritic cells activates the NALP3 inflammasome," *Proceedings of the National Academy of Sciences of the United States of America*, vol. 106, no. 3, pp. 870–875, 2009.
- [83] S. L. Demento, S. C. Eisenbarth, H. G. Foellmer et al., "Inflammasome-activating nanoparticles as modular systems for optimizing vaccine efficacy," *Vaccine*, vol. 27, no. 23, pp. 3013–3021, 2009.
- [84] C. Thomas, V. Gupta, and F. Ahsan, "Influence of surface charge of PLGA particles of recombinant hepatitis B surface antigen in enhancing systemic and mucosal immune responses," *International Journal of Pharmaceutics*, vol. 379, no. 1–2, pp. 41–50, 2009.
- [85] R. Ramya, P. C. Verma, V. K. Chaturvedi et al., "Poly(lactide-co-glycolide) microspheres: a potent oral delivery system to elicit systemic immune response against inactivated rabies virus," *Vaccine*, vol. 27, no. 15, pp. 2138–2143, 2009.
- [86] N. Brandhonneur, C. Loizel, F. Chevanne et al., "Mucosal or systemic administration of rE2 glycoprotein antigen loaded PLGA microspheres," *International Journal of Pharmaceutics*, vol. 373, no. 1–2, pp. 16–23, 2009.
- [87] C. Primard, N. Rochereau, E. Luciani et al., "Traffic of poly(lactic acid) nanoparticulate vaccine vehicle from intestinal mucus to sub-epithelial immune competent cells," *Biomaterials*, vol. 31, no. 23, pp. 6060–6068, 2010.
- [88] C. Clawson, C. T. Huang, D. Futalan et al., "Delivery of a peptide via poly(D,L-lactic-co-glycolic) acid nanoparticles enhances its dendritic cell-stimulatory capacity," *Nanomedicine: Nanotechnology, Biology, and Medicine*, vol. 6, no. 5, pp. 651–661, 2010.
- [89] A. M. Carcaboso, R. M. Hernández, M. Igartua, J. E. Rosas, M. E. Patarroyo, and J. L. Pedraz, "Enhancing immunogenicity and reducing dose of microparticulated synthetic vaccines: single intradermal administration," *Pharmaceutical Research*, vol. 21, no. 1, pp. 121–126, 2004.
- [90] A. M. Carcaboso, R. M. Hernández, M. Igartua, J. E. Rosas, M. E. Patarroyo, and J. L. Pedraz, "Potent, long lasting systemic antibody levels and mixed Th1/Th2 immune response after nasal immunization with malaria antigen loaded PLGA microparticles," *Vaccine*, vol. 22, no. 11–12, pp. 1423–1432, 2004.
- [91] J. E. Rosas, J. L. Pedraz, R. M. Hernández et al., "Remarkably high antibody levels and protection against *P. falciparum* malaria in Aotus monkeys after a single immunisation of SPf66 encapsulated in PLGA microspheres," *Vaccine*, vol. 20, no. 13–14, pp. 1707–1710, 2002.
- [92] J. S. Lambert, M. Keefer, M. J. Mulligan et al., "A Phase I safety and immunogenicity trial of UBI® microparticulate monovalent HIV-1 MN oral peptide immunogen with parenteral boost in HIV-1 seronegative human subjects," *Vaccine*, vol. 19, no. 23–24, pp. 3033–3042, 2001.
- [93] R. R. C. New, "Influence of liposome characteristics on their properties and fate," in *Liposomes as Tools in Basic Research and Industry*, J. R. Philippot and F. Schuber, Eds., CRC Press, New York, NY, USA, 1995.
- [94] J. G. Altin and C. R. Parish, "Liposomal vaccines-targeting the delivery of antigen," *Methods*, vol. 40, no. 1, pp. 39–52, 2006.
- [95] M. Henriksen-Lacey, D. Christensen, V. W. Bramwell et al., "Liposomal cationic charge and antigen adsorption are important properties for the efficient deposition of antigen at the injection site and ability of the vaccine to induce a CMI response," *Journal of Controlled Release*, vol. 145, no. 2, pp. 102–108, 2010.
- [96] M. Brgles, L. Habjanec, B. Halassy, and J. Tomašić, "Liposome fusogenicity and entrapment efficiency of antigen determine the Th1/Th2 bias of antigen-specific immune response," *Vaccine*, vol. 27, no. 40, pp. 5435–5442, 2009.
- [97] S. Ohno, S. Kohyama, M. Taneichi et al., "Synthetic peptides coupled to the surface of liposomes effectively induce SARS coronavirus-specific cytotoxic T lymphocytes and viral clearance in HLA-A*0201 transgenic mice," *Vaccine*, vol. 27, no. 29, pp. 3912–3920, 2009.
- [98] A. Faham, D. Bennett, and J. G. Altin, "Liposomal Ag engrafted with peptides of sequence derived from HMGB1 induce potent Ag-specific and anti-tumour immunity," *Vaccine*, vol. 27, no. 42, pp. 5846–5854, 2009.
- [99] L. A. Palomares and O. T. Ramírez, "Challenges for the production of virus-like particles in insect cells: the case of rotavirus-like particles," *Biochemical Engineering Journal*, vol. 45, no. 3, pp. 158–167, 2009.
- [100] B. C. Bundy, M. J. Franciszkowicz, and J. R. Swartz, "Escherichia coli-based cell-free synthesis of virus-like particles," *Biotechnology and Bioengineering*, vol. 100, no. 1, pp. 28–37, 2008.
- [101] G. Guillén, J. C. Aguilar, S. Dueñas et al., "Virus-Like Particles as vaccine antigens and adjuvants: application to chronic disease, cancer immunotherapy and infectious disease preventive strategies," *Procedia in Vaccinology*, vol. 2, no. 2, pp. 128–133, 2010.
- [102] S. A. Keller, M. Bauer, V. Manolova, S. Muntwiler, P. Saudan, and M. F. Bachmann, "Cutting edge: limited specialization of dendritic cell subsets for MHC class II-associated presentation of viral particles," *Journal of Immunology*, vol. 184, no. 1, pp. 26–29, 2010.
- [103] S. Pejavar-Gaddy, Y. Rajawat, Z. Hilioti et al., "Generation of a tumor vaccine candidate based on conjugation of a MUC1 peptide to polyionic papillomavirus virus-like particles," *Cancer Immunology, Immunotherapy*, vol. 59, no. 11, pp. 1685–1696, 2010.
- [104] L. de Witte, Y. Zoughlami, B. Aengeneyndt et al., "Binding of human papilloma virus L1 virus-like particles to dendritic cells is mediated through heparan sulfates and induces immune activation," *Immunobiology*, vol. 212, no. 9–10, pp. 679–691, 2008.
- [105] C. Li, F. Liu, M. Liang et al., "Hantavirus-like particles generated in CHO cells induce specific immune responses in C57BL/6 mice," *Vaccine*, vol. 28, no. 26, pp. 4294–4300, 2010.
- [106] W. Akahata, Z. Y. Yang, H. Andersen et al., "A virus-like particle vaccine for epidemic Chikungunya virus protects nonhuman primates against infection," *Nature Medicine*, vol. 16, no. 3, pp. 334–338, 2010.
- [107] H. Song, V. Wittman, A. Byers et al., "In vitro stimulation of human influenza-specific CD8+ T cells by dendritic cells pulsed with an influenza virus-like particle (VLP) vaccine," *Vaccine*, vol. 28, no. 34, pp. 5524–5532, 2010.

- [108] C. Ludwig and R. Wagner, "Virus-like particles-universal molecular toolboxes," *Current Opinion in Biotechnology*, vol. 18, no. 6, pp. 537–545, 2007.
- [109] J.-M. Song, J. Hossain, D.-G. Yoo et al., "Protective immunity against H5N1 influenza virus by a single dose vaccination with virus-like particles," *Virology*, vol. 405, no. 1, pp. 165–175, 2010.
- [110] S. M. Kang, D. G. Yoo, A. S. Lipatov et al., "Induction of long-term protective immune responses by influenza H5N1 virus-like particles," *PLoS ONE*, vol. 4, no. 3, Article ID e4667, 2009.
- [111] R. Zhang, S. Zhang, M. Li, C. Chen, and Q. Yao, "Incorporation of CD40 ligand into SHIV virus-like particles (VLP) enhances SHIV-VLP-induced dendritic cell activation and boosts immune responses against HIV," *Vaccine*, vol. 28, no. 31, pp. 5114–5127, 2010.
- [112] M. Herbst-Kralovetz, H. S. Mason, and Q. Chen, "Norwalk virus-like particles as vaccines," *Expert Review of Vaccines*, vol. 9, no. 3, pp. 299–307, 2010.
- [113] Clinicaltrials.gov, "Studies with search fo: VLP," 2010, <http://clinicaltrials.gov/ct2/results?term=VLP>.
- [114] A. Homhuan, S. Prakongpan, P. Poomvises et al., "Virosome and ISCOM vaccines against Newcastle disease: preparation, characterization and immunogenicity," *European Journal of Pharmaceutical Sciences*, vol. 22, no. 5, pp. 459–468, 2004.
- [115] A. Huckriede, L. Bungener, T. Stegmann et al., "The virosome concept for influenza vaccines," *Vaccine*, vol. 23, supplement 1, pp. S26–S38, 2005.
- [116] L. Bungener, A. Huckriede, A. De Mare, J. De Vries-Idema, J. Wilschut, and T. Daemen, "Virosome-mediated delivery of protein antigens in vivo: efficient induction of class I MHC-restricted cytotoxic T lymphocyte activity," *Vaccine*, vol. 23, no. 10, pp. 1232–1241, 2005.
- [117] J. Angel, L. Chaperot, J. P. Molens et al., "Virosome-mediated delivery of tumor antigen to plasmacytoid dendritic cells," *Vaccine*, vol. 25, no. 19, pp. 3913–3921, 2007.
- [118] S. L. Okitsu, U. Kienzl, K. Moehle et al., "Structure-activity-based design of a synthetic malaria peptide eliciting sporozoite inhibitory antibodies in a virosomal formulation," *Chemistry and Biology*, vol. 14, no. 5, pp. 577–587, 2007.
- [119] M. S. Mueller, A. Renard, F. Boato et al., "Induction of parasite growth-inhibitory antibodies by a virosomal formulation of a peptidomimetic of loop I from domain III of Plasmodium falciparum apical membrane antigen 1," *Infection and Immunity*, vol. 71, no. 8, pp. 4749–4758, 2003.
- [120] S. L. Okitsu, M. S. Mueller, M. Amacker et al., "Preclinical profiling of the immunogenicity of a two-component subunit malaria vaccine candidate based on virosome technology," *Human Vaccines*, vol. 4, no. 2, pp. 106–114, 2008.
- [121] B. Genton, G. Pluschke, L. Degen et al., "A randomized Placebo-controlled phase Ia malaria vaccine trial of two virosome-formulated synthetic peptides in healthy adult volunteers," *PLoS ONE*, vol. 2, no. 10, p. e1018, 2007.
- [122] H. X. Sun, Y. Xie, and Y. P. Ye, "ISCOMs and ISCOMATRIX(TM)," *Vaccine*, vol. 27, no. 33, pp. 4388–4401, 2009.
- [123] B. Pahar, M. A. Cantu, W. Zhao et al., "Single epitope mucosal vaccine delivered via immuno-stimulating complexes induces low level of immunity against simian-HIV," *Vaccine*, vol. 24, no. 47–48, pp. 6839–6849, 2006.
- [124] W. Huisman, E. J. A. Schrauwen, S. D. Pas, G. van Amerongen, G. F. Rimmelzwaan, and A. D. M. E. Osterhaus, "Evaluation of ISCOM-adjuvanted subunit vaccines containing recombinant feline immunodeficiency virus Rev, OrfA and envelope protein in cats," *Vaccine*, vol. 26, no. 21, pp. 2553–2561, 2008.
- [125] J. L. Garcia, J. D. S. Guimarães Jr., S. A. Headley et al., "Eimeria tenella: utilization of a nasal vaccine with sporozoite antigens incorporated into Iscom as protection for broiler breeders against a homologous challenge," *Experimental Parasitology*, vol. 120, no. 2, pp. 185–190, 2008.
- [126] P. E. Shewen, L. Carrasco-Medina, B. A. McBey, and D. C. Hodgins, "Challenges in mucosal vaccination of cattle," *Veterinary Immunology and Immunopathology*, vol. 128, no. 1–3, pp. 192–198, 2009.
- [127] Clinicaltrials.gov, "Studies with search of: ISCOM," 2010, <http://clinicaltrials.gov/ct2/results?term=iscom>.
- [128] R. S. Pandey and V. K. Dixit, "Evaluation of ISCOM vaccines for mucosal immunization against hepatitis B," *Journal of Drug Targeting*, vol. 18, no. 4, pp. 282–291, 2010.
- [129] L. Agrawal, W. Haq, C. V. Hanson, and D. N. Rao, "Generating neutralizing antibodies, Th1 response and MHC non restricted immunogenicity of HIV-I env and gag peptides in liposomes and ISCOMs with in-built adjuvanticity," *Journal of Immune Based Therapies and Vaccines*, vol. 1, no. 1, Article ID 5, 2003.
- [130] M. J. Pearse and D. Drane, "ISCOMATRIX™ adjuvant: a potent inducer of humoral and cellular immune responses," *Vaccine*, vol. 22, no. 19, pp. 2391–2395, 2004.
- [131] E. Maraskovsky, M. Schnurr, N. S. Wilson, N. C. Robson, J. Boyle, and D. Drane, "Development of prophylactic and therapeutic vaccines using the ISCOMATRIX adjuvant," *Immunology and Cell Biology*, vol. 87, no. 5, pp. 371–376, 2009.
- [132] J. Boyle, D. Eastman, C. Millar et al., "The utility of ISCOMATRIX™ adjuvant for dose reduction of antigen for vaccines requiring antibody responses," *Vaccine*, vol. 25, no. 14, pp. 2541–2544, 2007.
- [133] M. T. Sanders, G. Deliyannis, M. J. Pearse, M. K. McNamara, and L. E. Brown, "Single dose intranasal immunization with ISCOMATRIX™ vaccines to elicit antibody-mediated clearance of influenza virus requires delivery to the lower respiratory tract," *Vaccine*, vol. 27, no. 18, pp. 2475–2482, 2009.
- [134] A. Vujanic, J. L. K. Wee, K. J. Snibson et al., "Combined mucosal and systemic immunity following pulmonary delivery of ISCOMATRIX™ adjuvanted recombinant antigens," *Vaccine*, vol. 28, no. 14, pp. 2593–2597, 2010.
- [135] D. E. Clements, B. A. G. Collier, M. M. Lieberman et al., "Development of a recombinant tetravalent dengue virus vaccine: immunogenicity and efficacy studies in mice and monkeys," *Vaccine*, vol. 28, no. 15, pp. 2705–2715, 2010.
- [136] J. G. M. Heldens, H. G. W. Pouwels, C. G. G. Derks, S. M. A. Van de Zande, and M. J. H. Hoeijmakers, "The first safe inactivated equine influenza vaccine formulation adjuvanted with ISCOM-Matrix that closes the immunity gap," *Vaccine*, vol. 27, no. 40, pp. 5530–5537, 2009.
- [137] I. D. Davis, W. Chen, H. Jackson et al., "Recombinant NY-ESO-1 protein with ISCOMATRIX adjuvant induces broad integrated antibody and CD4+ and CD8+ T cell responses in humans," *Proceedings of the National Academy of Sciences of the United States of America*, vol. 101, no. 29, pp. 10697–10702, 2004.
- [138] J. S. Anderson, J. Hoy, R. Hillman et al., "A randomized, placebo-controlled, dose-escalation study to determine the safety, tolerability, and immunogenicity of an HPV-16 therapeutic vbaccine in HIV-positive participants with oncogenic HPV infection of the anus," *Journal of Acquired Immune Deficiency Syndromes*, vol. 52, no. 3, pp. 371–381, 2009.

- [139] W. T. McBurney, D. G. Lendemann, J. Myschik, T. Hennessy, T. Rades, and S. Hook, "In vivo activity of cationic immune stimulating complexes (PLUSCOMs)," *Vaccine*, vol. 26, no. 35, pp. 4549–4556, 2008.
- [140] P. L. Mottram, D. Leong, B. Crimeen-Irwin et al., "Type 1 and 2 immunity following vaccination is influenced by nanoparticle size: formulation of a model vaccine for respiratory syncytial virus," *Molecular Pharmaceutics*, vol. 4, no. 1, pp. 73–84, 2007.
- [141] T. Fifis, P. Mottram, V. Bogdanoska, J. Hanley, and M. Plebanski, "Short peptide sequences containing MHC class I and/or class II epitopes linked to nano-beads induce strong immunity and inhibition of growth of antigen-specific tumour challenge in mice," *Vaccine*, vol. 23, no. 2, pp. 258–266, 2004.
- [142] T. Fifis, A. Gamvrellis, B. Crimeen-Irwin et al., "Size-dependent immunogenicity: therapeutic and protective properties of nano-vaccines against tumors," *Journal of Immunology*, vol. 173, no. 5, pp. 3148–3154, 2004.
- [143] J. P. Y. Scheerlinck, S. Gloster, A. Gamvrellis, P. L. Mottram, and M. Plebanski, "Systemic immune responses in sheep, induced by a novel nano-bead adjuvant," *Vaccine*, vol. 24, no. 8, pp. 1124–1131, 2006.
- [144] M. T. Montero Vega, "A new era for innate immunity," *Allergologia et Immunopathologia*, vol. 36, no. 3, pp. 164–175, 2008.
- [145] E. M. Creagh and L. A. J. O'Neill, "TLRs, NLRs and RLRs: a trinity of pathogen sensors that co-operate in innate immunity," *Trends in Immunology*, vol. 27, no. 8, pp. 352–357, 2006.
- [146] D. C. Hargreaves and R. Medzhitov, "Innate sensors of microbial infection," *Journal of Clinical Immunology*, vol. 25, no. 6, pp. 503–510, 2005.
- [147] B. Pulendran and R. Ahmed, "Translating innate immunity into immunological memory: implications for vaccine development," *Cell*, vol. 124, no. 4, pp. 849–863, 2006.
- [148] C. J. M. Melief, S. H. Van der Burg, R. E. M. Toes, F. Ossendorp, and R. Offringa, "Effective therapeutic anti-cancer vaccines based on precision guiding of cytolytic T lymphocytes," *Immunological Reviews*, vol. 188, no. 1, pp. 177–182, 2002.
- [149] A. Yano, A. Onozuka, Y. Asahi-Ozaki et al., "An ingenious design for peptide vaccines," *Vaccine*, vol. 23, no. 17–18, pp. 2322–2326, 2005.
- [150] J. E. Rosas, R. M. Hernández, A. R. Gascón et al., "Biodegradable PLGA microspheres as a delivery system for malaria synthetic peptide SPf66," *Vaccine*, vol. 19, no. 31, pp. 4445–4451, 2001.
- [151] S. Hamdy, O. Molavi, Z. Ma et al., "Co-delivery of cancer-associated antigen and Toll-like receptor 4 ligand in PLGA nanoparticles induces potent CD8+ T cell-mediated anti-tumor immunity," *Vaccine*, vol. 26, no. 39, pp. 5046–5057, 2008.
- [152] N. De Carvalho, J. Teixeira, C. M. Roteli-Martins et al., "Sustained efficacy and immunogenicity of the HPV-16/18 AS04-adjuvanted vaccine up to 7.3 years in young adult women," *Vaccine*, vol. 28, no. 38, pp. 6247–6255, 2010.
- [153] N. Brandhonneur, F. Chevanne, V. Vié et al., "Specific and non-specific phagocytosis of ligand-grafted PLGA microspheres by macrophages," *European Journal of Pharmaceutical Sciences*, vol. 36, no. 4–5, pp. 474–485, 2009.
- [154] A. Lahiri, P. Das, and D. Chakravorty, "Engagement of TLR signaling as adjuvant: towards smarter vaccine and beyond," *Vaccine*, vol. 26, no. 52, pp. 6777–6783, 2008.
- [155] E. Schlosser, M. Mueller, S. Fischer et al., "TLR ligands and antigen need to be coencapsulated into the same biodegradable microsphere for the generation of potent cytotoxic T lymphocyte responses," *Vaccine*, vol. 26, no. 13, pp. 1626–1637, 2008.
- [156] J. D. Turner, R. S. Langley, K. L. Johnston et al., "Wolbachia lipoprotein stimulates innate and adaptive immunity through toll-like receptors 2 and 6 to induce disease manifestations of filariasis," *Journal of Biological Chemistry*, vol. 284, no. 33, pp. 22364–22378, 2009.
- [157] V. Durand, J. MacKenzie, J. de Leon et al., "Role of lipopolysaccharide in the induction of type I interferon-dependent cross-priming and IL-10 production in mice by meningococcal outer membrane vesicles," *Vaccine*, vol. 27, no. 13, pp. 1912–1922, 2009.
- [158] C. Trumpfheller, M. Caskey, G. Nchinda et al., "The microbial mimic poly IC induces durable and protective CD4+ T cell immunity together with a dendritic cell targeted vaccine," *Proceedings of the National Academy of Sciences of the United States of America*, vol. 105, no. 7, pp. 2574–2579, 2008.
- [159] C. Bannon, P. J. Davies, A. Collett, and G. Warhurst, "Potentiation of flagellin responses in gut epithelial cells by interferon- γ is associated with STAT-independent regulation of MyD88 expression," *Biochemical Journal*, vol. 423, no. 1, pp. 119–128, 2009.
- [160] A. Goodchild, N. Nopper, A. King et al., "Sequence determinants of innate immune activation by short interfering RNAs," *BMC Immunology*, vol. 10, Article ID 40, 2009.
- [161] K. K. B. Gorden, X. Qiu, J. J. L. Battiste, P. P. D. Wightman, J. P. Vasilakos, and S. S. Alkan, "Oligodeoxynucleotides differentially modulate activation of TLR7 and TLR8 by imidazoquinolines," *Journal of Immunology*, vol. 177, no. 11, pp. 8164–8170, 2006.
- [162] D. M. Klinman, S. Klaschik, T. Sato, and D. Tross, "CpG oligonucleotides as adjuvants for vaccines targeting infectious diseases," *Advanced Drug Delivery Reviews*, vol. 61, no. 3, pp. 248–255, 2009.
- [163] Y. Krishnamachari and A. K. Salem, "Innovative strategies for co-delivering antigens and CpG oligonucleotides," *Advanced Drug Delivery Reviews*, vol. 61, no. 3, pp. 205–217, 2009.
- [164] A. Takagi, M. Matsui, S. Ohno et al., "Highly efficient antiviral CD8+ T-cell induction by peptides coupled to the surfaces of liposomes," *Clinical and Vaccine Immunology*, vol. 16, no. 10, pp. 1383–1392, 2009.
- [165] B. Salaun, M. Greutert, and P. Romero, "Toll-like receptor 3 is necessary for dsRNA adjuvant effects," *Vaccine*, vol. 27, no. 12, pp. 1841–1847, 2009.
- [166] R. M. Verdijk, T. Mutis, B. Esendam et al., "Polyriboinosinic polyribocytidylic acid (poly(I:C)) induces stable maturation of functionally active human dendritic cells," *Journal of Immunology*, vol. 163, no. 1, pp. 57–61, 1999.
- [167] M. L. Salem, S. A. EL-Naggar, A. Kadima, W. E. Gillanders, and D. J. Cole, "The adjuvant effects of the toll-like receptor 3 ligand polyinosinic-cytidylic acid poly (I:C) on antigen-specific CD8+ T cell responses are partially dependent on NK cells with the induction of a beneficial cytokine milieu," *Vaccine*, vol. 24, no. 24, pp. 5119–5132, 2006.
- [168] Z. Cui and F. Qiu, "Synthetic double-stranded RNA poly(I:C) as a potent peptide vaccine adjuvant: therapeutic activity against human cervical cancer in a rodent model," *Cancer Immunology, Immunotherapy*, vol. 55, no. 10, pp. 1267–1279, 2006.
- [169] O. Schulz, S. S. Diebold, M. Chen et al., "Toll-like receptor 3 promotes cross-priming to virus-infected cells," *Nature*, vol. 433, no. 7028, pp. 887–892, 2005.

- [170] C. Wischke, J. Zimmermann, B. Wessinger et al., "Poly(I:C) coated PLGA microparticles induce dendritic cell maturation," *International Journal of Pharmaceutics*, vol. 365, no. 1-2, pp. 61–68, 2009.
- [171] M. J. Heffernan, S. P. Kasturi, S. C. Yang, B. Pulendran, and N. Murthy, "The stimulation of CD8+ T cells by dendritic cells pulsed with polyketal microparticles containing ion-paired protein antigen and poly(inosinic acid)-poly(cytidylic acid)," *Biomaterials*, vol. 30, no. 5, pp. 910–918, 2009.
- [172] L. J. Cruz, P. J. Tacken, R. Fokkink et al., "Targeted PLGA nano- but not microparticles specifically deliver antigen to human dendritic cells via DC-SIGN in vitro," *Journal of Controlled Release*, vol. 144, no. 2, pp. 118–126, 2010.
- [173] A. Badiee, N. Davies, K. McDonald et al., "Enhanced delivery of immunoliposomes to human dendritic cells by targeting the multilectin receptor DEC-205," *Vaccine*, vol. 25, no. 25, pp. 4757–4766, 2007.

Review Article

Enhanced Transport Capabilities via Nanotechnologies: Impacting Bioefficacy, Controlled Release Strategies, and Novel Chaperones

Thomai Panagiotou¹ and Robert J. Fisher²

¹Microfluidics International Corporation, P.O. Box 9101, Newton, MA 02464, USA

²Chemical Engineering Department, Massachusetts Institute of Technology, Building 66, Room 305, 77 Massachusetts Avenue, Cambridge, MA 02139-4307, USA

Correspondence should be addressed to Thomai Panagiotou, mimip@mfics.com

Received 31 December 2010; Revised 22 February 2011; Accepted 23 February 2011

Academic Editor: Giorgia Pastorin

Copyright © 2011 T. Panagiotou and R. J. Fisher. This is an open access article distributed under the Creative Commons Attribution License, which permits unrestricted use, distribution, and reproduction in any medium, provided the original work is properly cited.

Emerging nanotechnologies have, and will continue to have, a major impact on the pharmaceutical industry. Their influence on a drug's life cycle, inception to delivery, is rapidly expanding. As the industry moves more aggressively toward continuous manufacturing modes, utilizing Process Analytical Technology (PAT) and Process Intensification (PI) concepts, the critical role of transport phenomena becomes elucidated. The ability to transfer energy, mass, and momentum with directed purposeful outcomes is a worthwhile endeavor in establishing higher production rates more economically. Furthermore, the ability to obtain desired drug properties, such as size, habit, and morphology, through novel manufacturing strategies permits unique formulation control for optimum delivery methodologies. Bottom-up processing to obtain nano-sized crystals is an excellent example. Formulation and delivery are intimately coupled in improving bio-efficacy at reduced loading and/or better controlled release capabilities, minimizing side effects and providing improved therapeutic interventions. Innovative nanotechnology applications, such as simultaneous targeting, imaging and delivery to tumors, are now possible through use of novel chaperones. Other examples include nanoparticles attachment to T-cells, release from novel hydrogel implants, and functionalized encapsulants. Difficult tasks such as drug delivery to the brain via the blood brain barrier and/or the cerebrospinal fluid are now easier to accomplish.

1. Introduction

A large number of hydrophobic compounds with potentially high pharmacological value fail to pass initial screening tests because of the perception that they will be too difficult to deliver effectively due to anticipated formulation limitations. Fortunately, nanosuspensions of such drugs may be used to increase bioavailability and offer a variety of delivery options. Historically most formulation strategies aim for particle size reduction [1–4]. Typically these limit the dimensions obtainable since the strategies use high shear processing of preformed entities. To achieve nanoscale dimensions by these size reduction technologies (“top down” processing), an excessive amount of energy and time needs to be expended [5, 6]. Unfortunately, they often not only proved ineffective but lead to possible product degradation. Because nanosuspensions and novel targeting chaperones, for example

T-cells, can deliver much larger amounts of drug in a smaller volume than the solvent diluted drug systems [1–4, 7–9], they have a potential advantage as a formulation strategy.

Emerging nanotechnologies are having a major impact throughout the pharmaceutical industry. The focus here is on how these techniques influence delivery strategies and efficacy through enhancement of the transport phenomena involved in all phases of a drug's life cycle. For example, the ability to obtain desired drug properties, such as size, habit, and morphology, through novel manufacturing strategies permits unique formulation control for optimum delivery methodologies. The ability to transfer energy, mass, and momentum with directed purposeful outcomes is imperative in establishing higher production rates of these carefully engineered nanoparticles at elevated technoeconomic stature.

The role of transport phenomena becomes critically apparent as the industry moves more aggressively toward continuous manufacturing modes, utilizing Process Analytical Technology (PAT) and Process Intensification (PI) concepts. Although these advances rely upon more effective sensor-reporter systems, based on nanoprobe technology, they are not the focus here and therefore will only be briefly touched upon in the following discussions. The emphasis is on the clinical aspects that drive all the other phases needed to get to this stage. That is, once available, these nanoscale entities can be utilized quite effectively in both traditional and novel delivery techniques, relying heavily on *in vivo* transport capabilities. The topics to be addressed in the following sections all capitalize on how carefully these drugs were designed, developed, and engineered for desired properties and capabilities. Specificity of uptake, clearance control, and transport to the brain via the blood brain barrier, cerebrospinal fluid, or in smart implants are a few examples.

Currently, there are a number of nanotechnology drugs in the market [10]. This first generation of such drugs relies mainly on the small size of the particles to increase the surface area and therefore bioavailability of poorly soluble drugs, and to a lesser extent in the structure of the particle for delayed release, and so forth. Examples of nanotechnology drugs in the US market include Rapamune®/Pfizer, Emend®/Merck, INVEGA® SUSTENNA®/Janssen, all based on Elan's NanoCrystal® technology. Abraxane®/Abraxis Bioscience and Triglide™/Sciele Pharma are also in the US market. In emerging technologies, the particles have improved functionalities that include diagnosis, targeting, and drug delivery functions and enhance transport and uptake characteristics. The focus of this paper will be in these emerging technologies rather than the current status of the market drugs.

The credibility of the techniques (topics) being presented here is established through either prior extensive testing, preliminary results from proof-of-concept tests, or derived from analogous successes for what are believed to be realistic projected applications. Presented here therefore will be discussions relative to (a) crystal size and morphology control, via bottom-up processing, for direct use with traditional delivery methods, (b) simultaneous targeting/delivery techniques incorporating novel chaperones obtained from functionalized surfactant encapsulants and T-cells, and (c) controlled release using nanotechnology innovations involving single and multiple drug interventions and tissue therapies (e.g., angiogenesis, wound healing, and artificial organs for autoimmune diseases). In these cases, attempts are made to identify the underlying fundamental physicochemical principles/mechanisms associated such that projected extensions are feasible, and scaleup where necessary can be accomplished reliably.

2. Techniques/Applications

In the recent article by G. Liversidge [10], as mentioned previously, a number of specific pharmaceutical companies

and associated drugs are identified that combine control-release and nanotechnologies. This combination is identified as a key market driver for this industry. Based upon documented recent advances and successful applications, various potential opportunities are outlined. Powerful extensions to many of the concepts and methods mentioned there are being developed and some are currently being implemented throughout the industry. For example, the concept of minitables has a profound impact on many release formulations, (i) delayed-, (ii) extended-, and (iii) pulsatile-release systems.

An objective of ours via this paper is to identify the importance and effectiveness of nanotechnological innovations on the enhancement of transport processes that improve therapeutic protocols. Of the techniques being discussed, the bottom-up method for nanocrystal formation will be used as an example because it provides the basis for our ability to carefully engineer the nanoparticles for the drug delivery protocols. These entities are an essential component for the clinical implementation of all the transport enhanced techniques in use and/or proposed. Whenever available, the results from the various levels of experimental programs executed are presented and discussed, conclusions drawn, and recommendations for future efforts set forth.

Presented in Table 1 below is an outline of the current and emerging methods and nanotechnology applications in drug delivery platforms. These topics will be discussed or referenced in the sections that follow.

2.1. Formation of Engineered Crystalline Nanoparticles. A continuous bottom-up approach to the solvent/antisolvent crystallization process allows precise control of product properties. Achievement of specified quality goals associated with overall performance criteria has been demonstrated [11–14]. These include crystal habit, morphology, and size distribution. The technique involves generating a large number of nucleation sites and limiting subsequent growth. With this method crystal size control is via molecular approaches that utilize various mechanistic pathways governed by transport phenomena, thermodynamics principles, and/or intrinsic kinetics.

The design and operation of commercial scale crystallizers are optimized based on minimizing the formation of agglomerates, impurities included within crystals, liquid entrapped within crystal aggregates, and mother liquor retained by the crystal cake [15–17]. The various crystallization mechanisms that contribute to the observed phenomenological events and how they affect these objectives will be addressed throughout this section.

The generation of nanoscale homogeneous regions dispersed throughout the active crystallization volume is essential for the success of this bottom-up process. Estimating the size of these regions is reasonably straightforward using proven turbulence calculation algorithms [18–20]. The significance is that the length scale over which no further mixing takes place is established and thus molecular diffusion now dictates timing for the steps involved in the homogeneous nucleation and growth processes within these regions. Since

TABLE 1: Current and emerging nanotechnology.

	Methods	Applications
Current	(i) Top down (ii) Batch manufacturing	(i) Enhanced bioavailability
		(ii) Delayed delivery
		(iii) Extended delivery
		(iv) Pulsatile delivery
Emerging	(i) Bottom up (ii) Continuous manufacturing (iii) PAT	(i) Targeted delivery
		(ii) Simultaneous targeted, imaging, and delivery
		(iii) Delivery to the brain (overcoming the Blood Brain Barrier)
		(iv) Delivery through novel targeting chaperons, (example T-cells)
		(v) Artificial organs, tissue therapy, wound healing, and so forth.

hydrodynamics has a significant impact upon mass, energy, and momentum transport rates and reaction proficiency it is imperative that the role it plays not be underestimated. It is also essential to identify the energy dissipation mechanisms present and thereby quantify the intensity of mixing (i.e., macro-, meso-, or micro-), contact efficacy, and associated level of turbulence with its resultant eddy cascade. The length scale of the Kolmogorov (i.e., smallest) eddies, when formed at high energy dissipation levels, can easily be at the nanoscale. The important point is that the magnitude of this energy dissipation rate per unit volume establishes both the time and length scales over which events occur. These can be key control variables manipulated by mixing intensity once the thermodynamic state of the working fluid is established through other processing variables. Observed rates are highly dependent on the concentration differences beyond the solubility limit and hydrodynamic scales. Hence, the local degree of supersaturation can be used as the primary metric to account for both the kinetics and thermodynamic behavior of the system [11, 12, 21, 22].

Crystal characteristics, such as crystal size distribution (CSD), surface area and topography, morphology, dissolution rate, and strength (affected by any impurities and flaws present), depend heavily upon their formation processing conditions. An inclusion of mother liquor for example affects not only product quality for its desired applications but also storage stability, particularly with respect to CSD and morphology. This is of considerable importance to the pharmaceutical industry since polymorphic systems exhibit different physicochemical properties due to the existence of these different crystal structures. Polymorphism influences the dissolution characteristics, which along with CSD affects product formulation strategies and bioavailability [1, 2, 11–14, 23–26].

To understand how to form crystalline nanoparticles of hydrophobic active pharmaceutical ingredients (APIs) via this bottom-up process requires knowledge of the fundamental thermodynamic and rate processes involved in the generation of solid particles from a liquid phase. This involves solubility limits of the target species (with associated degree of supersaturation), nucleation and growth rates, and turbulence intensity to obtain the requisite mixing levels. It is the energy dissipation levels developed by turbulence that determine the appropriate length and time scales

required to control the phenomenological events occurring. Although these topics are discussed in some detail for specific applications elsewhere [11–22], a brief summary of each is included here for clarity of purpose.

The various aspects and important parameters that affect the “bottom-up” crystallization process to be discussed are the following.

- (i) *Thermodynamics*; describes phase characteristics, solubility limits and phase stability, establishing the driving force for crystallization.
- (ii) *Nucleation and crystal growth*; related to crystallization rates, particle sizes, and crystal structures.
- (iii) *Complications*; describes some of the issues that need to be addressed in designing a process and getting the desired product quality.
- (iv) *Flow Patterns, Mixing, and Transport Phenomena*; describes the role of mixing in crystallization processes, relevant to processes that involve mixing of multiple streams, heating or cooling.
- (v) *Creating Nanoscale Entities*; describes strategies of achieving mixing in the nanometer scale and techniques used.
- (vi) *Energy Dissipation*; gives an overview of the mechanisms that absorb energy during the process.

2.1.1. Thermodynamics. Generating solids from a liquid phase is initiated by changes in the thermodynamic state of the solution, thereby reducing the solubility of the target species. Initiation may be through temperature adjustment(s), concentration changes, or by altering solution activity coefficients as in the solvent/antisolvent method. Phase stability is an important factor in determining both when and how fast events progress. The Temperature-Composition phase behavior, see Figure 1, can be used to illustrate some important concepts. A solubility curve represents thermodynamic equilibrium between the phases. For most liquid systems with a composition and temperature above its solubility curve a stable unsaturated liquid exists. Beyond this solubility limit the liquid may not be in thermodynamic equilibrium with respect to the formation of the solid phase, that is, it exists as a supersaturated (SS)

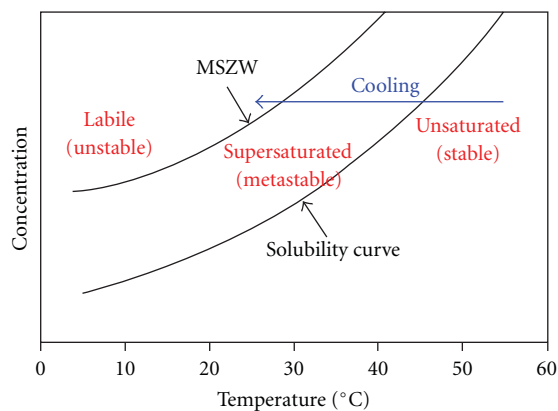


FIGURE 1: Solubility Curve and Metastable Zone plotted against temperature and concentration.

liquid. System behavior can be determined by this degree of SS since there is a region, referred to as the metastable zone, where the system may not always be considered thermodynamically unstable. Heterogeneous nucleation sites are thus necessary to initiate the formation of the solid phase. However, beyond the boundary of this metastable zone, these seed nucleation sites are no longer required. In this region a SS liquid is neither stable nor in equilibrium, and is subject to spontaneous nucleation and rapid growth of the solids.

Unfortunately, due to the large increase in entropy, some undesired events may occur. The crystal matrix may have flaws, such as dislocations, impurity molecules, or liquid inclusions. When a system exhibits various polymorphs, this spontaneity could be problematic or beneficial, depending on the morphology sought and its stability. Since our objective is to create a large number of nucleation sites and thereby restrict the ultimate size of the individual particles, and possibly control morphology, this unstable zone is the desired initial operational region. To control the nucleation and growth rates, the strategy used must establish the desired supersaturation state, level of energy input, and energy dissipation mechanisms. The need for the latter two will be discussed in subsequent sections.

2.1.2. Nucleation and Growth. The degree of supersaturation influences the rate of the individual steps involved in forming the solid as well as which crystal polymorph is formed. In general, the process proceeds as follows: (1) feed streams are mixed in a process unit selected to meet required specifications for the energy dissipation rate per unit volume. The time to achieve homogeneity is dependent on diffusivity of the target species and the distance they must travel within the smallest eddies obtained (see the discussion on mixing for the role of turbulence and the Kolmogorov scale); (2) mixing to obtain the desired local degree of supersaturation, leading to a nucleation rate, which increases proportionally with SS. The features of the product formed depends significantly on this rate; (3) growth of the nuclei is by diffusion of solute molecules from the bulk solution to the surface and then along the surface to be integrated

into the matrix. This continues until a limiting particle size is reached, determined by the magnitude of the shear force present; (4) further growth is by mechanisms whereby particles collide and adhere to each other. Particle number thus decreases with time as the particle size increases.

The ability to create and control a supersaturation driving force is paramount to having a robust process. It can be generated by various methods including indirect cooling, evaporation, adiabatic evaporative cooling, antisolvent addition and salting out, chemical reactions, and pH adjustment. Note that temperature changes may be detrimental for some systems, for example when dealing with protein-based drugs. Alternative methods most frequently used to reduce solubility are pH adjustment to the isoelectric point, increasing ionic strength, addition of nonionic polymers, and addition of a miscible nonsolvent.

2.1.3. Complications. Many factors can restrict productivity and purity. Of particular interest for the bottom-up approach are agglomeration, liquid inclusions, and inefficient mother liquor removal.

Agglomeration. The particle size can clearly be affected by agglomeration and fracture mechanisms. When growing crystals collide they may stick together and form new particles, that is, agglomerates form when the collisions are inelastic. The strength of the physical bonds thus formed determines their stability upon further collisions. For the bottom-up processing to be effective in limiting crystal size the probability of agglomeration needs to be low. Unfortunately, a large number of small particles are produced when operating in the unstable supersaturation region and collision frequency is high. To offset this concentration effect, it is necessary to limit the time for interaction and/or relieve SS quickly. Also, a surfactant may be effective in limiting the probability that the particles will stick to one another.

Liquid Inclusion in Individual Crystals and Agglomerates. This is particularly undesired when liquid impurities are present. High growth rates can contribute to increased amounts of liquid entrapped within a crystal. Also, liquid can get trapped between colliding particles during agglomeration and higher supersaturation levels increase the probability of that occurrence. Thus high supersaturation can have both beneficial and problematic outcomes. One can mitigate any associated problems by limiting the interaction time and/or relieve the supersaturation condition rapidly.

2.1.4. Flow Patterns, Mixing, and Transport Phenomena. Mixing at the nanometer scale occurs as reactants, which may include several liquid and solid phases, are subjected to high shear stresses and turbulence. The energy dissipation rate determines whether the macro-, meso-, or micromixing level is attained. The overall mixing process occurs within a flow field continuum which covers the wide range of length and time scales indicative of each of these mixing levels, each with distinct characteristics. For example, consider two miscible fluids. The large scale distribution by flow patterns that

causes gross dispersion is considered macromixing. Next, the breakdown of large eddies into smaller ones via the “eddy cascade” is termed mesomixing. Fluid engulfment in small eddies with subsequent laminar stretching of them, where molecular diffusion is now the final mechanism to obtain uniform composition, is referred to as micromixing [18–20]. The length scale for this diffusional process is determined by the size of the smallest eddies formed and is referred to as the Kolmogorov length scale. Along with time and kinetic energy scales, each determined by these local flow conditions alone, (i.e., related to kinematic viscosity and the energy dissipation rate per unit mass), the so called Kolmogorov scales are established. Estimating the magnitude of these Kolmogorov parameters can be accomplished with reasonable confidence using proven theoretical turbulence calculations. The significance is that the length scale over which no further mixing takes place is established and molecular diffusion now dictates timing for the necessary steps involved in the homogeneous nucleation and growth processes.

These mixing subprocesses generally occur in series, but often to some extent, in parallel. Turbulent energy dissipation rates, for example in modified impinging jet technologies [11, 12, 27–29], are estimated to be on the order 10^7 W/kg and higher when using these micromixing models. At these levels, rapid micromixing and mesomixing (on time scales of 4 and $20 \mu\text{s}$, resp.) are achieved, and the length scale of the smallest eddies are at the nanoscale. Note that residence times in many of the microreactors systems used for PI applications [30], particularly those utilizing impinging jets, are of the order 1 ms and lower.

Incorporating these fundamental principles and using appropriately designed equipment it is possible to precisely control each step in the crystallization process. Mixing at the nanometer scale provides a uniform supersaturation ratio. The onset of the nucleation process can be manipulated by controlling the timing and location of the mixing of the solvent and antisolvent streams that are used to generate the supersaturated state. This in combination with an evenly dispersed homogeneous supersaturation ratio results in uniform crystal growth and stabilization rates.

2.1.5. Creating Nanoscale Entities. The generation of nanoscale homogeneous regions dispersed throughout the system is a major requirement for the success of this bottom-up process. When accomplished, it is reasonable to consider these regions as nanoreactors. This concept is ideal for our purposes since both length and time scales are quite small for the processes involved in creating these monodispersed nanoparticles. Consequently, it is immaterial whether or not these regions are stabilized, as for example, by use of surface active agents.

It is important to reiterate that the length scale over which no further mixing takes place is established and molecular diffusion now dictates timing for the necessary steps involved in the homogeneous nucleation and growth processes. In the absence of seed crystals or other nucleation sites, a critical number of molecules must collide and remain

aggregated forming stable clusters, (i.e., nuclei). Subsequent growth requires diffusion to and along the surface, followed by a specific integration process that incorporates these molecules into the crystal matrix of a particular polymorph. The observed crystallization rate is, therefore, highly dependent on length scales and the local degree of supersaturation. The polymorph that is obtained is dependent on thermodynamic considerations, such as component activity coefficients (solvent/antisolvent/solute species interactions, composition/concentrations, and temperature) and entropy generated due to the spontaneous nature of the process, that is, rates influenced by supersaturation ratios.

To generate the high energy dissipation rates used to produce nanoparticles, many processing techniques utilize high shear fields. Jet impingement, on a solid surface or with another jet, has been shown to be a highly efficient method [11, 12, 27, 28]. Systems that incorporate high velocity linear fluid jets that collide can rapidly reduce the scale of segregation between the streams. High-energy dissipation is observed because the kinetic energy of each stream is converted into a turbulent-like motion as the result of the collision and redirection of the flow within a very small volume. More thorough discussions on the phenomenological events, equipment design criteria, and characterization studies are given elsewhere [11–15, 18–26].

2.1.6. Energy Dissipation. Surface tension and various molecular forces between the species present are key variables associated with the crystal size distribution. Thus, surface active agents can play a significant role whether as a contributor to growth mechanisms or as a size stabilizer. For example, they are involved in self-assembly mechanisms, and can act as barrier components that restrict transport, as possible chaperones that target specific sites during drug delivery, as sequestering agents to facilitate contact efficacy, as promoters of interfacial phenomena, and as inhibitors to agglomeration.

The fraction of the input energy available for formation of surfaces is instrumental in establishing system efficacy. Performing an energy audit to determine overall requirements is an essential task for this systems analysis approach. This entails determining the amount of input energy transformed into kinetic energy of the jets, identifying all forms of dissipation (whether desired or not), and ascertaining the amount stored as internal energy. Although the system energy requirements are not readily identified *a priori*, the total energy input and the amount dissipated and stored are measurable. Estimates of the various losses occurring can be made, and the energy utilization for the desired processes can also be estimated. This permits energy considerations to be used in predicting performance from the estimated length and time scales obtained. System validation is accomplished when these length and time scales can be corroborated with observed kinetics phenomena [12, 27, 28].

2.1.7. Examples of Successful Applications. Confined impinging jet systems have been used in our laboratory to

consistently produce submicron API suspensions via a continuous process that involves crystallization via the solvent/antisolvent technique to generate supersaturation conditions. Microfluidics Reaction Technology (MRT) was selected for this bottom-up processing since it is based on novel multiple stream inlet capabilities coupled with the impinging jet concept [11–14, 26]. It is designed to produce jet velocities and energy dissipation orders of magnitude higher than those of conventional impinging jet reactors. The technology provides precise control of the feed rates, and the subsequent location and intensity of mixing of the reactants. It may provide significant technical and economical advantages due to its process intensification character that minimizes energy requirements, and the proven scalability of the reactor.

In our first proof of concept studies performed, nanosuspensions of several APIs were produced varying the key parameters of the technology [14]. Five different model APIs were used for testing and were selected to belong to different chemical families that exhibit different pharmacological activities. There were two antibiotics (*azithromycin* and *API-2*), an antihistamine (*loratadine*), an anticonvulsant (*oxycarbazepine*) and a non-steroidal anti-inflammatory (NSAIS, *API-1*). The particle size depended on the supersaturation ratio and energy dissipation expressed as process pressure. The nanosuspensions were stable with narrow particle size distributions and median particle sizes in the range of 50–760 nm. This “bottom up” process was compared to a “top down” process in which drug nanosuspensions were created as a result of particle size reduction. It was found that the “bottom up” process was substantially more efficient and resulted in smaller particles.

This first study did not attempt to identify crystalline structure and therefore no polymorph selectivity capabilities were evaluated. To accomplish this, two additional, more in depth studies were conducted on single APIs: Carbamazepine (CBZ), an anticonvulsant, and Norfloxacin (NFN), an antibacterial agent. The details of the experimental protocols and results are reported in separate papers, CBZ [12] and NFN [11]. A few brief comments are given here to help validate the benefits of bottom up processing with respect to the stated objectives of creating carefully engineered particles with “tunable” characteristics.

The NFN nanosuspensions had narrow particle size distributions and median particle sizes in the range of 170–350 nm depending on the supersaturation ratio and energy dissipation expressed as process pressure. However, the particle size was found to be insensitive to the presence of the surfactant used. The crystalline structure of NFN was not affected by the processing conditions for this particular solvent/antisolvent system, but it was different than the initial crystalline structure of the drug. This implies the product is tunable.

The particle habit was needle-shaped. Two miscible fluids were used as the solvent (DMSO) and antisolvent (water). The effect of process pressure (determining the energy input), the NFN concentration, the supersaturation ratio, and the presence of surfactant on the particle size and

TABLE 2: List of various “bottom up” processes and influence on particle properties.

Bottom up processes	Properties controlled
Crystallization	(i) Size, shape
	(ii) Crystalline structure—Crystalline/amorphous
	(iii) Polymorph
Precipitation	(i) Size, shape
	(ii) Surface area
Encapsulation in polymers	(i) Size, shape
	(ii) API concentration
	(iii) Particle nanostructure
Chemical reactions	(i) Size, shape
	(ii) Purity
	(iii) Surface area

the crystallized material was investigated. Higher pressures resulted in smaller particle sizes, as did lowering NFN concentration and supersaturation ratios. The surfactant that was used (Solutol) did not affect the particle size. The crystalline structure was not affected by the shear rate of the process. It was identical to those formed in a beaker under low shear conditions. However, the crystallite size of the material decreased threefold from no shear to high shear conditions.

CBZ was selected as a model system since it is known to exhibit polymorph multiplicity. Several solvents and antisolvents were used to determine their effect on the crystalline structure and particle size. CBZ is also known to form hydrates, therefore both aqueous and nonaqueous solvent/antisolvent systems were used for comparison. They were Dichloromethane (DCM)/Hexane, Poly(ethylene-glycol) (PEG) 300/Water, and Dimethyl sulfoxide (DMSO)/Water.

The results obtained with respect to processing conditions are consistent with those of the NFN study. Particle sizes obtained with all bottom up experiments were consistently in the range of 250–320 nm. Unfortunately, the results obtained with respect to polymorph selectivity were not as definitive. What was observed is that the solvent/antisolvent system does matter, but it is unclear if the degrees of supersaturation or processing intensity had significant roles in that study. Three different morphologies were detected via XRD patterns and a hypothesis is given to explain the detailed observations presented there. Although not conclusive and thus more thorough studies must be performed, the explanations are consistent with those results.

Although the emphasis in the previous paragraphs was in crystallization, other processes can be used to manufacture nanosized materials with tailored properties. Encapsulation of functional ingredients in polymers is another method, which will be discussed in more detail in the sections that follow. Table 2 summarizes the processes used in the bottom up production of nanoparticles and the properties controlled via such methodologies.

2.2. Simultaneous Targeting/Delivery Techniques. Creative advances in nanotechnologies, coupled with systems biology, has led to novel chaperone systems for simultaneous targeting/delivery, and in certain instances, enhanced controlled release strategies. The systems selected for illustration here are (1) polymer nanosuspensions, (2) functionalized designer surfactant encapsulants, and (3) attachment to T-cell surfaces.

2.2.1. Polymer Nanosuspensions. The creation and use of chaperone systems in targeting, drug delivery, and diagnostic imaging has greatly broadened the applications, and thus needs, for polymer nanosuspensions. The enhanced surface to volume ratios provides unique capabilities for functionalization of the surface for these high degrees of specificity requirements.

The intended use of these nanosuspensions dictates control of both the mean particle size and distribution. These parameters determine performance and toxicity through the selectivity and rate of receptor-ligand interactions and/or the ability and rate of cellular uptake. The implementation of systems that can control nanoscale phenomena is required and has been reported previously [13]. The techniques reported there can create nanosuspensions of many different polymer types with varying particle sizes by controlling the formulation and process variables. These nanosuspensions may also contain encapsulated species via either coprecipitation or other less efficient cargo loading techniques that rely upon diffusional uptake strategies.

Encapsulation of active pharmaceuticals and contrast agents within these biocompatible polymers is readily accomplished using bottom-up techniques for coprecipitation processes that are reproducible and scalable. Nanosuspensions in the range of 50–500 nm with different polymers with high encapsulation efficiencies have been created successfully. For example, suspensions of poly(ϵ -caprolactone) (PCL) (a polymer that has been extensively used for parenteral drug delivery) were created using MRT (as discussed above in previous sections). By mixing a 20 mg/mL (PCL/acetone) solvent stream with water at a ratio 1:10 (solvent/antisolvent) a nanosuspension with a mean particle size of 220 nm was prepared. Their size and spherical habit was confirmed using SEM instrumentation.

2.2.2. Functionalized Designer Surfactant Encapsulants. There has always been an active interest in targeted drug delivery to tumors to specifically kill cancer cells. Ongoing research in this area has provided significant advances due to the ability to carefully engineer both the vesicle, for its specificity and imaging characteristics, and its cargo API.

A collaborative team has developed a highly adaptable amphiphilic alternating copolymer system that self-assembles into micelles for therapeutic delivery applications in cancer [8, 9]. The synthetic scheme includes the enzymatic polymerization of multifunctional linker molecules (dimethyl 5-hydroxyisophthalate) with poly(ethylene glycol). This chemoenzymatic synthesis is much faster and more convenient than an entirely chemical synthesis. Subsequent

synthetic steps have been developed to attach ligands (for targeting), perfluorocarbons (19F MR imaging), fluorescent dyes (NIRF imaging), and radioiodine (nuclear imaging and radioimmunotherapy) to the backbone polymer.

Attachment of hydrocarbon or perfluorocarbon side chains provides amphiphilicity to produce the multimodal self-assembling micelles. Additionally, encapsulation procedures for chemotherapeutic agents, that is, doxorubicin and paclitaxel, have been established. These unique alternating copolymer micelle nanoparticles were designed as delivery vehicles targeted to human cancer cells expressing the underglycosylated mucin-1 antigen, which is found on almost all epithelial cell adenocarcinomas, by use of the peptide EPPT, or the folate receptor (FR) by using folate.

Development of the synthetic schemes has been coupled with *in vitro* toxicity tests using various cell viability assays to minimize the toxic effect of these copolymer structures. The nontoxic polymers were brought forward into drug delivery and uptake experiments. Cell death due to doxorubicin increased with encapsulation in these alternating copolymers. Additional slight improvements were observed when targeting ligands were attached to the encapsulating polymer. Similar results were obtained with paclitaxel as the cargo.

Cellular uptake determined by 125I or 3H radioactive analysis and fluorescence confocal microscopy was also investigated in other *in vitro* studies. Microscopy images of the labeled polymer alone demonstrated that the polymer was most likely confined to vesicles within the cytoplasm and not found in the nucleus, whereas encapsulated doxorubicin was shown to be largely confined to the nucleus. Theoretical models of polyvalent binding were employed to guide the design of the targeting polymers. Unfortunately, the polymers used in this study appeared largely nonspecific for the targeted cells when studied *in vitro*. However, the versatility of these polymer constructs suggests that continuing to optimize for a targeting delivery system for drugs and imaging agents using this polymer platform could be extremely beneficial.

2.2.3. Attachment to T-cell Surfaces. Before discussing the specifics of the use of T-cells in drug delivery protocols, a few general comments about the underlying principles are appropriate. The basis of this approach is attributed to the new, burgeoning field of biohybrid materials which will have a significant impact on the efficacy of drug delivery. This is in addition to their obvious use in bioimaging, cellular functionalization, immune system and tissue engineering, and cell-based therapeutics where cell-environment interactions are critical.

Of particular interest here are synthetic materials systems such as magnetic micromanipulators, nanoparticulate cellular patches, and functional cell backpacks [31, 32]. These offer exciting possibilities for symbiosis between synthetic building blocks and native biological behavior. The key is the ability to systematically modify the surface of living cells. This was clearly demonstrated by the collaborative efforts of the Cohen and Rubner research groups [31]

with functional polyelectrolyte multilayer (PEM) patches attached to a fraction of the surface area of living, individual lymphocytes. These cells remained viable, and with patches containing magnetic nanoparticles the cells could be spatially manipulated using a magnetic field. Since the patches did not completely occlude the cellular surface from the surrounding environment a functional payload could be attached without interfering with the cells ability to perform its native functions. This initial work has led to what is now referred to as cellular “backpacks”; nanoscale thickness, micrometer-sized, photolithographically patterned heterostructured multilayer systems capable of noncytotoxicity attaching to the membrane of a living cell. It is interesting to note that these “backpacks” can play an integral part in tissue engineering applications, such as in cell aggregate self-assembly [32] which will be discussed briefly in a later section.

To illustrate the use of this concept in a drug delivery scenario, an extension of this technique was exploited as follows. In a recently published study, a method of attaching carefully engineered nanoparticles to the surface of T-cells was identified [7]. Although their application was for a cell therapy approach, the T-cells were used as chaperones for the stimulant drugs. They designed drug carrying nanoscale vesicles with lipid characteristics for coupling with the sulfur containing molecules on T-cell surfaces. In their study the researchers injected these cargo carrying cells, each with approximately 100 vesicles loaded with interleukins IL-15 and IL-21, into mice with lung and bone marrow tumors. Once reaching the tumors these packets gradually degraded releasing the drugs over a period of one week. Their concept was for the drug molecules being released to reattach to these chaperone T-cells, stimulating them to replicate and thus provide the requisite tissue therapy. The techniques proved successful in that within 16 days, all tumors in the mice treated in this fashion disappeared and these mice survived for the entire 100-day experiment. Mice that received no treatment died within 25 days and those that received either T-cells alone or T-cells with injections of interleukins died within 75 days.

A few details of their procedure are presented here to stress the relatively straight forward nature of these protocols and instill confidence that the proposed clinical applications can be realized with a high degree of certainty. Their method exploits the fact that T-cells, like many cell lines, have high levels of reduced thiol groups on their surface, and thus stable coupling of the synthetic drug carrying nanospecies to them is possible. Specifically, liposomes and liposome-like synthetic entities 100–300 nm in diameter, with a drug loaded core and phospholipid exterior layer, were linked to the cells via the thiol reactive maleimide head-groups. A simple two-step process achieved the desired conjugation. The donor cells were first incubated with nanoparticles to accomplish the thiol-maleimide coupling. This is followed by *in situ* conjugation to thiol-terminated poly ethylene glycol (i.e., PEGylation) to quench the residual reactive groups to ensure that only about 20% of the surface thiol groups were involved with the initial coupling, that is, linked with approximately 150 nanoparticles. Stable, nontoxic linkages to live cells were thus accomplished with particles ranging

from simple liposomes to complex multilamellar lipid nanoparticles or lipid coated polymers. This benign behavior was anticipated since only 3% of the surface of a typical 7 μm diameter T-cell would be blocked by 200 nm diameter particles occupying 150 sites.

These results suggest therapeutic cells are promising vectors (chaperones) for actively targeted imaging and drug delivery. Furthermore, the attached entities can be engineered for controlled release of individual or multiple drug sequencing capabilities. What can be envisioned is the use of different vesicles with specific transport or degradation properties or a vesicle composed of, for example, multiple polymeric materials, as will be discussed in the following section devoted to release strategies.

2.3. Controlled Release Using Nanotechnology Innovations.

For a large number of health care/wellness interventions the controlled release of therapeutic agents is a necessary strategy. Carefully designed API formulations can accommodate a broad spectrum of requirements. The release concepts employed range from (i) simplistic steady release rates {via dissolution, etc.}, (ii) intermittent timed release, (iii) programmed simultaneous and or sequential release of multiple species {antigenic drugs and adjuvants}, to (iv) smart systems responding to stimuli: including single and multiple drug interventions and tissue therapies (e.g., angiogenesis, wound healing, and artificial organs for autoimmune diseases). The applications discussed in the following sections demonstrate the breadth of nanotechnologies that impact these release strategies. These all capitalize on how carefully these drugs were designed, developed, and engineered for desired properties and capabilities. Specificity of uptake, clearance control, and ability to perform extremely difficult tasks, such as drug delivery to the brain via transport across the blood brain barrier, the cerebrospinal fluid, or in smart implants, are highly desired capabilities. Coupling advanced materials development and processing techniques with nanoscience and technology creates innovative opportunities not only for traditional drug delivery capabilities, but helps establish the impact platform technologies necessary for tissue engineering/therapy methodologies.

2.3.1. Passive Delivery Mechanisms.

These traditional schemes are governed by classical thermodynamic and transport phenomena principles. They are highly dependent upon the physicochemical properties and geometric features of a drug's formulation. In addition to solubility limits, size distribution, habit and morphology (when applicable), compaction or encapsulation technique, and diffusivity/mass transfer coefficients are significant contributors to accomplishing a successful therapeutic event. For example, nanosized APIs are more readily distributed uniformly with an excipient and/or adjuvant. They also exhibit greater dissolution rates than larger sized entities having the same total mass of drug retained within the product matrix. These methods utilize the dissolution capabilities of the entrapping matrices. Variable release rates can easily be obtained using a composite structure;

each layer having different transport properties. The design of release protocols for multiple APIs, sequenced for optimum efficacy and synergism, is thus straightforward. Furthermore, nontherapeutic layers can be included to (i) provide a delay mechanism, (ii) possibly be a barrier for protection until arrival to the desired local or organ system, and/or (iii) be a sacrificial layer containing an adjuvant or other functional component that would, for example, pre-condition the microenvironment [33]. These techniques have been well documented and need not be reiterated here. Obvious extensions to these methods are incorporated into implant systems with hindered diffusion capabilities, in addition to facilitated delivery due to targeting features. Demonstrated implementations of a few of these, along with some conceptualizations are presented below.

2.3.2. Functionalizing for Specificity and Facilitated Delivery. Novel nanomaterials are designed to possess unique features using molecular engineering concepts. Innovative drug delivery protocols have evolved capitalizing on these and recognizing the analogous processes present during successful applications in related areas. Understanding the binding properties and characterization of transport mechanisms within modified hydrogels and biomembranes [34] provides the bases for designing implants with entrapped vesicles and the controlled release of their cargo APIs. Included here is the concept of pulsatile—release systems [10]; that is, the drug is released as bolus pulses in well defined time intervals (see later section referring to future opportunities for additional comment).

Therapies that require the sequencing of multiple drugs can therefore be accomplished by logical extensions. As examples; (i) amphoteric core-shell microgels, that is, contraphilic two compartment colloidal particles [35, 36] could be used as smart systems; either as implants or chaperones, (ii) the concept of chaperones within a larger vector could also prove feasible; to minimize clearance of the smaller entities, or their catabolism, prior to their uptake at difficult to reach sites such as to the brain and subsequent transport across the blood brain barrier, and (iii) stimulate angiogenesis through release of multiple cytokines (growth factors) from nanovesicles entrapped in functionalized hydrogel beads used as immunoprotective barriers for tissue therapy applications [37–41]. Additional details with respect to the research studies involved in formulating these extensions and conceptualizations can be found in the following sections.

Transport and Drug Delivery through the Blood-Brain Barrier and Cerebrospinal Fluid. There are multiple barriers in the central nervous system that inhibit API therapies. The blood-brain barrier (BBB) and blood-CSF (cerebrospinal fluid) barriers are vascular in nature, whereas the other, the brain-CSF barrier, exists between brain tissue and the CSF. The wall of the cerebral microvessels in the brain parenchyma constitutes the BBB. Due to its unique structure it maintains very low permeability to water and solutes. The multicell layer present in the middle of the brain parenchyma is

known as the blood-CSF barrier. Present there are ventricular cavities (ventricles) filled with CSF secreted by the epithelial cells of the choroid plexus, a highly vascular tissue with leaky, fenestrated capillaries covered with ependymal epithelium, which has relatively tight junctions. The third barrier, the interface between the CSF and brain tissue, is unlike the other two tight blood barriers since it is relatively leaky. Since it does not prove to be a significant resistance to mass transport it is a probable route for drug delivery once the transport issues with the other barriers are resolved. Given that the area of the BBB is about 1000 times that of the blood-CSF barrier, it is more important to circumvent its impermeability, and therefore that is the focus for continued discussion [42]. Furthermore, since it is not considered as limiting as compared to the BBB, further discussions related to CSF transport are not given here but can be found elsewhere [43].

The transport of substances from capillary blood into the brain tissue is dependent upon molecular size, lipid solubility, binding to specific transporters, and electrical charge [44]. Compared to the peripheral microvessel wall, the additional structure of the BBB and tighter endothelial junctions greatly restricts transport of hydrophilic molecules through the gaps between the cells, that is, the paracellular pathway of the BBB [45]. In contrast, small hydrophobic molecules such as O₂ and CO₂ diffuse freely across plasma membranes following their concentration gradients, that is, the transcellular lipophilic diffusion pathway. The BBB permeability to most molecules can be estimated on the basis of their octanol/water partition coefficients. For example, diphenhydramine (Benadryl), which has a high partition coefficient, can cross the BBB with relative ease, whereas water-soluble loratadine (Claritin) is blocked. However, the octanol/water partition coefficients do not completely reflect solute transport. Some solutes with low partition coefficients easily cross the BBB by active or facilitated transport mechanisms, which rely on ion channels, specific transporters, energy-dependent pumps, and a limited amount of receptor-mediated transcytosis. Small drug molecules analogous to glucose, amino acids, and small intermediate metabolites, for example, reach brain tissue via facilitated transport mediated by specific transport proteins, whereas larger molecules, such as insulin and other protein type therapeutic agents, are carried across the BBB via receptor-mediated or adsorptive transcytosis. Furthermore, some small molecules with high octanol/water partition coefficients are seemingly blocked. Thorough data analysis suggests that they are actively pumped back into the blood by efflux systems. For instance, members of the adenosine triphosphate-binding cassette family of exporters are potent energy-dependent transporters. They contribute greatly to the efflux of xenobiotics and due to this protective role impede the delivery of therapeutic agents. Consequently, to develop effective and efficient methods for drug delivery to the brain through the BBB, it is imperative to control its permeability. This requires understanding the mechanism by which these structural components, as well as transporters, receptors, efflux pumps and other components at the endothelium and astrocyte foot processes determine it.

Various methods such as intracerebral implantation, microdialysis, convection-enhanced distribution (CED), osmotic shock, and chemical modification of the BBB have been developed for delivering drugs into the brain. However, the applications of these methods are limited and they can only partially keep with the demands of modern therapies. For instance, the efficiency of intracerebral implantation, microdialysis and CED methods are low since their major transport mechanisms are diffusion and convection of interstitial fluid. For effective treatment of CNS diseases, an adequate amount of therapeutic agents must reach the specific regions of the brain. As discussed earlier, functionalized target chaperones have this ability. They can directly deliver therapeutic agents via these transporters by closely mimicking their substrates, or conjugating the drugs to ligands of the specific surface receptors expressed for transcytosis (receptor-mediated transcytosis, RMT-Trojan horse approach). Furthermore, these functionalized target chaperones are used in delivering cationized proteins, peptides, and as nanoparticle carriers for adsorptive mediated transcytosis (AMT).

Although the exact mechanisms of RMT are not fully understood, the development of drug delivery protocols using receptor targeting has been successful [46–50]. This physiological approach is often referred to as the molecular Trojan horse approach since the therapeutic compounds are delivered to specific sites for transcytosis by various forms of vector carriers. This approach also improves the drug loading capacity. The technique is very promising, but unfortunately there remain a number of hurdles to overcome [48–50]. In particular, even if the total amount of drug transported to the brain is large, most of it may not be efficacious since it might remain associated with brain microvessel endothelial cells and not reach the brain parenchyma. If drug translocation is accomplished by conjugation with an antibody, there exists the challenge of dissociation due to the high affinity of antibodies. Furthermore, specificity for uptake in the brain may be compromised since the BBB receptors utilized there could also have a widespread distribution on peripheral organs; in effect, resulting in a seemingly nonspecific uptake. Not only will this limit efficacy, but could induce additional toxicity.

Improvements in Encapsulation Technologies for Tissue Therapies. The success of an implant protocol utilizing entrapped tissue for a therapeutic intervention is highly dependent upon controllability of transport characteristics and the microenvironment [33]. Improving the oxygen supply to encapsulated insulin producing cells has been selected for illustration. The basic concepts are to improve the permeability of the encapsulating hydrogel and maintain a high oxygen partial pressure in the surrounding microenvironment. A number of approaches have been suggested, with some tested and validated [51]. Those that utilize nanotechnology, with their inherent improvement qualities, are the focus in this section. The results of two independent studies that address the individual concepts mentioned above will be discussed briefly. When coupled they should provide a

synergistic response. Permeability enhancement was accomplished by entrapping a perfluorocarbon nanoemulsion within the hydrogel capsule [51]. Oxygen supply to the capsule surfaces was enhanced through greater vascularization in the microenvironment by stimulation of angiogenesis by cytokines released from the implant [37–41]. Use of cargo-loaded functionalized nanovesicles that control individual cytokine release rates is an obvious extension to that work. One important goal of these angiogenesis studies was to quantitatively evaluate the rates at which different individual growth factors (GFs) are released from their hyaluronic acid hydrogel implants. The ability of added amounts of heparin to specifically regulate basic fibroblast growth factor (bFGF) or vascular endothelial growth factor (VEGF), release from their gels without loss of ability to stimulate a neovascularization response was investigated both *in vitro* and *in vivo*. For both of these growth factors, the rate of release declined monotonically with increasing heparin (Hp) content. As little as 0.03% w/w Hp significantly moderated the time course of release, while inclusion of 0.3% Hp resulted in sustained release over several weeks [40].

The results of that study suggest the possibility of delivery of growth factors in specified sequences at regulated rates, simply by controlling the composition of the gels. Inclusion of as little as 0.3% Hp in the gels led to significant differences in the rates of release of individual GFs. By taking advantage of those differences, it may be possible to design implants that are capable of both storing and providing sustained, localized *in vivo* release of the growth factors, without loss of their biologic effectiveness.

Co-delivery of a combination of more rapidly released GFs together with more slowly released factors may then permit engineered control of desired physiologic processes such as angiogenesis through use of this selective release sequence concept.

The Johnson et al. study [51] is an example that illustrates the usefulness of permeability enhancement, through nanotechnology techniques, for delivery of tissue based therapeutic agents. Their efforts were to enhance the performance of a bioartificial pancreas to treat diabetes that uses microencapsulation as an immune barrier for transplanted islets of Langerhans. Unfortunately, the barrier also imposes oxygen diffusional limitations that can result in loss of viability and function. It is critical that the necessary amount of oxygen be delivered to encapsulated tissue after transplantation in order to maintain normal levels of insulin secretion. Without a solution that allows for effective oxygen delivery, transplantation of encapsulated tissue may never be successful.

Their investigation included methods to reduce oxygen transport limitations by enhancing encapsulant oxygen permeability, for example, by combination of a highly concentrated perfluorocarbon (PFC) nanoemulsion with alginate (PFC alginate). A theoretical reaction—diffusion model was used to predict the three-dimensional distribution of oxygen partial pressure in a spherical microcapsule and a planar slab containing islet tissue, from which the loss of cell viability and the reduction in insulin secretion rate are estimated. Numerical simulations were carried out for normal alginate

and PFC alginate to examine the effect of surface oxygen partial pressure, capsule diameter, slab thickness, and the size and density of dispersed islet tissue. Results show that hypoxic conditions can be reduced, thereby enhancing islet viability and substantially maintaining insulin secretion rate when the PFC nanoemulsion is incorporated in the encapsulation material for both geometries.

The approach was also evaluated experimentally, and the ability to enhance encapsulated tissue survival and function was successfully demonstrated, both *in vitro* and *in vivo*. Intact islets encapsulated in normal alginate and in PFC alginates having the composition described in the numerical predictions were used as model systems. Recovery of viable tissue after culture under various O_2 partial pressure conditions was expressed as the oxygen consumption rate (OCR)/unit volume of capsule divided by the same parameter measured immediately after encapsulation and before culture. When cultured at very low pO_2 , fractional OCR recovery was substantially greater with PFC alginate than with normal alginate. Furthermore, examination of histological sections revealed necrosis in some islets in normal alginate capsules cultured at 3.5 and 142 mmHg, whereas no necrosis was observed in islets within PFC alginate capsules. The findings and insights gained from both the theoretical and experimental studies will increase the probability of a successful cell therapy for the treatment of diseases such as diabetes.

The concept of “backpacks” discussed earlier with respect to drug chaperones can also be applied to encapsulation techniques and tissue therapies. The commonality rests with the use of nanofabrication approaches to create these entities, for example, the photolithographic method reported previously [31, 32]. The product of this manufacturing step can be either the cell-backpack complexes or freely suspended backpacks. Since these backpacks can carry a myriad of compounds with differing functionalities, their applications seem boundless. Of particular interest here with respect to tissue engineering is the ability of these freely suspended backpacks to promote cell aggregate self-assembly. The size of these aggregates, as influenced by backpack diameter and ratio of cells to backpacks in the culture medium, has been shown to be reproducible [32]. Furthermore, the binding strength is quite strong; which was demonstrated by forcing the complexes through small pores and noting that the backpacks were not removed from the surface of the cells. The importance lies in the ability to use injection techniques (as in a needle tip of a syringe assemble), or for the movement from blood to tissue (extravasation) via narrow gaps. Based on these successes, one can envision applications that would create organoids of various types, such as lymphoid and beta cell clusters (analogous to islet of Langerhans). In these cases, the cargo could consist of drugs, adjuvants, and/or growth factors (for angiogenesis stimulation, reproduction, etc.). There also appears the potential for wound healing protocols.

To support our conjectures, some specific results should be elucidated. In their paper [32], the Cohen group presents fundamental studies on forming cellular aggregates using injectable cellular backpacks, how to control aggregate size,

and observations on association strength. Using confocal microscopy, flow cytometry, and laser diffraction, they observed that, while very large (>1 mm) aggregates can form, they may also dissociate and reform. Aggregates were forced through a nylon mesh filter and observed afterward: as the filter size decreased, resultant aggregates were smaller. When the pore size was reduced to less than the diameter of an individual cell, the backpacks were still attached. This implied to them that the attachment is sufficiently strong such that the backpacks would remain attached to a lymphocyte undergoing extravasation *in vivo*. In conclusion, they feel that an injectable backpack system could have applications in lymphoid tissue engineering as described by others [52, 53], as well as more general cellular engineering applications requiring close cell association.

3. Challenges and Future Opportunities

In this section, challenges such as safety considerations and reformulation strategies to overcome loading limitations, overdosing, and clearance issues are addressed. The opportunities lie in the enhanced capabilities with respect to improves therapeutic intervention strategies and additional applications for nanomedicine in the healthcare sector.

The perception that nanomaterials have inherent incompatibility issues with respect to the uptake into the human systemic environment has been addressed by many nanobiotechnology researchers (see Zook et al. [54] for a representative paper from the Biochemical Science Division of the National Institute of Standards and Technology).

Concerns such as toxicity, leaching, clearance, reproducibility/nonuniformity, chaperone characteristics/use of surface active agents and stability are major factors affecting the revolutionization of nanomedicine. The presence of multiple nanotechnology based drugs in the market place attests to the resolution of many of these issues. However, many more related to bioefficacy, loading capacity, and other features associated with performance optimization present ongoing challenges and opportunities for advances in nanomedicine thereby ensuring that it represents the future of medical care. General discussions, with key literature references, can be found in sources such as the Biomedical Engineering Handbook [55]. Of particular interest would be the section devoted to bionanotechnology with specific articles related to nanomaterials: perspectives and possibilities in nanomedicine [56]. The following comments are excerpts from their work and that of many other previously mentioned researchers [1–10, 31, 32, 35, 45, 52], along with summary statements from previous sections of this paper.

Specific illness treatments via nanomedicine protocols each have unique detriments that can be remedied by providing a range of delivery systems. The concept is to develop methods of controlled therapeutic delivery and release to specific tissues and tumors over a desired timeline. These systems are designed specifically to deliver soluble drugs, proteins, vaccine adjuvants, and plasmid DNA for gene therapy by exposing target cells to their cargo. The chaperone is thus required to enter the cells via endocytic

or phagocytic pathways and release its payload through degradation and diffusion mechanisms. The major challenge here is to accomplish these tasks while addressing the issues of biocompatibility, biodegradation, and the capture and clearance by the reticuloendothelial system (RES). Although excelling at some aspects, the current systems often fail to incorporate all required characteristics for high *in vivo* performance.

The chaperones for therapeutic nanoentities include viral carriers, organic and inorganic nanoparticles, and peptides. Although the efficient targeted delivery of therapeutic drugs continues to present challenges (with tremendous potential benefits), the emerging research into proteomics, for gene therapy as the future of nanomedicine treatments is attracting more attention. Fortunately, the necessary gene transfection considerations are directly applicable to drug delivery systems also.

The current carriers used for transfection are mainly adeno- and retroviruses. Although highly efficient they pose immunogenic and mutagenic hazards which led researchers to seek nonviral vectors. These include liposomes and nanoparticles of peptides and polymers, both synthetic and natural. Selection of vector type is dictated by the therapeutic agent, required pharmacokinetics, and the target cellular system, in addition to physical properties such as zeta potential (positive surface charge). The binding to blood proteins, clearance by the RES, and circulation times in the range of hours, rather than minutes, can be key performance targets/specifications. Hydrophilic polyethylene glycol (PEG) or longer chain polyethylene oxide (PEO) are commonly used synthetic polymers. Chitosan and alginate are useful natural polymers due to their excellent biodegradability characteristics. Biocompatible peptides show significant promise since they are able to bypass traditional endocytic pathways. Specific details can be found in Douglas et al. [56] and their accompanying literature references. The practical considerations enumerated there stress the need for the control of zeta potential, surface functionality via physical and chemical modifications, and the attainment of desired sizing. The method used to determine size is also important since dynamic light scattering (DLS) frequently gives larger measurement values than electron microscopy. Furthermore, DLS is particularly dependent on the presence of aggregate-inducing ions and proteins.

Vehicle surface characteristics are essential to control the contact time these vectors remain in the vasculature of a target region with respect to endocytosis and/or cargo release kinetics. Thus, in addition to chemical functionalization there exists numerous opportunities for magnetic, heat, and light affected systems influenced by external stimulus/fields.

These technological advances will translate into significant market enhancements. This is clear for both new and old drugs. For example, nanosizing of current marketed products is a means of providing these old drugs a new delivery platform offering new benefits and improved performance. FDA records indicate that the majority of approvals are reformulations or combinations of previously approved products. As a new candidate proceeds through its clinical testing program, it can be refined and/or postprocessed from

its discovery formulation to meet the requirements of the emerging target product profile; that is, its delivery route, dosage, and pharmacokinetic behavior.

Considering its vast potential it becomes evident that nanotechnology will have a significant impact upon the drug delivery sector and its ability to provide sound technological solutions for drug development programs. Consequently, market expectations for the nanotechnology drug delivery platform are high, and it is estimated that it will increase to about \$ 16 billion (USD) by 2014 [10].

4. Conclusions

Novel nanomaterial manufacturing methods and emerging nanotechnology applications for the pharmaceutical industry have been discussed in this paper. These manufacturing methods combine features such as bottom up nanoparticle formation for control of size and crystal structure with continuous manufacturing and Process Analytical Technology (PAT) for quality control and compatibility with the strict requirements imposed upon the pharmaceutical industry. The production of carefully engineered nanoparticles produced at high throughput rates and elevated technoeconomic stature demonstrates the role that transport phenomena has in path forward approaches for advanced drug delivery.

References

- [1] B. Rabinow, "Pharmacokinetics of nanosuspensions," in *Proceedings of the Nanotechnology for Drug Delivery Conference*, Philadelphia, Pa, USA, 2005.
- [2] B. E. Rabinow, "Nanosuspensions in drug delivery," *Nature Reviews Drug Discovery*, vol. 3, no. 9, pp. 785–796, 2004.
- [3] E. Merisko-Liversidge, G. G. Liversidge, and E. R. Cooper, "Nanosizing: a formulation approach for poorly-water-soluble compounds," *European Journal of Pharmaceutical Sciences*, vol. 18, no. 2, pp. 113–120, 2003.
- [4] R. Saffie-Siebert, J. Ogden, and M. Parry-Billings, "Nanotechnology approaches to solving the problems of poorly water-soluble drugs," *Drug Discovery World*, vol. 6, no. 3, pp. 71–76, 2005.
- [5] Microfluidicss Homepage, <http://www.microfluidicscorp.com/>.
- [6] Elan: NanoCrystal(R)Technology, http://www.elandrugtechnologies.com/nanocrystal_technology.
- [7] M. T. Stephan, J. J. Moon, S. H. Um, A. Bersthteyn, and D. J. Irvine, "Therapeutic cell engineering with surface-conjugated synthetic nanoparticles," *Nature Medicine*, vol. 16, no. 9, pp. 1035–1041, 2010.
- [8] R. Kumar, R. Tyagi, V. S. Parmar et al., "Perfluorinated amphiphilic polymers as nano probes for imaging and delivery of therapeutics for cancer," *Polymer Preprints*, vol. 45, p. 2, 2005.
- [9] M. T. Miller, *In vitro evaluation of cytotoxicity and cellular uptake of alternating copolymers for use as drug delivery vehicles*, Ph.D. dissertation, Department of Chemical Engineering, Massachusetts Institute of Technology, 2009.
- [10] G. Liversidge, "Controlled release and nanotechnologies: recent advances and future opportunities," *Drug Development and Delivery*, vol. 11, p. 1, 2011.

- [11] T. Panagiotou, S. V. Mesite, and R. J. Fisher, "Production of norfloxacin nanosuspensions using microfluidics reaction technology through solvent/antisolvent crystallization," *Industrial and Engineering Chemistry Research*, vol. 48, no. 4, pp. 1761–1771, 2009.
- [12] T. Panagiotou and R. Fisher, "Nano-particle formation via controlled crystallization: a "bottom-up" approach," *Chemical Engineering Progress*, vol. 104, p. 33, 2008.
- [13] T. Panagiotou, S. V. Mesite, J. M. Bernard, K. J. Chomistek, and R. J. Fisher, "Production of polymer nanosuspensions using Microfluidizer® processor based technologies," in *Proceedings of the Nanotechnology Conference and Trade Show*, pp. 688–691, June 2008.
- [14] T. Panagiotou, S. Mesite, R. Fisher, and I. Gruverman, "Production of stable drug nanosuspensions using microfluidics reaction technology," in *Proceedings of the NSTI Nanotechnology Conference and Trade Show*, pp. 246–249, May 2007.
- [15] A. Myerson, *Handbook of Industrial Crystallization*, Butterworth-Heinemann, Boston, Mass, USA, 2nd edition, 2002.
- [16] S. Rohani, S. Horne, and K. Murthy, "Control of product quality in batch crystallization of pharmaceuticals and fine chemicals—part 2: external control," *Organic Process Research and Development*, vol. 9, no. 6, pp. 873–883, 2005.
- [17] K. J. Carpenter and W. M. L. Wood, "Industrial crystallization for fine chemicals," *Advanced Powder Technology*, vol. 15, no. 6, pp. 657–672, 2004.
- [18] J. Baldyga and J. Bourne, *Turbulent Mixing and Chemical Reactions*, John Wiley & Sons, New York, NY, USA, 1999.
- [19] W. M. Deen, *Analysis of Transport Phenomena*, Oxford University Press, New York, NY, USA, 1998.
- [20] C. E. Brennen, *Cavitation and Bubble Dynamics*, Oxford University Press, London, UK, 1995.
- [21] K. D. Samant and L. O'Young, "Understanding crystallization and crystallizers," *Chemical Engineering Progress*, vol. 102, no. 10, pp. 28–37, 2006.
- [22] W. Genek, "Ask the experts: understanding crystallization," 2008, <http://www.aiche.org/cep/>.
- [23] J. Zhong, Z. Shen, Y. Yang, and J. Chen, "Preparation and characterization of uniform nanosized cephadrine by combination of reactive precipitation and liquid anti-solvent precipitation under high gravity environment," *International Journal of Pharmaceutics*, vol. 301, no. 1-2, pp. 286–293, 2005.
- [24] J. Midler, "Crystallization method to improve crystal structure and size," US Patent no. 5,314,506, 1994.
- [25] J. Kipp, J. Wong, M. Doty, and C. Rebbeck, "Microprecipitation method for preparing submicrometer suspensions," US Patent no. 6,869,617, 2001.
- [26] T. Panagiotou, S. Mesite, and R. Fisher, "Production of crystalline nanoparticles using microfluidics reaction technology," in *Proceedings of the 17th International Symposium on Industrial Crystallization Maastricht*, the Netherlands, 2008.
- [27] A. J. Mahajan and D. J. Kirwan, "Micromixing effects in a two-impinging-jets precipitator," *AIChE Journal*, vol. 42, no. 7, pp. 1801–1814, 1996.
- [28] B. K. Johnson and R. K. Prud'homme, "Chemical processing and micromixing in confined impinging jets," *AIChE Journal*, vol. 49, no. 9, pp. 2264–2282, 2003.
- [29] A. J. Mahajan and D. J. Kirwan, "Rapid precipitation of biochemicals," *Journal of Physics D*, vol. 26, no. 8 B, pp. B176–B180, 1993.
- [30] R. Costello, "Tiny reactors aim for big role," *Chemical Processing*, vol. 69, no. 12, pp. 14–19, 2006.
- [31] A. J. Swiston, C. Cheng, S. H. Um, D. J. Irvine, R. E. Cohen, and M. F. Rubner, "Surface functionalization of living cells with multilayer patches," *Nano Letters*, vol. 8, no. 12, pp. 4446–4453, 2008.
- [32] A. J. Swiston, J. B. Gilbert, D. J. Irvine, R. E. Cohen, and M. F. Rubner, "Freely suspended cellular "backpacks" lead to cell aggregate self-assembly," *Biomacromolecules*, vol. 11, no. 7, pp. 1826–1832, 2010.
- [33] R. J. Fisher and R. A. Peattie, "Controlling tissue microenvironments: biomimetics, transport phenomena, and reacting systems," *Advances in Biochemical Engineering/Biotechnology*, vol. 103, pp. 1–73, 2006.
- [34] A. M. Sokolnicki, R. J. Fisher, D. L. Kaplan, and T. P. Harrah, "Permeability studies with bacterial cellulose membranes," *Journal of Membrane Science*, vol. 6793, pp. 1–13, 2005.
- [35] K. E. Christodoulakis and M. Vamvakaki, "Amphoteric core-shell microgels: contraphilic two-compartment colloidal particles," *Langmuir*, vol. 26, no. 2, pp. 639–647, 2010.
- [36] E. Stratakis, A. Mateescu, M. Barberoglou, M. Vamvakaki, C. Fotakis, and S. H. Anastasiadis, "From superhydrophobicity and water repellency to superhydrophilicity: smart polymer-functionalized surfaces," *Chemical Communications*, vol. 46, no. 23, pp. 4136–4138, 2010.
- [37] R. A. Peattie, D. B. Pike, B. Yu et al., "Effect of gelatin on heparin regulation of cytokine release from hyaluronan-based hydrogels," *Drug Delivery*, vol. 15, no. 6, pp. 389–397, 2008.
- [38] R. A. Peattie, A. P. Nayate, M. A. Firpo, J. Shelby, R. J. Fisher, and G. D. Prestwich, "Stimulation of in vivo angiogenesis by cytokine-loaded hyaluronic acid hydrogel implants," *Biomaterials*, vol. 25, no. 14, pp. 2789–2798, 2004.
- [39] R. A. Peattie, A. P. Nayate, M. A. Firpo et al., "Stimulation of in vivo angiogenesis by cytokine-loaded hyaluronic acid hydrogel implants and potential gene expression mechanisms for new vessel growth," in *Proceedings of the IEEE Engineering in Medicine and Biology 24th Annual Conference*, pp. 873–874, October 2002.
- [40] D. B. Pike, S. Cai, K. R. Pomraning et al., "Heparin-regulated release of growth factors in vitro and angiogenic response in vivo to implanted hyaluronan hydrogels containing VEGF and bFGF," *Biomaterials*, vol. 27, no. 30, pp. 5242–5251, 2006.
- [41] R. A. Peattie, E. R. Rieke, E. M. Hewett, R. J. Fisher, X. Z. Shu, and G. D. Prestwich, "Dual growth factor-induced angiogenesis in vivo using hyaluronan hydrogel implants," *Biomaterials*, vol. 27, no. 9, pp. 1868–1875, 2006.
- [42] W. M. Pardridge, "Drug targeting to the brain," *Pharmaceutical Research*, vol. 24, no. 9, pp. 1733–1744, 2007.
- [43] Y. Lv, N. K. V. Cheung, and B. M. Fu, "A pharmacokinetic model for radioimmunotherapy delivered through cerebrospinal fluid for the treatment of leptomeningeal metastases," *Journal of Nuclear Medicine*, vol. 50, no. 8, pp. 1324–1331, 2009.
- [44] G. Li, W. Yuan, and B. M. Fu, "A model for water and solute transport across the blood-brain barrier," *Journal of Biomechanics*, vol. 43, no. 11, pp. 2133–2140, 2010.
- [45] G. Li, M. J. Simon, L. M. Cancel et al., "Permeability of endothelial and astrocyte cocultures: in vitro blood-brain barrier models for drug delivery studies," *Annals of Biomedical Engineering*, pp. 1–13, 2010.
- [46] R. Gabathuler, "Approaches to transport therapeutic drugs across the blood-brain barrier to treat brain diseases," *Neurobiology of Disease*, vol. 37, no. 1, pp. 48–57, 2010.

- [47] W. M. Pardridge, "Blood-brain barrier drug targeting: the future of brain drug development," *Mol Interv*, vol. 3, no. 2, pp. 90–51, 2003.
- [48] W. M. Pardridge, "Molecular Trojan horses for blood-brain barrier drug delivery," *Current Opinion in Pharmacology*, vol. 6, no. 5, pp. 494–500, 2006.
- [49] G. Miller, "Drug targeting: breaking down barriers," *Science*, vol. 297, no. 5584, pp. 1116–1118, 2002.
- [50] S. Gosk, C. Vermehren, G. Storm, and T. Moos, "Targeting anti-transferrin receptor antibody (OX26) and OX26-conjugated liposomes to brain capillary endothelial cells using in situ perfusion," *Journal of Cerebral Blood Flow and Metabolism*, vol. 24, no. 11, pp. 1193–1204, 2004.
- [51] A. S. Johnson, R. J. Fisher, G. C. Weir, and C. K. Colton, "Oxygen consumption and diffusion in assemblages of respiring spheres: performance enhancement of a bioartificial pancreas," *Chemical Engineering Science*, vol. 64, no. 22, pp. 4470–4487, 2009.
- [52] N. Doshi, A. J. Swiston, J. B. Gilbert et al., "Cell-based drug delivery devices using phagocytosis-resistant backpacks," *Advanced Materials*, vol. 23, no. 12, pp. H105–H109, 2011.
- [53] S. Suematsu and T. Watanabe, "Generation of a synthetic lymphoid tissue-like organoid in mice," *Nature Biotechnology*, vol. 22, no. 12, pp. 1539–1545, 2004.
- [54] J. M. Zook, R. I. MacCuspie, L. E. Locascio, M. D. Halter, and J. T. Elliott, "Stable nanoparticle aggregates/agglomerates of different sizes and the effect of their size on hemolytic cytotoxicity," *Nanotoxicology*. In press.
- [55] J. D. Bronzino, Ed., *Biomedical Engineering Handbook*, Taylor and Francis Group, Boca Raton, Fla, USA, 3rd edition, 2006.
- [56] K. L. Douglas, S. D. Carrigan, and M. Tabrizian, "Nanomaterials; perspectives and possibilities in nano-medicine," in *BME Handbook, Tissue Engineering and Artificial Organs Volume*, Chapter 26, Taylor and Francis Group, Boca Raton, Fla, USA, 3rd edition, 2006.

Research Article

Preparation of DNA/Gold Nanoparticle Encapsulated in Calcium Phosphate

Tomoko Ito,¹ Koyuki Ibe,² Tomohiro Uchino,¹ Hiroyuki Ohshima,² and Makoto Otsuka¹

¹ Research Institute of Pharmaceutical Sciences, Musashino University, Shinmachi 1-1-20, Nishitokyo-Shi, Tokyo 202-8585, Japan

² Graduate School of Pharmaceutical Sciences, Tokyo University of Science, 2641 Yamazaki, Noda-Shi, Chiba-Ken 278-8510, Japan

Correspondence should be addressed to Makoto Otsuka, motsuka@musashino-u.ac.jp

Received 27 October 2010; Revised 4 March 2011; Accepted 5 April 2011

Academic Editor: Guru V. Betageri

Copyright © 2011 Tomoko Ito et al. This is an open access article distributed under the Creative Commons Attribution License, which permits unrestricted use, distribution, and reproduction in any medium, provided the original work is properly cited.

Biocompatible DNA/gold nanoparticle complex with a protective calcium phosphate (CaP) coating was prepared by incubating DNA/gold nanoparticle complex coated by hyaluronic acid in SBF (simulated body fluid) with a Ca concentration above 2 mM. The CaP-coated DNA complex was revealed to have high compatibility with cells and resistance against enzymatic degradation. By immersion in acetate buffer (pH 4.5), the CaP capsule released the contained DNA complex. This CaP capsule including a DNA complex is promising as a sustained-release system of DNA complexes for gene therapy.

1. Introduction

Gene therapy has been proposed as a novel strategy for the treatment of refractory disease. However, direct injection of naked DNA coding a therapeutic gene generally fails to exhibit a satisfactory therapeutic effect [1, 2]. The low efficiency is due to the negative charge of the DNA molecules, which interferes with the binding of the complex to the cells. Too large DNA molecules also cause poor uptake by cells. DNase, which is present everywhere in the living body, seems to lower the efficiency of gene expression. Therefore, viral vectors have been widely used as carriers to deliver the therapeutic nucleic acids efficiently to the target cells. However, viral vectors have risks such as random recombination and immunogenicity [2]. Thus, safer alternative nonviral vectors such as polycations or cationic lipids have been explored as transfection mediators [2]. The DNA molecules can electrostatically associate with the cationic reagents and form small particles [3]. However, these DNA complexes are usually positively charged, which invites an adverse interaction with blood components or cells [4–6]. Moreover, the therapeutic effect is not satisfactory because of the short duration of gene expression [7].

Recently, drug delivery systems composed of inorganic nanoparticles, such as silica nanoparticles [8] or gold nanoparticles [9], have been developed. Gold nanoparticles

have the advantages of easy preparation and the possibility of chemical modification on the surface [10]. They also have distinctive optical properties, showing strong surface plasmon bands from the visible region to the near-IR region depending on their shape [11, 12]. Absorbed photoenergy is transformed to thermal energy, which stimulates drug release [13]. It should, thus, be possible to prepare an optically responsive DNA release system by binding DNA complexes to gold nanoparticles through thermodegradable bonds.

However, DNA/gold particle complexes are generally unstable in plasma because of their positive surface charge [14] and show nonspecific side effects with biocomponents as mentioned above. On the other hand, it is known that calcium-phosphate-based compounds, which have similar inorganic components to bone and teeth, are very biocompatible, and have been used as biomaterials, such as artificial bone or teeth [15]. In addition, they are dissolved and absorbed by the acid secreted from osteoclasts [16]. Such biocompatible and biodegradable materials are promising candidates as novel biocompatible and highly durable drug-releasing devices [17].

In this study, we developed novel DNA/gold nanoparticle complexes with protective calcium phosphate (CaP) coating. The effects of the CaP coating on the protection against degradation by DNase and suppression of adverse interactions with cells were investigated.

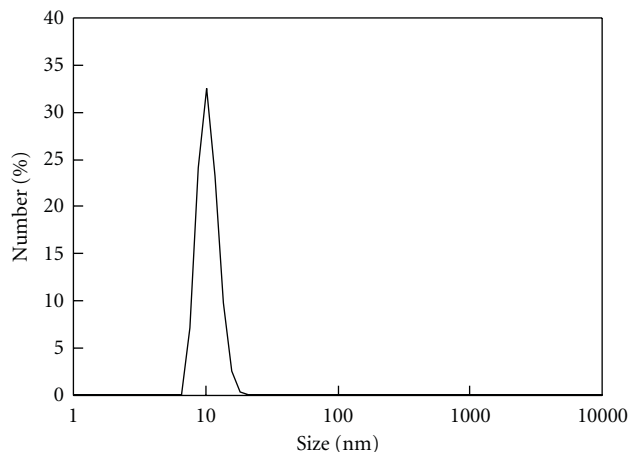


FIGURE 1: Size distribution profile of the gold nanoparticles.

2. Materials and Methods

2.1. Materials. Chloroauric acid (HAuCl_4), sodium borohydride (NaBH_4), and 2-aminoethanethiol were purchased from Wako Pure Chemical Industries, Ltd. Hyaluronic acid sodium salt (from a microorganism) and YOYO-1 iodide were obtained from Nacalai Tesque, Inc, and Invitrogen Corp, respectively. GFP-coding plasmid DNA (pDNA) with cytomegalovirus promoter was obtained from Clontech Laboratories, Inc. It was amplified in *Escherichia coli* and purified with a QIAGEN Plasmid Mega Kit.

2.2. Preparation of DNA/Gold (Au) Nanoparticle Complex. A solution of 0.01% HAuCl_4 (2 mL) was reduced using 1 μL of 0.38% NaBH_4 solution to produce Au nanoparticles. Five microliters of 330 $\mu\text{g}/\text{mL}$ pDNA aqueous solution was mixed with aminoethanethiol (AET) solution (5.6 mg/mL, 0.5–8 μL ; DNA : AET = 1 : 1.8, 3.6, 7.2, 14.4, and 28.7 (w/w)). After 10 min, 60 μL of Au suspension prepared as described above was added to the DNA/AET solution.

2.3. Preparation of DNA/Au Encapsulated by Calcium Phosphate. HA aqueous solution (0.5 μL –20 μL , 4.8 mg/mL) was added to 67 μL of pDNA/AET/Au suspension (pDNA : AET = 1 : 7.2 (w/w)). After stirring at room temperature for 30 min, 1.5 times concentrated simulated body fluid (SBF) [18] was added to the pDNA/AET/Au/HA suspension at a ratio of pDNA : AET : HA = 1 : 7.2 : 23.3 (w/w). The mixture was stirred at 37°C for 24 h.

2.4. Electrophoresis. A suspension of pDNA/AET/Au/HA with 1.5 SBF was mixed with an equal volume of 30% NaCl solution and incubated for 24 hours at 37°C to dissociate the DNA complex. The DNA complex was then diluted with pure water to adjust DNA concentration ($[\text{DNA}] = 2 \mu\text{g}/\text{mL}$), and dissociation of DNA complex was evaluated by agarose gel electrophoresis ([agarose gel] = 1%).

2.5. Measurement of ζ -Potential and Size. The sizes of Au nanoparticles and DNA/AET/Au/HA complex encapsulated in calcium phosphate were measured by a dynamic light scattering method (DLS) with a particle analyzer (Malvern Zetasizer Nano ZS). DNA/AET/Au complex or DNA/AET/Au/HA complex suspension was diluted with water to 1 mL, and ζ -potential was measured using the same particle analyzer.

2.6. SEM-EDS Analysis. DNA/AET/Au/HA encapsulated by calcium phosphate was dropped onto adhesive carbon tape and vacuum-dried overnight. The surface was evaluated by SEM-EDS (JSM-7600F, JEOL Ltd., Japan) operated at 5 kV.

2.7. Cytotoxicity. Cytotoxicity of DNA/AET/Au/HA encapsulated by calcium phosphate was evaluated by WST-1 assay as follows: MLC-6 cells, an osteoclast-like cell line derived from a mouse, were seeded onto 24-well plates at 9×10^3 cells per well and cultured for 2 days in McCoy 5A media supplemented with 20% fetal bovine serum (FBS). The primary growth medium was then replaced with 500 μL of fresh McCoy 5A with FBS. DNA/AET/Au/HA encapsulated by calcium phosphate was added to the cells (1.65 μg of plasmid per well). After incubation for 4 hours at 37°C, 500 μL of fresh medium was added to each well. After an additional 20 h of incubation at 37°C, the cells were assayed with Premix WST-1 Cell Proliferation Assay System (Takara Bio Inc.).

2.8. Cellular Uptake of the Particles. Plasmid DNA was fluorescently labeled with YOYO-1 at a YOYO-1/nucleotide ratio of 0.1. DNA/AET/Au/HA complex was then made of the fluorescent DNA and mixed with 1.5 SBF to be encapsulated by calcium phosphate (final Ca = 2.6 mM). It was added to the cells (1.65 μg of plasmid per well). After incubation for 4 hours at 37°C, 500 μL of fresh medium was added to each well. After an additional 20 h of incubation at 37°C, the cells were observed by a fluorescence microscopy.

2.9. Enzymatic Degradation of DNA. The protective effect against the enzymatic degradation of DNA by encapsulation with calcium phosphate was evaluated using Hind III (Takara Bio Inc.) as follows: Hind III (0.5 unit) was added to the DNA/AET/Au/HA encapsulated by calcium phosphate suspension (DNA = 190 ng) in accordance with the instructions for the reagent. The degradation of DNA was evaluated by agarose gel electrophoresis ([agarose gel] = 1%).

2.10. Statistical Analysis. Significant differences between two independent groups were examined by Student's *t*-test. One-way analysis of variance (ANOVA) was used to determine significant differences among six groups.

3. Results and Discussion

3.1. Formation of DNA/AET/Au/HA Complex Encapsulated in Calcium Phosphate. Small gold nanoparticles were readily

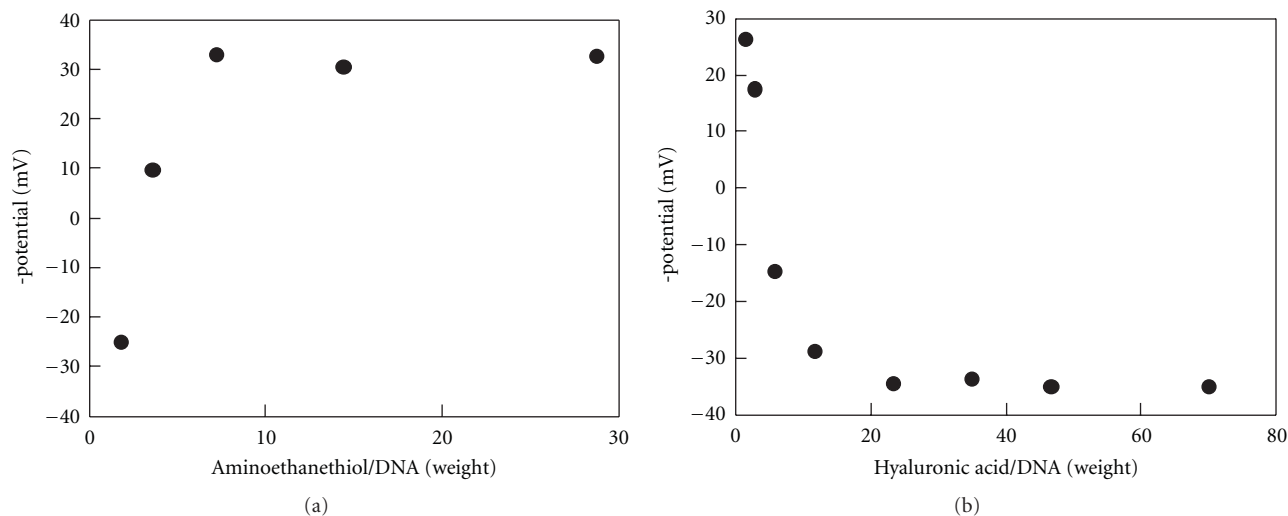


FIGURE 2: ζ -potential of the complex particles composed of (a) DNA, AET, and Au; (b) DNA, AET, Au, and HA.

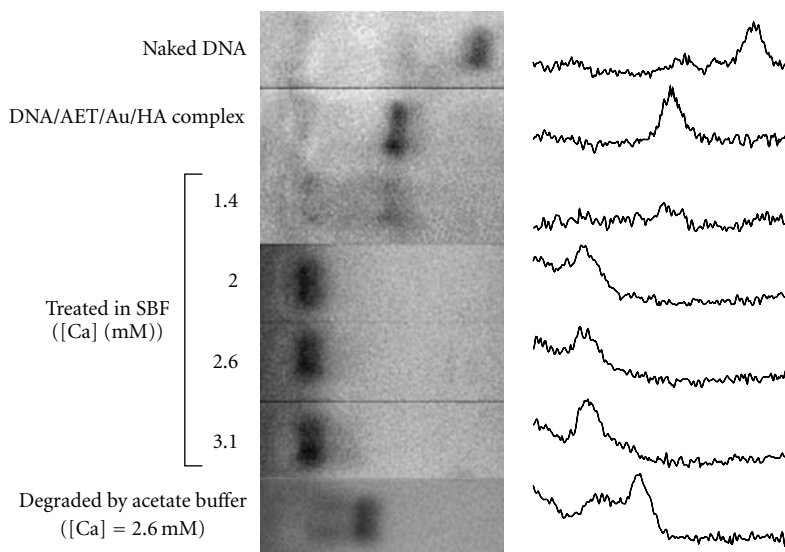


FIGURE 3: Agarose gel electrophoresis profile of the DNA complexes treated in SBF with various Ca concentrations. Complexes were electrophoresed after dissociation in 15% NaCl. The lowest line represents the result with a DNA complex treated in SBF with [Ca] = 2.6 mM and degraded in an acetate buffer.

obtained by reduction of HAuCl_4 by NaBH_4 . As shown in Figure 1, gold nanoparticles have a relatively narrow distribution in size with PDI = 0.834. Their number-average size was 10.5 nm with the standard deviation of 1.90 nm. It is known that thiol groups bind to gold nanoparticles [10]. AET was added to positively charge the gold nanoparticle surface. To decide on a suitable ratio of AET to DNA, various volumes of AET solution were premixed with DNA solution and then added to Au suspension. With increasing AET/DNA ratio, ζ -potential of the DNA/AET/Au complex increased and was saturated at 33 mV at AET/DNA = 7.2 (in weight) (Figure 2(a)). This ratio, where the highest potential was obtained with the minimal amount of AET, was employed in the following experiments.

DNA/AET/Au complex was then encapsulated in a CaP membrane using SBF. An SBF has a similar inorganic ion concentration to that of human blood plasma and is supersaturated against hydroxyapatite (Ca ion = 2.5 mM). In this study, 1.5 times concentrated SBF (Ca ion = 3.8 mM, pH 7.25) was used to deposit apatite onto the DNA/gold complex surfaces. An apatite layer is known to be formed on bioactive materials with phosphoric acid or carboxylic acid groups [19]. Hyaluronic acid (HA) was then added to coat the pDNA/AET/Au complex suspension to facilitate the deposition of calcium phosphate on the complex.

Various amounts of HA were added to DNA/AET/Au complex (DNA:AET = 1:7.2 in weight), and ζ -potential

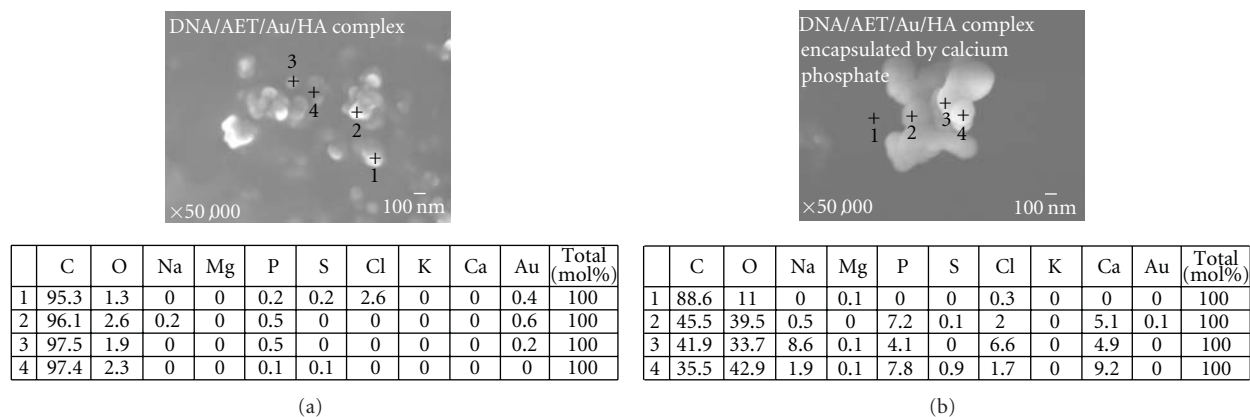


FIGURE 4: SEM-EDS analysis of (a) DNA/AET/Au/HA complex; (b) DNA/AET/Au/HA complex encapsulated in calcium phosphate (prepared in SBF with $[Ca] = 2.6$ mM).

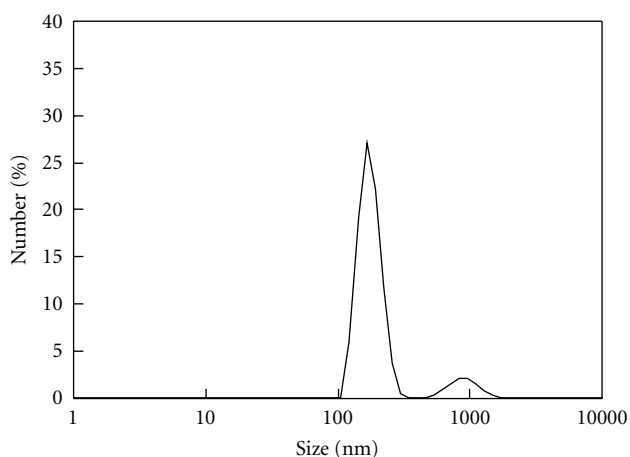


FIGURE 5: Size distribution profile of the DNA/AET/Au/HA complex encapsulated in calcium phosphate (prepared in SBF with $Ca = 2.6$ mM).

was measured. In line with the amount of HA, the surface charge of the DNA/AET/Au/HA complex decreased and was saturated at -35 mV at HA/DNA ratio = 23.3 (in weight). This ratio, where the ζ -potential reaches the lowest level by minimum HA (Figure 2(b)), was employed in the following experiments.

DNA/AET/Au complex coated by HA (DNA : AET : HA = 1 : 7.2 : 23.3 in weight) was added to the SBF, and deposition of CaP layer on the surface of DNA/AET/Au/HA complex was attempted. DNA complex suspension was added to 1.5 times concentrated SBF at a final Ca concentration of 1.4, 2.0, 2.6, or 3.1 mM. To examine the deposition of CaP, dissociation behavior of the DNA complex in a concentrated NaCl solution was evaluated. DNA complex immersed in SBF with 1.4 mM Ca ion concentration was dissociated by concentrated NaCl solution and showed bands at similar positions to those of DNA complex without SBF. On the other hand, the DNA complexes immersed in SBF with more than 2.0 mM Ca did not show bands from dissociated DNA

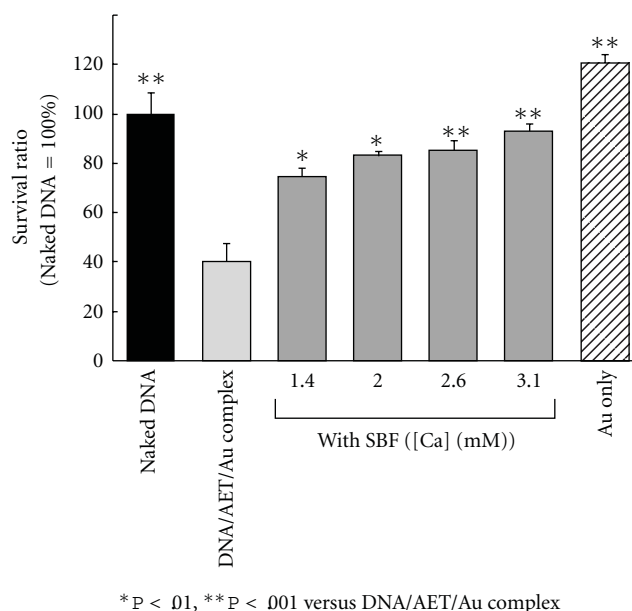


FIGURE 6: Cytotoxicity of Au nanoparticle and the DNA complexes with or without calcium phosphate envelope.

molecules. This indicates that CaP could be deposited onto a surface of DNA complex coated by HA by immersion in SBF with more than 2.0 mM Ca and form a stable encapsulated complex (Figure 3).

Degradation of the CaP capsule in an acidic solution was then examined. An equal volume of pH 4.5 acetate buffer was added to the suspension of DNA/AET/Au/HA complex encapsulated in CaP, which was prepared with 2.6 mM Ca. After stirring at 37°C for 24 h, 30% NaCl solution was added. When it was electrophoresed, a clear band of the dissociated DNA molecule was observed (Figure 3). This shows that the DNA complex was coated with a CaP layer, which could be dissolved in the acidic conditions, and released the DNA complex encapsulated inside.

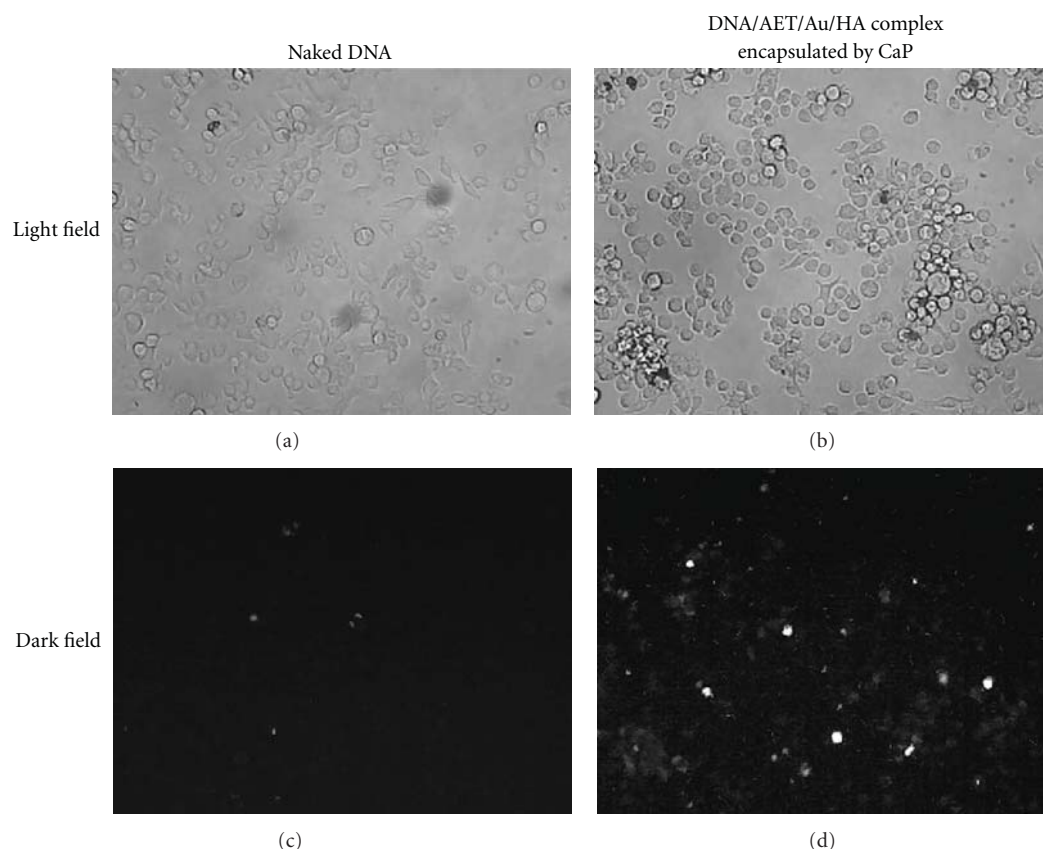


FIGURE 7: Cellular uptake of fluorescence-labeled naked DNA and its complex with Au encapsulated with CaP.

In SEM-EDS images, differences in surface morphology and composition were observed (Figure 4). Large aggregation of particles with a diameter of ca. 100 nm was seen in the SEM image of DNA/AET/Au/HA complex, and Au was detected in the particle by EDS analyses (Figure 4(a)). On the other hand, the DNA/AET/Au/HA complex encapsulated in CaP was an aggregation of particles of 200 nm in diameter. Calcium and phosphorus were detected in it instead of Au (Figure 4(b)). It was confirmed that the DNA/AET/Au complex coated with HA could be encapsulated with CaP by immersion in SBF. The number average size of the DNA/AET/Au/HA complex encapsulated by CaP suspended in water was 175 nm with the standard deviation of 33.4 nm (Figure 5). The large aggregation of the encapsulated complex would be formed through the drying procedure for SEM observation.

3.2. Cytotoxicity of DNA Complex Encapsulated in Calcium Phosphate. Figure 6 shows the cytotoxicity of the DNA/AET/Au/HA complex and the encapsulated particles. Judging from the WST-1 assay, DNA/AET/Au complex showed apparent toxicity and only 40% of the cells survived, while Au itself showed much less toxicity. This was due to the cationic surface of the DNA/AET/Au complex. On the other hand, DNA complex encapsulated by CaP showed apparently

lower toxicity, and more than 80% of the cells were still alive. Encapsulation by the biocompatible apatite appeared to cause diminished toxicity.

3.3. Cellular Uptake of the Particles. Plasmid DNA was fluorescently labeled by YOYO-1, complexed with gold, and then packaged by CaP. When they were incubated with MLC-6 cells, the cells became luminescent, while the cells treated with naked DNA/YOYO-1 complex did not show the fluorescence (Figure 7).

3.4. Enzymatic Degradation of DNA Complex Encapsulated in Calcium Phosphate. Enzymatic degradation behavior of the DNA molecule was evaluated by incubation with Hind III followed by agarose gel electrophoresis. DNA molecule in the DNA/AET/Au/HA complex without CaP was degraded by the enzyme and showed bands of degradation products. A smeared band was observed, unlike for the naked DNA (Figure 8). This was considered to be due to the interaction of the degraded DNA fragments with the cationic polymer. DNA complex not completely encapsulated by CaP, which was prepared in final $[Ca] = 1.4$ mM, also showed bands of degraded products. On the other hand, DNA complex encapsulated by CaP at more than final $[Ca] = 2.0$ did not show any DNA fragments (Figure 8). Efficient inhibition of

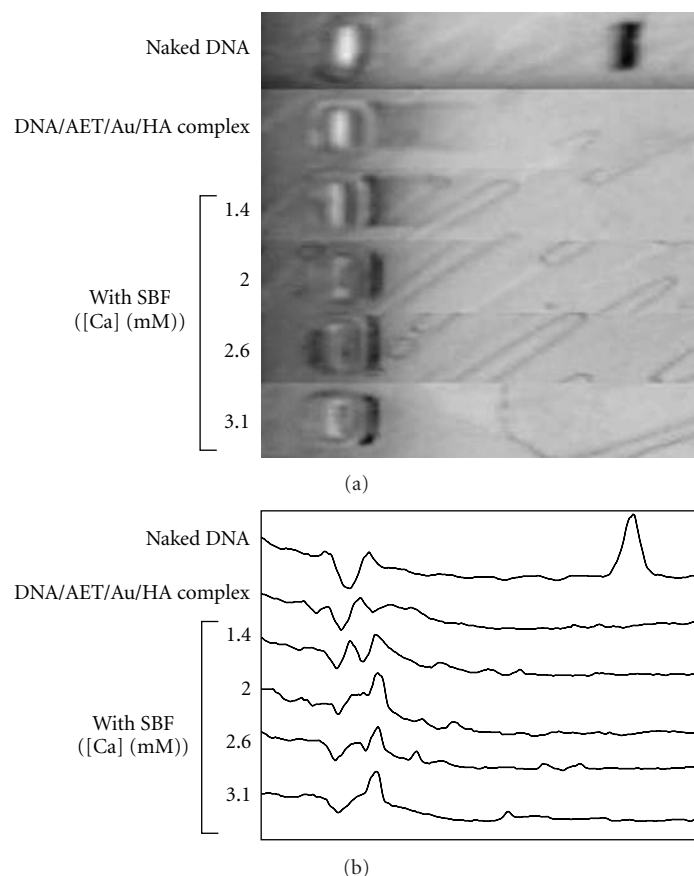


FIGURE 8: Agarose gel electrophoresis profile of the DNA complex encapsulated in CaP after degradation by Hind III.

DNA degradation by an enzyme by encapsulation with CaP was confirmed.

CaP-encapsulated DNA/gold nanoparticle has high biocompatibility and resistance against enzymatic degradation and also the releasing property by cellular degradation. It is expected to be a safe and durable nonviral system for gene therapy.

4. Conclusion

DNA/gold complex was efficiently included in a CaP capsule by coating the complex with hyaluronic acid followed by immersion in SBF with a Ca concentration above 2 mM. Biocompatibility and resistance against enzymatic degradation were apparently enhanced by the encapsulation with CaP. Incubation of the CaP capsule including DNA complex in an acidic acetate buffer invited the release of DNA complex from the capsule. This shows the high potential of the CaP capsule as an injectable slow-release device, which would release the contained DNA complex by degradation by osteoclasts.

Acknowledgments

The authors thank Professor K. Yoshikawa (Kyoto University) for his help with the ζ -potential and size measurements. This work was partly supported by the Japan Society for the Promotion of Science (no. 21700494), Foundation for

Promotion of Material Science and Technology of Japan, and MEXT HAITEKU (2008) from the Ministry of Education.

References

- [1] X. Zhou and L. Huang, "DNA transfection mediated by cationic liposomes containing lipopolylysine: characterization and mechanism of action," *Biochimica et Biophysica Acta*, vol. 1189, no. 2, pp. 195–203, 1994.
- [2] K. Taira, K. Kataoka, and T. Niidome, Eds., *Non-Viral Gene Therapy: Gene Design and Delivery*, Springer, Tokyo, Japan, 2005.
- [3] S. M. Mel'nikov, V. G. Sergeev, and K. Yoshikawa, "Discrete coil—globule transition of large DNA induced by cationic surfactant," *Journal of the American Chemical Society*, vol. 117, no. 9, pp. 2401–2408, 1995.
- [4] C. Plank, K. Mechtler, F. C. Szoka Jr., and E. Wagner, "Activation of the complement system by synthetic DNA complexes: a potential barrier for intravenous gene delivery," *Human Gene Therapy*, vol. 7, no. 12, pp. 1437–1446, 1996.
- [5] Y. Koyama, T. Ito, H. Matsumoto et al., "Novel poly(ethylene glycol) derivatives with carboxylic acid pendant groups: synthesis and their protection and enhancing effect on non-viral gene transfection systems," *Journal of Biomaterials Science, Polymer Edition*, vol. 14, no. 6, pp. 515–531, 2003.
- [6] T. Ito, N. Iida-Tanaka, and Y. Koyama, "Efficient in vivo gene transfection by stable DNA/PEI complexes coated by

- hyaluronic acid,” *Journal of Drug Targeting*, vol. 16, no. 4, pp. 276–281, 2008.
- [7] D. Olton, J. Li, M. E. Wilson et al., “Nanostructured calcium phosphates (NanoCaPs) for non-viral gene delivery: influence of the synthesis parameters on transfection efficiency,” *Biomaterials*, vol. 28, no. 6, pp. 1267–1279, 2007.
- [8] C. Kneuer, M. Sameti, E. G. Haltner et al., “Silica nanoparticles modified with aminosilanes as carriers for plasmid DNA,” *International Journal of Pharmaceutics*, vol. 196, no. 2, pp. 257–261, 2000.
- [9] T. Niidome, M. Yamagata, Y. Okamoto et al., “PEG-modified gold nanorods with a stealth character for in vivo applications,” *Journal of Controlled Release*, vol. 114, no. 3, pp. 343–347, 2006.
- [10] P. Ghosh, G. Han, M. De, C. K. Kim, and V. M. Rotello, “Gold nanoparticles in delivery applications,” *Advanced Drug Delivery Reviews*, vol. 60, no. 11, pp. 1307–1315, 2008.
- [11] G. Schmid, “Large clusters and colloids. Metals in the embryonic state,” *Chemical Reviews*, vol. 92, no. 8, pp. 1709–1727, 1992.
- [12] X. Huang, I. H. El-Sayed, W. Qian, and M. A. El-Sayed, “Cancer cell imaging and photothermal therapy in the near-infrared region by using gold nanorods,” *Journal of the American Chemical Society*, vol. 128, no. 6, pp. 2115–2120, 2006.
- [13] I. H. El-Sayed, X. Huang, and M. A. El-Sayed, “Surface plasmon resonance scattering and absorption of anti-EGFR antibody conjugated gold nanoparticles in cancer diagnostics: applications in oral cancer,” *Nano Letters*, vol. 5, no. 5, pp. 829–834, 2005.
- [14] T. Kawano, M. Yamagata, H. Takahashi et al., “Stabilizing of plasmid DNA in vivo by PEG-modified cationic gold nanoparticles and the gene expression assisted with electrical pulses,” *Journal of Controlled Release*, vol. 111, no. 3, pp. 382–389, 2006.
- [15] S. V. Dorozhkin and M. Epple, “Biological and medical significance of calcium phosphates,” *Angewandte Chemie—International Edition*, vol. 41, no. 17, pp. 3130–3146, 2002.
- [16] S. A. Redey, S. Razzouk, C. Rey et al., “Osteoclast adhesion and activity on synthetic hydroxyapatite, carbonated hydroxyapatite, and natural calcium carbonate: relationship to surface energies,” *Journal of Biomedical Materials Research*, vol. 45, no. 2, pp. 140–147, 1999.
- [17] M. P. Ginebra, T. Traykova, and J. A. Planell, “Calcium phosphate cements as bone drug delivery systems: a review,” *Journal of Controlled Release*, vol. 113, no. 2, pp. 102–110, 2006.
- [18] T. Kokubo and H. Takadama, “How useful is SBF in predicting in vivo bone bioactivity?” *Biomaterials*, vol. 27, no. 15, pp. 2907–2915, 2006.
- [19] M. Tanahashi and T. Matsuda, “Surface functional group dependence on apatite formation on self-assembled monolayers in a simulated body fluid,” *Journal of Biomedical Materials Research*, vol. 34, no. 3, pp. 305–315, 1997.

Research Article

Unveiling Stability Criteria of DNA-Carbon Nanotubes Constructs by Scanning Tunneling Microscopy and Computational Modeling

Svetlana Kilina,¹ Dzmityr A. Yarotski,² A. Alec Talin,³ Sergei Tretiak,^{2,4}
Antoinette J. Taylor,² and Alexander V. Balatsky^{2,4}

¹Department of Chemistry and Biochemistry, North Dakota State University, Fargo, ND 58108-6050, USA

²Los Alamos National Laboratory, Center for Integrated Nanotechnologies, Los Alamos, NM 87545, USA

³NIST Center for Nanoscale Science and Technology, Energy Research Group, Gaithersburg, MD 20899, USA

⁴Los Alamos National Laboratory, Theoretical Division, Los Alamos, NM 87545, USA

Correspondence should be addressed to Alexander V. Balatsky, avb@lanl.gov

Received 1 November 2010; Accepted 22 January 2011

Academic Editor: Giorgia Pastorin

Copyright © 2011 Svetlana Kilina et al. This is an open access article distributed under the Creative Commons Attribution License, which permits unrestricted use, distribution, and reproduction in any medium, provided the original work is properly cited.

We present a combined approach that relies on computational simulations and scanning tunneling microscopy (STM) measurements to reveal morphological properties and stability criteria of carbon nanotube-DNA (CNT-DNA) constructs. Application of STM allows direct observation of very stable CNT-DNA hybrid structures with the well-defined DNA wrapping angle of 63.4° and a coiling period of 3.3 nm. Using force field simulations, we determine how the DNA-CNT binding energy depends on the sequence and binding geometry of a single strand DNA. This dependence allows us to quantitatively characterize the stability of a hybrid structure with an optimal π -stacking between DNA nucleotides and the tube surface and better interpret STM data. Our simulations clearly demonstrate the existence of a very stable DNA binding geometry for (6,5) CNT as evidenced by the presence of a well-defined minimum in the binding energy as a function of an angle between DNA strand and the nanotube chiral vector. This novel approach demonstrates the feasibility of CNT-DNA geometry studies with subnanometer resolution and paves the way towards complete characterization of the structural and electronic properties of drug-delivering systems based on DNA-CNT hybrids as a function of DNA sequence and a nanotube chirality.

1. Introduction

The development of highly specific drug delivery systems (DDSs) holds a great promise for increased therapeutic treatment efficiency and elimination of often harmful side effects. However, it is a formidable task due to additional strict requirements posed on DDS, such as high stability, ability to penetrate cellular membranes, and low cytotoxicity. Several important breakthroughs have been achieved in recent years using biologically inspired liposome, ligand, and antibody-based DDS, some of which are already used in clinical environment for cancer treatment with positive results [1, 2]. Despite initial success, these results provide only a hint of the potential capabilities of properly designed drug carriers, and further improvements of DDS are necessary,

including yet another leap in specificity and better drug-load capacity.

Recently, inorganic nanomaterials, such as carbon nanotubes (CNTs), nanowires, and metal or semiconductor nanoparticles, have attracted much attention due to their remarkable physical and chemical properties and, especially, the tunability of these properties provided by the system size. Unique functionality makes these nanoscale entities very attractive for applications in a wide range of biological and chemical problems, and, specifically, in the development of drug carrying platforms [3]. So far, the majority of preclinical studies of nanomaterial-based DDS have focused on oncology, thus making cancer the primary candidate for future clinical trials of these DDS. For example, gold nanoparticles have been extensively used

to selectively precipitate in cancer cells and subsequently destroy them through laser light absorption and generation of large intracellular heat loads [4].

Among all the novel DDSs, however, CNTs appear to be one of the most promising materials. This view is rationalized by many potential advantages of functionalized CNTs over other types of DDS developed for cancer therapy [5]. First of all, CNTs feature high surface-to-volume and length-to-diameter ratios, allowing large drug loads while still being small enough to penetrate cellular walls. Second, CNT functionalization with various binding agents provides virtually unlimited tunability of binding specificity. Several research groups have already demonstrated that CNTs coated with lipid conjugates [6], copolymers, and surfactants [7] can deliver various molecular loads through cellular membranes *in vivo* and *in vitro* with high targeting specificity and low cytotoxicity [8, 9]. Third, the unique optical properties of CNTs permit efficient electromagnetic stimulation and highly sensitive detection of CNT-based DDS using various imaging modalities. For example, strong light absorption in the cell transparency region (0.7–1.1 μm) allows CNTs to serve as a local heat source inside a target cell [10] or to be remotely triggered to release some of its drug-load with high spatial, temporal, and chemical selectivity [11, 12]. Driven by the intense global research to take advantage of the unique properties of CNTs, the use of CNTs in medicine has started to shift from proof-of-principle experiments to preclinical trials in a variety of therapeutic applications. Nevertheless, we still need to develop a better understanding of CNT functionalities in order to fully exploit all the potential benefits of CNTs in drug delivery and diagnostics and to assess the risks and benefits of these DDS.

One of the prominent ways to improve delivery specificity, DDS stability, and cell penetration reliability is functionalization of the nanotube surface with single-stranded DNA. Such CNT-DNA hybrids are widely used for biological sensing [13–15], as well as for separating CNTs based on dimensions and conductivity [16, 17]. CNT-DNA hybrids promise significant advantages over existing DDS: (i) adsorbed DNA strands remarkably improve the dispersibility of the nanotubes in water and biologically compatible buffers, while simultaneously offering a stable and flexible platform for further derivatization and binding agent attachment. (ii) The DNA strands also provide very stable interaction with CNT surface and help to control the length of the tubes [18]. Because DNA-CNT binding energy is fairly large, “fortification” of the nanotube segments covered by DNA is expected. When the CNT breakage occurs (e.g., because of thorough sonication [17]), it will take place in the regions with a lower tensile strength, that is, the uncovered parts of the nanotube, leaving the tubes of the length of the DNA-wrapped structures. All these features are very important for medical applications, since it has been shown that shortened, better isolated and dispersed, functionalized CNTs demonstrate an improved toxicological profile in *in vivo* studies [19–22].

It is widely recognized that structural and surface characteristics of DDS should critically influence their biological performance. Yet little is known about the detailed structure

of CNT-DNA hybrids. Different computational approaches reported in the literature predict a large variation of the possible DNA binding geometries [23] from linear DNA alignment along the CNT [24] to wrapping of DNA around the CNT [25], with a finite probability of the DNA insertion into the interior volume of the CNT [26, 27]. In addition, recent experimental studies have empirically demonstrated that DNA oligomers with a particular sequence prefer to form stable structures with a specific kind of nanotubes and ignore others. These observations suggest that the chemical structure of DNA and the chirality of the CNT play a significant, if not determining, role in establishing the final hybrid geometry [16, 28, 29]. Unfortunately, the current theoretical framework cannot explain the wide geometry variations and sequence selectivity of the DNA-CNT binding. Additional complexity comes from the lack of understanding of the exact mechanisms of cellular membrane penetration by CNTs [12, 30]: it is unclear how the given hybrid structure influences penetration efficiency, as well as how the penetration process influences stability of a hybrid DDS.

As such, new methods have to be developed for reliable prediction of the properties of DDS based on CNT-DNA hybrids and accurate control of drug binding and delivery. Considering its importance, the stability of DNA coating of the nanotube surface has to be analyzed in order to avoid the risk of macromolecule desorption or exchange with serum proteins and other blood components following administration. Hence, theoretical modeling and simulations capable of describing the DNA-CNT binding mechanisms and predicting the hybrid stable structure and its relevant properties will significantly benefit experimental *in vitro* and *in vivo* studies of CNT-DNA-based DDS. Such studies will also require an application of high-resolution nanoscale probes to test the theoretical predictions, visualize the DDS geometries, and provide feedback for gradual modeling refinement.

Here, we report on such a combined approach that involves, first, modeling to determine the stability criteria for CNT-DNA hybrid binding and, second, scanning tunneling microscopy (STM) for simultaneous structural and electronic characterization of hybrid structure and electronic properties with subnanometer resolution. We present the observed topographic images of the CNT-DNA hybrids with highly resolved morphological details. The STM images reveal very stable hybrid structures where DNA is wrapped around the CNT with a well-defined wrapping angle of 63.4° and a coiling period of 3.3 nm. Our previous studies [18, 31] of the helical nature of the charge density distribution in the nanotubes have demonstrated a strong correlation between CNT chirality and DNA wrapping geometry. In the current work, we further investigate this correlation and describe the dependence of the DNA-CNT binding energy on the chemical structure and wrapping geometry of a single strand DNA (ssDNA) around the (6,5) CNT. This information allows quantitative characterization of the stability of the hybrid structure with an optimal π -stacking between ssDNA bases and the nanotube surface. Our simulations clearly show the existence of a very stable DNA binding geometry for

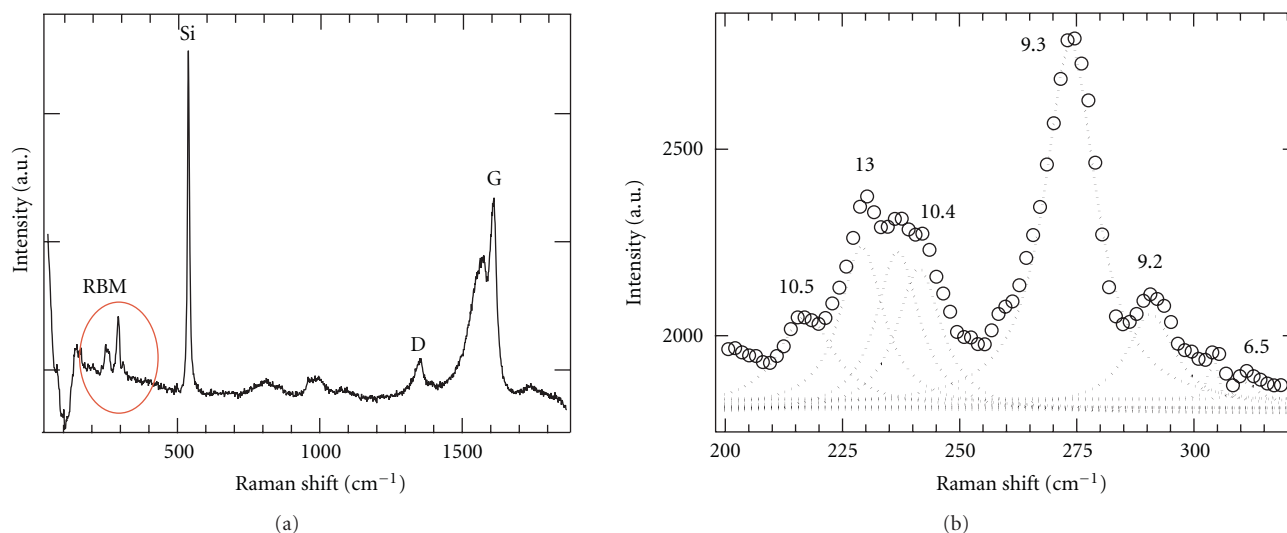


FIGURE 1: Raman spectra of the prepared DNA-CNT solution. (a) The wide frequency window showing all vibronic bands. (b) The frequency range associated with RBM bands of nanotubes.

the (6,5) CNT which is determined by a strong dependence of the binding energy on angular detuning of DNA strand from the nanotube chiral vector. Finally, we provide the additional evidence that the stable binding geometry of DNA nucleotides and CNTs arises from the π -stacking interactions, which tend to align the molecular plane of nucleotide parallel to the tube surface.

2. Experimental Details

We used surfactant-based nanotube suspensions that were prepared by 2.5 hours of sonication of purified single-walled CNT (SWCNT) powder obtained from SES Research in 1% by weight of Triton X-100 in water. The final concentration of SWCNTs was ~ 0.1 mg/ml. To form DNA-based nanotube suspensions, a 20-mer DNA sequence of 5'NH₂(C-6) GAGAAGAGAGCAGAAGGAGA-3' was diluted to approximately 5 mg/ml in phosphate buffer solution with pH 7.4 (PBS 7.4). One mg of SWCNT was dissolved in approximately 250 microliters of the DNA solution and then diluted to approximately 0.75 ml with PBS 7.4. The resulting mixture was sonicated at 0°C for at least 90 min and then centrifuged at 14000 rpm for 90 min. 0.5 ml of the DNA/SWCNT solution was decanted and purified over a NAP-10 column using deionized water as the buffer, with only first 1/2 of the eluted volume being collected. The filtered solution was finally passed again through the NAP-10 column with deionized water as eluent.

As shown in Figure 1, Raman spectra of thus prepared solution contain six major radial breathing mode (RBM) frequencies, which can be attributed to (13,0), (10,4), (9,3), (9,2), (6,5), and (10,5) tubes [32]. The (9,3) tubes have the highest RBM intensity and, therefore, seem to be the most common type in the sample. It is known that functionalization of the tubes with DNA increases the optical response of CNTs due to enhanced dispersion and isolation

of DNA-coated tubes [28, 29]. However, the high intensity of the Raman peak associated with (9,3) species is not necessary the sign of the preferable DNA attachment to the (9,3) tubes and most likely originates from the higher concentration of these tubes in the original solution.

After Raman characterization, a small drop of the CNT-DNA solution was deposited onto p-doped Si(110) substrate and allowed to dry. The samples were then transferred into the STM vacuum chamber and are annealed at 550°C for 30 min in order to remove the organic residue and the freshly formed oxide layer from the Si surface. Even though CNT-DNA hybrids in aqueous solution are unstable above 80°C, the critical temperature for the same constructs adsorbed onto Si(110) surface appears to be much higher, and heating up to 550°C does not destroy samples. Although the mechanism of such an improved thermal stability of CNT-DNA hybrids is not clear yet, we assume that a strong π - π interaction between the CNT surface and DNA bases is responsible for this stability, when it is not disturbed and screened by solvent interactions. A commercial UHV variable-temperature STM system (RHK Technology Inc., UHV300) was used to obtain the topographic images of CNT-DNA hybrids shown in Figure 2(a). All measurements were performed at a pressure of 2×10^{-10} Torr and a temperature of 50 K.

3. Theoretical Modeling and Computational Details

We have chosen a specific (6,5) nanotube for hybrid structure simulations since it provides the best match to the STM results, as was discussed in our previous studies of the CNT-DNA structures [18]. We use force field calculations to determine detailed geometrical features of an ssDNA adsorbed on the (6,5) SWNT (diameter of 0.8 nm and the chiral angle of 27°). Two configurations of the (6,5) SWNT

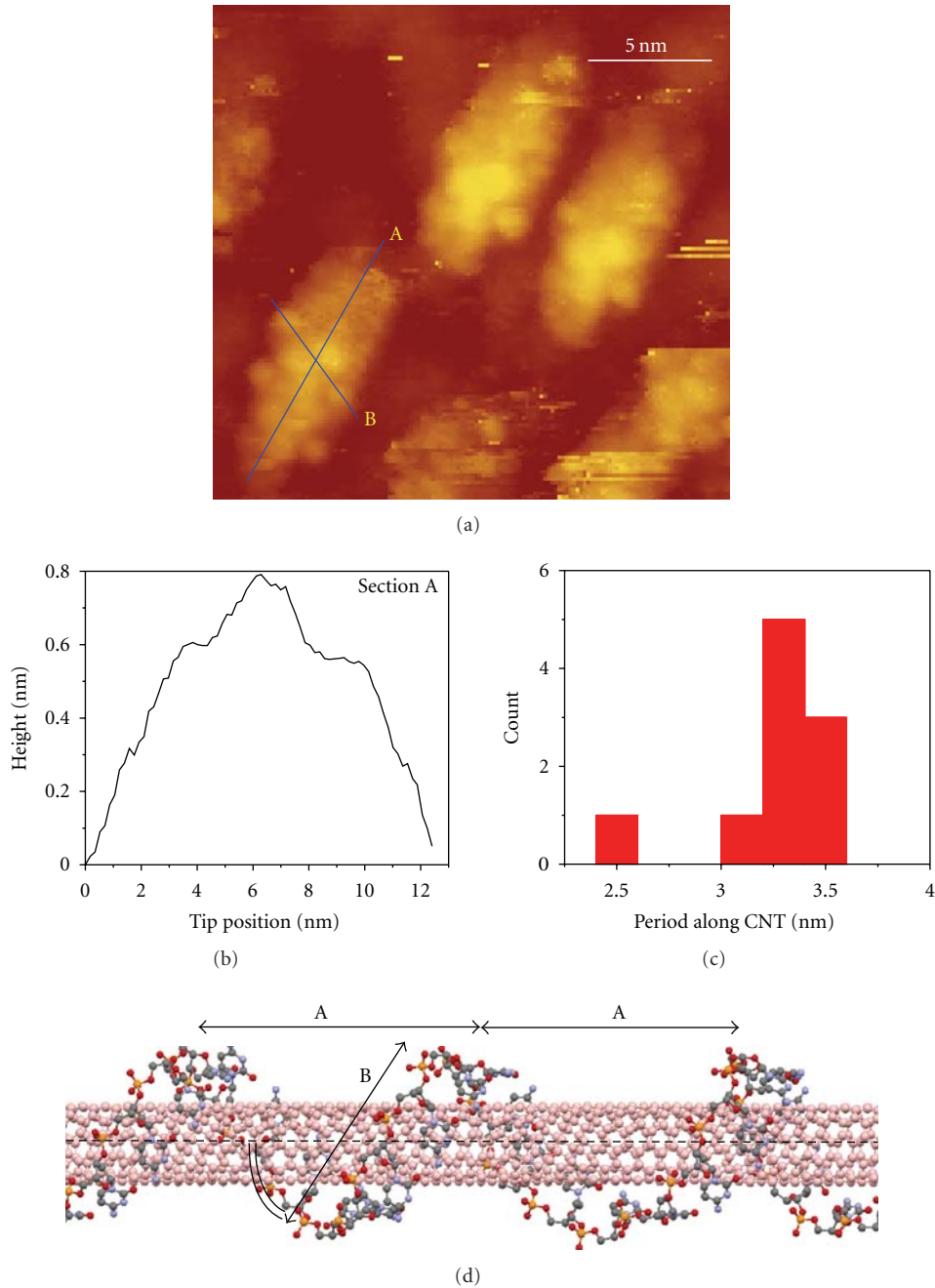


FIGURE 2: STM data and theoretical interpretation: (a) 21×21 nm STM topographic image of CNT-DNA hybrids on Si(110) substrate acquired at $I_t = 10$ pA and $U_b = 3$ V at 50 K; (b) height profile along Section A; (c) statistical distribution of characteristic lengths of periodic modulations extracted from height profiles along the Section A. (d) Optimized structures of (6,5) tube wrapped in GAGAAGAGAGCAGAAGGAGA-oligomer. For the simulated geometry, the average period of DNA helices along the tube is $A = 3.0$ – 3.3 nm and the wrapping angle is $\alpha \sim 63^\circ$, which are in good agreement with an STM experiment.

are considered: with the length of three (~ 12 nm) and four (~ 16 nm) nanotube repeat units. To model the DNA adsorption on the CNT surface, we use an experimental 20-mer DNA sequence of 5'-GAGAAGAGAGCAGAAGGAGA-3' and homogeneous ssDNA oligonucleotides with 23, 25, 29, 31, and 42 cytosine bases (C-23-mer, C-25-mer, C-29-mer, and C-31-mer and C-42-mer, resp.) and 25 guanine bases

(G-25-mer). The size of the ssDNA is chosen to be shorter than the tube length to avoid interactions of the DNA with the tube edges.

To construct different CNT-DNA hybrid configurations, the ssDNA is wrapped around the tube at angles varying from 10° to 80° with respect to the tube axis, as illustrated in Figure 3. For the initial configurations of the homogeneous

ssDNA on the SWNT surface, we start with a single DNA unit consisting of a DNA base attached to a phosphate-deoxyribose molecule. First, we optimize the initial unit on the tube surface by placing it at a random angle α with respect to the tube axis. The coordinates of each atom i of the optimized unit are defined as (x_i^n, y_i^n, z_i^n) , where the index n is the number of the unit ($n = 0$ for the initial unit). Subsequent DNA bases ($n = 1, 2, 3, \dots$) are added as the replicas of the first adsorbed unit but are shifted along the tube axis by Δz and twisted by the angle ϕ_i^n . Defining the size L of the unit as the distance between terminated atoms in the DNA base, the single increment along z is $\Delta z = L \sin \alpha$. Then, the z -coordinates of each DNA atom of the next unit n satisfy the equation $z_i^n = z_i^0 + n\Delta z$, while x_i^n and y_i^n can be obtained from the coordinates x_i^0 and y_i^0 of the corresponding DNA atoms from the initial unit by applying the rotational matrix

$$\hat{V}(\phi_i^n) = \begin{bmatrix} \cos(\phi_i^n) & -\sin(\phi_i^n) \\ \sin(\phi_i^n) & \cos(\phi_i^n) \end{bmatrix}. \quad (1)$$

Here, $\phi_i^n = z_i^n / (R \tan \alpha)$ is the rotational angle of the i th base of the n th unit of the ssDNA. Thus, each atom of the DNA backbone is placed along the helix curve with a helical angle α , the DNA wrapping angle with respect to the tube axis. When $\phi_i^n = 2\pi$, the z -coordinate defines the period length of the DNA wrapping along the tube axis. $R = R_0 + \Delta$ stands for the helix radius, where R_0 is a tube radius and $\Delta \sim 0.33$ nm is a typical distance between the tube surface and DNA molecules in the π -stacking geometry. As a next step, these initial configurations of (6,5) SWNT and ssDNA are further optimized to obtain energetically favorable morphologies. Compared to the initial geometries, the DNA wrapping angles undergo small changes during geometrical optimization. Thus, we obtain many conformations of CNT-DNA hybrids with various DNA wrapping angles.

It is known that potential energy surfaces of biomolecules are extremely complicated [33]. Therefore, there are many distinct local potential minima where the hybrid system can be trapped depending on its initial configuration during the optimization procedure. This suggests a strong dependence of the total energy of the system on the wrapping angle of the ssDNA around the tube. However, optimized configurations obtained by the method described above often have loops at the center or ends of the tube leading to a variation of a wrapping angle along the CNT, as shown in Figure 3 (right panel). To obtain a more homogeneous distribution of the DNA wrapping angles, we fix the very end bases of the DNA and let all other atoms of the DNA and the tube move freely during geometrical optimization. This allows us to compare the dependence of the binding energies on the wrapping angle for two cases—with free and fixed DNA ends.

The binding energy, that is, the strength of the interaction between the ssDNA and the tube, is calculated as the difference between the total energies of the optimized CNT-DNA hybrid, the optimized bare CNT, and the optimized isolated DNA molecule. To find the optimized geometry of an isolated ssDNA, the DNA configuration obtained from the optimization of the CNT-DNA hybrid geometry and

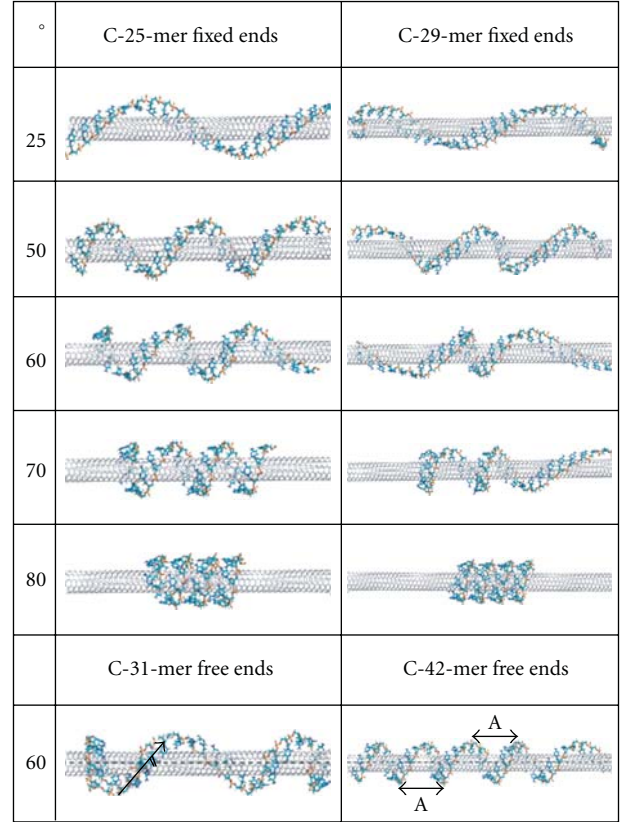


FIGURE 3: Optimized geometries of the (6,5) tube with adsorbed C-mers obtained from different initial wrapping configurations. First column shows the averaged final wrapping angle α of the DNA. Second and third columns correspond to hybrid configurations constructed from the 3 and 4 repeat units long (6,5) nanotube and DNA consisting of 25 (C-25-mer) and 29 (C-29-mer) cytosine bases, respectively. The bottom panel shows 31 and 42 C-mers wrapped along (6,5) tube of 4 units in length.

subsequent removal of all the CNT atoms is used as an initial approximation for the force field energy optimization. Finally, the optimized DNA configuration with the smallest total energy is chosen as the final configuration of the isolated DNA molecule. All geometrical optimizations are performed by means of the HyperChem software package [34] using the CHARM27 force field approach [35, 36] and an energy convergence limit of 0.001 KCal/(Åmol).

4. Experimental Results

A characteristic STM image of the CNT-DNA sample is shown in Figure 2(a). The DNA-covered parts of the nanotube are visible as large island-like protrusions on a flat substrate surface. Three notable features of the samples are evident in Figure 2(a). First, all observed islands have similar structure. This suggests that either we are able to resolve the structure of only one type of CNT-DNA hybrids or else hybrids consisting of different SWNT types have the same geometry. However, the latter assumption contradicts previous experimental [16, 18, 28, 37] and theoretical

[17, 25, 28, 38] results that demonstrated strong dependence of the DNA wrapping geometry on CNT chirality. Therefore, we conclude that only one type of CNT-DNA sample is observable due to the selectivity of the DNA wrapping with respect to the tube chirality.

Second, there are no uncovered ends of SWNTs visible in the image as one might expect from the length differences between a typical SWNT (~ 100 's of nm) and 20-mer ssDNA. This discrepancy can be explained by the sonication step in the sample preparation procedure [18]. Previously, it was found that thorough sonication leads to multiple nanotube breakages resulting in significant nanotube length reduction [17]. In our case, DNA-covered segments serve as fortified islands along the nanotube length, causing the breaks to occur at the edges of such regions and leaving only short, 10–15 nm, fragments of the original SWNT for observation. This suggests that the length of the CNT-DNA hybrids can be controlled with some degree of precision by varying the length of the ssDNA-covered segments and subsequent thorough sonication. This observation might be important for medicinal application of these materials. For instance, there is good agreement between multiple preclinical studies that shortening of functionalized CNT helps to reduce cytotoxicity [5, 39].

Third, the STM image in Figure 2(a) and height profile in Figure 2(b) clearly demonstrate the coiling character of the DNA strand binding to the nanotube surface. Regular height modulations of the DNA-covered segments of the CNTs are also visible in the image. Two sections of the hybrid profile emphasize the periodic nature of these modulations both along the nanotube (Section A) and across it (Section B). We attribute the three height peaks in Section A, Figure 2(b), to the three DNA coils lying on top of the nanotube surface. Indeed, the modulation depth of ~ 2 Å matches quite well an expected ~ 3 Å distance between the nanotube surface and the nucleotides that are aligned parallel to it in the π -stacking geometry [23, 25]. Section B represents the CNT-DNA hybrid profile variations in the direction of DNA coiling. Importantly, this section is oriented at a 63.4° angle with respect to the nanotube axis obtained in the same way as explained in [18]. This angle represents the DNA wrapping angle and should depend on the particular DNA sequence and the nanotube type, because nucleotides tend to arrange themselves on the nanotube surface in such a way as to minimize tension in the combined CNT-DNA system [33].

The overall observed width of the CNT-DNA composite is on the order of 5 nm. This value deviates significantly from the expected $2 \div 3$ nm combined width of the CNT-DNA hybrid. The width of $2 \div 3$ nm is expected due to the contribution of the CNT diameter of ~ 1 -2 nm and DNA-CNT separation of ~ 0.3 nm (a typical π -stacking distance) on both sides of the CNT, as was discussed previously in [18]. We believe that DNA detachment from the nanotube sidewalls during annealing causes this discrepancy, increasing the overall hybrid width. The periodicity of the height profile in Section B also suggests that there are longitudinal DNA strand distortions that cannot be associated with any predicted binding stoichiometries [18]. However, it is impossible to directly detect the DNA detachment from

the CNT surface using STM. The exposed CNT regions, if any occur during annealing, will protrude by about a nanometer and will not be accessible for direct imaging due to the cone-like shape of the STM tip.

To extract more quantitative information about the observed DNA wrapping geometry, we use the following procedure. First, cross-sections along the longitudinal axis of several SWNTs analogous to Section A in Figure 2(a) are taken. In this way, peaks in the topography can be attributed to the DNA strand, and dips represent the underlying SWNT surface between them. The Fourier transformation (FT) of such a section with respect to the longitudinal coordinate provides well-defined peaks in the spatial frequency domain due to the periodic nature of the profile variation, as shown in Figure 2(b). The characteristic length of the topographic height modulation is obtained by inversion of the spatial frequency of the corresponding peak maximum. Although observation of more cycles will provide higher accuracy in determining of the wrapping period, we believe that the precision achieved with three wrapping cycles observed in our experiments should suffice for comparison with the modeling results and nanotube identification. Indeed, experimental height modulation profile in Figure 2(b) can be approximated by the sine wave, and the width of the peak in the fast-FT spectrum of sine wave spanning N periods (λ) is $\sim 2\lambda/N$ at zero level. Due to noise in the measured profiles, any point above 90% of the maximum peak amplitude level can be considered as a center peak frequency. However, it will result in only $\sim 0.12\lambda$ spread of the measured period around the actual value, which in our case is ~ 0.3 nm. This error is much smaller than the difference between the wrapping periods for all the types of nanotubes present in the solution and should allow reliable separation of hybrids containing nanotubes of different chiralities as described below. The nanotube edges influence the DNA-CNT binding and, thus, the wrapping geometry. This causes small coil-to-coil distance variations, so that the DNA wrapping is not perfectly aligned with the nanotube chiral vector. However, these variations are on the order of 0.1-0.2 nm and fall well within the experimental error. Hence, they also can be neglected in the comparison of the modeled structure with the STM images.

Using this procedure, the dependence of the frequency of occurrence of a particular period on its magnitude for all hybrids in our images was extracted and is plotted in Figure 2(c). As can be seen, the characteristic period of the height variation along the CNT is 3.3 nm and represents the coiling period of the DNA strand around CNT. Thus, our STM images reveal the DNA wrapping angle of $\sim 63^\circ$ and the most probable DNA coiling period of ~ 3.3 nm.

5. Simulations Results and Discussion

Previous molecular simulations [33] predict that short ssDNA strands can adopt a number of helical conformations when placed on a nanotube. The geometries observed by STM here suggest an existence of very specific stable structure with the DNA helical period of 3.3 nm and

the wrapping angle of $\sim 63^\circ$. Our simulations of CNT-DNA hybrid constructed from the (6,5) tube and 20-mer ssDNA that was used in STM imaging have also resulted in a very stable configuration with the binding energy of -0.8 eV per base, wrapping angles of $\sim 63^\circ$, and wrapping period of 3.0–3.3 nm, as shown in Figure 2(d). The optimized structure of the hybrid also confirms that the stable binding geometry of DNA nucleotides and CNT arises from the π -stacking interactions, which tend to align the nucleotide molecular plane parallel to the tube surface.

For further examination of the stability of different CNT-DNA hybrid structures, we calculated the binding energy between various adsorbed ssDNA C-mers and G-mers and the (6,5) tube at different wrapping geometries, as shown in Figure 3. It is obvious that the distribution of wrapping angles along the nanotube length is not homogeneous with most deviations occurring at the edges of the nanotube. For the fixed DNA geometries, when a few DNA bases at the ends are not free to move with other atoms of the systems during geometry optimization, the homogeneity of wrapping angles improves significantly; see Figure 3 (left panel). Overall, the deviation from a mean value of wrapping angle is about 10° – 15° for the structures with fixed ends and up to 20° – 30° for structures with free ends.

Figure 4 shows the binding energy of the DNA and the (6,5) SWNT as a function of the average wrapping angle. The minimum of the curve indicates the most stable hybrid configuration with the strongest interaction between the tube surface and the DNA strand. For all C-mers, a well-defined minimum is found in the range of 58° – 63° ; these wrapping angles correlate well with the chiral angle of the (6,5) tube. For the G-mer, the minimum is slightly shifted towards smaller angles of 50° – 60° . For all hybrids we considered, the energy barrier around the minimum is about 0.2–0.3 eV, which is significantly higher than thermal fluctuation energies. The CNT-DNA interactions are also very substantial (-0.6 eV and -0.8 eV) implying very stable hybrid configurations for wrapping angles of 50° – 63° . Thus, we conclude that hybrids with DNA wrapped in correlation with the (6,5) chirality of nanotube have extremely stable configurations. For these structures, ssDNA is unlikely to be detached from the tube because of external perturbations, such as ambient thermal vibrations, solvent effects, and exchanges with blood serum. All these observations point to the utility of DNA-functionalized CNT for medicinal purposes.

The smaller the wrapping angle of C-mers, the larger the energy, reflecting much weaker interaction of cytosine-oligomers with the CNT for these geometries. In contrast, G-mers provide very stable configurations not only at 50° – 60° but also at small wrapping angles of 10° – 20° . Interestingly, not all guanine molecules are oriented parallel to the tube surface at small wrapping angles, as observed for cytosine-oligomers: a few guanine bases have nearly normal orientation to the tube surface and form the π - π stacking with each other. This behavior most likely originates from a larger size of guanines compared to cytosines, which favors such interactions. The difference between C-mer and G-mer optimal wrapping angles, at which the most stable hybrid

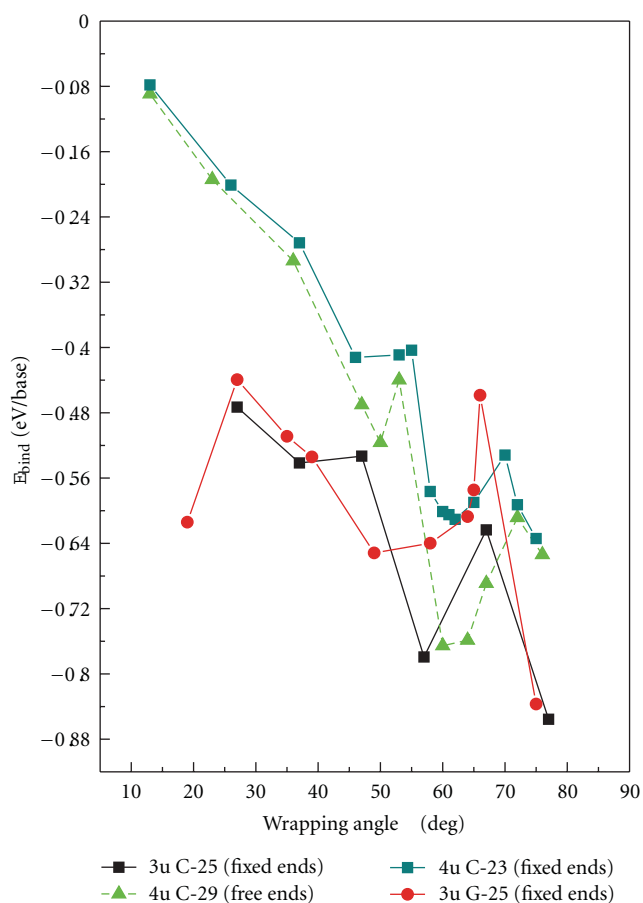


FIGURE 4: Variation of the binding energy of the CNT-DNA hybrids with the DNA wrapping angle. The solid lines correspond to hybrid configurations with fixed ends, that is, where the end bases of the DNA molecule are fixed and all other atoms of the hybrid system are free to move during geometry optimization. Dashed lines represent the optimized hybrid structure where all the atoms are allowed to move during optimization. The red line corresponds to the hybrid constructed out of 3 unit-long (6,5) tube (3u) and DNA strand consisting of 25 guanine bases (G-25); the black line represents the same tube but with 25-mer cytosine bases (C-25); the dark green line represents (6,5) tube of 4 repeat units in length (4u) with adsorbed 23-mer cytosine bases (C-23). The light green dashed line corresponds to configurations constructed from the (6,5) nanotube of 4 repeat units in length (4u) and 29-mer cytosine bases (C-29).

conformations occur, may explain a previously observed difference in stability of CNT-DNA hybrids with respect to the chemical structure/sequence of the adsorbed DNA.

For the large angles $\alpha > 70^\circ$, the binding energy decreases for both G-mer and C-mers. For the short tubes and short DNA oligomers, the binding energy at $\alpha \sim 75^\circ$ becomes even smaller than that of configurations with $\sim 60^\circ$ angles. This decrease most likely originates from formation of additional bonds between DNA bases and the phosphate groups due to a very small separation of DNA loops on CNT surface; see Figure 3. Interestingly, such bonding is favored by the presence of the SWNT, since optimized

configurations of an isolated DNA strand do not indicate similar tendency. If solvent media are introduced, formation of these hydrogen bonds will likely be suppressed by solvent-phosphate backbone interactions.

It is important to mention that structures with large wrapping angles result in much smaller wrapping periods of about 1 nm. The short wrapping periods, if present in the experimental samples, mean that the gaps between the DNA strands on the tube surface have to be also very small, on the order of 0.2–0.8 nm, as compared to ~2.2 nm observed in STM images. The fact that we have only observed geometries with ~63° wrapping angle in our experiments can be, thus, attributed to the inability of our instrument to resolve such small gaps. This is confirmed by the data presented in Figure 2(b), where dome-like modulation structure due to convolution of tip shape with sample structure is visible instead of expected 0.47 nm and 0.35 nm steps formed by the DNA backbone and nucleotides, correspondingly.

6. Conclusions

Characterization of CNT-DNA hybrids using STM reveals a very stable structure of DNA binding to a single CNT where DNA wraps around the tube at 63° angle with a coiling period of 3.3 nm. To complement and help interpret STM measurements, we have performed force field simulations that provided insight into the energetic stability of CNT-DNA hybrids. The modeling results are in very good agreement with experimental observations and clearly show the existence of a stable DNA binding geometry to (6,5) SWNT as determined by the strong dependence of the binding energy on angular detuning of the DNA strand from the CNT chiral vector. The calculations also confirm that such a correlation between the DNA wrapping and nanotube chirality arises from optimization of π -stacking interactions between molecular orbitals of DNA bases and the π orbitals of the nanotube. Based on STM data and calculated stability criteria for different DNA conformations on the nanotube surface, we conclude that ssDNA wraps around the (6,5) tube in accordance to the tube chirality. Substantial binding energies of 0.6–0.8 eV and high energy barriers of 0.1–0.3 eV separating the hybrid configurations of coiled and uncoiled ssDNA imply an extreme stability of such hybrid systems. This result suggests that external disturbances caused by body heat, solvent effects, and exchanges with blood serum are highly unlikely to detach the DNA from the CNT surface. Therefore, CNT-DNA hybrids hold great promise for development of very reliable and stable DDS.

We also found that sonication of CNT-DNA hybrids leads to reduction of nanotube ends uncoated by DNA. Thus, we suggest that the length of the CNT-DNA hybrids can be reduced with a precise control by applying sonication and varying the DNA sequence length adsorbed on the tube surface. This observation might be important for medical application of these materials, since shortening of functionalized CNTs reduces their cytotoxicity.

Overall, our results demonstrate the feasibility of CNT-DNA geometry studies with subnanometer resolution and

pave the way towards complete characterization of the hybrid structural and electronic properties as a function of DNA sequence and nanotube type. In addition, our combined approach can be used in the future to predict and characterize important properties of hybrid-based DDS and details of their interaction with the drug molecules, such as controlled drug release triggered by the heat or laser-induced unwrapping of DNA strand from the nanotube surface.

Acknowledgments

The authors are grateful to T. Kawai and H. Tanaka for useful discussions. They acknowledge support from the Los Alamos National Laboratory LDRD Program, UCOP-027 and NNEDC Funds. This work was performed, in part, at the Center for Integrated Nanotechnologies, a US Department of Energy, Office of Basic Energy Sciences user facility. Los Alamos National Laboratory, an affirmative action/equal opportunity employer, is operated by Los Alamos National Security, LLC, for the National Security administration of the US Department of Energy under Contract DE-AC52-06NA25396.

References

- [1] M. A. Moses, H. Brem, and R. Langer, "Advancing the field of drug delivery: taking aim at cancer," *Cancer Cell*, vol. 4, no. 5, pp. 337–341, 2003.
- [2] R. Sinha, G. J. Kim, S. Nie, and D. M. Shin, "Nanotechnology in cancer therapeutics: bioconjugated nanoparticles for drug delivery," *Molecular Cancer Therapeutics*, vol. 5, no. 8, pp. 1909–1917, 2006.
- [3] M. Ferrari, "Cancer nanotechnology: opportunities and challenges," *Nature Reviews Cancer*, vol. 5, no. 3, pp. 161–171, 2005.
- [4] S. Lal, S. E. Clare, and N. J. Halas, "Nanoshell-enabled photothermal cancer therapy: impending clinical impact," *Accounts of Chemical Research*, vol. 41, no. 12, pp. 1842–1851, 2008.
- [5] K. Kostarelos, A. Bianco, and M. Prato, "Promises, facts and challenges for carbon nanotubes in imaging and therapeutics," *Nature Nanotechnology*, vol. 4, no. 10, pp. 627–633, 2009.
- [6] Z. Liu, W. Cai, L. He et al., "In vivo biodistribution and highly efficient tumour targeting of carbon nanotubes in mice," *Nature Nanotechnology*, vol. 2, no. 1, pp. 47–52, 2007.
- [7] C. J. Gannon, P. Cherukuri, B. I. Yakobson et al., "Carbon nanotube-enhanced thermal destruction of cancer cells in a noninvasive radiofrequency field," *Cancer*, vol. 110, no. 12, pp. 2654–2665, 2007.
- [8] N. W. S. Kam, T. C. Jessop, P. A. Wender, and H. Dai, "Nanotube molecular transporters: internalization of carbon nanotube-protein conjugates into mammalian cells," *Journal of the American Chemical Society*, vol. 126, no. 22, pp. 6850–6851, 2004.
- [9] A. A. Bhirde, V. Patel, J. Gavard et al., "Targeted killing of cancer cells in vivo and in vitro with EGF-directed carbon nanotube-based drug delivery," *ACS Nano*, vol. 3, no. 2, pp. 307–316, 2009.
- [10] K. König, "Multiphoton microscopy in life sciences," *Journal of Microscopy*, vol. 200, no. 2, pp. 83–104, 2000.

- [11] N. W. S. Kam, M. O'Connell, J. A. Wisdom, and H. Dai, "Carbon nanotubes as multifunctional biological transporters and near-infrared agents for selective cancer cell destruction," *Proceedings of the National Academy of Sciences of the United States of America*, vol. 102, no. 33, pp. 11600–11605, 2005.
- [12] N. W. S. Kam, Z. Liu, and H. Dai, "Carbon nanotubes as intracellular transporters for proteins and DNA: an investigation of the uptake mechanism and pathway," *Angewandte Chemie International Edition*, vol. 45, no. 4, pp. 577–581, 2006.
- [13] D. A. Heller, H. Jin, B. M. Martinez et al., "Multimodal optical sensing and analyte specificity using single-walled carbon nanotubes," *Nature Nanotechnology*, vol. 4, no. 2, pp. 114–120, 2009.
- [14] E. L. Gui, L. J. Li, P. S. Lee et al., "Electrical detection of hybridization and threading intercalation of deoxyribonucleic acid using carbon nanotube network field-effect transistors," *Applied Physics Letters*, vol. 89, no. 23, Article ID 232104, 2006.
- [15] J. Wang, G. Liu, and M. R. Jan, "Ultrasensitive electrical biosensing of proteins and dna: carbon-nanotube derived amplification of the recognition and transduction events," *Journal of the American Chemical Society*, vol. 126, no. 10, pp. 3010–3011, 2004.
- [16] M. Zheng, A. Jagota, M. S. Strano et al., "Structure-based carbon nanotube sorting by sequence-dependent DNA assembly," *Science*, vol. 302, no. 5650, pp. 1545–1548, 2003.
- [17] M. Zheng, A. Jagota, E. D. Semke et al., "DNA-assisted dispersion and separation of carbon nanotubes," *Nature Materials*, vol. 2, no. 5, pp. 338–342, 2003.
- [18] D. A. Yarotski, S. V. Kilina, A. A. Talin et al., "Scanning tunneling microscopy of DNA-Wrapped carbon nanotubes," *Nano Letters*, vol. 9, no. 1, pp. 12–17, 2009.
- [19] L. Lacerda, H. Ali-Boucetta, M. A. Herrero et al., "Tissue histology and physiology following intravenous administration of different types of functionalized multiwalled carbon nanotubes," *Nanomedicine*, vol. 3, no. 2, pp. 149–161, 2008.
- [20] R. Singh, D. Pantarotto, L. Lacerda et al., "Tissue biodistribution and blood clearance rates of intravenously administered carbon nanotube radiotracers," *Proceedings of the National Academy of Sciences of the United States of America*, vol. 103, no. 9, pp. 3357–3362, 2006.
- [21] H. Wang, J. Wang, X. Deng et al., "Biodistribution of carbon single-wall carbon nanotubes in mice," *Journal of Nanoscience and Nanotechnology*, vol. 4, no. 8, pp. 1019–1024, 2004.
- [22] L. Lacerda, M. A. Herrero, K. Venner, A. Bianco, M. Prato, and K. Kostarelos, "Carbon-nanotube shape and individualization critical for renal excretion," *Small*, vol. 4, no. 8, pp. 1130–1132, 2008.
- [23] H. Gao and Y. Kong, "Simulation of DNA-nanotube interactions," *Annual Review of Materials Research*, vol. 34, pp. 123–150, 2004.
- [24] X. Zhao and J. K. Johnson, "Simulation of adsorption of DNA on carbon nanotubes," *Journal of the American Chemical Society*, vol. 129, no. 34, pp. 10438–10445, 2007.
- [25] R. R. Johnson, A. T. C. Johnson, and M. L. Klein, "Probing the structure of DNA-carbon nanotube hybrids with molecular dynamics," *Nano Letters*, vol. 8, no. 1, pp. 69–75, 2008.
- [26] T. Kaneko, T. Okada, and R. Hatakeyama, "DNA encapsulation inside carbon nanotubes using micro electrolyte plasmas," *Contributions to Plasma Physics*, vol. 47, no. 1-2, pp. 57–63, 2007.
- [27] H. Gao, Y. Kong, D. Cui, and C. S. Ozkan, "Spontaneous insertion of DNA oligonucleotides into carbon nanotubes," *Nano Letters*, vol. 3, no. 4, pp. 471–473, 2003.
- [28] X. Tu, S. Manohar, A. Jagota, and M. Zheng, "DNA sequence motifs for structure-specific recognition and separation of carbon nanotubes," *Nature*, vol. 460, no. 7252, pp. 250–253, 2009.
- [29] L. Zhang, X. Tu, K. Welsher, X. Wang, M. Zheng, and H. Dai, "Optical characterizations and electronic devices of nearly pure (10,5) single-walled carbon nanotubes," *Journal of the American Chemical Society*, vol. 131, no. 7, pp. 2454–2455, 2009.
- [30] K. Kostarelos, L. Lacerda, G. Pastorin et al., "Cellular uptake of functionalized carbon nanotubes is independent of functional group and cell type," *Nature Nanotechnology*, vol. 2, no. 2, pp. 108–113, 2007.
- [31] S. Kilina, S. Tretiak, S. K. Doorn et al., "Cross-polarized excitons in carbon nanotubes," *Proceedings of the National Academy of Sciences of the United States of America*, vol. 105, no. 19, pp. 6797–6802, 2008.
- [32] A. Jorio, R. Saito, J. H. Hafner et al., "Structural (n, m) determination of isolated single-wall carbon nanotubes by resonant Raman scattering," *Physical Review Letters*, vol. 86, no. 6, pp. 1118–1121, 2001.
- [33] S. Meng, P. Maragakis, C. Papaloukas, and E. Kaxiras, "DNA nucleoside interaction and identification with carbon nanotubes," *Nano Letters*, vol. 7, no. 1, pp. 45–50, 2007.
- [34] *HyperChem Lite v. 2*, Hypercube Inc., Gainesville, Fla, USA, 1991.
- [35] N. Foloppe and A. D. MacKerell Jr., "All-atom empirical force field for nucleic acids: I. Parameter optimization based on small molecule and condensed phase macromolecular target data," *Journal of Computational Chemistry*, vol. 21, no. 2, pp. 86–104, 2000.
- [36] A. D. MacKerell Jr. and N. K. Banavali, "All-atom empirical force field for nucleic acids: II. Application to molecular dynamics simulations of DNA and RNA in solution," *Journal of Computational Chemistry*, vol. 21, no. 2, pp. 105–120, 2000.
- [37] S. N. Kim, Z. Kuang, J. G. Grote, B. L. Farmer, and R. R. Naik, "Enrichment of (6,5) single wall carbon nanotubes using genomic DNA," *Nano Letters*, vol. 8, no. 12, pp. 4415–4420, 2008.
- [38] S. R. Lustig, A. Jagota, C. Khripin, and M. Zheng, "Theory of structure-based carbon nanotube separations by Ion-exchange chromatography of DNA/CNT hybrids," *Journal of Physical Chemistry B*, vol. 109, no. 7, pp. 2559–2566, 2005.
- [39] K. Kostarelos, "The long and short of carbon nanotube toxicity," *Nature Biotechnology*, vol. 26, no. 7, pp. 774–776, 2008.

Research Article

Transplantation of Porcine Hepatocytes Cultured with Polylactic Acid-O-Carboxymethylated Chitosan Nanoparticles Promotes Liver Regeneration in Acute Liver Failure Rats

Zhong Chen, Renan Chang, Weijun Guan, Hongyu Cai, Fei Tang, Wencai Zhu, and Jiahui Chen

Department of Hepatobiliary Surgery, Affiliated Hospital, Nantong University, 20 Xisi Road, Nantong 226001, China

Correspondence should be addressed to Zhong Chen, chenz999@hotmail.com

Received 15 November 2010; Revised 18 January 2011; Accepted 31 January 2011

Academic Editor: Giorgia Pastorin

Copyright © 2011 Zhong Chen et al. This is an open access article distributed under the Creative Commons Attribution License, which permits unrestricted use, distribution, and reproduction in any medium, provided the original work is properly cited.

In this study, free porcine hepatocytes suspension (Group A), porcine hepatocytes embedded in collagen gel (Group B), porcine hepatocytes cultured with PLA-O-CMC nanoparticles and embedded in collagen gel (Group C), and PLA-O-CMC nanoparticles alone (Group D) were transplanted into peritoneal cavity of ALF rats, respectively. The result showed that plasma HGF levels were elevated post-transplantation with a peak at 12 hr. The rats in Group C showed highest plasma HGF levels at 2, 6, 12, 24 and 36 hr post-transplantation and lowest HGF level at 48 hr. Plasma VEGF levels were elevated at 48 hr post-transplantation with a peak at 72 hr. The rats in Group C showed highest plasma HGF levels at 48, 72, and 96 hr post-transplantation. The liver functions in Group C were recovered most rapidly. Compared with Group B, Group C had significant high liver Ki-67 antigen labeling index (Ki-67 LI) at day 1 post-HTx ($P < .05$). Ki-67 LI in groups B and C was higher than that in groups A and D at days 5 and 7 post-HTx. In conclusion, intraperitoneal transplantation of porcine hepatocytes cultured with PLA-O-CMC nanoparticles and embedded in collagen gel can promote significantly liver regeneration in ALF rats.

1. Introduction

Acute Liver Failure (ALF) is a life-threatening clinicopathological condition with a high rate of fatality. Impaired liver regeneration is one of the most critical issues in the prognosis. Because of the larger potential regeneration capacity of liver, temporary and effective liver function support will make the patients with ALF have time to wait for liver transplantation and have the possibility of recovery through the regeneration of remaining hepatocytes. Hepatocytes transplantation (HTx) is anticipated to be an effective method to substitute liver functions [1, 2]. But because of the shorter survival time of transplanted hepatocytes, emphasis in study of HTx has been put on getting the better functions of transplanted hepatocytes and the better liver regeneration of ALF recipients. Nanomaterial scaffold is helpful to adherence, proliferation, and differentiated functions of cells [3]. In our previous study, we found that hepatocytes could proliferate rapidly and represent better functions on

nanomaterial scaffold [4]. In this study, porcine hepatocytes cultured with polylactic acid-O-carboxymethylated chitosan (PLA-O-CMC) nanoparticles and embedded in collagen gel were transplanted into the peritoneal cavity of ALF rats to study the liver regeneration reaction.

Hepatocyte growth factor (HGF) is a multipotent growth factor that is a powerful stimulator of DNA synthesis in a variety of cell types, especially hepatocytes [5]. HGF plays a key role in the regulation of liver regeneration after hepatocyte damage. It was reported that HGF activity increases in proportion to the decrease in functional liver mass before the initiation of liver regeneration and rapidly decreases to near normal levels after recovery [6]. Changes in HGF production reflect the status of regeneration process. Vascular endothelial growth factor (VEGF) is a strongest factor in a number of known endogenous factors promoting vessel regeneration. VEGF derived from hepatocytes is associated with processes of liver regeneration. HTx has been used by many investigators to demonstrate metabolic

support and improve survival in rats with ALF. However, few of these reports have examined the impact of cell therapy on the regenerative response in the native liver. To our knowledge, there was no detailed study about liver regeneration response in HTx with nanomaterials. In the present study, levels of HGF and VEGF, albumen (ALB), alanine aminotransferase (ALT), total bilirubin (TB), and NH_3 in the plasma and liver Kiel 67 antigen labeling index (Ki-67 LI) of ALF rats after HTx were observed. The aim of the present study was to investigate the effect of transplantation of porcine hepatocytes cultured with PLA-O-CMC nanoparticles and embedded in collagen gel on liver regeneration in ALF rats.

2. Materials and Methods

2.1. Animals. Chinese experimental miniature pigs ($n = 5$, male and female, body weight 2 to 4 Kg), Sprague-Dawley rats ($n = 220$, male and female, weight 250 to 280 g) were supplied by Experimental Animal Center of Nantong University. All operations were performed between 9 AM and noon. The pigs and rats were allowed free access to water and were fasted for 12 hr before experiment. The research protocol was in compliance with Chinese guidelines for the humane care of experimental animals. The study was approved by the hospital ethics committee.

2.2. Reagents. D-galactosamine (D-Gal) was purchased from the Department of Chemistry, Chongqing Medical University, China. Collagenase IV, RPMI1640, new-born bovine serum (NBS), and HGF were purchased from Gibco BRL, Life Technologies, USA. Polylactic acid was from Sigma Chemical Co., USA (St. Louis, MO). O-carboxymethylated chitosan was from Weikang Biotechnology Company Limited, Shanghai, China.

2.3. Preparation of PLA-O-CMC Nanoparticles. PLA-O-CMC nanoparticles were prepared with polylactic acid and O-carboxymethylated chitosan by ultrasonic method as described previously [7].

2.4. ALF Rat Model and Groups. 10% D-Gal was injected into the peritoneal cavity of Sprague-Dawley rats at 1.2 g/Kg. The rats ($n = 165$) were divided randomly into four groups: simple hepatocyte transplantation group (Group A), collagen and hepatocyte transplantation group (Group B), and nanoparticles, collagen, and hepatocyte transplantation group (Group C), and nanoparticles transplantation group (Group D).

2.5. Porcine Hepatocyte Culture. Porcine hepatocytes were isolated by an *in situ* recirculating collagenase perfusion method as described previously [8–11]. The yield of hepatocytes was $(4.5\sim 5.0) \times 10^7/\text{g}$. The mean viability of hepatocytes was 97% by trypan blue exclusion. The isolated hepatocytes were suspended in RPMI1640 medium supplemented with 10% NBS, 200 $\mu\text{g}/\text{L}$ hydrocortisone, 100 $\mu\text{g}/\text{L}$ insulin, 200 $\mu\text{g}/\text{L}$ HGF, 100000 U/L penicillin, and 100 $\mu\text{g}/\text{L}$

streptomycin. The isolated hepatocytes were divided into three groups and incubated at $5 \times 10^6/\text{mL}$ in 5% CO_2 atmosphere with 100% humidity at 37°C. Group A: isolated hepatocytes were cultured for 24 hr. In the first 12 hr, the hepatocyte suspensions were agitated for 5 min every 30 min. Then they were centrifuged at 800 rpm and hepatocytes were resuspended in the above medium for 12 hr. 5 mL hepatocyte suspensions with 1×10^7 cells/mL were transplanted into the peritoneal cavity of ALF rats. Group B: isolated hepatocytes were cultured for 12 hr and agitated for 5 min every 30 min. Then they were centrifuged at 800 rpm and hepatocytes were resuspended in the above medium. The hepatocyte suspensions with 4×10^7 cells/mL, collagen type I (0.4% collagen type in 0.1 N acetic acid), $10 \times \text{RPMI1640}$, 100% NBS, and 1 N NaOH were mixed. The volume ratio of the above five components was 2.5 : 5 : 1 : 1 : 0.5. The final collagen concentration was 2 mg/mL, the density of hepatocytes was $1 \times 10^7/\text{mL}$, and pH of solution was 7.4. The mixture was dropped into 6-well cell culture plates at 5 mL for every well and cultured in 5% CO_2 incubator at 37°C. Porous gel was formed after 2 to 3 hr. Then 5 mL RPMI1640 medium was added to make the gel suspended in the medium. The hepatocyte suspensions were further cultured in 5% CO_2 incubator at 37°C. The total culture time after collagen addition was 12 hr. At last, the gel containing hepatocytes was transplanted into the peritoneal cavity of ALF rats. Group C: isolated hepatocytes were cultured with 100 mg/L PLA-O-CMC nanoparticles for 12 hr and agitated for 5 min every 30 min. Then the medium was centrifuged at 800 rpm and hepatocytes were resuspended in the above medium. The hepatocyte suspensions, collagen type I, $10 \times \text{RPMI1640}$, 100% NBS, and 1N NaOH were mixed in the same method as Group B. The final collagen concentration was 2 mg/mL, the density of hepatocytes was $1 \times 10^7/\text{mL}$, concentration of the nanoparticles was 100 mg/L, and pH of solution was 7.4. The mixture was dropped into 6-ell cell culture plates at 5 mL for every well and cultured in 5% CO_2 incubator at 37°C. Porous gel was formed after 2-3 hr. Then RPMI1640 medium was added to make the gel suspended in the medium. The hepatocyte suspensions were further cultured in 5% CO_2 incubator at 37°C. The total culture time after collagen addition was 12 hr. At last, the gel containing hepatocytes was transplanted into the peritoneal cavity of ALF rats.

2.6. HTx. HTx was done in Sprague-Dawley rats at 48 hr after D-gal injection. Under ether anesthesia, the abdomen cavity was opened through median incision of abdomen. In Group A, hepatocyte suspensions were injected into the lesser omentum sac of ALF rats. In Groups B and C, gel containing hepatocytes and gel containing hepatocytes cultured with nanoparticle were transplanted into the peritoneal cavity of ALF rats and wrapped up with greater omentum, respectively. The total number of transplanted hepatocytes was 5×10^7 . In Group D, 100 mg/L PLA-O-CMC nanoparticles were injected into the lesser omentum sac of ALF rats. Abdomen wall was sutured in layer. After transplantation, the rats in three groups were raised in different cages and drank water with 10% glucose. No immunosuppressive reagents were administered throughout the experiment.

2.7. Determination of Plasma HGF and VEGF Levels. Plasma HGF level was determined in batches of five rats each before HTx and at 2, 6, 12, 24, 36, and 48 hr after HTx. Plasma VEGF level was determined in batches of five rats each before HTx and at 48, 72, 84, and 96 hr after HTx. Blood sample was collected from abdominal aorta of rats and put into the test tube with ethylene diamine tetraacetic acid (EDTA). The samples were centrifuged at 3000 rpm for 10 min and stored at -80°C until growth factor assays were performed. The levels of plasma HGF and VEGF were analyzed by an enzyme-linked immunosorbent assay (kits were supplied by Fanbang Co, Dalian, China), according to the manufacturer's protocols. All samples were tested in duplicate. The optical density was read within 30 min using enzyme mark meter set to wavelength of 450 nm and 630 nm. The levels of HGF and VEGF were calculated from a standard curve.

2.8. Determination of Liver Functions. Changes of albumen (ALB), alanine aminotransferase (ALT), total bilirubin (TB), and NH_3 levels in the plasma were determined with an automatic biochemical analyzer (7600-020, Hitachi, Japan).

2.9. Determination of Kiel 67 Antigen Labeling Index (Ki-67 LI). Ki-67 LI was evaluated. Immunocytochemistry technique was used. The paraffin sections of recipients' livers were stained with hematoxylin. Under light microscope, 5 visual fields were randomly selected, and the number of cells with buffy nucleus among 1000 cells per visual field was counted, and then the percentage of cells with buffy nucleus was calculated [12].

2.10. Statistical Analyses. All results were expressed as mean \pm standard deviation. Statistical analyses were performed using Stata 7.0 software. Statistical significance was determined by analysis of variance (ANOVA) with Student's *t*-test. A *P* value of less than .05 was considered statistically significant.

3. Results

3.1. Plasma HGF Levels. Plasma HGF levels were undetectable in normal rats. They were increased at 48 hr after D-Gal injection. They continued to elevate after HTx with a distinct peak at 12 hr. They gradually declined thereafter (Figure 1). The rats in Group C showed highest plasma HGF levels at 2, 6, 12, 24, and 36 hr after HTx and lowest HGF level at 48 hr compared with other groups ($P < .05$). Plasma HGF levels at 2, 6, 12, 24, and 36 hr after HTx in Group B were higher than other groups ($P < .05$).

3.2. Plasma VEGF Levels. Plasma VEGF levels were undetectable at 48 hr after D-Gal injection. They were increased at 48 hr after HTx with a distinct peak at 72 hr. They gradually declined thereafter (Figure 2). The rats in Group C showed highest plasma VEGF levels at 48, 72, 84, and 96 hr after HTx compared with other groups ($P < .05$). Plasma VEGF levels at 48, 72, 84, and 96 hr after HTx in Group B were higher than other groups ($P < .05$).

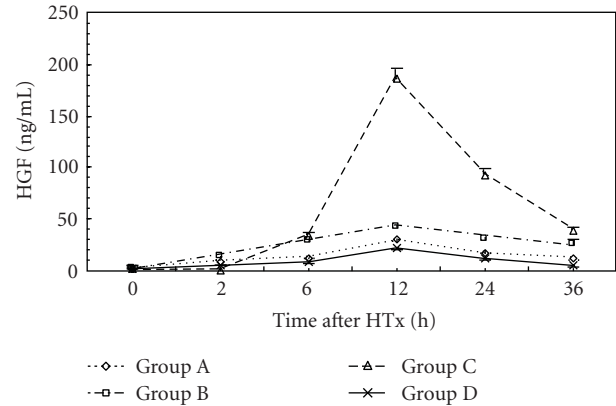


FIGURE 1: Time course of changes in plasma HGF levels in three groups. Error bars indicate standard deviations ($n = 5$). Statistical differences were determined by ANOVA using Stata 7.0 software.

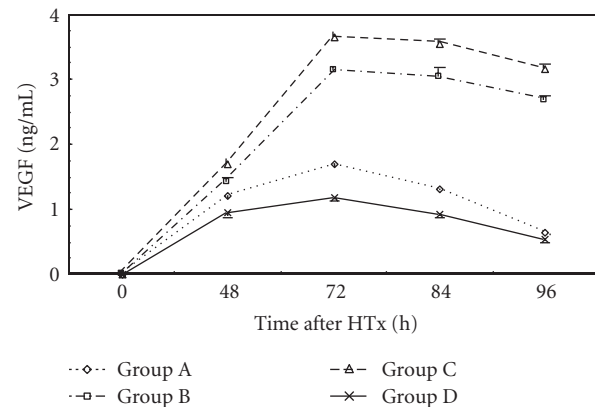


FIGURE 2: Time course of changes in plasma VEGF levels in three groups. Error bars indicate standard deviations ($n = 5$). Statistical differences were determined by ANOVA using Stata 7.0 software.

3.3. Liver Functions. At 24 hr after HTx, ALB level in Group C was higher than that in Groups A and D ($P < .05$). NH_3 level in groups B and C was lower than that in Groups A and D ($P < .05$). At 72 hr after HTx, ALT and NH_3 levels in Group C were lower than those in Groups A and D ($P < .05$). ALB level in Group C was higher than that in Groups A and D ($P < .05$). ALT level in Group C was lower than that in other groups. There was no significance in ALB, ALT, TB, and NH_3 levels between Groups A and B. At days 5 and 7 after HTx, there were no significance in ALB, ALT, TB, and NH_3 levels in all groups (Figures 3, 4, 5, and 6).

3.4. Ki-67 LI in Hepatic Tissue. Figure 7 showed pathology of livers of ALF rat at 5d after HTx under light microscopy. Compared with Group B, Group C had significant high Ki-67 LI at day 1 after HTx ($P < .05$). Ki-67 LI in Groups B and C was higher than that in Groups A and D at days 5 and 7 after HTx ($P < .05$) (Figure 8).

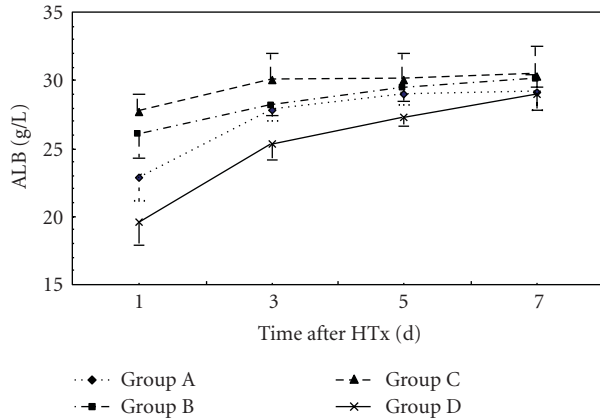


FIGURE 3: Time course of changes in plasma ALB levels in three groups. Error bars indicate standard deviations ($n = 5$). Statistical differences were determined by ANOVA using Stata 7.0 software.

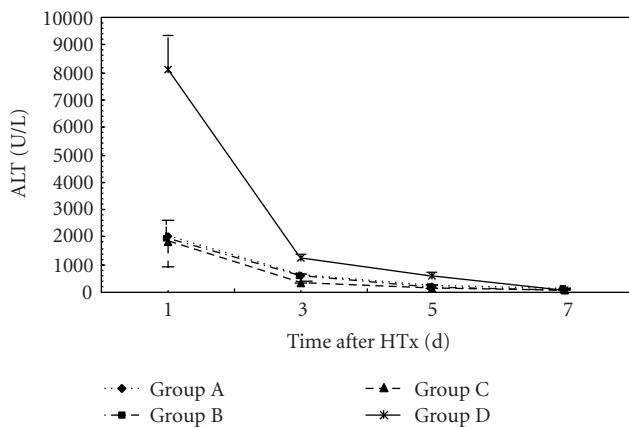


FIGURE 4: Time course of changes in plasma ALT levels in three groups. Error bars indicate standard deviations ($n = 5$). Statistical differences were determined by ANOVA using Stata 7.0 software.

4. Discussion

ALF is associated with a high mortality. Patient survival depends in part on the regenerative capacity of the remaining hepatocytes. Orthotopic liver transplantation has emerged as an effective treatment for ALF [13]. However, wide application of this therapeutic modality is limited primarily by lack of donors, inability to procure organs on short notice, and high cost. Making a decision about transplantation depends on whether sufficient liver regeneration can occur before the onset of irreversible complications of liver failure.

HTx can provide opportunity of liver regeneration for ALF patients by liver function support. Liver regeneration is a complex course in which many factors participate in regulation [14]. The process of liver regeneration mainly included three key stages. Start stage: hepatocytes in phase G0 entered phase G1 under the regulation of TNF- α , IL-6, and growth factors. Progress stage: hepatocytes in phase G1 entered phase S under the regulation of cyclin-dependent kinase system, HGF, and TGF- α . Termination stage: growth

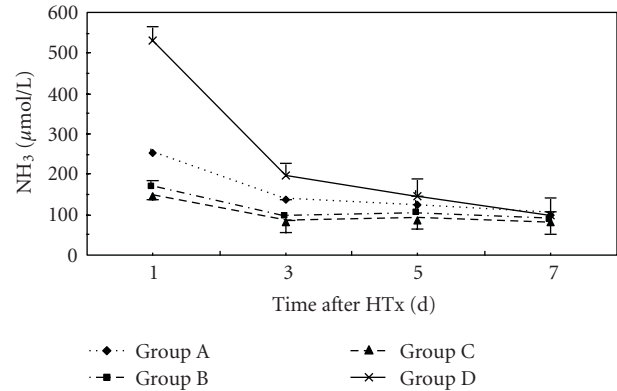


FIGURE 5: Time course of changes in plasma NH₃ levels in three groups. Error bars indicate standard deviations ($n = 5$). Statistical differences were determined by ANOVA using Stata 7.0 software.

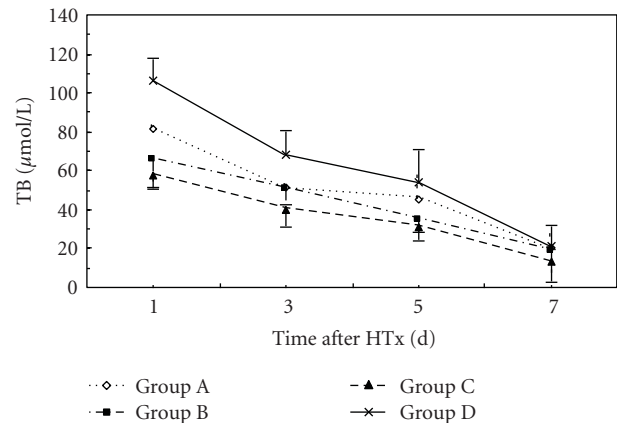


FIGURE 6: Time course of changes in plasma TB levels in three groups. Error bars indicate standard deviations ($n = 5$). Statistical differences were determined by ANOVA using Stata 7.0 software.

of hepatocytes stopped under the regulation of TGF- β and nandrolone phenylpropionate [15, 16].

It was showed that the hepatic parenchymal cells in phase G0 could be activated after 30 min of hepatic injury and entered the cell proliferation cycle. Their DNA synthesis arrived at peak at 24 hr. Their proliferation was completed on the whole at 72 hr. Then the structural and functional reconstruction of liver began. After 7 to 10 days, the liver recovered both in the volume and weight [17].

HGF has been isolated and purified from the plasma of patients with fulminant hepatic failure and from rat platelets. It is a heterodimeric molecule composed of a 69-kD alpha chain and a 34-kD beta chain. HGF is produced by hepatic mesenchymal cells such as lipocyte (Ito cells), Kupffer cells, and sinusoidal endothelial cells (SEC). HGF is considered to be important in the stimulation of DNA synthesis of hepatocytes. HGF produced in nonparenchymal liver cells acts on injured parenchymal hepatocytes through a paracrine mechanism via the c-met tyrosine kinase receptor in the surface of cellular membrane. It promoted liver regeneration by enhancing mitosis of hepatocytes, inhibiting apoptosis of

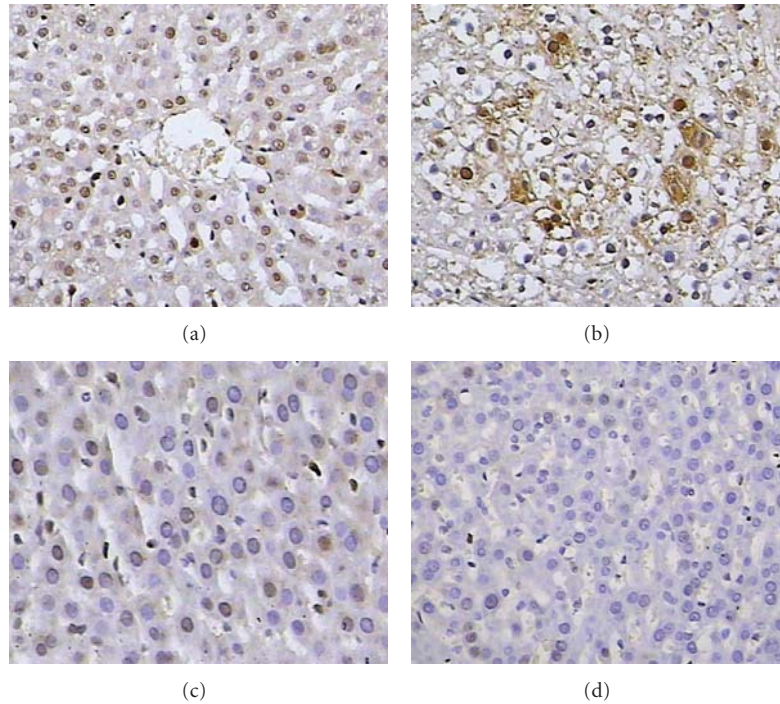


FIGURE 7: Liver Ki-67 LI of ALF rats at 5d after HTx ($\times 400$).

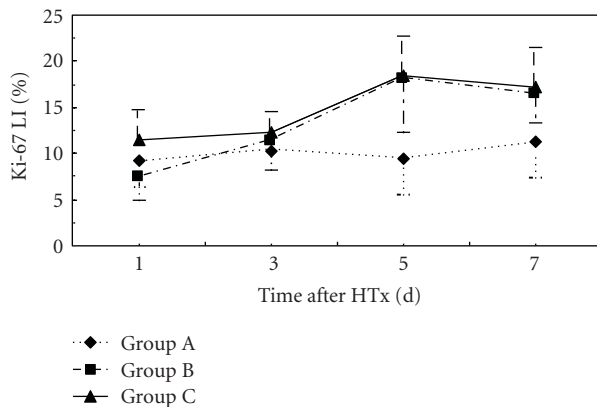


FIGURE 8: Time course of changes in liver Ki-67 LI in three groups. Error bars indicate standard deviations ($n = 5$). Statistical differences were determined by ANOVA using Stata 7.0 software.

hepatocytes, promoting the recovery and reconstruction of morphology of liver tissue, and promoting growth of blood vessel endothelium and formation of capillary. Elevated serum HGF levels have been reported after partial liver resection and in the settings of ALF [18, 19]. Arkadopoulos et al. [20] induced ALF rat model by total liver resection after transplanting hepatocytes into spleen. They found that plasma HGF increased at 12 hr after operation. In this study, we found that plasma HGF levels were increased at 48 hr after D-Gal injection, which was consistent with other reports.

Recent studies have shown that VEGF, a most potent angiogenic factor, plays an essential role in liver regeneration.

Exogenous VEGF administration is able to stimulate liver regeneration following acute severe liver injury and partial hepatectomy in rats [21]. It has also shown that the serum VEGF levels in the survivors of ALF significantly increased in the recovery phases compared with corresponding levels on admission, suggesting that VEGF plays an important role in liver regeneration after ALF. Namisaki et al. [22] has shown that HGF is a potent inducer of VEGF secretion by HepG2 cells. Liver SEC proliferation is induced by VEGF during liver regeneration. Shimizu et al. [23] found that proliferation of liver SECs followed hepatocyte proliferation by 24 to 48 hr. This is probably related to formation of new vasculature to supply blood to the regenerated tissue. The authors suggested that induction of VEGF secretion by hepatocytes may constitute a pathway, whereby HGF originating from either nonparenchymal liver cells or distant organs not only stimulates hepatocyte proliferation but also mediates liver SEC proliferation and survival as an indirect angiogenic effect. In addition, VEGF produced by hepatocytes may stimulate liver SEC to produce growth factors, including HGF, with liver protective/proliferative effects. Thus, VEGF and HGF appear to have complementary roles in liver injury and regeneration.

It has been shown that the VEGF expression increased markedly during liver regeneration induced either by partial hepatectomy or drug intoxication [23]. Akiyoshi et al. [24] found that VEGF level correlated with Child-Pugh class of liver function. The lower the Child-Pugh class was, the lower the level of VEGF was. In our study, plasma VEGF levels in every group were increased at 48 hr after HTx with a peak at 72 hr. Liver regeneration involves in the reconstitution of hepatic sinusoids. VEGF promoted proliferation of SEC

and hepatocytes and reconstitution of hepatic sinusoids [22]. VEGF produced effect through combination with high affinity receptor, KDR/Flk-1, that is expressed almost exclusively on the surface of SECs [25]. It was found that VEGF expressed predominantly in periportal hepatocytes at 48 to 72 hr after partial hepatectomy. Gupta et al. [26] transplanted the hepatocytes into the spleen of inbreeding line, F344 rats and found that expression of VEGF could be detected when the transplanted hepatocytes entered the hepatic sinusoids and integrated into hepatic plates through endothelial fenestrations after 8 hr of transplantation.

Ki-67 antigen, a sensitive indicator of liver regeneration, is involved in DNA synthesis and is closely related to cell proliferation [27, 28]. In our study, all groups showed liver regeneration signs at different degrees and in different times after HTx, which indicated the effect of HTx. The increase of Ki-67 LI appeared earliest in Group A. Compared with Group B, Group C had significant higher Ki-67 LI at day 1 after HTx. Ki-67 LI in Groups B and C was higher than that in Group A at days 5 and 7 after HTx ($P < .05$). We speculated that the increase of Ki-67 LI may be related to the increase of plasma HGF and VEGF levels. Boudjema et al. [29] considered that the main mechanism of raising survival rate of ALF patients included supplying temporary liver function support, promoting remnant liver regeneration and recovery of liver function through production of HGF. In this study, HGF levels were elevated before HTx and continued to increase after HTx with a peak at 12 hr. Whether this is caused by impaired HGF clearance, increased synthesis at extrahepatic sites, or both remains to be seen. VEGF level increased at 48 hr after HTx with a peak at 72 hr. The results indicated that elevated blood HGF level switched on liver regeneration. The continuous elevation of blood HGF level promoted liver regeneration further. VEGF played an important role in reconstitution of hepatic sinusoids. Plasma HGF levels were decreased after 12 hr following HTx, which may be related with the increased clearance of HGF.

In this study, plasma HGF levels during 36 hrs after HTx and VEGF levels after HTx in Group C were found to be highest in all groups. Ki-67 LI was highest in Group C at days 5 to 7 after HTx, which indicated the most active liver regeneration. The improvement of liver functions in Group C was most rapid than other groups. It was postulated that better liver regeneration was mainly due to the higher cytoactive porcine hepatocytes cultured with PLA-O-CMC nanoparticles and embedded in collagen gel. These hepatocytes had better effect on liver function substitution and could make livers produce more HGF and VEGF which could promote the regeneration and restoration of injured liver [5].

In summary, we have demonstrated that rats with ALF triggered a regenerative response in the native liver because of elevated plasma HGF levels after D-Gal injection and continuous increase of HGF after HTx. Elevated plasma VEGF after HTx was helpful in reconstitution of hepatic sinusoids. Transplantation of porcine hepatocytes cultured with PLA-O-CMC nanoparticles and embedded in collagen gel promotes liver regeneration in ALF rats.

Acknowledgments

This study was supported by a grant from National Natural Science of China (30772130), a grant from Natural Science of Jiangsu Province (BK200544), and a grant from the Health Department of Jiangsu Province (H200215), China.

References

- [1] A. Dhawan and S. C. Strom, "Human hepatocyte transplantation," *Methods in Molecular Biology*, vol. 640, pp. 525–534, 2010.
- [2] A. G. Bonavita, K. Quaresma, V. Cotta-De-Almeida, M. A. Pinto, R. M. Saraiva, and L. A. Alves, "Hepatocyte xenotransplantation for treating liver disease: review Article," *Xenotransplantation*, vol. 17, no. 3, pp. 181–187, 2010.
- [3] N. Moniaux and J. Faivre, "Will nano-fibers permit to turn liver cell transplantation into a curative tool against liver failure?" *Journal of Hepatology*, vol. 52, no. 2, pp. 150–152, 2010.
- [4] H. Y. Gu, Z. Chen, R. X. Sa et al., "The immobilization of hepatocytes on 24 nm-sized gold colloid for enhanced hepatocytes proliferation," *Biomaterials*, vol. 25, no. 17, pp. 3445–3451, 2004.
- [5] S. Z. Jin, X. W. Meng, X. Sun et al., "Hepatocyte growth factor promotes liver regeneration induced by transfusion of bone marrow mononuclear cells in a murine acute liver failure model," *Journal of Hepato-Biliary-Pancreatic Sciences*. In press.
- [6] H. Tsubouchi, S. Hirono, E. Gohda et al., "Clinical significance of human hepatocyte growth factor in blood from patients with fulminant hepatic failure," *Hepatology*, vol. 9, no. 6, pp. 875–881, 1989.
- [7] Z. Chen, X. Z. Dai, X. R. Yang, and W. C. Zhu, "Preparation of polylactic acid-O-carboxymethylated chitosan nanoparticles and their influences on the cultured porcine hepatocytes," *World Chinese Journal of Digestology*, vol. 14, no. 17, pp. 1669–1674, 2006.
- [8] Z. Chen, Y. Ding, and H. Zhang, "Cryopreservation of suckling pig hepatocytes," *Annals of Clinical and Laboratory Science*, vol. 31, no. 4, pp. 391–398, 2001.
- [9] Z. Chen, Y. Ding, Q. Xu, and D. Yu, "Bioartificial liver inoculated with porcine hepatocyte spheroids for treatment of canine acute liver failure model," *Artificial Organs*, vol. 27, no. 7, pp. 613–622, 2003.
- [10] Z. Chen, Y. Ding, and G. Li, "Configuration of a new bioartificial liver support system and in vitro evaluation of its functions," *Annals of Clinical and Laboratory Science*, vol. 35, no. 1, pp. 7–14, 2005.
- [11] Z. Chen and Y. T. Ding, "Functional evaluation of a new bioartificial liver system in vivo and in vivo," *World Journal of Gastroenterology*, vol. 12, no. 8, pp. 1312–1316, 2006.
- [12] A. Morinaga, T. Ogata, M. Kage, H. Kinoshita, and S. Aoyagi, "Comparison of liver regeneration after a splenectomy and splenic artery ligation in a dimethylnitrosamine-induced cirrhotic rat model," *HPB*, vol. 12, no. 1, pp. 22–30, 2010.
- [13] R. M. Merion, "Current status and future of liver transplantation," *Seminars in Liver Disease*, vol. 30, no. 4, pp. 411–421, 2010.
- [14] N. Selzner, M. Selzner, Y. Tian, Z. Kadry, and P. A. Clavien, "Cold ischemia decreases liver regeneration after partial liver transplantation in the rat: a TNF- α /IL-6-dependent mechanism," *Hepatology*, vol. 36, no. 4 I, pp. 812–818, 2002.

- [15] A. Zimmermann, "Liver regeneration: the emergence of new pathways," *Medical Science Monitor*, vol. 8, no. 3, pp. RA53–RA63, 2002.
- [16] R. Pawlowski and J. Jura, "ALR and liver regeneration," *Molecular and Cellular Biochemistry*, vol. 288, no. 1-2, pp. 159–169, 2006.
- [17] J. Kountouras, P. Boura, and N. J. Lygidakis, "Liver regeneration after hepatectomy," *Hepato-Gastroenterology*, vol. 48, no. 38, pp. 556–562, 2001.
- [18] P. M. Lindroos, R. Zarnegar, and G. K. Michalopoulos, "Hepatocyte growth factor (hepatopoietin A) rapidly increases in plasma before DNA synthesis and liver regeneration stimulated by partial hepatectomy and carbon tetrachloride administration," *Hepatology*, vol. 13, no. 4, pp. 743–749, 1991.
- [19] S. Eguchi, A. Kamlot, J. Ljubimova et al., "Fulminant hepatic failure in rats: survival and effect on blood chemistry and liver regeneration," *Hepatology*, vol. 24, no. 6, pp. 1452–1459, 1996.
- [20] N. Arkadopoulos, H. Lilja, K. S. Suh, A. A. Demetriou, and J. Rozga, "Intrasplenic transplantation of allogeneic hepatocytes prolongs survival in anhepatic rats," *Hepatology*, vol. 28, no. 5, pp. 1365–1370, 1998.
- [21] E. Granot, P. Boros, and C. M. Miller, "Differential effect of hepatocyte growth factor and tumor growth factor- β on early release of vascular endothelial growth factor from HepG cells: possible implications in post-transplant liver regeneration," *Transplantation Proceedings*, vol. 33, no. 6, pp. 2926–2928, 2001.
- [22] T. Namisaki, H. Yoshiji, H. Kojima et al., "Salvage effect of the vascular endothelial growth factor on chemically induced acute severe liver injury in rats," *Journal of Hepatology*, vol. 44, no. 3, pp. 568–575, 2006.
- [23] H. Shimizu, M. Miyazaki, Y. Wakabayashi et al., "Vascular endothelial growth factor secreted by replicating hepatocytes induced sinusoidal endothelial cell proliferation during regeneration after partial hepatectomy in rats," *Journal of Hepatology*, vol. 34, no. 5, pp. 683–689, 2001.
- [24] F. Akiyoshi, M. Sata, H. Suzuki et al., "Serum vascular endothelial growth factor levels in various liver diseases," *Digestive Diseases and Sciences*, vol. 43, no. 1, pp. 41–45, 1998.
- [25] H. Shimizu, N. Mitsuhashi, M. Ohtsuka et al., "Vascular endothelial growth factor and angiopoietins regulate sinusoidal regeneration and remodeling after partial hepatectomy in rats," *World Journal of Gastroenterology*, vol. 11, no. 46, pp. 7254–7260, 2005.
- [26] S. Gupta, P. Rajvanshi, R. Sokhi et al., "Entry and integration of transplanted hepatocytes in rat liver plates occur by disruption of hepatic sinusoidal endothelium," *Hepatology*, vol. 29, no. 2, pp. 509–519, 1999.
- [27] S. C. Schmidt, G. Schumacher, N. Klage, S. Chopra, P. Neuhaus, and U. Neumann, "The impact of carbon dioxide pneumoperitoneum on liver regeneration after liver resection in a rat model," *Surgical Endoscopy and Other Interventional Techniques*, vol. 24, no. 1, pp. 1–8, 2010.
- [28] K. Furrer, Y. Tian, T. Pfammatter et al., "Selective portal vein embolization and ligation trigger different regenerative responses in the rat liver," *Hepatology*, vol. 47, no. 5, pp. 1615–1623, 2008.
- [29] K. Boudjema, P. Bachellier, P. Wolf, J. D. Tempé, and D. Jaeck, "Auxiliary liver transplantation and bioartificial bridging procedures in treatment of acute liver failure," *World Journal of Surgery*, vol. 26, no. 2, pp. 264–274, 2002.

Research Article

Preparation of a Nanoscaled Poly(vinyl alcohol)/Hydroxyapatite/DNA Complex Using High Hydrostatic Pressure Technology for *In Vitro* and *In Vivo* Gene Delivery

Tsuyoshi Kimura,^{1,2} Yoichi Nibe,¹ Seiichi Funamoto,¹ Masahiro Okada,³
Tsutomu Furuzono,³ Tsutomu Ono,⁴ Hidekazu Yoshizawa,⁴ Toshiya Fujisato,⁵
Kwangwoo Nam,^{1,2} and Akio Kishida^{1,2}

¹Institute of Biomaterials and Bioengineering, Tokyo Medical and Dental University, 2-3-10 Kanda-Surugadai, Chiyoda-ku, Tokyo 101-0062, Japan

²Japan Science and Technology Agency, CREST 5, Sanbancho, Chiyoda-ku, Tokyo 102-0075, Japan

³Department of Biomedical Engineering, National Cardiovascular Center Research Institute, 5-7-1 Fujishirodai, Suita, Osaka 656-8565, Japan

⁴Department of Environmental Chemistry and Materials, Okayama University, 3-1-1 Tsushimanaka, Okayama 700-8530, Japan

⁵Department of Biomedical Engineering, Osaka Institute of Technology, 5-16-1 Omiya, Asahi-ku, Osaka 573-0196, Japan

Correspondence should be addressed to Akio Kishida, kishida.fm@tmd.ac.jp

Received 1 December 2010; Revised 21 February 2011; Accepted 14 March 2011

Academic Editor: Sanyog Jain

Copyright © 2011 Tsuyoshi Kimura et al. This is an open access article distributed under the Creative Commons Attribution License, which permits unrestricted use, distribution, and reproduction in any medium, provided the original work is properly cited.

Our previous research showed that poly(vinyl alcohol) (PVA) nanoparticles incorporating DNA with hydrogen bonds obtained by high hydrostatic pressurization are able to deliver DNA without any significant cytotoxicity. To enhance transfection efficiency of PVA/DNA nanoparticles, we describe a novel method to prepare PVA/DNA nanoparticles encapsulating nanoscaled hydroxyapatites (HAPs) prepared by high hydrostatic pressurization (980 MPa), which is designed to facilitate endosomal escape induced by dissolving HAPs in an endosome. Scanning electron microscopic observation and dynamic light scattering measurement revealed that HAPs were significantly encapsulated in PVA/HAP/DNA nanoparticles. The cytotoxicity, cellular uptake, and transgene expression of PVA/HAP/DNA nanoparticles were investigated using COS-7 cells. It was found that, in contrast to PVA/DNA nanoparticles, their internalization and transgene expression increased without cytotoxicity occurring. Furthermore, a similar level of transgene expression between plasmid DNA and PVA/HAP/DNA nanoparticles was achieved using *in vivo* hydrodynamic injection. Our results show a novel method of preparing PVA/DNA nanoparticles encapsulating HAP nanocrystals by using high hydrostatic pressure technology and the potential use of HAPs as an enhancer of the transfection efficiency of PVA/DNA nanoparticles without significant cytotoxicity.

1. Introduction

Polymeric gene delivery systems are of great interest in gene therapy because of their greater degree of safety compared to that of viral vectors. Many types of cationic polymers, such as poly-L-lysine and its derivatives [1, 2], polyethyleneimine [3], polyamidoamine dendrimer [4], and vinyl polymers [5], have been developed as gene carriers to aim at effective and safe *in vitro* and *in vivo* gene transfection into cells. They can

spontaneously condense DNA by electrostatic interaction between positive charged groups of polycation and phosphate groups of DNA and form complexes, which are called polyplexes. The polyplex formation protects DNA from degradation by DNases in extracellular and intracellular pathways, resulting in the enhancement of gene transfection efficacy. However, the cytotoxicity of cationic polymers is an essential problem in the polyplex-based gene transfer field [6]. In addition, polymeric gene carriers may elicit

nonspecific immune responses [7]. Therefore, significant efforts have been made towards decreasing the toxicity of polymeric gene carriers.

Two main strategies have been proposed to address this issue. One is to attach polyethylene glycol (PEG), which is widely used as a nonionic, highly soluble, low toxicity polymer, to polymeric gene carriers, a process that is called "PEGylation." PEGylation increases the water solubility of polyplexes and reduces the interaction of polyplex and serum and blood components, resulting in effective transfection without toxicity [8, 9]. The other is the use of non- or less cationic polymers, which can form complexes via nonelectrostatic interactions, such as hydrogen bonding. Double strand schizophyllan, which is one type of polysaccharide (β -1, 3 glucan), forms a triple helical complex with single-strand DNA through hydrogen bonding interaction [10]. Protective interactive noncondensing (PINC) polymers, poly (N-vinyl pyrrolidone) (PVP), and poly (vinyl alcohol) (PVA), form flexible polyplexes with DNA via hydrogen bonds [11, 12]. In addition, we have developed a novel formulation method of DNA complexes with nonionic, water-soluble polymers through hydrogen bonding interaction using high hydrostatic pressure technology. Under high hydrostatic pressure conditions, inter- and intramolecular hydrogen bonding interaction is effectively formed [13–15]. We previously reported that nanoscaled PVA/DNA complexes via hydrogen bonding interaction were obtained by high hydrostatic pressurization at 980 MPa and 40°C for 10 min [16]. The PVA/DNA nanoparticles were taken up by RAW264 cells with nontoxicity, and no significant gene expressions were observed.

Traditionally, the calcium phosphate (CaP)-DNA coprecipitation method has been used for *in vitro* gene transfection because of CaP's biocompatibility, biodegradability, and ease of handling [17, 18]. Many CaP-DNA coprecipitation methods that particulate formation, being affected by pH [19], temperature [20], and buffer conditions [21], have been developed to aim at effective gene transfection. In addition, several researchers have proposed the idea of applying CaP-DNA coprecipitates produced in polyplexes to gene delivery. It is considered that polyplexes including CaP were internalized into cells through endocytosis pathways, in which the pH was lower than 5.5, and then the rupture of endosome and endosomal releases of polyplex were induced by osmotic shock [22, 23]. Currently, nanoscaled HAp, which are one of the forms of CaP, have been synthesized with well-controlled size and shape and utilized as gene carriers because of the capability of HAp to absorb DNA molecules [24].

On the basis of this background, in the current study, we used nanoscaled HAp (about 50 nm) as an endosomal escape reagent because of their ability to dissolve in endosome vesicles under low pH conditions. We investigated a method of preparing the PVA/DNA complexes encapsulating HAp by using high hydrostatic pressure technology in detail. Using the obtained PVA/HAp/DNA nanoparticles, the cellular uptake, cytotoxicity, and *in vitro* and *in vivo* transfection efficiency were examined to aim at effective and safe gene transfection.

2. Materials and Methods

2.1. Materials. PVA with a degree of polymerization of 1700 and a degree of saponification of 99.3% was kindly supplied from Kuraray Co. Ltd. (Osaka, Japan). HAp with an average diameter of 50 nm was synthesized by an emulsion system [25, 26] and then suspended in water. Plasmid DNA encoding a luciferase gene under an SV40 promoter (pGL3: 5.2 kbp) was purchased from Promega Co., Ltd., (Madison, USA).

2.2. Preparation of PVA/HA/pDNA Complexes. An aqueous PVA solution of 5 w/v% was prepared by autoclaving it three times for 30 min at 121°C and diluting it to various concentrations. An aqueous HAp suspension prepared by ultrasonication was added to the PVA solution. The DNA solution was mixed with the PVA/HAp suspension (final concentrations: PVA 0.001–1.0 w/v%, HA 0.0001–0.1 w/v%, DNA 0.0025 w/v%). The mixture solution of PVA, HAp, and DNA was hydrostatically pressurized at 980 MPa and 40°C for 10 min using a high hydrostatic pressure machine (Dr. Chef: Kobe steel, Kobe, Japan).

2.3. Characterization of PVA/HAp/DNA Complexes. The shapes of PVA/DNA (PVA: 1.0 w/v%) and PVA/HAp/DNA (PVA: 1.0 w/v%, HAp: 0.1 w/v%) complexes obtained by the high hydrostatic pressurization were observed with a scanning electron microscope (SEM, JSM-6301F, JEOL Co., Tokyo, Japan). One μ L of the complex solutions was dropped on a glass slide and dried in air. The sizes of the PVA/DNA and PVA/HAp/DNA complexes obtained by the high hydrostatic pressurization were measured by dynamic light scattering (DLS) using a Zetasizer Nano product (Malvern, Worcestershire, UK). The stability of DNA in PVA/DNA complex on 10% serum condition was investigated. The PVA/DNA complexes were incubated with medium containing 10% serum for 20 h. Then, they were subjected to *in vitro* transcription and translation system (TNT Quick coupled Transcription/Translation System, Promega Co., Ltd., Madison, USA), and the luciferase activity was measured by using an AB-2200 luminometer (ATTO, Corp., Tokyo, Japan) for 10 s.

2.4. Cytotoxicity of PVA/HAp/DNA Complexes. A mixture solution of PVA (2 w/v%) and HAp (0.2 w/v%) was prepared and diluted stepwise to 0.01 w/v% of PVA and 0.001 w/v% of HAp. An aqueous DNA solution of 0.005 w/v% was mixed with PVA/HAp mixtures for each concentration at an equal volume. Their mixtures were treated under 980 MPa at 40°C for 10 min using a high hydrostatic pressure machine. The COS-7 cells used were purchased from RIKEN Bioresource Center (BRC, Saitama, Japan). They were cultured in a complete modified eagle medium (DMEM, Life technologies Japan Ltd, Tokyo, Japan), supplemented with non-inactivated 10% fetal bovine serum (FBS), 50 IU/mL of penicillin, and 50 μ g/mL of streptomycin (ICN Biomaterials, Ohio, USA). The COS-7 cells (2.0×10^4) on a 96-well plate were incubated with PVA/DNA and PVA/HAp/DNA complexes of various concentrations at 37°C for 20 h in

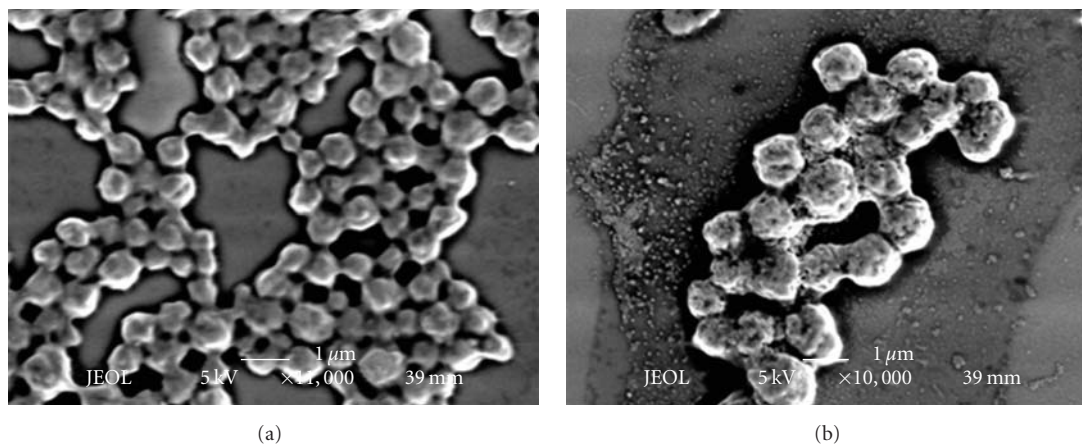


FIGURE 1: SEM images of (a) PVA/DNA complex (PVA: 1.0 w/v%) and (b) PVA/HAp/DNA complex (PVA: 1.0 w/v%, HAp: 0.1 w/v%) obtained by high hydrostatic pressurization (980 MPa, 10 min, 40°C). DNA conc.: 0.0025 w/v%.

the presence of FBS (10%). The cellular viability was assessed using a Cell Counting Kit-8 (Dojindo Laboratory, Tokyo, Japan) according to the manufacturer's instructions.

2.5. Cellular Uptake of PVA/HAp/DNA Complexes. The pGL3 plasmid DNA was labeled with rhodamine using a Label It kit (Panvera, Wis, USA) according to the manufacturer's instructions (Rh-DNA). HAp/Rh-DNA (HAp: 0.4 w/v%). PVA/Rh-DNA, and PVA/HAp/Rh-DNA complexes (PVA: 0.001 w/v%, HAp: 0.0001 w/v%) were added to COS-7 cells (1.0×10^5) cultured in 24-well plates in the presence of FBS (10%), and incubated at 37°C for one and 24 h. After washing with PBS twice, the cells were observed under a fluorescent microscope.

2.6. In Vitro Transfection. COS-7 cells (8.0×10^4) were cultured overnight in a 48-well plate. HAp/DNA (HAp: 0.4 w/v%), PVA/DNA, and PVA/HAp/DNA complexes (PVA: 0.001 w/v%, HAp: 0.0001 w/v%) were added to cells and incubated at 37°C for 24 h. The medium was removed from each well and washed with PBS twice. 50 μ L of a 1x luciferase cell culture lysis buffer (Promega Co., Ltd., Madison, USA) was added onto cells. For luciferase assay, 10 μ L of cell extract was mixed with 100 μ L of a luciferase assay reagent (Promega Co., Ltd., Madison, USA) and the luciferase activity was measured by using an AB-2200 luminometer (ATTO, Corp., Tokyo, Japan) for 10 s. The protein concentration of the supernatant was determined by using a DC protein assay kit (Bio-Rad laboratories, Inc., USA) according to the manufacturer's instructions.

2.7. In Vivo Transfection Using Hydrodynamic Injection Method. 1.6 mL of the saline solution of PVA/DNA and PVA/HAp/DNA complexes (PVA: 0.001 w/v% or 0.01 w/v%, HAp: 0.0001 w/v% or 0.001 w/v%, DNA: 0.0025 w/v%) were prepared by high hydrostatic pressurization and injected by a hydrodynamic technique as previously described [27]. Briefly, mice were restrained, and the tail vein was accessed with a 25 gauge needle. Administration of the solution was

performed in 10 seconds or less without extravasation; each group was represented by three or more animals. After 12, 24, and 72 h injection, the liver and lung were dissected from dead animals using the standard surgical procedures. 1 mL of lysis buffer (0.1 M Tris-HCl, 2 mM EDTA, and 0.1% Triton X-100, pH 7.8) was added to a piece of liver with wet weight of approximately 200 mg. The liver was homogenized for 15–20 s with a homogenizer (PT2100, KINEMATICA AG, Lucerne, Switzerland) at maximal speed, and the tissue homogenate was then centrifuged in a microcentrifuge for 10 min at 13000 g at 4°C. The protein concentration of the supernatant was determined by using a DC protein assay kit. For luciferase assay of the liver extract, the supernatant was further diluted 60-fold using an HEPES buffer. 10 μ L of supernatant of diluted liver extract was mixed with 100 μ L of luciferase assay reagent, and the luciferase activity was measured by using the AB-2200 luminometer for 10 s.

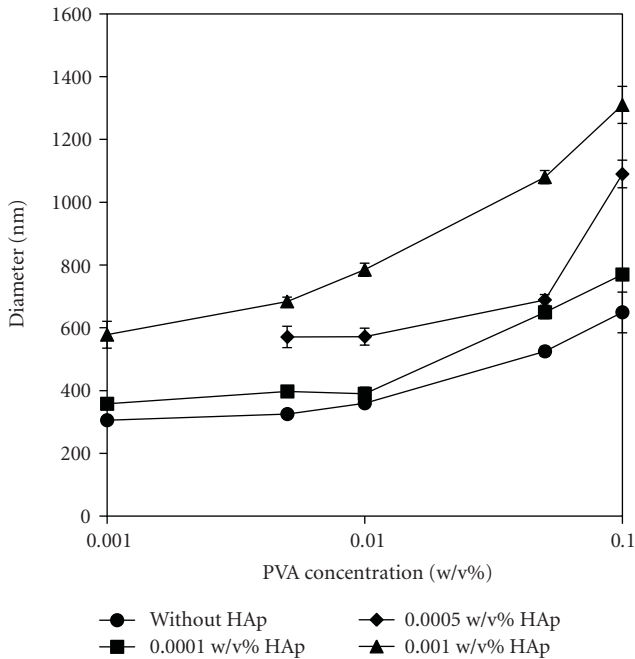
2.8. Statistical Analysis. All experiments were repeated at least three times (five times for DLS analysis), and the values are expressed as means \pm standard deviations. Statistical analysis was performed using student's *t*-test, with the significant level set at $P < .05$.

3. Results and Discussion

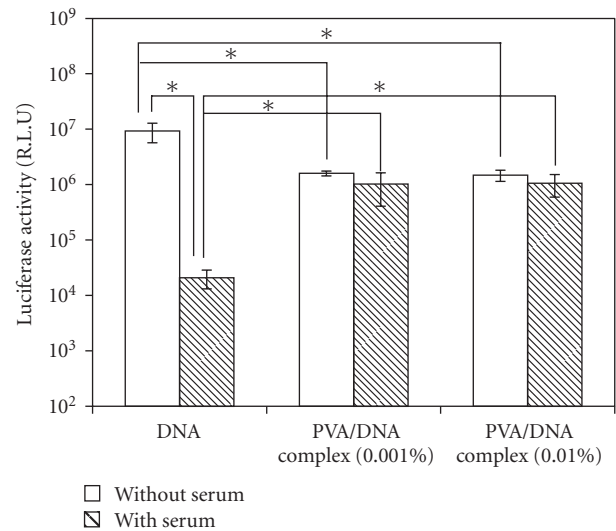
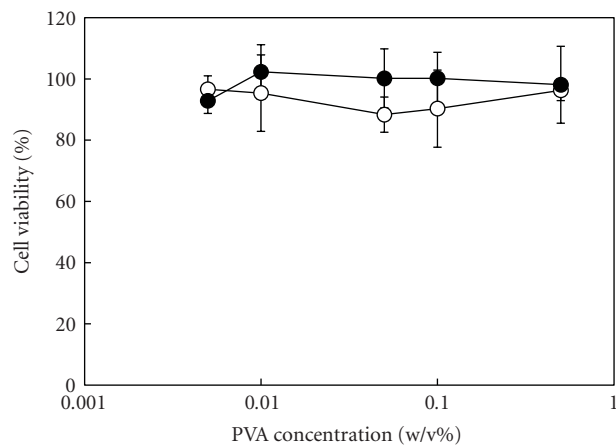
3.1. Preparation and Characterization of PVA/HAp/DNA Complexes. The mixture solution of PVA, HAp, and DNA was hydrostatically pressurized at 980 MPa and 40°C for 10 min using a high hydrostatic pressure machine. After removal of pressure, the obtained PVA/HAp/DNA complexes were observed by SEM. Figure 1 shows typical SEM images of PVA/DNA (PVA: 1.0%) and PVA/HAp/DNA complexes (PVA: 1.0%, HAp: 0.1%). Many particles less than 1 μ m were observed for the PVA/DNA complex. The surface of PVA/DNA particles was smooth. On the other hand, in the case of PVA/HAp/DNA complexes, irregular particle surfaces were observed without any significant HAp absorption on the particles, showing that HAp particles were

TABLE 1: DLS measurement of PVA/DNA and PVA/HAp/DNA complexes at various PVA and HAp concentrations. DNA conc.: 0.0025 w/v%.

HAp (%)	Average diameter (nm) (PDI) PVA (%)				
	0.001	0.005	0.01	0.05	0.1
0	306 ± 7 (0.08 ± 0.02)	325 ± 8 (0.13 ± 0.02)	360 ± 11 (0.16 ± 0.02)	525 ± 16 (0.07 ± 0.03)	649 ± 65 (0.11 ± 0.02)
0.00001	346 ± 4 (0.12 ± 0.02)	393 ± 8 (0.13 ± 0.02)	355 ± 14 (0.20 ± 0.02)	602 ± 17 (0.08 ± 0.03)	756 ± 17 (0.12 ± 0.03)
0.0001	358 ± 3 (0.11 ± 0.03)	397 ± 8 (0.10 ± 0.03)	390 ± 8 (0.19 ± 0.01)	649 ± 21 (0.12 ± 0.03)	770 ± 20 (0.08 ± 0.03)
0.0005		571 ± 34 (0.24 ± 0.13)	572 ± 27 (0.15 ± 0.03)	689 ± 17 (0.05 ± 0.03)	1090 ± 44 (0.21 ± 0.03)
0.001	578 ± 42 (0.278 ± 0.04)	684 ± 14 (0.11 ± 0.21)	785 ± 21 (0.11 ± 0.02)	1080 ± 21 (0.25 ± 0.02)	1310 ± 59 (0.23 ± 0.03)

FIGURE 2: DLS measurement of PVA/DNA and PVA/HAp/DNA complexes at various PVA and HAp concentrations. DNA conc.: 0.0025 w/v%. Each value represents the mean ± SD ($n = 5$).

encapsulated in the PVA/HAp/DNA complexes. When excess Haps were mixed with PVA and DNA, many aggregates of Haps on the PVA/HAp/DNA particles obtained by the pressurization were clearly visible (data not shown). The particle size of PVA/DNA and PVA/HAp/DNA complexes at various concentrations of PVA and HAp were measured by DLS measurement (Figure 2, Table 1). The diameter of PVA/DNA particles without HAp increased with increased PVA concentration, which corresponds to our previous report [1–4]. This tendency was exhibited for the particle size of PVA/HAp/DNA complexes, irrespective of HAp concentration. At each PVA concentration, the diameter of PVA/HAp/DNA particles increased with increased HAp concentration, indicating that HAp particles were significantly encapsulated in PVA/HAp/DNA complexes at these concentrations of PVA and HAp. From these results of SEM observation and DLS measurement, it was clear that nano-, microscaled composites of PVA, Hap, and DNA were obtained by high hydrostatic pressurization, and the size of PVA/HAp/DNA particles depended on PVA and HAp concentrations. To investigate the stability of DNA in the

FIGURE 3: Stability of DNA in PVA/DNA complexes in the presence of serum. Each value represents the mean ± SD ($n = 3$). * $P < .05$.FIGURE 4: Viability of COS-7 cells incubated with (white) PVA/DNA complexes and (black) PVA/HAp/DNA complexes for 24 h. DNA conc.: 0.0025 w/v%. Each value represents the mean ± SD ($n = 3$).

PVA/DNA particles on serum condition, PVA/DNA particles were incubated in medium containing 10% serum for 20 h, and then subjected to in vitro transcription and translation (Figure 3). The high luciferase activity of DNA was showed on the condition without serum, whereas the luciferase activity was remarkably reduced after incubation with serum.

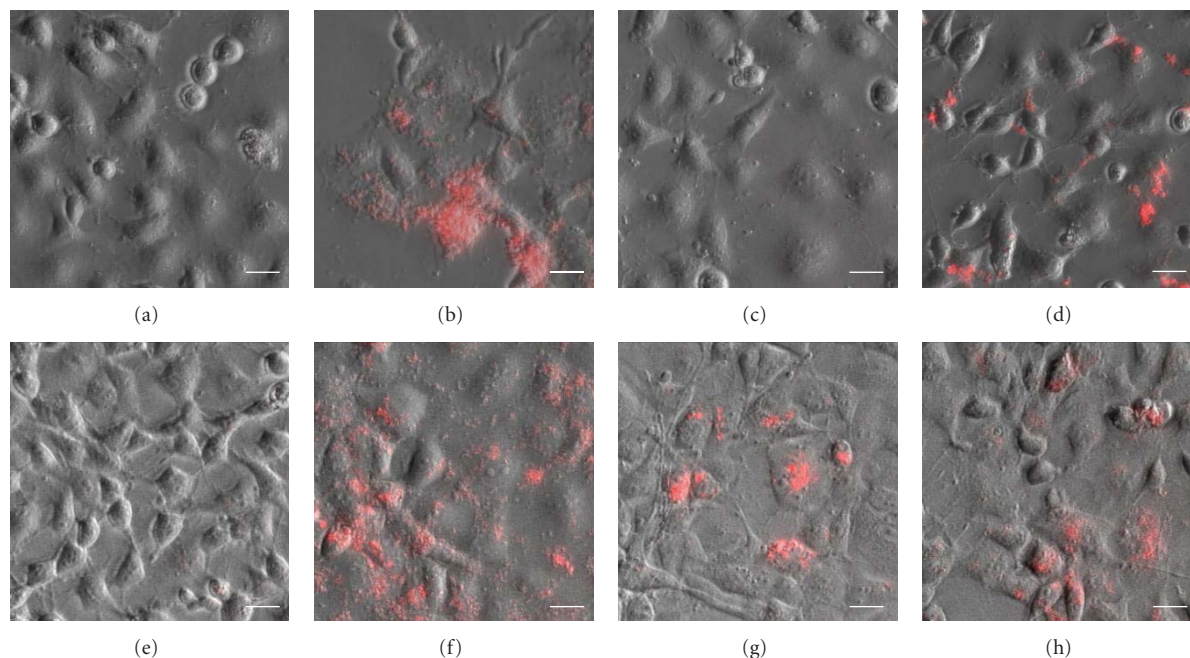


FIGURE 5: Fluorescent microscopic images of COS-7 cells incubated with (a, e) DNA, (b, f) HAp/DNA complex, (c, g) PVA/DNA complex, and (d, h) PVA/HAp/DNA complex for (a–d) 1 h and (e–h) 24 h. Scale bars are 10 μm .

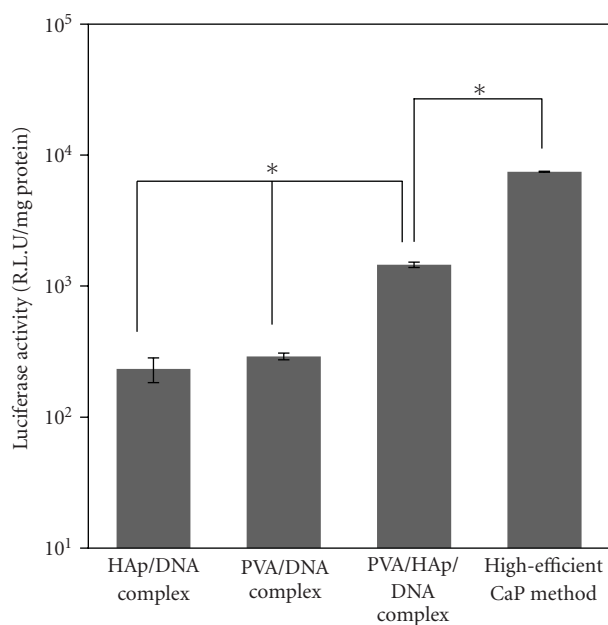


FIGURE 6: *In vitro* transfection using HAp/DNA, PVA/DNA and PVA/HAp/DNA complexes. Each value represents the mean \pm SD ($n = 3$). * $P < .05$.

On the other hand, there is no difference in the luciferase activity of DNA in PVA/DNA particles before and after incubation with serum, indicating the high stability of DNA in PVA/DNA particles against serum.

To date, many methods for preparation of composite materials of PVA and HAp, such as in situ crystallization of HAp in PVA hydrogel [28], gelation of PVA solution mixed with HAp crystals [29], and alternating soaking reaction,

which promote HAp crystallization on/in gel [30], have been reported. Large-scaled composite hydrogels (several centimeters) have been prepared for use in biomedical applications such as cartilage and bone. However, few preparation methods of nanocomposites of PVA and HAp have been reported. In this study, the nano-, microparticles of PVA, HAp and DNA were obtained by using high hydrostatic pressure technology. It is thought that this is achieved by the pressure-induced quick formation of PVA particles that could incorporate secondary and third substrates, such as DNA and HAp, without phase separation [15, 31].

3.2. Cytotoxicity Test. Figure 4 shows the result of the cytotoxicity test of PVA/DNA and PVA/HAp/DNA complexes. The high viability of COS-7 cells incubated with them is shown, irrespective of the concentration of PVA and HAp. PVA and HAp are biocompatible materials [32, 33]. The PVA/DNA complex is nontoxic because of the composite formation of PVA and DNA via hydrogen bonding interaction [16]. HAp was encapsulated in PVA/HAp/DNA complexes. Consequently, it is considered that the nontoxicity of PVA/HAp/DNA complexes was achieved by these combinations.

3.3. Cellular Uptake of PVA/HAp/DNA Nanoparticles. In order to investigate cellular uptake of the HAp/DNA complex, PVA/DNA, and PVA/HAp/DNA nanoparticles, rhodamine-labeled plasmid DNA was used. Figure 4 shows fluorescent microscopic images of COS-7 cells incubated with complexes of PVA, HAp, and rhodamine-labeled DNA for one and 24 h. After 1 h incubation, fluorescent spots were poorly observed for DNA and PVA/DNA nanoparticles (Figures 5(a) and 5(c)), whereas a lot of bright red

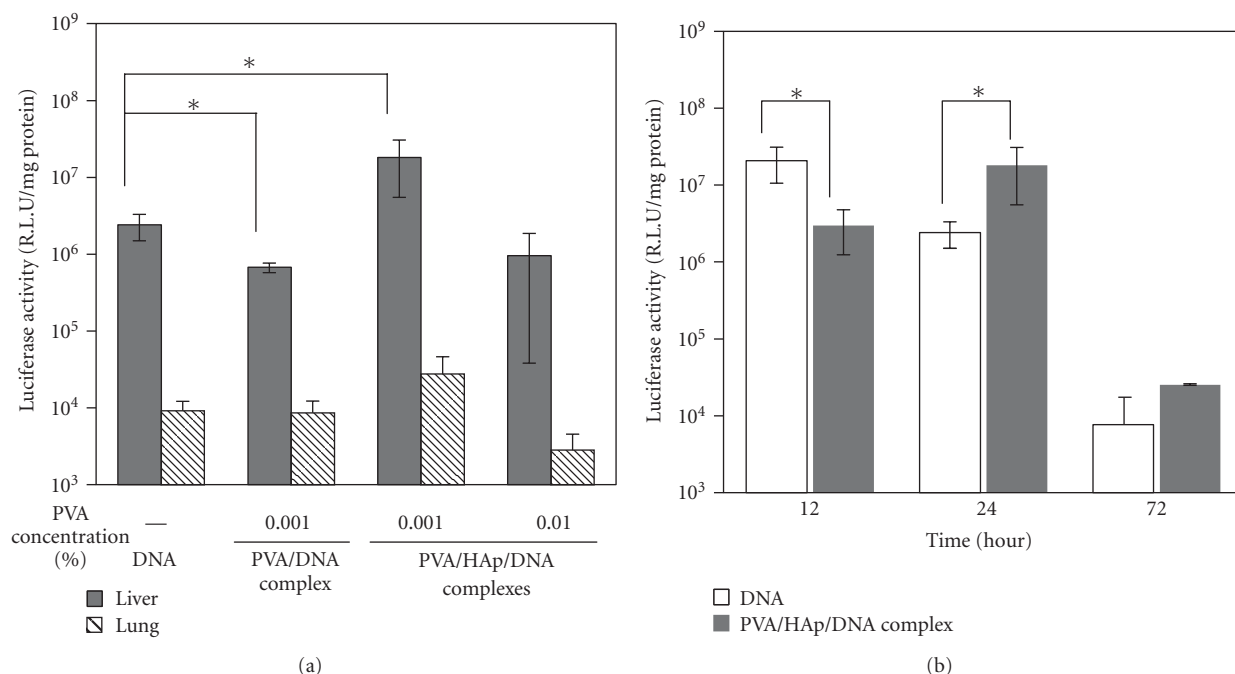


FIGURE 7: Transgene expression (luciferase activity) of plasmid DNA, PVA/DNA, and PVA/HAP/DNA complexes injected by *in vivo* hydrodynamic method. (b) Time course of transgene expression of plasmid DNA and PVA/HAP/DNA complexes injected by *in vivo* hydrodynamic method. Each value represents the mean \pm SD ($n = 3$). * $P < .05$.

fluorescent spots on many cells were shown in the case of HAp/DNA and PVA/HAp/DNA complexes (Figures 5(b) and 5(d)), indicating the effective absorption of them onto cells because of their higher specific gravity. However, strong aggregation of HAp/DNA complexes was observed due to the fact that the nature of HAp particles tends to result in an aggregation in the aqueous medium [34]. For PVA/HAp/DNA nanoparticles, PVA bearing HAp could attenuate the aggregation property of HAp. After 24 h incubation, the aggregation of the HAp/DNA composite was still observed (Figure 5(f)). The internalization of PVA/HAp/DNA nanoparticles into cells was exhibited. Also, the subcellular distribution of DNA was observed in some cells (Figure 5(h)) similar to that of PVA/DNA nanoparticles (Figure 5(g)). This strongly suggests that HAp in PVA/HAp/DNA nanoparticles could be dissolved during the intracellular process, probably due to the endocytosis pathway.

3.4. In Vitro Transfection Using PVA/HAp/DNA Nanoparticles. The expressing of the delivered DNA compositing with PVA and HAp was assayed by measuring luciferase activity (Figure 6). Low luciferase activity was shown for the HAp/DNA complex. This is caused by the strong aggregation of HAp/DNA complexes [20]. The level of luciferase activity of PVA/DNA nanoparticles was similar to that of the HAp/DNA complex due to the slow internalization of PVA/DNA nanoparticles into cells, which could probably permit DNA degradation. In the case of the PVA/HAp/DNA nanoparticles, which can be taken up by cells quickly, high luciferase activity was shown, indicating that the encapsulation of HAp in PVA/DNA nanoparticles could

enhance the transfection efficiency *in vitro*. However, the transfection efficiency of the PVA/HAp/DNA nanoparticles was lower than in the high-efficient calcium phosphate transfection method, which is optimized for *in vitro* transfection [21].

3.5. In Vivo Transfection Using Hydrodynamic Injection. *In vivo* transfection was performed by using a hydrodynamic method (Figure 7). This method is known as an effective plasmid DNA transfection method without gene carrier to liver [35]. Figure 7(a) shows the results of *in vivo* hydrodynamic injection using various nanoparticles. The luciferase activity of the PVA/DNA complex (PVA: 0.001 w/v%) was lower than that of DNA injection, whereas high luciferase activity was achieved for PVA/HAp/DNA nanoparticles at the PVA concentration of 0.001 w/v% (HAp: 0.0001 w/v%). At PVA concentration of 0.01 w/v% (HAp: 0.001 w/v%), the luciferase activity of PVA/HAp/DNA nanoparticles decreased compared to that of 0.001 w/v%. This is thought to be caused by the insignificant uptake of the large particles of PVA/HAp/DNA nanoparticles (about 780 nm, Figure 2, Table 1) by hepatocytes [36]. When the luciferase activity in lung was also investigated, the low activity was detected in lung compared to that in liver, irrespective of type of nanoparticles.

The time-course of transgene activity was also investigated (Figure 7(b)). For plasmid DNA, the highest value for luciferase activity was detected after 12 hours, and the level of gene expression significantly decreased over time. On the other hand, in the case of PVA/HAp/DNA nanoparticles, the highest value for luciferase activity was achieved for 24 hours.

This result indicates that the PVA/HAp/DNA nanoparticles could prolong the gene expression. We assumed that PVA/HAp/DNA nanoparticles could be accumulated due to the relative high stability, which are continuously transcribed and translated (Figure 3).

4. Conclusion

We successfully developed PVA/DNA nanoparticles encapsulating HAPs by using simple high hydrostatic pressure technology. They could enhance the transfection efficiency without any significant cytotoxicity *in vitro* and *in vivo* hydrodynamic injection. Consequently, the potential use of HAp could be expected as an enhancer of gene transfer activity of PVA/DNA nanoparticles.

Acknowledgments

This work was partly supported by grants from the Ministry of Health, Labor and Welfare, the Ministry of Education, Culture, Sports, Science and Technology, and Core Research for Evolutional Science and Technology (CREST) of the Japan Science and Technology Agency (JST). We thank Kuraray, Co., Ltd., for supplying the poly(vinyl alcohol).

References

- [1] T. Niidome and Y. Katayama, "Use of synthetic peptides for non-viral gene delivery," in *Non-Viral Gene Therapy; Gene Design and Delivery*, K. Taira, K. Kataoka, and T. Niidome, Eds., pp. 87–102, Springer, Tokyo, Japan, 2005.
- [2] T. Kimura, T. Yamaoka, R. Iwase, and A. Murakami, "Effect of physicochemical properties of polyplexes composed of chemically modified PL derivatives on transfection efficiency *in vitro*," *Macromolecular Bioscience*, vol. 2, no. 9, pp. 437–446, 2002.
- [3] M. Neu, D. Fischer, and T. Kissel, "Recent advances in rational gene transfer vector design based on poly(ethylene imine) and its derivatives," *Journal of Gene Medicine*, vol. 7, no. 8, pp. 992–1009, 2005.
- [4] C. Dufès, I. F. Uchegbu, and A. G. Schätzlein, "Dendrimers in gene delivery," *Advanced Drug Delivery Reviews*, vol. 57, no. 15, pp. 2177–2202, 2005.
- [5] P. Dubruel and E. Schacht, "Vinyl polymers as non-viral gene delivery carriers: current status and prospects," *Macromolecular Bioscience*, vol. 6, no. 10, pp. 789–810, 2006.
- [6] D. Fischer, Y. Li, B. Ahlemeyer, J. Krieglstein, and T. Kissel, "In vitro cytotoxicity testing of polycations: influence of polymer structure on cell viability and hemolysis," *Biomaterials*, vol. 24, no. 7, pp. 1121–1131, 2003.
- [7] K. Itaka and K. Kataoka, "Recent development of nonviral gene delivery systems with virus-like structures and mechanisms," *European Journal of Pharmaceutics and Biopharmaceutics*, vol. 71, no. 3, pp. 475–483, 2009.
- [8] M. Lee and S. W. Kim, "Polyethylene glycol-conjugated copolymers for plasmid DNA delivery," *Pharmaceutical Research*, vol. 22, no. 1, pp. 1–10, 2005.
- [9] M. Ogris, S. Brunner, S. Schüller, R. Kircheis, and E. Wagner, "PEGylated DNA/transferrin-PEI complexes: reduced interaction with blood components, extended circulation in blood and potential for systemic gene delivery," *Gene Therapy*, vol. 6, no. 4, pp. 595–605, 1999.
- [10] N. Shimada, C. Coban, Y. Takeda et al., "A polysaccharide carrier to effectively deliver native phosphodiester CpG DNA to antigen-presenting cells," *Bioconjugate Chemistry*, vol. 18, no. 4, pp. 1280–1286, 2007.
- [11] R. J. Mumper, J. G. Duguid, K. Anwer, M. K. Barron, H. Nitta, and A. P. Rolland, "Polyvinyl derivatives as novel interactive polymers for controlled gene delivery to muscle," *Pharmaceutical Research*, vol. 13, no. 5, pp. 701–709, 1996.
- [12] R. J. Mumper, J. Wang, S. L. Klakamp et al., "Protective interactive noncondensing (PINC) polymers for enhanced plasmid distribution and expression in rat skeletal muscle," *Journal of Controlled Release*, vol. 52, no. 1-2, pp. 191–203, 1998.
- [13] E. Doi, A. Shimizu, and N. Kitabatake, "Gel-sol transition of ovalbumin by high pressure," in *Hayashi R(ed) High Pressure Bioscience and Food Science*, pp. 171–177, Sanei Press, Kyoto, Japan, 1993.
- [14] T. Kimura, S. Iwai, T. Moritan et al., "Preparation of poly(vinyl alcohol)/DNA hydrogels via hydrogen bonds formed on ultra-high pressurization and controlled release of DNA from the hydrogels for gene delivery," *Journal of Artificial Organs*, vol. 10, no. 2, pp. 104–108, 2007.
- [15] T. Ono, S. Mutsuo, K. Yamamoto, T. Furuzono, T. Kimura, and A. Kishida, "Pressure-induced molecular assembly of hydrogen-bonded polymers," *Journal of Polymer Science B*, vol. 46, no. 7, pp. 743–750, 2008.
- [16] T. Kimura, A. Okuno, K. Miyazaki et al., "Novel PVA-DNA nanoparticles prepared by ultra high pressure technology for gene delivery," *Materials Science and Engineering C*, vol. 24, no. 6–8, pp. 797–801, 2004.
- [17] F. L. Graham and A. J. Van Der Eb, "A new technique for the assay of infectivity of human adenovirus 5 DNA," *Virology*, vol. 52, no. 2, pp. 456–467, 1973.
- [18] C. Chen and H. Okayama, "High-efficiency transformation of mammalian cells by plasmid DNA," *Molecular and Cellular Biology*, vol. 7, no. 8, pp. 2745–2752, 1987.
- [19] Y. W. Yang and J. C. Yang, "Calcium phosphate as a gene carrier: electron microscopy," *Biomaterials*, vol. 18, no. 3, pp. 213–217, 1997.
- [20] E. H. Chowdhury, T. Sasagawa, M. Nagaoka, A. K. Kundu, and T. Akaike, "Transfecting mammalian cells by DNA/calcium phosphate precipitates: effect of temperature and pH on precipitation," *Analytical Biochemistry*, vol. 314, no. 2, pp. 316–318, 2003.
- [21] M. Jiang and G. Chen, "High Ca²⁺-phosphate transfection efficiency in low-density neuronal cultures," *Nature Protocols*, vol. 1, no. 2, pp. 695–700, 2006.
- [22] Y. Kakizawa and K. Kataoka, "Block copolymer self-assembly into monodisperse nanoparticles with hybrid core of antisense DNA and calcium phosphate," *Langmuir*, vol. 18, no. 12, pp. 4539–4543, 2002.
- [23] Y. Kakizawa, S. Furukawa, and K. Kataoka, "Block copolymer-coated calcium phosphate nanoparticles sensing intracellular environment for oligodeoxynucleotide and siRNA delivery," *Journal of Controlled Release*, vol. 97, no. 2, pp. 345–356, 2004.
- [24] P. N. Kumta, C. Sfeir, D. H. Lee, D. Olton, and D. Choi, "Nanostructured calcium phosphates for biomedical applications: novel synthesis and characterization," *Acta Biomaterialia*, vol. 1, no. 1, pp. 65–83, 2005.
- [25] T. Furuzono, D. Walsh, K. Sato, K. Sonoda, and J. Tanaka, "Effect of reaction temperature on the morphology and size of hydroxyapatite nanoparticles in an emulsion system," *Journal of Materials Science Letters*, vol. 20, no. 2, pp. 111–114, 2001.

- [26] K. Sonoda, T. Furuzono, D. Walsh, K. Sato, and J. Tanaka, "Influence of emulsion on crystal growth of hydroxyapatite," *Solid State Ionics*, vol. 151, no. 1–4, pp. 321–327, 2002.
- [27] F. Liu, Y. K. Song, and D. Liu, "Hydrodynamics-based transfection in animals by systemic administration of plasmid DNA," *Gene Therapy*, vol. 6, no. 7, pp. 1258–1266, 1999.
- [28] A. Sinha, S. Nayar, A. Agrawal, D. Bhattacharyya, and P. Ramachandrarao, "Synthesis of nanosized and microporous precipitated hydroxyapatite in synthetic polymers and biopolymers," *Journal of the American Ceramic Society*, vol. 86, no. 2, pp. 357–359, 2003.
- [29] X. Huang, Y. Zuo, J. D. Li, and Y. B. Li, "Study on crystallisation of nano-hydroxyapatite/polyvinyl alcohol composite hydrogel," *Materials Research Innovations*, vol. 13, no. 2, pp. 98–102, 2009.
- [30] T. Taguchi, A. Kishida, and M. Akashi, "Hydroxyapatite formation on/in poly(vinyl alcohol) hydrogel matrices using a novel alternate soaking process," *Chemistry Letters*, no. 8, pp. 711–712, 1998.
- [31] J. Negishi, K. Nam, T. Kimura, T. Fujisato, and A. Kishida, "High-hydrostatic pressure technique is an effective method for the preparation of PVA–heparin hybrid gel," *European Journal of Pharmaceutical Science*, vol. 41, pp. 617–672, 2010.
- [32] T. Noguchi, T. Yamamuro, M. Oka et al., "Poly(vinyl alcohol) hydrogel as an artificial articular cartilage: evaluation of biocompatibility," *Journal of Applied Biomaterials*, vol. 2, no. 2, pp. 101–107, 1991.
- [33] M. Jarcho, J. F. Kay, K. I. Gumaer, R. H. Doremus, and H. P. Drobeck, "Tissue, cellular and subcellular events at a bone-ceramic hydroxyapatite interface," *Journal of Bioengineering*, vol. 1, no. 2, pp. 79–92, 1977.
- [34] L. Borum and O. C. Wilson Jr., "Surface modification of hydroxyapatite—part II: silica," *Biomaterials*, vol. 24, no. 21, pp. 3681–3688, 2003.
- [35] T. Suda and D. Liu, "Hydrodynamic gene delivery: its principles and applications," *Molecular Therapy*, vol. 15, no. 12, pp. 2063–2069, 2007.
- [36] M. G. Sebestyén, V. G. Budker, T. Budker et al., "Mechanism of plasmid delivery by hydrodynamic tail vein injection. I. Hepatocyte uptake of various molecules," *Journal of Gene Medicine*, vol. 8, no. 7, pp. 852–873, 2006.

Research Article

Nanoprodugs of NSAIDs: Preparation and Characterization of Flufenamic Acid Nanoprodugs

Bong-Seop Lee, Chi Woo Yoon, Arsen Osipov, Nuriel Moghavem, Daniel Nwachokor, Rina Amatya, Rebekah Na, Joe L. Pantoja, Michael D. Pham, Keith L. Black, and John S. Yu

Department of Neurosurgery, Cedars-Sinai Medical Center, 8631 West Third Street, Suite 800 East, Los Angeles, CA 90048, USA

Correspondence should be addressed to John S. Yu, john.yu@cshs.org

Received 16 December 2010; Revised 31 January 2011; Accepted 6 February 2011

Academic Editor: Sanyog Jain

Copyright © 2011 Bong-Seop Lee et al. This is an open access article distributed under the Creative Commons Attribution License, which permits unrestricted use, distribution, and reproduction in any medium, provided the original work is properly cited.

We demonstrated that hydrophobic derivatives of the nonsteroidal anti-inflammatory drug (NSAID) flufenamic acid (FA), can be formed into stable nanometer-sized produgs (nanoprodugs) that inhibit the growth of glioma cells, suggesting their potential application as anticancer agent. We synthesized highly hydrophobic monomeric and dimeric produgs of FA via esterification and prepared nanoprodugs using spontaneous emulsification mechanism. The nanoprodugs were in the size range of 120 to 140 nm and physicochemically stable upon long-term storage as aqueous suspension, which is attributed to the strong hydrophobic interaction between produg molecules. Importantly, despite the highly hydrophobic nature and water insolubility, nanoprodugs could be readily activated into the parent drug by porcine liver esterase, presenting a potential new strategy for novel NSAID produg design. The nanoprodug inhibited the growth of U87-MG glioma cells with IC_{50} of 20 μM , whereas FA showed IC_{50} of 100 μM , suggesting that more efficient drug delivery was achieved with nanoprodugs.

1. Introduction

Nonsteroidal anti-inflammatory drugs (NSAIDs) are a class of drugs with analgesic, antipyretic and anti-inflammatory effects and have been widely used in the treatment of pain, fever, and inflammation. NSAIDs exert their anti-inflammatory activity through the inhibition of cyclooxygenase (COX) derived prostaglandin synthesis. COX has been recognized as the first enzyme in the formation of prostaglandin (PG) and thromboxane (TX) from arachidonic acid at the site of inflammation or after infection [1]. COX-1 isozyme is expressed constitutively in many tissues, whereas COX-2 isozyme is expressed only at the site of inflammation [2]. Recent studies have conjectured that elevated expression of COX-2 has been detected in various cancers, including colorectal, lung, breast, liver, head and neck, and brain tumors, whereas COX-1 expression was unaffected [3–5]. Several studies have also demonstrated that NSAIDs may be effective in the prevention and treatment of certain types of cancers [6–9]. The chemopreventive and antitumorigenic effects of NSAIDs are believed to be exerted through

the induction of apoptosis followed by inhibition of COX-2 [10–13]. Some data also suggest a COX-2-independent mechanism because apoptosis induction by NSAIDs does not always correlate with their ability to inhibit COX-2 [14–17].

However, the major mechanism by which NSAIDs exert their anti-inflammatory activity, the inhibition of cyclooxygenase-derived prostaglandin synthesis, is also responsible for the adverse side effects, such as irritation and ulceration of the gastrointestinal (GI) mucosa [18]. It is generally believed that these GI side effects result from the combined effect of the irritation caused by the free carboxylic groups in NSAIDs and blockage of prostaglandin biosynthesis in the GI tract [19].

Prodrug strategy is widely recognized as a potential approach to overcome toxic side effects that are ascribed to the irritation caused by the free carboxylic groups in NSAIDs and blockage of prostaglandin biosynthesis in the GI tract. There have been several attempts to develop produgs of NSAIDs to overcome the adverse side effects as well as to improve their bioavailability by masking the carboxylic acid groups through the formation of bioreversible bonds [20–24].

The development of nanostructured biomaterials with antitumorigenic efficacy has received significant attention from the pharmaceutical industry, mainly because of their potential for precise targeting with less severe toxic side effects. Many effective anticancer therapeutics are low water soluble and must be in excessive amounts of organic cosolvents to obtain a therapeutically effective dose. This limits clinical applicability of these drugs. The formation into compact nanostructures obviates the need to use organic solvents, eliminating the interference of toxic side effects caused by cosolvents [25, 26]. In addition, by using a nanometer-sized delivery system, a significant drug loading per unit volume can be achieved, which is of crucial importance when high dosing is required.

In our effort to combine the prodrug concept and nanostructured drug/drug delivery system we demonstrated that water-insoluble prodrug compounds can be transformed into stable nanostructures obviating the need to dissolve the compounds in organic solvents. In our previous report we demonstrated six hydrophobic derivatives of NSAIDs (Figure 1) and their nanoprodugs [27, 28]. In this study, we synthesized monomeric and dimeric produgs of flufenamic acid (FA, 2-[(3-trifluoromethylphenyl)amino]benzoic acid) and prepared nanoprodugs through spontaneous emulsification of the produgs in acetone. Further, we demonstrated the antiproliferative effect of FA nanoprodugs on U87GM glioma cells.

2. Materials and Methods

2.1. General Procedures and Materials. Unless otherwise noted, solvents and chemicals were obtained at highest purity from Sigma-Aldrich Chemical Co. (St Louis, MO, USA) and used without further preparation. Chromatographic purification of the synthesized compounds was performed using silica gel (60 Å, 200–400 mesh). The compounds were confirmed by thin layer chromatography (TLC) silicagel plate (Merck 60 F254). Compounds containing α -lipoic acid were visualized by treatment with a solution of: 1.5 g of KMnO_4 , 10 g of K_2CO_3 , and 1.25 mL of 10% NaOH in 200 mL of H_2O , followed by gentle heating. The oxidized derivatives of FA were visualized under UV light. ^1H and ^{13}C NMR spectra were conducted on a Varian 400 MHz spectrometer and chemical shifts (δ) were given in ppm relative to TMS. The spectra were recorded with the solvent CDCl_3 at room temperature.

2.2. High-Performance Liquid Chromatography. HPLC analysis was performed on a Merck-Hitachi analytical LaChrom D-7000 HPLC/UV detector system (Merck, Darmstadt, Germany) with a CAPCELL PAK, Type SG 120 (phenomenex, Torrance, CA, USA) C_{18} reversed phase column (250/4.6 mm, 5 μm). The separation was performed under isocratic condition at a flow rate of 1 mL/min. The composition of the mobile phase (acetonitrile/water mixture containing 0.1% (v/v) trifluoroacetic acid) was adjusted for produgs and their degradation products in order to provide

an appropriate retention time and separation. The detection was carried out at 254 nm.

2.3. Synthesis of FA Prodrugs. The synthesis and characterization of the monomeric derivative of α -lipoic acid (ALA) with tetraethylene glycol (TEG) (ALA-TEG-OH, Scheme 1(a)) was performed as described in [27]. The synthesis and characterization of the monomeric (Scheme 1(a)) and the dimeric (Scheme 1(b)) FA derivatives were performed as follows.

ALA-TEG-OH (3.8 mmol) and FA (4.1 mmol, FA) in 20 mL of anhydrous dichloromethane (DCM) were reacted with 4-(dimethylamino)-pyridine (DMAP, 4.1 mmol) in the presence of molecular sieve for 10 min at room temperature. *N*-(3-Dimethylaminopropyl)-*N*-ethylcarbodiimide hydrochloride (EDCI, 4.1 mmol) was added portionwise over 10 min and the reaction mixture was stirred for 5 h at room temperature in the dark, filtered, and then concentrated under vacuum at room temperature. The products were purified using column chromatography (100:1 $\text{CH}_3\text{Cl}:\text{MeOH}$) and characterized as described above (Section 2.1).

For the synthesis of dimeric derivative FA_2TEG , FA (6 mmol), and TEG (2.5 mmol) in 40 mL of anhydrous DCM were reacted with DMAP (6 mmol) in the presence of molecular sieve for 10 min at room temperature. EDCI (6 mmol) was added portionwise over 10 min and the reaction mixture was stirred for 5 h at room temperature in the dark, filtered, and then concentrated under vacuum. The products were purified using column chromatography (100:0.5 $\text{CH}_3\text{Cl}:\text{MeOH}$) and characterized as described above (Section 2.1).

FA-TEG-OH was synthesized and used for the identification of the degradation products of the monomeric and dimeric produgs during enzymatic hydrolysis. FA (10 mmol) and TEG (30 mmol) in 50 mL of anhydrous dichloromethane (DCM) were reacted with DMAP (15 mmol) in the presence of a molecular sieve (Fluka, 3 Å, 10–20 mesh beads) for 10 min at room temperature. EDCI (10 mmol) was added portionwise over 10 min and the reaction mixture was stirred for 5 h at room temperature in the dark, filtered, and then concentrated under vacuum to reduce the volume. The product FA-TEG-OH and dimeric byproduct FA_2TEG were separated using column chromatography by loading the concentrated reaction mixture on the column without prior preparation and characterized as described above.

FA-TEG-OH. The column chromatography on silica gel ($\text{CHCl}_3:\text{MeOH}$ 100:1) gave the compound as a colorless oil (75%). TLC ($\text{CHCl}_3:\text{MeOH}$ 100:1) R_f 0.33; ^1H NMR (400 MHz, CDCl_3): δ = 3.51 (t, 2 \times H), 3.60 (m, 10 \times H), 3.82 (t, 2 \times H), 4.42 (t, 2 \times H), 6.80 (t, 1 \times H), 7.18 (m, 2 \times H), 7.40 (m, 4 \times H), 8.05 (t, 1 \times H), 9.53 (s, 1 \times H). ^{13}C NMR (100 MHz, CDCl_3): δ = 61.66, 63.92, 69.15, 70.27, 70.52, 70.64, 70.68, 72.57, 113.02, 114.31, 117.93, 118.36, 119.49, 124.45, 129.90, 131.61, 131.99, 132.25, 134.31, 141.66, 146.63, 168.21.

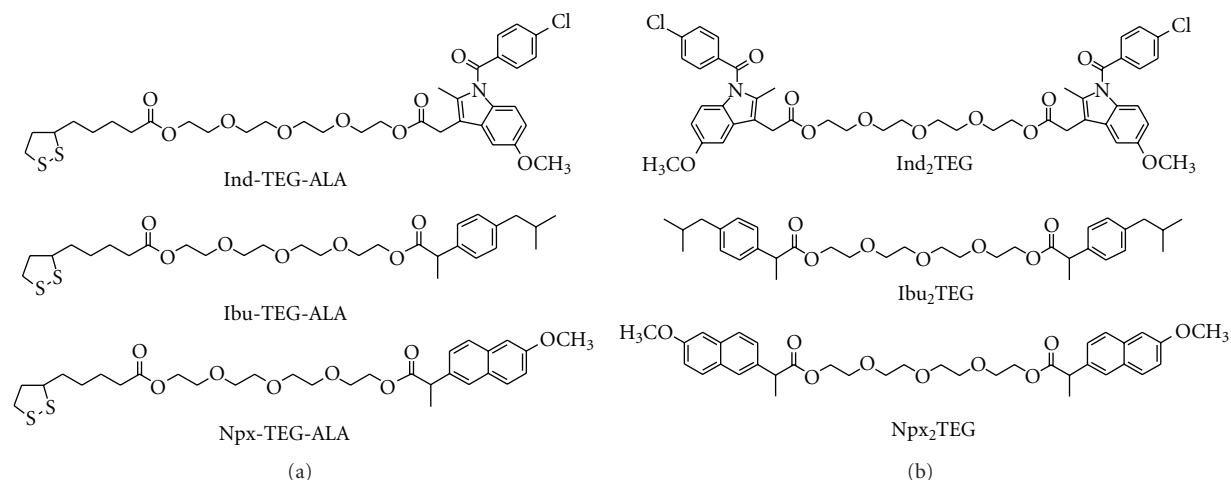
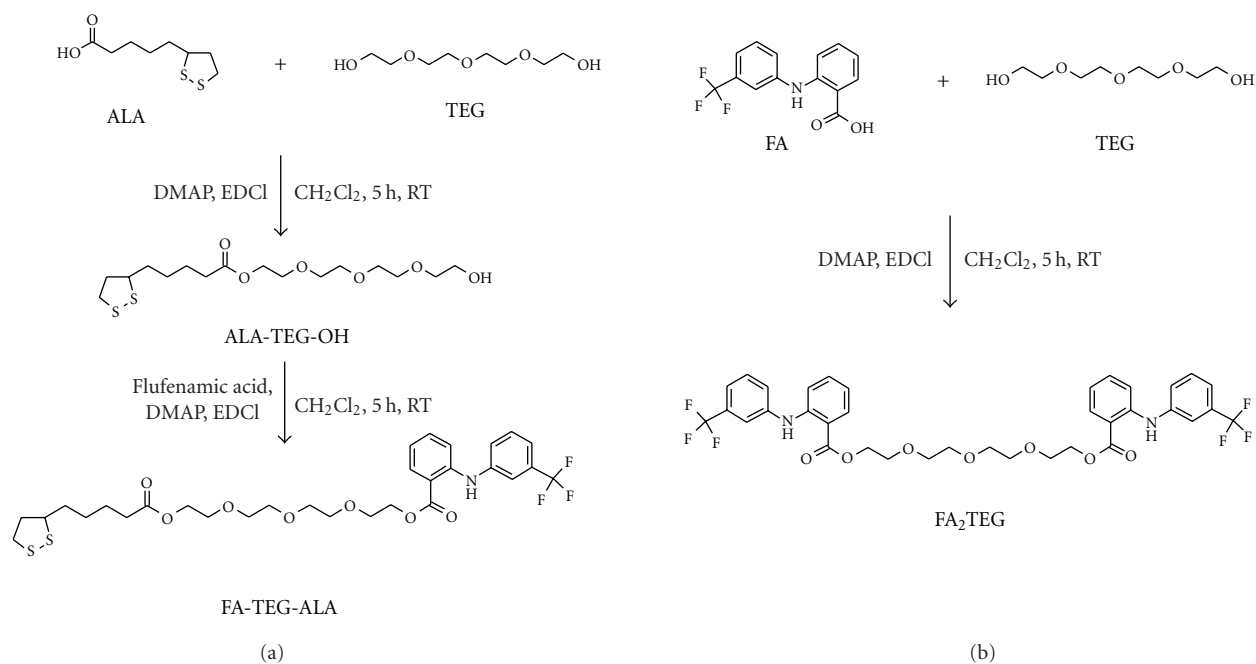


FIGURE 1: Nanoprodrugs of NSAIDs. ALA: α -lipoic acid; Ind: indomethacin; Ibu: ibuprofen; Npx: naproxen; TEG: tetraethylene glycol.



SCHEME 1: Synthesis of hydrophobic derivatives of FA.

FA-TEG-ALA. The column chromatography on silica gel (CHCl₃:MeOH 100:1) gave the compound as a yellow oil (65%). TLC (CHCl₃:MeOH 100:1) R_f 0.55; ¹H NMR (400 MHz, CDCl₃): δ = 1.49 (m, 2 \times H), 1.70 (m, 4 \times H), 1.90 (m, 1 \times H), 2.45 (m, 1 \times H), 3.10 (m, 2 \times H), 3.59 (m, 1 \times H), 3.70 (m, 10 \times H), 3.82 (t, 2 \times H), 4.20 (t, 2 \times H), 4.45 (t, 2 \times H), 6.80 (t, 1 \times H), 7.25 (m, 2 \times H), 7.35 (m, 4 \times H), 8.07 (t, 1 \times H), 9.52 (s, 1 \times H). ¹³C NMR (100 MHz, CDCl₃): δ = 24.61, 28.73, 33.94, 34.59, 38.48, 40.22, 56.34, 63.45, 63.96, 69.17, 70.56, 70.67, 70.75, 113.03, 114.33, 117.97, 118.08, 118.34, 119.52, 124.50, 129.11, 129.91, 131.98, 134.32, 141.69, 146.67, 168.22, 173.44.

FA₂TEG. The column chromatography on silica gel (CHCl₃:MeOH 100:1) gave the compound as a colorless oil (75%). TLC (CHCl₃:MeOH 100:1) R_f 0.75; ¹H NMR (400 MHz, CDCl₃): δ = 3.65 (m, 8 \times H), 3.85 (t, 4 \times H), 4.45 (t, 4 \times H), 6.80 (t, 1 \times H), 7.20 (m, 2 \times H), 7.40 (m, 4 \times H), 8.00 (t, 1 \times H), 9.53 (s, 2 \times H). ¹³C NMR (100 MHz, CDCl₃): δ = 63.95, 69.16, 70.72, 70.75, 113.02, 114.31, 117.96, 118.33, 119.51, 122.62, 125.33, 129.89, 131.67, 131.99, 134.31, 141.65, 146.67, 168.22.

2.4. Preparation of FA Nanoprodrugs. Nanoprodrugs were prepared according to the method using spontaneous emulsification as described [27]. Briefly, 25 mg of the FA

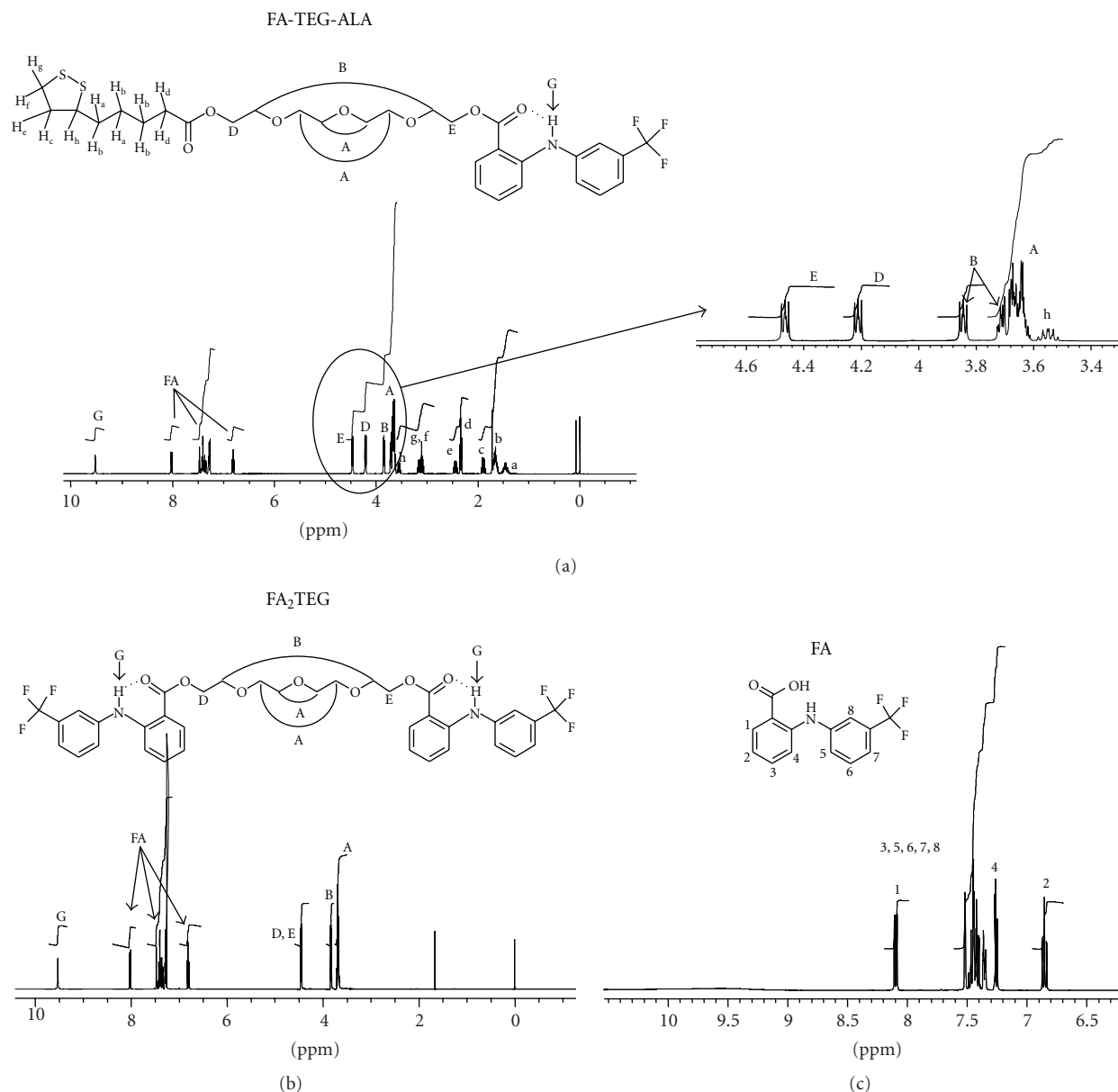


FIGURE 2: ¹H NMR spectra of (a) FA-TEG-ALA, (b) FA₂TEG, and (c) flufenamic acid (FA).

derivatives and 5 mg of α -tocopherol were dissolved in acetone (5 mL) containing polysorbate 80 (0.1% w/v). The organic solution was poured under moderate stirring on a magnetic plate into an aqueous phase prepared by dissolving 25 mg of Pluronic F68 in 10 mL distilled water (0.25% w/v). Following 15 min of magnetic stirring, the acetone was removed under reduced pressure at room temperature. The suspensions were filtered through 0.8 μ m hydrophilic syringe filter (Corning, Part no 431221, Fisher Scientific Co., Pittsburgh, PA, USA), dialyzed in cellulose membrane tube (Sigma, code D9777) overnight in distilled water and stored at 4°C. A control nanosphere was prepared with 25 mg of α -tocopherol in the absence of FA derivatives using the same procedure as described above. To demonstrate cellular uptake, nanoprodugs containing a hydrophobic fluorescent

dye, coumarin 6 (Sigma, code 442631), were prepared using identical procedure except that 50 μ g of the dye was added to the organic FA prodrug solution prior to spontaneous emulsification. The incorporated dye remains associated with nanoprodugs during dialysis overnight.

2.5. Size Measurements and Visualization of Nanoprodugs. The hydrodynamic size measurement and size distribution of the nanoprodugs were performed by the dynamic light scattering (DLS) using a Coulter N4-Plus Submicron Particle Sizer (Coulter Corporation, Miami, FL, USA) as described [27]. For each preparation mean diameter and mean polydispersity index (PI) of three determinations were calculated. The error bar (SD) was calculated from triplicate determinations. For visualization of the nanoprodugs,

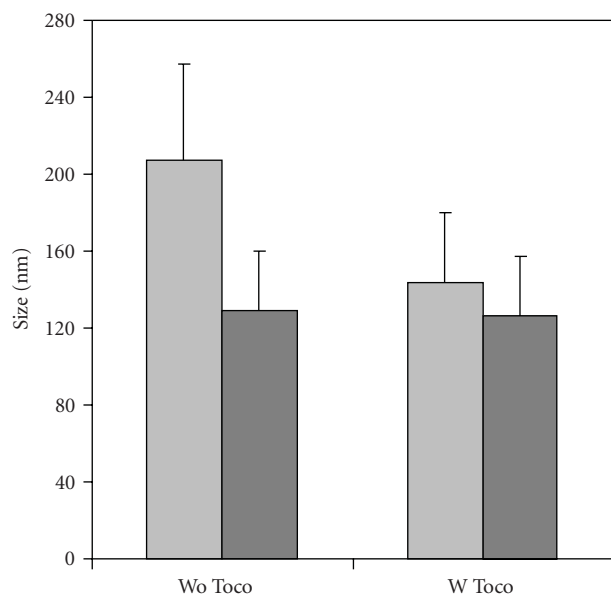


FIGURE 3: Size of the nanoprodrugs in the absence (wo Toco) and presence (w Toco) of α -tocopherol. Light gray bar: monomeric FA-TEG-ALA; dark gray bar: dimeric FA₂-TEG.

nanoparticle tracking analysis (NTA) experiments were performed using a digital microscope LM10 System (NanoSight, Amesbury, UK). A small amount of the diluted nanoprodrug suspension in water was introduced into the chamber by a syringe. The particles in the sample were observed using the digital microscope. The movement of nanoprodrugs under Brownian motion was analyzed by the NTA, version 1.3 (B196) image analysis software (NanoSight).

2.6. Stability of FA Nanoprodrugs during Long-Term Storage. The stability of the nanoprodrugs was assessed by measuring the nanoprodrug size and concentrations of prodrug molecules after 8-week storage at 4°C.

The size of the nanoprodrugs was measured as described above (Section 2.5). The amount of intact FA prodrugs was assessed by RP-HPLC as follows: the suspensions of nanoprodrugs (100 μ L) were added to acetonitrile (400 μ L) and analyzed using RP-HPLC as described (Section 2.2). The recovery yield was calculated as follows:

$$\text{Recovery yield (\%)} = \frac{\text{Amount of prodrugs after incubation}}{\text{Amount of prodrugs before incubation}} \times 100. \quad (1)$$

The error bar (S.D.) was calculated from triplicate determinations.

2.7. Enzymatic Hydrolysis of FA Nanoprodrugs. The nanoprodrugs were suspended in phosphate buffered saline (PBS, pH 7.4) and esterase (porcine liver, Sigma, code E3019) was added to the final concentration of 5 U/mL. The mixture

was incubated for up to 24 h in a water bath at 37°C. To determine the amount of enzymatically hydrolyzed species of the FA prodrugs, the suspensions of nanoprodrugs (100 μ L) were added to acetonitrile (300 μ L) and analyzed using RP-HPLC as described in Section 2.2.

2.8. Intracellular Uptake of Fluorescent-Labeled FA Nanoprodrug in U87 Glioma Cells. To demonstrate intracellular uptake of the nanoprodrugs, cells were incubated in the presence of fluorescent-labeled nanoprodrugs. Four chamber culture slides (BD Biosciences, Bedford, MA) were seeded with U87 cells, and the cells were allowed to attach for 24 h. The medium was replaced with 1.0 mL of freshly prepared suspension of the fluorescent-labeled nanoprodrugs in medium (0.25 μ g coumarin 6/mL medium), and the chamber slides were incubated for 5 h. To examine the uptake of free dye, cells were incubated in the dye-treated medium. The dye-treated medium was prepared by incubating the medium in the presence of dye (0.25 μ g/mL) for 5 h and sterile filtration. Cells were washed three times with PBS to remove uninternalized nanoprodrugs, one drop of mounting medium with DAPI (Vectashield, Vector Laboratories, Burlingame, CA) was added and then cover slide was placed. For microscopic analysis of intracellular uptake of the fluorescent-labeled nanoprodrugs, a Carl Zeiss Axio Imager Z1 fluorescence microscope equipped with ApoTome (Carl Zeiss MicroImaging, Inc., Thornwood, NY, USA) and Leica DMIRE2 confocal laser-scanning microscope with Confocal Software (Leica Microsystems, Bannockburn, IL, USA) were used. For processing and analysis of the images, AxioVision (Rel. 4.6.3) software (Carl Zeiss) was used. The Carl Zeiss filter with excitation/emission wavelength at 470/525 nm was used.

2.9. Cell Counting. U87-MG human glioma cell line was obtained from American Type Culture Collection (ATCC, Bethesda, MD, USA). The cells were grown and maintained as described in [28]. The glioma cells were seeded at 5×10^4 cells per well in 6-well plates containing 2 mL of culture medium and grown for 24 h. The cells were treated with FA nanoprodrugs for 4 days. After treatment, the culture medium was removed and cells were washed with PBS. 0.5 mL of 0.25% Trypsin/EDTA was added to each well and the detached cells were counted immediately in a hemocytometer. The antiproliferative effect of the nanoprodrugs was presented as a cell number % of control, which was calculated as follows:

$$\text{Cell number \% of control} = \left(\frac{\text{Cell number}_{\text{treated}}}{\text{Cell number}_{\text{control}}} \right) \times 100, \quad (2)$$

where Cell number_{treated} is the number of cells after treatment with nanoprodrugs, and Cell number_{control} is the number of cells of control culture which was incubated with culture medium only. The cells were also treated with control nanosphere prepared from α -tocopherol only. The error bar (SD) was calculated from triplicate determinations.

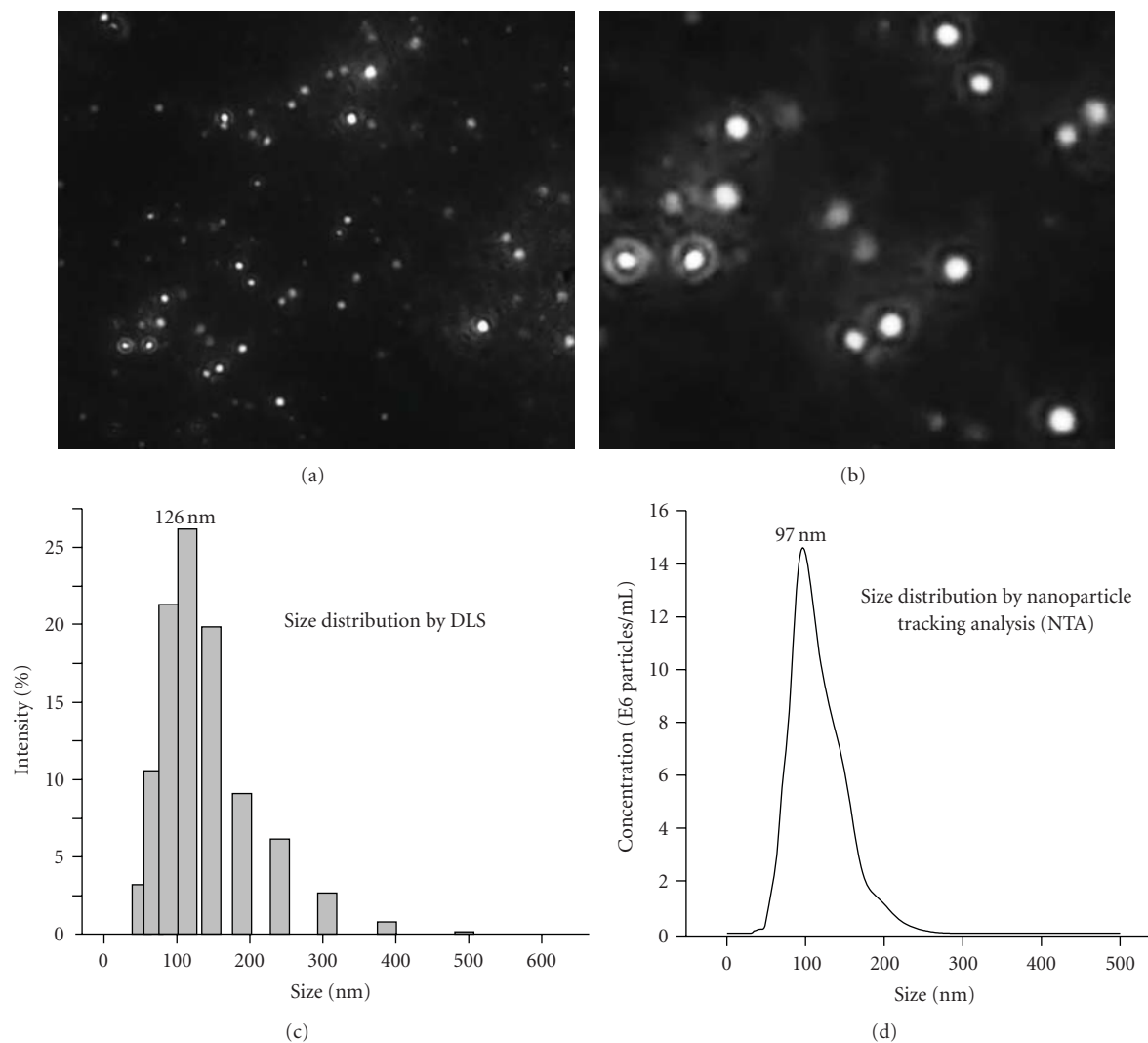


FIGURE 4: Image of FA-TEG-ALA nanoprodrug obtained from nanoparticle tracking analysis (NTA) (a, b) and size distribution of FA-TEG-ALA nanoprodrug as measured by (c) dynamic light scattering (Coulter N4-Plus Submicron Particle Sizer) and (d) NTA. Image (b) is a magnification of a part of the image (a).

2.10. Statistical Analysis. The results were analyzed and expressed as mean \pm standard deviation (S.D.). Statistical analysis of the results was carried out using Student's *t*-test. For all tests, differences with a $P < .05$ were considered to be significant.

3. Results and Discussion

3.1. Preparation of Nanoprodugs of FA. The synthesis of hydrophobic produgs of FA and conversion into nanometer sized produgs (nanoprodugs) offer several advantages which are attributed to the specific characteristics of nanostructures. One of the most remarkable properties of the nanostructured drug and drug delivery system is that a huge surface area is created by transformation of bulk materials into the nanometer-sized. This surface area provides opportunities for chemical and biological interactions between the

drugs and biological molecules/enzymes in the physiological environment, leading to an enhanced therapeutic efficacy of the drugs [29, 30]. These properties of nanostructured biomaterials have been routinely exploited for the development of nanostructured produgs and drug delivery system.

The increase in hydrophobicity through chemical modification is a crucial factor for the preparation of stable nanostructures using spontaneous emulsification. This is because more hydrophobic compounds can be transformed into more stable nanostructures due to the stronger hydrophobic interaction between the molecules. The resulting hydrophobic nanostructures are stable for a prolonged period of time in an aqueous biological environment, mainly due to the insolubility of the hydrophobically modified compounds and hydrophobic interaction, leading to a strong assembly of the molecules [14]. The hydrophobicity and compact structure may reduce the interaction with water, and thus increase the structural integrity of the nanostructures.

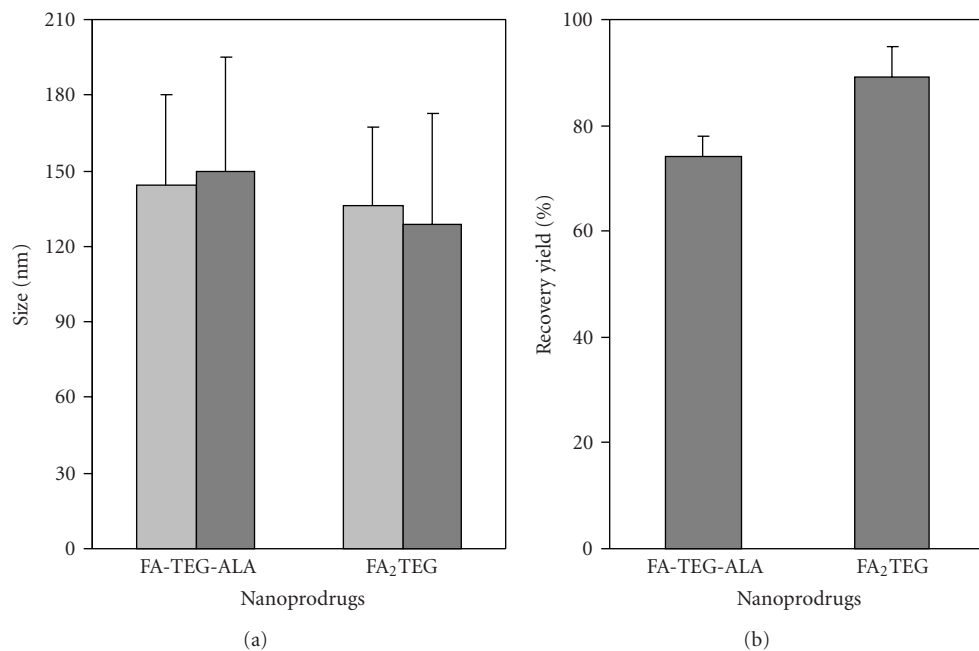


FIGURE 5: Long-term stability of nanoprodugs measured by size (a) and recovery yield (b). Light gray bar: before storage; dark gray bar: after 8 weeks of storage. Monomeric nanoprodug: FA-TEG-ALA; dimeric nanoprodug: FA₂TEG. The results are the mean \pm SD of three experiments.

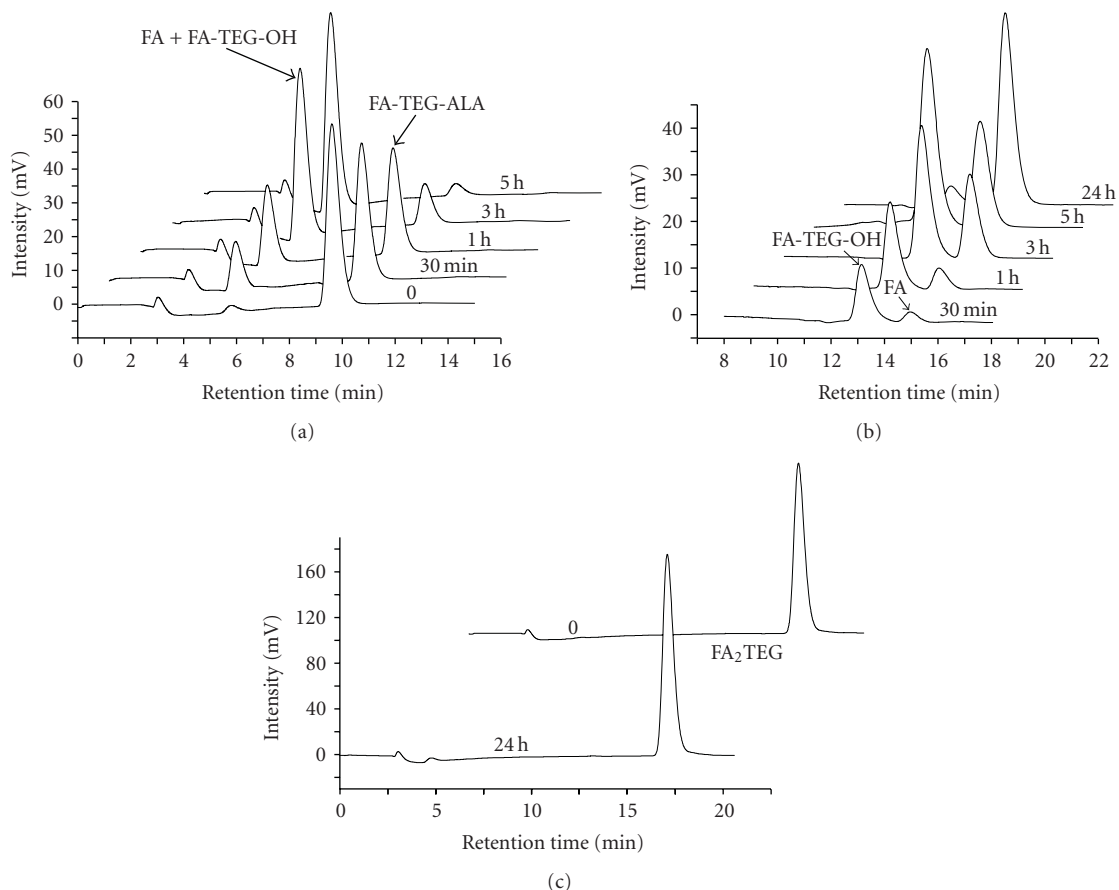


FIGURE 6: Enzymatic hydrolysis of prodrugs FA-TEG-ALA (a, b) and FA₂TEG (c) from nanoprodugs at 37°C. The separation was performed under isocratic condition with a 80/20 (a, c) and 50/50 (b) mixture of acetonitrile/water at a flow rate of 1 mL/min.

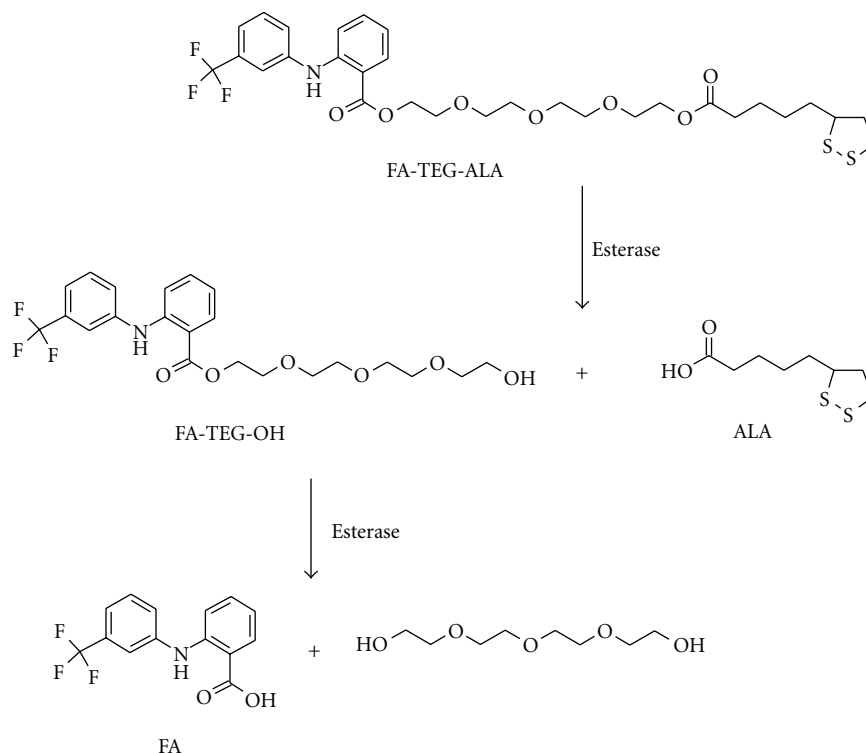


FIGURE 7: Sequence of enzymatic hydrolysis of FA prodrug FA-TEG-ALA.

FA belongs to the acidic NSAIDs that have anti-inflammatory properties linked to COX inhibition [31]. This drug has been reported as an efficient inhibitor of the chlorinating activity of myeloperoxidase (MPO). MPO is a heme-containing enzyme of the peroxidase family that catalyzes the formation of hypochlorous acid (HOCl) in the presence of hydrogen peroxide (H₂O₂) and chloride anions (Cl⁻) in the complex defense system against exogenous aggregations [32, 33]. Klabunde et al. showed that FA, along with several NSAIDs and structurally similar compounds, strongly inhibited the formation of insoluble transthyretin (TTR) amyloid fibrils which is known to cause familial amyloid cardiomyopathy and senile systemic amyloidosis [34].

The monomeric derivative FA-TEG-ALA was synthesized using a two-step synthesis as described in Scheme 1(a). TEG was converted to the mono-ALA derivative ALA-TEG-OH, which was followed by the esterification with FA. The secondary aromatic amine in FA did not interfere with the esterification. The dimeric derivative of FA was synthesized using a one-step procedure (Scheme 1(b)).

The structures were confirmed by ¹H and ¹³C NMR spectroscopy. The ¹H NMR data indicate that the resulting spectra are essentially a composite of FA and TEG in the dimeric derivative and a composite of FA, ALA, and TEG in the monomeric derivative (Figure 2). The amine proton in FA is probably involved in a H-bridge with carbonyl oxygen (C=O) as shown in Figure 2. This proton peak at 9.5 ppm was not observed in the spectrum of free FA (Figure 2(c)). The integral of the H-bridged proton was equivalent to

one proton in FA-TEG-ALA, while it was equivalent to two protons in FA₂TEG, reflecting the one and two FA in the FA-TEG-ALA and FA₂TEG, respectively. The purity of each synthesized compound was analyzed by TLC and RP-HPLC.

3.2. Preparation and Characterization of Nanoprodrugs of FA. The hydrophobic derivatives of FA (Schemes 1(a) and 1(b)) dissolved in acetone spontaneously formed into nanoprodrugs upon the addition into an aqueous solution containing hydrophilic surfactants by spontaneous emulsification process [27, 28, 35–38]. In this study, formulation parameters were kept the same except for the addition of α -tocopherol. In the absence of α -tocopherol the size of the nanoprodrug prepared from the dimeric FA₂TEG was significantly smaller than the size of the nanoprodrug prepared from the monomeric FA-TEG-ALA, suggesting that a more compact spatial arrangement of the symmetrical dimeric derivative led to the formation of the compact and smaller nanoprodrug.

Notably, the retention time of the dimeric FA₂TEG in RP-HPLC was almost twice as much longer than that of the monomeric FA-TEG-ALA, suggesting a higher hydrophobicity of FA₂TEG [39, 40]. It can be assumed that the size decreases with increasing hydrophobicity of the compounds, probably due to a stronger hydrophobic interaction between the molecules. In the presence of α -tocopherol the size of the FA-TEG-ALA nanoprodrug became significantly smaller when compared with the size in the absence of α -tocopherol (Figure 2).

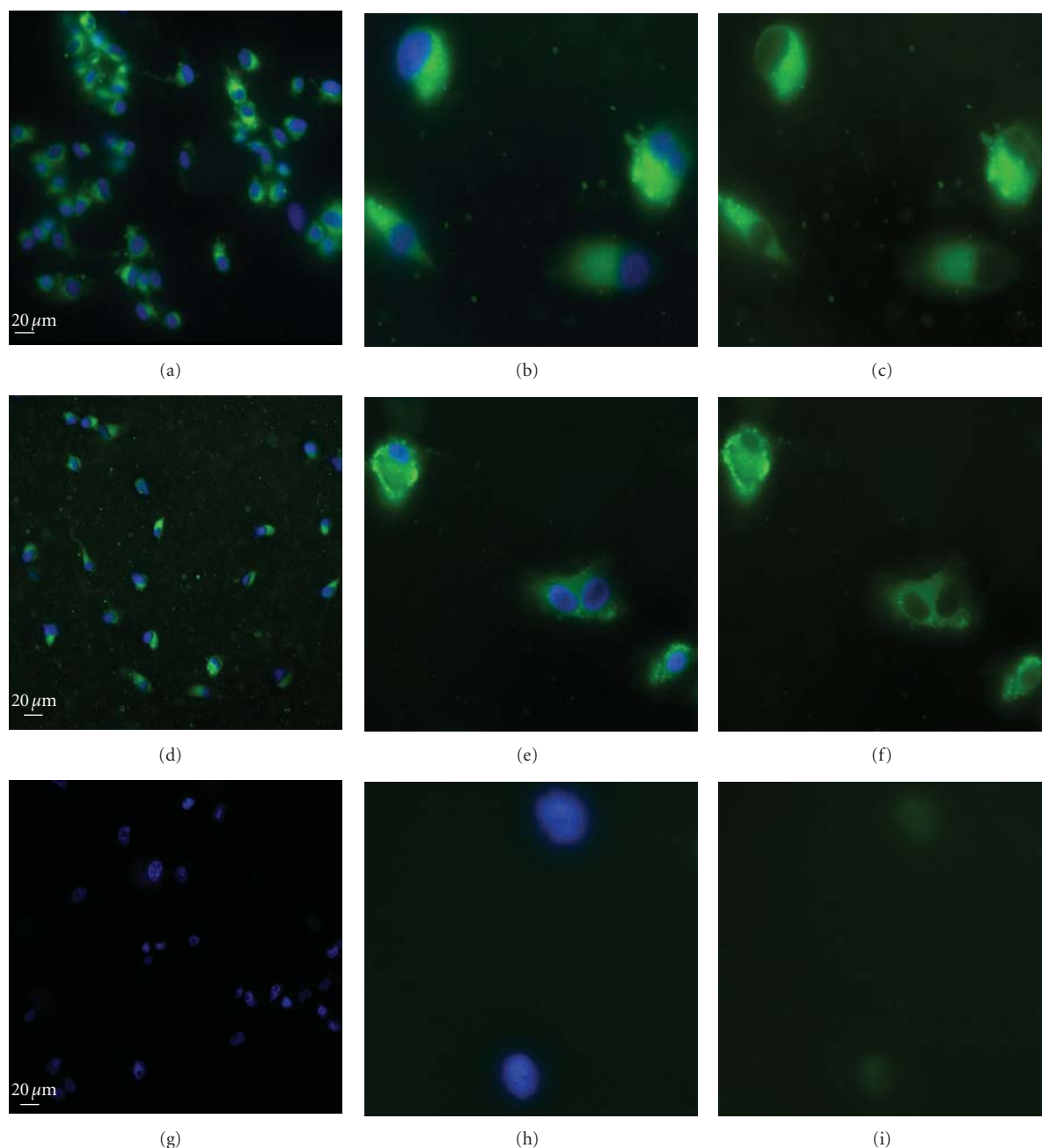


FIGURE 8: Cellular uptake of fluorescent-labeled nanoprodrugs in U87 glioma cells. Cells were incubated with FA-TEG-ALA nanoprodrug ((a)–(c)), FA₂TEG nanoprodrug ((d)–(f)) and in dye-treated medium as control ((g)–(i)). Left and middle panels show images of overlapped fluorescence of DAPI and coumarin 6, left with lower and middle with higher magnification. Right panel shows images of fluorescence of coumarin 6 only.

Interestingly, practically no difference in the size was observed for the FA₂TEG nanoprodrugs in the absence and presence of α -tocopherol. This can be explained by the significant increase in the overall hydrophobicity through the addition of α -tocopherol in the case of FA-TEG-ALA, whereas it was negligible in the case of FA₂TEG, probably due to the significant initial hydrophobicity of FA₂TEG.

In the presence of α -tocopherol the difference in size between the FA₂TEG and FA-TEG-ALA nanoprodrugs became smaller, which is especially crucial when the therapeutic efficacies of the two nanoprodrugs are to be compared. This is because differences in the therapeutic efficacy can be attributed directly to the different prodrug molecules in the nanoprodrugs when the size and other components do not differ significantly from each other. Thus, the nanoprodrugs

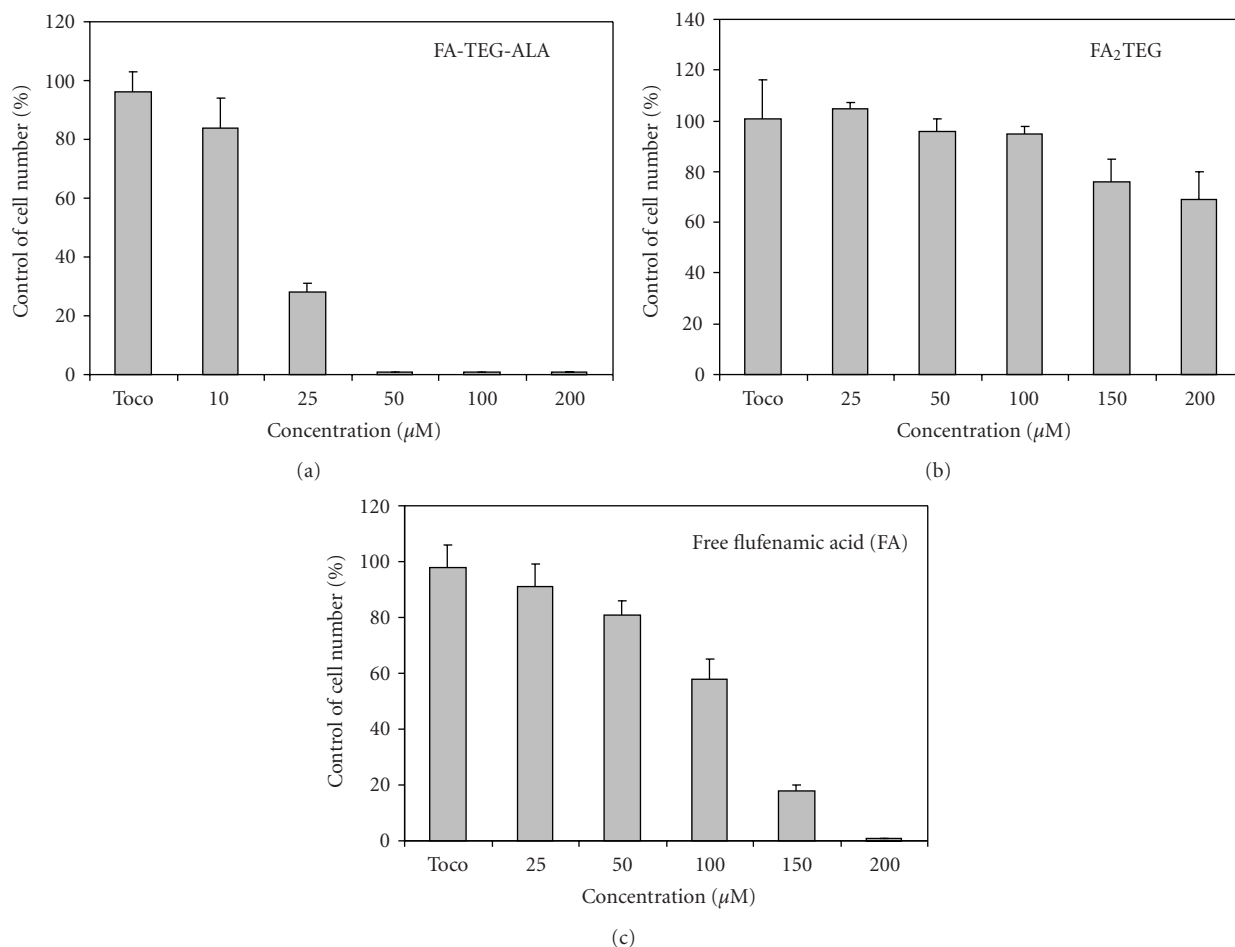


FIGURE 9: Effect of nanoprodrug of FA-TEG-ALA (a), nanoprodrug of FA₂TEG (b), and free flufenamic acid (c) on the viability of U87-MG glioma cells.

were prepared in the presence of α -tocopherol for further experiments.

To give a visualization of the nanoprodrugs, we applied the nanoparticle tracking and analysis (NTA) technique which allows direct and real-time visualization of nanoparticles in a liquid as shown in Figures 4(a) and 4(b) [41].

Whereas dynamic light scattering (DLS) is an ensemble technique that tries to recover a particle size distribution from the combined signal of all particles present in the sample, nanoparticle tracking analysis (NTA) investigates the diffusion of individual particles. Thus, DLS calculates the average particle diameter by measuring fluctuation in scattering intensity, is highly affected by the presence of a few large particles, and tends to be weighted to the larger particles sizes [42]. Indeed, using DLS (Coulter N4-Plus Submicron Particle Sizer) and NTA for an identical FA-TEG-ALA nanoprodrug, the average size calculated by DLS was 126 nm, which was larger than the size calculated by NTA (97 nm) (Figures 4(c) and 4(d)). The comparison of size distribution and average size from DLS and NTA indicate that few larger nanoprodrugs (>300 nm) have significant influence on the size calculation in DLS.

The stability of the nanoprodrugs was assessed by measuring the size and contents of the intact FA prodrug molecules after 8-week storage at 4°C. In this study, the size of the nanoprodrugs remained almost unchanged (Figure 5), and the recovery yield of the prodrugs was 75% and 90% for the FA-TEG-ALA and FA₂TEG, respectively. It is believed that the nanoprodrugs from the more hydrophobic FA₂TEG formed more stable and compact nanostructures, which can be ascribed to the stronger hydrophobic assembly of FA₂TEG. This may reduce the interaction with water, and consequently decrease hydrolytic degradation and increase the structural integrity of the nanoprodrug.

3.3. Enzymatic Hydrolysis of FA Nanoprodrugs. In order to assess the enzymatic prodrug activation from the nanoprodrugs, the rate of enzymatic reconversion of the prodrugs into FA and other degradation products was investigated *in vitro* with porcine liver esterase. As shown in Figure 6(a), FA-TEG-ALA nanoprodrug was activated nearly completely after 5 h of incubation at 37°C, whereas no activation was observed in the FA₂TEG nanoprodrug during the same period of time. This can be attributed to the more

hydrophobic nature of the dimeric FA₂TEG prodrug which makes the interaction between the molecules and enzymes more difficult. In addition, FA is bulkier than ALA, which may increase the steric hindrance towards the enzymes [43, 44]. This assumption was confirmed by the observation that the ALA was first hydrolyzed from FA-TEG-ALA followed by the breakdown of FA-TEG-OH to FA and TEG (Figures 6(c) and 7).

3.4. Intracellular Uptake of Fluorescent-Labeled FA Nanoprodrug in U87 Glioma Cells. In order to demonstrate the cellular uptake of nanoprodrugs, we prepared fluorescent-labeled nanoprodrugs with the hydrophobic dye, coumarin 6. Due to the hydrophobic nature, the dye remained associated with the nanoprodrugs after overnight dialysis and even after the incubation in PBS buffer and cell culture medium [45]. Confocal laser scanning microscopy of U87 glioma cells treated with fluorescent-labeled nanoprodrugs showed strong internalization of the nanoprodrugs within 5 h of incubation. Both nanoprodrugs FA-TEG-ALA (Figures 8(a)–8(c)) and FA₂TEG (Figures 8(d)–8(f)) showed similar cellular uptake, whereas cells incubated in the dye-treated control medium did not show any detectable fluorescence (Figures 8(g)–8(i)).

Some cells showed a stronger accumulation along the membrane area, while other showed more evenly distributed pattern in the cytoplasm. Interestingly, cells contained numerous tiny vesicles that were dispersed in the cytoplasmic compartment. The vesicles are probably endosomal vesicles (endosomes), suggesting that the cellular uptake occurs via endocytosis. Considering the different spatial intensity and localization of the fluorescent signals within the cells, it can be concluded that after endocytosis the nanoprodrugs escape from the endosomes to the cytoplasm and are dispersed evenly throughout the cytoplasm.

3.5. Effect of FA Nanoprodrug on Cell Proliferation. In order to evaluate the effect of FA nanoprodrugs on tumor cell growth, we studied the effect on the cell growth of U87-MG glioma cells. Glioma cells were treated with nanoprodrugs from FA-TEG-ALA and FA₂TEG, and also with FA in the concentration range of 10 to 200 μ M. Cells were also treated with control nanospheres prepared from α -tocopherol only by exposure to an equimolar concentration of α -tocopherol. As shown in Figure 6, the nanoprodrug of FA-TEG-ALA completely inhibited the cell proliferation at the concentration of 50 μ M, whereas the nanoprodrug of FA₂TEG inhibited only 30% at the highest concentration of 200 μ M. These results were well expected because the prodrug FA₂TEG was almost inert towards chemical and enzymatic hydrolysis (Sections 3.2 and 3.3). Based on the results of this study, the stability and biodegradability of the nanoprodrugs may be adjusted to meet the needs for diverse practical applications via modification of prodrug structures. Interestingly, the inhibitory effect of the nanoprodrug FA-TEG-ALA was much higher than that of the FA (Figure 9(c)), suggesting the existence of more efficient cellular delivery mechanism for the nanoprodrug.

4. Conclusion

In this study we showed that hydrophobic derivative of FA can be formed into stable nanoprodrug that is readily activated by hydrolytic enzyme and inhibits the growth of malignant cells, suggesting their potential application as anticancer agents. Nanoprodrugs of FA were prepared by spontaneous emulsification of the monomeric prodrug FA-TEG-ALA and dimeric FA₂TEG, and their antiproliferative effects were demonstrated using U87-MG glioma cells. The nanoprodrug from FA-TEG-ALA inhibited the cell growth significantly and induced cell death, whereas the nanoprodrug from FA₂TEG did not show any comparable effect on cell growth and viability. We demonstrated using fluorescent-labeled nanoprodrugs that both nanoprodrugs FA-TEG-ALA and FA₂TEG showed similar cellular uptake. Obviously, the more potent effect of the monomeric nanoprodrug is due to the higher parent drug concentration which is ascribed to the higher enzymatic activation. In addition, the FA-TEG-ALA nanoprodrug inhibited cell growth more efficiently than free FA, suggesting a delivery mechanism specific to the nanoprodrug. We are currently investigating the mechanisms of the cellular uptake and the molecular events leading to the antiproliferative effect of the FA nanoprodrug.

Acknowledgment

The authors wish to thank Mr. Duncan Griffiths (Nanosight USA) for performing nanoparticle tracking analysis (NTA) and providing many helpful comments.

References

- [1] J. A. Mitchell and T. D. Warner, "Cyclo-oxygenase-2: pharmacology, physiology, biochemistry and relevance to NSAID therapy," *British Journal of Pharmacology*, vol. 128, no. 6, pp. 1121–1132, 1999.
- [2] S. Kargman, S. Charleson, M. Cartwright et al., "Characterization of prostaglandin G/H synthase 1 and 2 in rat, dog, monkey, and human gastrointestinal tracts," *Gastroenterology*, vol. 111, no. 2, pp. 445–454, 1996.
- [3] W. Dempke, C. Rie, A. Grothey, and H. J. Schmolz, "Cyclooxygenase-2: a novel target for cancer chemotherapy?" *Journal of Cancer Research and Clinical Oncology*, vol. 127, no. 7, pp. 411–417, 2001.
- [4] D. B. Fournier and G. B. Gordon, "COX-2 and colon cancer: potential targets for chemoprevention," *Journal of Cellular Biochemistry*, vol. 77, no. 34, pp. 97–102, 2000.
- [5] E. Fosslie, "Molecular pathology of cyclooxygenase-2 in neoplasia," *Annals of Clinical and Laboratory Science*, vol. 30, no. 1, pp. 3–21, 2000.
- [6] J. J. Keller and F. M. Giardiello, "Chemoprevention strategies using NSAIDs and COX-2 inhibitors," *Cancer Biology & Therapy*, vol. 2, supplement 1, no. 4, pp. S140–S149, 2003.
- [7] R. A. Gupta and R. N. DuBois, "Colorectal cancer prevention and treatment by inhibition of cyclooxygenase-2," *Nature Reviews Cancer*, vol. 1, no. 1, pp. 11–21, 2001.
- [8] A. Umar, J. L. Viner, W. F. Anderson, and E. T. Hawk, "Development of COX inhibitors in cancer prevention and therapy," *American Journal of Clinical Oncology*, vol. 26, no. 4, pp. S48–S57, 2003.

- [9] R. E. Harris, J. Beebe-Donk, H. Doss, and D. Burr Doss, "Aspirin, ibuprofen, and other non-steroidal anti-inflammatory drugs in cancer prevention: a critical review of non-selective COX-2 blockade (review)," *Oncology Reports*, vol. 13, no. 4, pp. 559–583, 2005.
- [10] D. W. Lin and P. S. Nelson, "The role of cyclooxygenase-2 inhibition for the prevention and treatment of prostate carcinoma," *Clinical Prostate Cancer*, vol. 2, no. 2, pp. 119–126, 2003.
- [11] J. R. Mann and R. N. DuBois, "Cyclooxygenase-2 and gastrointestinal cancer," *Cancer Journal*, vol. 10, no. 3, pp. 145–152, 2004.
- [12] J. W. Basler, G. A. Piazza, B. Djavan et al., "Nonsteroidal anti-inflammatory drugs and cyclooxygenase-2 selective inhibitors for prostate cancer chemoprevention," *Journal of Urology*, vol. 171, no. 2, part 2, pp. S59–S63, 2004.
- [13] A. L. Sabichi and S. M. Lippman, "COX-2 inhibitors and other nonsteroidal anti-inflammatory drugs in genitourinary cancer," *Seminars in Oncology*, vol. 31, no. 7, pp. 36–44, 2004.
- [14] H. C. Chuang, A. Kardosh, K. J. Gaffney, N. A. Petasis, and A. H. Schönthal, "COX-2 inhibition is neither necessary nor sufficient for celecoxib to suppress tumor cell proliferation and focus formation in vitro," *Molecular Cancer*, vol. 7, article 38, 2008.
- [15] J. Marx, "Anti-inflammatories inhibit cancer growth—but how?" *Science*, vol. 291, no. 5504, pp. 581–582, 2001.
- [16] D. J. E. Elder, D. E. Halton, A. Hague, and C. Paraskeva, "Induction of apoptotic cell death in human colorectal carcinoma cell lines by a cyclooxygenase-2 (COX-2)-selective nonsteroidal anti-inflammatory drug: independence from COX-2 protein expression," *Clinical Cancer Research*, vol. 3, no. 10, pp. 1679–1683, 1997.
- [17] H. Jiang, J. J. Lin, Z. Z. Su, N. I. Goldstein, and P. B. Fisher, "Subtraction hybridization identifies a novel melanoma differentiation associated gene, mda-7, modulated during human melanoma differentiation, growth and progression," *Oncogene*, vol. 11, no. 12, pp. 2477–2486, 1995.
- [18] B. J. R. Whittle, "Gastrointestinal effects of nonsteroidal anti-inflammatory drugs," *Fundamental and Clinical Pharmacology*, vol. 17, no. 3, pp. 301–313, 2003.
- [19] G. Dannhardt and W. Kiefer, "Cyclooxygenase inhibitors—current status and future prospects," *European Journal of Medicinal Chemistry*, vol. 36, no. 2, pp. 109–126, 2001.
- [20] V. K. Tammara, M. M. Narurkar, A. M. Crider, and M. A. Khan, "Synthesis and evaluation of morpholinoalkyl ester prodrugs of indomethacin and naproxen," *Pharmaceutical Research*, vol. 10, no. 8, pp. 1191–1199, 1993.
- [21] F. P. Bonina, C. Puglia, T. Barbuzzi et al., "In vitro and in vivo evaluation of polyoxyethylene esters as dermal prodrugs of ketoprofen, naproxen and diclofenac," *European Journal of Pharmaceutical Sciences*, vol. 14, no. 2, pp. 123–134, 2001.
- [22] S. Chandrasekaran, A. M. Al-Ghananeem, R. M. Riggs, and P. A. Crooks, "Synthesis and stability of two indomethacin prodrugs," *Bioorganic and Medicinal Chemistry Letters*, vol. 16, no. 7, pp. 1874–1879, 2006.
- [23] I. C. Siskou, E. A. Rekkas, A. P. Kourounakis, M. C. Chrysselis, K. Tsiakitzis, and P. N. Kourounakis, "Design and study of some novel ibuprofen derivatives with potential nootropic and neuroprotective properties," *Bioorganic and Medicinal Chemistry*, vol. 15, no. 2, pp. 951–961, 2007.
- [24] C. A. Velázquez, P. N. Praveen Rao, M. L. Citro, L. K. Keefer, and E. E. Knaus, "O²-acetoxymethyl-protected diazeniumdiolate-based NSAIDs (NONO-NSAIDs): synthesis, nitric oxide release, and biological evaluation studies," *Bioorganic and Medicinal Chemistry*, vol. 15, no. 14, pp. 4767–4774, 2007.
- [25] M. Weiner and I. L. Bernstein, *Adverse Reactions to Drug Formulation Agents*, Marcel Dekker, New York, NY, USA, 1989.
- [26] S. C. Gad, *Drug Safety Evaluation*, chapter 13.8, John Wiley & Sons, New York, NY, USA, 2002.
- [27] B. S. Lee, X. Yuan, Q. Xu et al., "Stimuli-responsive antioxidant nanoprodrugs of NSAIDs," *International Journal of Pharmaceutics*, vol. 372, no. 1–2, pp. 112–124, 2009.
- [28] B. S. Lee, X. Yuan, Q. Xu et al., "Nanoprodrugs of NSAIDs inhibit the growth of U87-MG glioma cells," *Journal of Nanomaterials*, vol. 2010, Article ID 583970, 2010.
- [29] B. Huang, J. Zhang, J. Hou, and C. Chen, "Free radical scavenging efficiency of Nano-Se in vitro," *Free Radical Biology and Medicine*, vol. 35, no. 7, pp. 805–813, 2003.
- [30] E. G. Heckert, A. S. Karakoti, S. Seal, and W. T. Self, "The role of cerium redox state in the SOD mimetic activity of nanoceria," *Biomaterials*, vol. 29, no. 18, pp. 2705–2709, 2008.
- [31] P. van Antwerpen, F. Dufresne, M. Lequeux et al., "Inhibition of the myeloperoxidase chlorinating activity by non-steroidal anti-inflammatory drugs: flufenamic acid and its 5-chloro-derivative directly interact with a recombinant human myeloperoxidase to inhibit the synthesis of hypochlorous acid," *European Journal of Pharmacology*, vol. 570, no. 1–3, pp. 235–243, 2007.
- [32] J. Arnhold, P. G. Furtmüller, and C. Obinger, "Redox properties of myeloperoxidase," *Redox Report*, vol. 8, no. 4, pp. 179–186, 2003.
- [33] P. G. Furtmüller, U. Burner, W. Jantschko, G. Regelsberger, and C. Obinger, "Two-electron reduction and one-electron oxidation of organic hydroperoxides by human myeloperoxidase," *FEBS Letters*, vol. 484, no. 2, pp. 139–143, 2000.
- [34] T. Klabunde, H. M. Petrassi, V. B. Oza, P. Raman, J. W. Kelly, and J. C. Sacchettini, "Rational design of potent human transthyretin amyloid disease inhibitors," *Nature Structural Biology*, vol. 7, no. 4, pp. 312–321, 2000.
- [35] K. Bouchemal, S. Briançon, E. Perrier, H. Fessi, I. Bonnet, and N. Zydowicz, "Synthesis and characterization of polyurethane and poly(ether urethane) nanocapsules using a new technique of interfacial polycondensation combined to spontaneous emulsification," *International Journal of Pharmaceutics*, vol. 269, no. 1, pp. 89–100, 2004.
- [36] K. Bouchemal, S. Briançon, E. Perrier, and H. Fessi, "Nano-emulsion formulation using spontaneous emulsification: solvent, oil and surfactant optimisation," *International Journal of Pharmaceutics*, vol. 280, no. 1–2, pp. 241–251, 2004.
- [37] F. Chouinard, F. W. K. Kan, J. C. Leroux, C. Foucher, and V. Lenaerts, "Preparation and purification of polyisohexylcyanoacrylate nanocapsules," *International Journal of Pharmaceutics*, vol. 72, no. 3, pp. 211–217, 1991.
- [38] H. Fessi, F. Piusieux, J. Ph. Devissaguet, N. Ammoury, and S. Benita, "Nanocapsule formation by interfacial polymer deposition following solvent displacement," *International Journal of Pharmaceutics*, vol. 55, no. 1, pp. R1–R4, 1989.
- [39] W. E. Hammers, G. J. Meurs, and C. L. de Ligny, "Correlations between liquid chromatographic capacity ratio data on lichrosorb RP-18 and partition coefficients in the octanol-water system," *Journal of Chromatography A*, vol. 247, no. 1, pp. 1–13, 1982.
- [40] T. L. Hafkenscheid and E. Tomlinson, "Relationships between hydrophobic (lipophilic) properties of bases and their retention in reversed-phase liquid chromatography using aqueous methanol mobile phases," *Journal of Chromatography A*, vol. 292, no. 2, pp. 305–317, 1984.

- [41] B. Carr, P. Hole, A. Malloy, P. Nelson, M. Wright, and J. Smith, "Applications of nanoparticle tracking analysis in nanoparticle research: a mini review," *European Journal of Pharmaceutical Sciences*, vol. 14, pp. 45–50, 2009.
- [42] V. Filipe, A. Hawe, and W. Jiskoot, "Critical evaluation of nanoparticle tracking analysis (NTA) by NanoSight for the measurement of nanoparticles and protein aggregates," *Pharmaceutical Research*, vol. 27, no. 5, pp. 796–810, 2010.
- [43] J. Iley, R. Moreira, T. Calheiros, and E. Mendes, "Acyloxymethyl as a drug protecting group: part 4. The hydrolysis of tertiary amidomethyl-ester prodrugs of carboxylic acid agents," *Pharmaceutical Research*, vol. 14, no. 11, pp. 1634–1639, 1997.
- [44] P. R. Redden, R. L. Melanson, J. A. E. Douglas, and A. J. Dick, "Acyloxymethyl acidic drug derivatives: in vitro hydrolytic reactivity," *International Journal of Pharmaceutics*, vol. 180, no. 2, pp. 151–160, 1999.
- [45] S. K. Sahoo and V. Labhasetwar, "Enhanced antiproliferative activity of transferrin-conjugated paclitaxel-loaded nanoparticles is mediated via sustained intracellular drug retention," *Molecular Pharmaceutics*, vol. 2, no. 5, pp. 373–383, 2005.

Research Article

Encapsulation of Protein-Polysaccharide HIP Complex in Polymeric Nanoparticles

Ripal Gaudana, Varun Khurana, Ashwin Parenky, and Ashim K. Mitra

*Division of Pharmaceutical Sciences, School of Pharmacy, University of Missouri-Kansas City,
2464 Charlotte Street, Kansas City, MO 64108-2718, USA*

Correspondence should be addressed to Ashim K. Mitra, mitraa@umkc.edu

Received 17 December 2010; Accepted 18 February 2011

Academic Editor: Giorgia Pastorin

Copyright © 2011 Ripal Gaudana et al. This is an open access article distributed under the Creative Commons Attribution License, which permits unrestricted use, distribution, and reproduction in any medium, provided the original work is properly cited.

The objective of the present study is to formulate and characterize a nanoparticulate-based formulation of a macromolecule in a hydrophobic ion pairing (HIP) complex form. So far, HIP complexation approach has been studied only for proteins with molecular weight of 10–20 kDa. Hence, we have selected bovine serum albumin (BSA) having higher molecular weight (66.3 kDa) as a model protein and dextran sulphate (DS) as a complexing polymer to generate HIP complex. We have prepared and optimized the HIP complex formation process of BSA with DS. Ionic interactions between basic amino acids of BSA with sulphate groups of DS were confirmed by FTIR analysis. Further, nanoparticles were prepared and characterized with respect to size and surface morphology. We observed significant entrapment of BSA in nanoparticles prepared with minimal amounts of PLGA polymer. Finally, results of circular dichroism and intrinsic fluorescence assay have clearly indicated that HIP complexation and method of nanoparticle preparation did not alter the secondary and tertiary structures of BSA.

1. Introduction

Protein-based therapeutics such as antibodies, blood derived products, and vaccines have been widely investigated in the past decade to treat a variety of disorders [1]. Development of a nanoparticulate-based dosage form of these molecules is still considered as a major challenge by scientists in the drug delivery field. Single emulsion (O/W), double emulsion (W/O/W), and emulsion polymerization have been widely employed to prepare nanoparticles. Except emulsion polymerization, the other two methods (single and double emulsion) employ organic solvents and sonication during nanoparticle preparation. Protein-based therapeutics tend to exhibit rapid denaturation and conformational change due to sonication and exposure to organic solvents [2, 3]. These molecules may aggregate and eventually lose their biological activity due to physical and chemical stress observed during formulation development, for example, exposure to organic solvents and sonication. These molecules may also denature or lose their biological activity during storage and lyophilization [4–6]. Sonication is employed to ensure homogeneous dispersion of an emulsion. However, sonication may result

in large pressure and temperature gradient which may cause denaturation and aggregation of the protein molecule [7]. Moreover, sonication also causes generation of high shear force and free radicals which cause protein denaturation [7]. Organic solvents preferentially interact with nonpolar amino acids of protein via hydrophobic interactions. Normally, these nonpolar amino acids are present in the core of the protein structure. As a result, in presence of organic solvents, the native structure and conformation of the protein can be altered. This process may result in loss of biological activity of a protein molecule. Another crucial formulation-related limitation of protein molecules is their hydrophilicity. Due to their hydrophilic nature, these molecules often partition poorly into the polymeric matrix during encapsulation resulting in minimal loading in nanoparticles [1]. Due to poor loading of these molecules, a higher amount of polymer is needed to develop a formulation. Poly lactic-co-glycolic acid (PLGA) is one of the most widely employed biocompatible and biodegradable polymers utilized in the preparation of nanoparticles. However, higher amounts of PLGA can lower the stability of protein molecules as protein molecules were found to be unstable in presence of lactic acid

and glycolic acid which are degradation products of PLGA [6, 8, 9].

Hydrophobic ion pairing (HIP) complexation based approach has gained wide acceptance in the delivery of peptide and protein based therapeutics [10–14]. In this approach, ionizable functional groups of a drug molecule are ionically complexed with a surfactant or polymer with oppositely charged functional groups. The resulting drug-polymer or drug-surfactant complex is known as HIP complex. Since the hydrophilic protein molecule exists in a complex form which is relatively hydrophobic, its partition into the polymeric matrix can be significantly enhanced during encapsulation [10, 15]. Protein and polymer (used for HIP complexation) primarily interact due to ionic interactions resulting in the formation of a HIP complex. The complex can dissociate in presence of oppositely charged ions. Further, HIP complexation would obviate the use of any covalent modification in proteins to impart these molecules more hydrophobicity. Covalent modifications may also result in irreversible loss in the biological activity of these molecules. Various studies have been performed in the past to understand the nature of protein-surfactant interactions. HIP complexation approach has been studied with various peptide and protein based therapeutics such as leuprolide, insulin, melittin, lysozyme, and so forth [10–13]. HIP complexation of protein-based therapeutics has been attempted to overcome various barriers associated with delivery of protein molecules such as bioavailability and stability [13, 16]. Moreover, HIP complexation can also impart conformational stability to the protein molecule [13].

HIP complexation of large protein molecules is challenging primarily due to following reasons. Large molecules usually contain many groups with opposite charges which may hinder the complexation process. So far, basic amino acids have been employed (mainly lysines and arginines) to form a HIP complex with anionic surfactant molecules. However, in large protein, aspartic acid and glutamic acid are also present on the surface in significant numbers which would repel the negatively charged complexing molecules. Second, in a large molecule, charge density plays a very crucial role. There is usually more surface area per charge in a large protein than for a small protein molecule. Hence, selection of a surfactant or polymer with an appropriate chain length is necessary to form the HIP complex. Activity of a protein molecule also depends on its secondary and tertiary structures. These structures are stabilized by various noncovalent interactions such as electrostatic interactions, hydrogen bonds, Van der Waals forces, and hydrophobic interactions [17–19]. Hence, a complexing agent which would not perturb the secondary and tertiary structure of the protein must be selected. So far, various surfactant molecules have been selected to prepare HIP complex. In the present study, we have investigated HIP complex formation by employing dextran sulphate, a polysaccharide-based molecule.

Bovine serum albumin (BSA) is a 66.3 kDa molecule. It is globular in shape and has been widely used as a model protein [20, 21]. Dextran sulphate, (DS, molecular weight: 9–20 kDa), a polysaccharide-based polymer, has been selected for complexation. In this paper, HIP complex of BSA with DS

has been described. Solid in oil in water (S/O/W) emulsion method has been employed to prepare nanoparticles. After preparation, nanoparticles have been characterized with respect to particle size and surface morphology. Finally, the effect of HIP complexation and nanoparticle preparation on the secondary and tertiary structure of BSA has been studied by circular dichroism and intrinsic fluorescence assay, respectively.

2. Materials and Method

Materials: Bovine serum albumin, dextran sulfate sodium salt (molecular weight 9000–20000 da), Poly (DL-lactide-co-glycolide) (PLGA 85:15, molecular weight of 50,000–75,000 da), bicinchoninic acid (BCA), and copper sulphate were procured from Sigma Aldrich. Micro-BCA protein assay kit was purchased from Thermo scientific. All the solvents and other reagents of analytical grade were purchased from local suppliers and used as received without any further purification. Double distilled water (DDW) was used throughout the entire study.

2.1. Preparation of HIP Complex of BSA and DS. Stock solutions of BSA and DS were prepared in citrate buffer pH 4.4 and DDW, respectively. BSA consists of various basic amino acids (60 lysine and 26 arginine residues) while DS contains 2.3 sulphate groups per glucosyl residue. HIP complex was formed spontaneously as both the aqueous solutions were mixed.

2.2. Effect of Different Molar Ratios of DS to BSA on HIP Complex Formation. Stock solutions of BSA and DS were prepared as mentioned earlier. HIP complexes were prepared in different molar ratios of DS/BSA. The molar ratios studied were 0.29, 0.58, 0.87, and 1.15. These molar ratios represent the addition of different amounts of DS into previously prepared BSA solution (5 mg/mL in pH 4.4 citrate buffer). Once formed, HIP complex was vigorously vortexed for 3 minutes followed by centrifugation at 10000 RPM for 10 minutes to separate the supernatant. Uncomplexed BSA was measured in the supernatant using BCA assay. Percentage of complexed BSA was calculated according to the following equation:

% Complexed BSA

$$= \left[\frac{\text{Initial amount of BSA} - \text{amount of BSA in supernatant}}{\text{Initial amount of BSA}} \right] * 100. \quad (1)$$

2.3. Dissociation of BSA from HIP Complex. Dissociation of BSA from HIP complex was studied to characterize the nature of interaction between BSA and DS. Freeze dried complex containing 5 mg of BSA was accurately weighed and incubated in presence of DI water and aqueous solution containing 10 mM Na₂HPO₄. These solutions were vortexed and kept for equilibrium for 3 hrs at room temperature. After

3 hrs, these solutions were subjected to centrifugation and supernatant was collected. The concentration of dissociated protein in the supernatant was then measured with BCA assay.

2.4. FTIR Study. FTIR analysis of BSA, DS, and HIP complex was carried out with an infrared spectrophotometer (Perkin-Elmer, Waltman, MA). The samples were brought into intimate contact with the diamond crystal by applying a loading pressure. Samples were casted on diamond crystal top-plate of Attenuated Total Reflectance (ATR) accessory and scanned between 650–1800 cm^{-1} . Spectra obtained using this device represents the average of 32 individual scan possessing a spectral resolution of 4 cm^{-1} .

2.5. Preparation of Nanoparticles. PLGA 85:15 was used as a polymer to prepare nanoparticles. Nanoparticles were prepared by using solid in oil in water (S/O/W) emulsion method published earlier with minor modifications [15]. Briefly, 5 mg of BSA in complex form was used for preparation of nanoparticles. PLGA 85:15 was dissolved in methylene chloride. Two different ratios of BSA: PLGA 85:15 (1:5 and 1:10) were employed to prepare the nanoparticles. PLGA solution was gradually added to the earlier prepared HIP complex. Total volumes of methylene chloride and vortexing time were optimized to obtain S/O dispersion. About 4-5 mL of methylene chloride was required to completely disperse the HIP complex. Sonication was performed for about ≈ 3 minutes using tip sonicator (Fisher 100 Sonic dismembrator, Fisher Scientific) at power output of 25–30 W to obtain the fine S/O dispersion. To this S/O dispersion, external aqueous phase (30 mL, 1% PVA) was added followed by further sonication for ≈ 3 -4 minutes. This procedure resulted in S/O/W nanoemulsion which was kept on a shaker bath at room temperature for 15–20 minutes followed by complete evaporation of methylene chloride using a Rotavap. Following evaporation, the nanodispersion was centrifuged for 50 minutes at 22,000 g. Nanoparticles were washed two times with DI water to remove any surface bound BSA and PVA. Similarly, blank nanoparticles were also prepared by employing only polymer (PLGA 85:15) in similar amounts.

2.6. Characterization of Nanoparticles

2.6.1. Entrapment Efficiency of Nanoparticles. Entrapment efficiency was measured according to an earlier published protocol [20, 21] with minor modifications. Briefly, 1 mL of nanosuspension was added to 9 mL of methylene chloride solution which was then vortexed for 10–15 minutes to dissolve the polymer completely. Later, this solution was subjected to centrifugation which resulted in formation of a protein pellet. Methylene chloride was carefully separated and the pellet was dissolved in 10 mL of PBS buffer. Concentration of BSA in the aqueous phase was measured using Micro-BCA assay. Absorbance from the samples were corrected by subtracting the absorbance from blank nanoparticles prepared using PLGA 85:15.

2.6.2. Particle Size Measurement. Previously published protocol [15] was followed to measure the mean particle size and polydispersity of nanoparticles using a DLS instrument (Brookhaven Inst. Co., USA). Particle size analysis was carried out at an operating angle of 90°C and temperature of 25°C . A dilute sample of the nanosuspension was taken for particle size analysis, and at least three measurements of each batch were carried out.

2.7. SEM and TEM Analysis. For SEM analysis, freeze dried specimen was applied on a sticky carbon film positioned on an aluminum stub. Specimens were sputter coated with gold-palladium and observed with the field-emission SEM XL30 (FEI, Hillsboro, OR). For TEM study, a drop of nanosuspension was deposited on TEM cooper grid with carbon film. After drying, it was observed under Phillips TEM CM12 (FEI, Hillsboro, OR).

2.8. Evaluation of Secondary Structure of BSA after Dissociation from HIP Complex and Release from Nanoparticles with Circular Dichroism. HIP complex was dissociated in presence of 1 mL of 10 mM Na_2HPO_4 solution, and free BSA was quantified using BCA assay. Previously prepared PLGA nanoparticles were incubated in presence of 1 mL of 10 mM Na_2HPO_4 solution and kept overnight. BSA released from the nanoparticle formulation was quantified on the following day with BCA assay. Finally, standard solution of BSA was prepared in 10 mM Na_2HPO_4 solution and used as a control. Final concentration of each sample was adjusted to 0.05 mg/mL. Circular dichroism (CD) spectra were collected using Jasco 720 spectropolarimeter at room temperature. The spectra of all the samples were collected over a range of 200–250 nm with a cuvette of 1 cm path length at a scan speed of 20 nm/min. Data was further processed for blank subtraction and noise reduction and an average of three signals was recorded. All CD measurements are reported as ellipticities (θ , mdeg).

2.9. Evaluation of Tertiary Structure of BSA after Dissociation from HIP Complex and Release from Nanoparticles with Intrinsic Fluorescence Assay. Fluorescent measurements were carried out at room temperature with fluorescence spectrophotometer (Photon Technology International). The procedure to recover BSA after dissociation of HIP complex and from nanoparticles has been mentioned previously. Standard and test samples were prepared in 10 mM Na_2HPO_4 solution (final BSA concentration was adjusted to 0.1 mg/mL). We compared fluorescence spectra of standard with BSA obtained after dissociation from HIP complex and BSA released from nanoparticles. All samples were excited at a wavelength of λ_{ex} 295 nm, and emission spectra were collected between 310–400 nm. λ_{ex} 295 nm was chosen to selectively excite tryptophan amino acid of BSA. Quartz cells (12.5 L \times 12.5 mm W) having 3 mL of sample capacity were used for measurement. Fluorescent emission spectra were recorded and are displayed in terms of relative fluorescence.

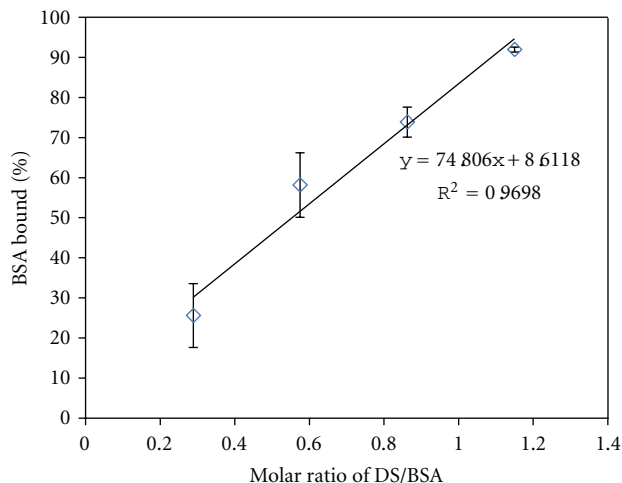


FIGURE 1: Effect of molar ratio of DS:BSA on HIP complex formation.

3. Result and Discussion

Proteins and peptides represent a rapidly growing class of therapeutic drugs with more than 200 biopharmaceuticals in the market and many more at different stages of development. Design of nanoparticle-based formulations for protein-based therapeutics has become a major challenge for drug delivery scientists because of poor encapsulation in polymeric matrix and rapid denaturation in presence of organic solvents and sonication [2, 3]. HIP complexation based approach can be explored to deliver peptide and protein-based therapeutics. It can overcome various stability related issues, enhance drug loading in nanocarriers and improve drug permeation across biological membrane [10–14, 22]. So far, HIP complex based approach has been only studied with small peptide and protein-based therapeutics. Hence, BSA was selected as a model protein in the present study because of its higher molecular weight (66.3 kDa) and well-known secondary and tertiary structure.

Isoelectric point (pI) of BSA is ≈ 4.5 , and the protein consists of various basic amino acids (60 lysine and 26 arginine residues). Hence, we have slightly altered the pH of BSA solution and prepared stock solution of BSA at pH 4.4 in citrate buffer. Being hydrophilic in nature, these amino acids are mostly found on the protein surface. Amino groups of these basic amino acids are protonated based on the pH of surrounding medium. At this pH, HIP complex was formed immediately upon mixing of aqueous solutions of BSA and DS. This data confirms the importance of pH of the protein solution prior to HIP complexation. In general, it is crucial to understand the effect of pH on stability of protein molecule. One should also consider the possibility of other stability related issues which may arise by changing the pH of protein solution prior HIP complexation.

The effect of molar ratios of DS/BSA on HIP complex formation has been studied. We calculated the molar ratios based on the total number of lysine amino acids present on the surface of BSA (60 lysine amino acid). HIP complexes

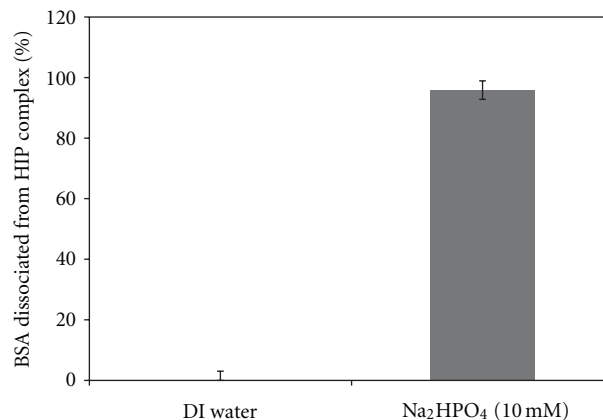


FIGURE 2: Comparative dissociation of BSA from HIP complex in the presence of DI water and 10 mM Na₂HPO₄ solution.

were prepared using the following molar ratios of DS/BSA (0.29, 0.58, 0.87, and 1.15). Theoretically, these molar ratios represent the amounts of DS added which was sufficient to complex with 15, 30, 45, and 60 basic amino acids of BSA. Figure 1 shows the complexation of BSA with DS at different molar ratios. An excellent correlation is observed between increments in the molar ratio of DS/BSA with the amount of BSA complexed with DS (Figure 1). In fact at a molar ratio of 1.15, more than 90% of BSA molecules were ionically complexed with DS. This data clearly indicates the involvement of basic amino acids in the formation of HIP complex.

We also hypothesized ionic interactions as a driving force for complexation of BSA with DS. In order to confirm our hypothesis, we performed dissociation studies of the HIP complex in presence of oppositely charged ions (HPO₄²⁻). Results of this experiment are shown in Figure 2. When HIP complex was incubated in DI water, no dissociation of BSA from HIP complex was observed. This could be due to low ionic strength of DI water. However, the presence of 1 mL of 10 mM Na₂HPO₄ solution caused complete dissociation of the HIP complex and the solution became clear. These data further confirm the presence of ionic interactions between amino group of basic amino acids in BSA and sulphate group of DS. Dissociation of HIP complex in presence of counter ions has also been reported by other investigators [13, 15].

FTIR study was performed to understand the nature of interactions between amino group of basic amino acids in BSA and sulphate group of DS. FTIR analysis was performed by other investigators to characterize ionic interactions between oppositely charged functional groups [12, 23, 24]. Due to overlapping shift in a FTIR spectrum, we did not follow peak shift associated with the protein. Instead, the interaction of sulphate group of DS was studied in the IR region. Following are the characteristic peaks of sulphate group of DS in the IR region: (a) 802 cm⁻¹: S-O-S vibration, (b) 1017 cm⁻¹: symmetric SOO⁻ stretching vibration, and (c) 1225 cm⁻¹: asymmetric SOO⁻ stretching vibration. Appearance of these peaks in the IR spectra is close to previously published results [23–25]. Due to ionic

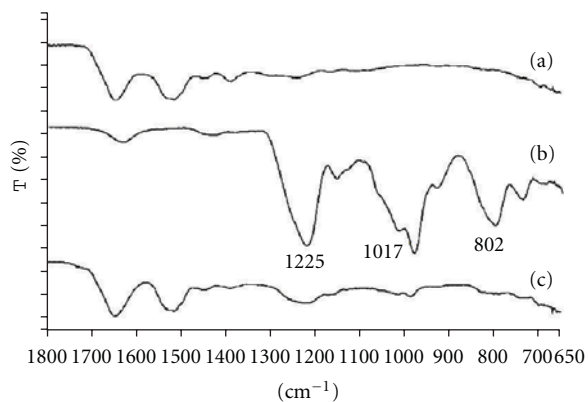


FIGURE 3: FTIR spectra of (a) BSA, (b), DS and (c) HIP complex.

TABLE 1: Particle size, polydispersity, and entrapment efficiency of different batches of nanoparticles. Values are given as means \pm SD ($n = 3$).

Ratio of BSA to PLGA 85 : 15	Particle size (nm)	Polydispersity	% Entrapment efficiency
1 : 5	193.4 \pm 3.1 nm	0.011	67.8 \pm 8.6
1 : 10	201.6 \pm 2.2 nm	0.010	79.7 \pm 4.1

interaction between amino and sulphate groups in HIP complex, the peak intensity of the sulphate group in the IR region may be attenuated significantly. Results of this study are shown in Figure 3. These results clearly indicate a significant reduction in the peak intensities of sulphate group in the IR region which again confirmed the presence of ionic interactions between amino and sulphate groups in the HIP complex.

We prepared nanoparticles of the complex using S/O/W emulsion method. This method of preparation offers significant advantages over conventional methods of nanoparticles preparation such as single and double emulsion method. In the conventional methods of preparation, protein is initially dissolved in an aqueous phase and later emulsified in the presence of an organic phase using sonication. Most protein denaturation occurs during this stage of nanoparticle preparation due to water-organic phase interface. Excessive stress during sonication process and generation of free radicals can cause protein unfolding and denaturation. In S/O/W emulsion method, protein-polysaccharide powder was employed in the preparation of nanoparticles instead of protein in solution form. Further, in the powder form, kinetic mobility of the protein is restricted compared to solution form [20, 21]. Moreover, complexation with DS would not only restrict conformational flexibility of BSA but would also impart additional *steric shielding* to the protein molecule. We optimized the total volume of organic solvent needed and the sonication time to prepare nanoparticles. Nanoparticles were also characterized with respect to particle size (Table 1) which range between 150–200 nm. SEM and TEM studies were performed to study the surface morphology. Results of these studies are shown in Figures 4 and

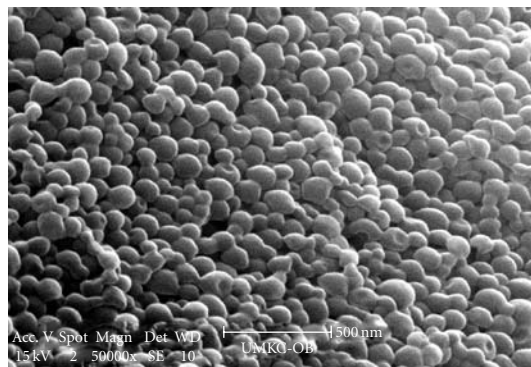


FIGURE 4: SEM images of nanoparticles.

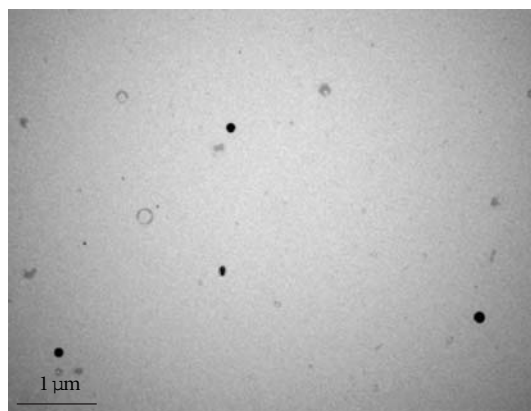


FIGURE 5: TEM images of nanoparticles.

5, respectively. These results confirmed that particles have smooth surface and spherical shape.

One of the important goal of the present study was to achieve higher encapsulation of BSA in nanoparticles by employing minimal amounts of polymer (PLGA 85 : 15). Nanoparticles were prepared by employing two different ratios of protein: PLGA (1 : 5 and 1 : 10). BSA entrapment in nanoparticles was more than 65% in both cases (Table 1). This data clearly shows a significant entrapment of BSA in PLGA matrix. As the amount of PLGA was increased to prepare nanoparticles, entrapment of BSA in nanoparticles was enhanced as well. This could be attributed to enhanced hydrophobic interactions of BSA in HIP complex with PLGA polymer. Due to these hydrophobic interactions, partition of BSA (in HIP complex form) in the polymeric matrix of PLGA was also significantly enhanced.

The effect of HIP complexation and nanoparticle preparation on secondary structure of BSA was evaluated by CD spectra. Weak physical interactions such as electrostatic interactions, hydrogen bonds, Van-der-waals forces, and hydrophobic interactions stabilize secondary structure of the protein. During HIP complex formation, DS interacts extensively with BSA which involves abovementioned forces. So, it is quite possible that DS has altered the native conformation of BSA. Similarly, during nanoparticle preparation, powder form of BSA-DS complex was sonicated in

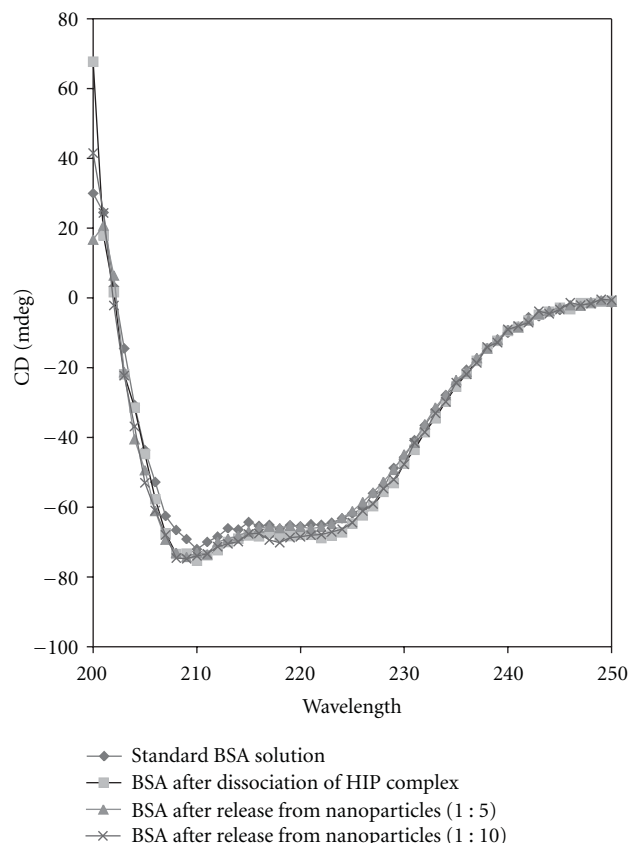


FIGURE 6: CD spectra of standard solution of BSA, BSA recovered after dissociation from HIP complex and BSA after release from different batches of nanoparticles.

presence of organic solvents. These processes could possibly denature BSA. CD analysis was performed to understand the impact of these formulation factors on secondary structure of BSA. Freshly prepared BSA in 10mM Na_2HPO_4 solution was selected as control. Figure 6 depicts the CD spectra of standard BSA solution, BSA obtained from dissociation of HIP complex, and BSA released from both batches of nanoparticles. Results clearly show a significant overlap in peak shape throughout the region studied. This data also confirms that the secondary structure of BSA was not perturbed due to HIP complexation or treatment with organic solvent and sonication. Enhanced stability of BSA towards organic solvents and sonication may be explained by the following reasons. First, HIP complexation might have provided conformation stability and steric shielding to the BSA molecule. Moreover, with S/O/W emulsion method, the probability of protein denaturation has been significantly minimized compared to conventional method such as W/O/W emulsion method. In S/O/W emulsion method, protein molecules are encapsulated in the solid state relative to W/O/W emulsion method where solution form of protein is employed. In the solid state, the detrimental effect of sonication at water-organic phase interface is also minimal.

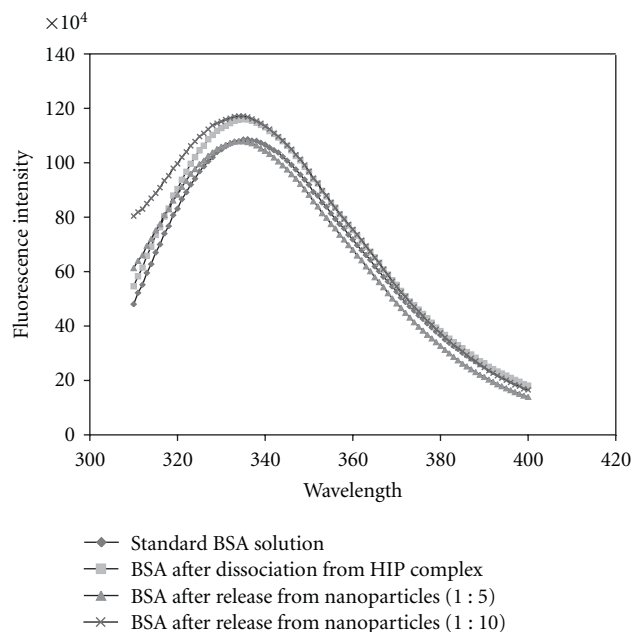


FIGURE 7: Intrinsic fluorescence assay of standard solution of BSA, BSA recovered after dissociation from HIP complex and BSA after release from different batches of nanoparticles.

We compared the intrinsic fluorescence spectra of freshly prepared BSA with BSA obtained after dissociation from HIP complex and BSA released from different batches of nanoparticles. BSA contains a buried tryptophan amino acid in its hydrophobic core. Fluorescence of tryptophan is extremely sensitive to polarity of its surrounding medium [26]. Changes in the fluorescence intensity, wavelength of maximum fluorescence emission, and quantum yield are accepted parameters to study tertiary structure of protein. Results of this study are shown in Figure 7. It is very clear from this data that intensity and wavelength of maximum fluorescence (335 nm) are similar in all the samples. This data confirmed that tertiary structure of BSA was not significantly altered following dissociation from HIP complex and also after release from nanoparticles. This result also corroborates with our previous CD spectra results where we have observed no significant change in secondary structure of BSA due to HIP complexation and nanoparticle preparation.

4. Conclusions

This study for the first time shows the feasibility of forming HIP complex of a large protein such as BSA with dextran sulphate as a complexing polymer. This study confirms the involvement of basic amino acids in the formation of HIP complexation. Dissociation studies of HIP complex in presence of oppositely charged ions (HPO_4^{2-}) as well as FTIR studies have revealed presence of ionic interactions between basic amino acids in BSA and sulphate groups of DS. We successfully prepared and characterized nanoparticles of BSA in HIP complex form using S/O/W emulsion method. SEM and TEM studies revealed smooth surface and spherical

shape of nanoparticles. Significant entrapment of BSA in nanoparticles was obtained when low amounts of PLGA 85 : 15 was employed. Finally, CD analysis and intrinsic fluorescence data revealed that secondary and tertiary structures of BSA were not affected due to HIP complexation and nanoparticle preparation. HIP complexation approach can be employed to enhance loading of large proteins including antibody-based therapeutic molecules in colloidal dosage forms.

References

- [1] S. Yang, W. Yuan, and T. Jin, "Formulating protein therapeutics into particulate forms," *Expert Opinion on Drug Delivery*, vol. 6, no. 10, pp. 1123–1133, 2009.
- [2] C. F. Van Der Walle, G. Sharma, and M. N. V. R. Kumar, "Current approaches to stabilising and analysing proteins during microencapsulation in PLGA," *Expert Opinion on Drug Delivery*, vol. 6, no. 2, pp. 177–186, 2009.
- [3] L. Jorgensen, E. H. Moeller, M. van de Weert, H. M. Nielsen, and S. Frokjaer, "Preparing and evaluating delivery systems for proteins," *European Journal of Pharmaceutical Sciences*, vol. 29, no. 3–4, pp. 174–182, 2006.
- [4] D. S. Pisal, M. P. Kosloski, and S. V. Balu-Iyer, "Delivery of therapeutic proteins," *Journal of Pharmaceutical Sciences*, vol. 99, no. 6, pp. 2557–2575, 2010.
- [5] S. Frokjaer and D. E. Otzen, "Protein drug stability: a formulation challenge," *Nature Reviews Drug Discovery*, vol. 4, no. 4, pp. 298–306, 2005.
- [6] M. Van De Weert, W. E. Hennink, and W. Jiskoot, "Protein instability in poly(lactic-co-glycolic acid) microparticles," *Pharmaceutical Research*, vol. 17, no. 10, pp. 1159–1167, 2000.
- [7] R. Krishnamurthy, J. A. Lumpkin, and R. Sridhar, "Inactivation of lysozyme by sonication under conditions relevant to microencapsulation," *International Journal of Pharmaceutics*, vol. 205, no. 1–2, pp. 23–34, 2000.
- [8] M. L. Houchin and E. M. Topp, "Chemical degradation of peptides and proteins in PLGA: a review of reactions and mechanisms," *Journal of Pharmaceutical Sciences*, vol. 97, no. 7, pp. 2395–2404, 2008.
- [9] S. P. Schwendeman, "Recent advances in the stabilization of proteins encapsulated in injectable PLGA delivery systems," *Critical Reviews in Therapeutic Drug Carrier Systems*, vol. 19, no. 1, pp. 73–98, 2002.
- [10] L. Yang, F. Cui, K. Shi, D. Cun, and R. Wang, "Design of high payload PLGA nanoparticles containing melittinsodium dodecyl sulfate complex by the hydrophobic ion-pairing technique," *Drug Development and Industrial Pharmacy*, vol. 35, no. 8, pp. 959–968, 2009.
- [11] H. Yuan, S. P. Jiang, Y. Z. Du, J. Miao, X. G. Zhang, and F. Q. Hu, "Strategic approaches for improving entrapment of hydrophilic peptide drugs by lipid nanoparticles," *Colloids and Surfaces B: Biointerfaces*, vol. 70, no. 2, pp. 248–253, 2009.
- [12] W. G. Dai and L. C. Dong, "Characterization of physicochemical and biological properties of an insulin/lauryl sulfate complex formed by hydrophobic ion pairing," *International Journal of Pharmaceutics*, vol. 336, no. 1, pp. 58–66, 2007.
- [13] H. S. Yoo, H. K. Choi, and T. G. Park, "Protein-fatty acid complex for enhanced loading and stability within biodegradable nanoparticles," *Journal of Pharmaceutical Sciences*, vol. 90, no. 2, pp. 194–201, 2001.
- [14] J. D. Meyer and M. C. Manning, "Hydrophobic ion pairing: altering the solubility properties of biomolecules," *Pharmaceutical Research*, vol. 15, no. 2, pp. 188–193, 1998.
- [15] R. Gaudana, A. Parenky, R. Vaishya, S. K. Samanta, and A. K. Mitra, "Development and characterization of nanoparticulate formulation of a water soluble prodrug of dexamethasone by HIP complexation," *Journal of Microencapsulation*, vol. 28, no. 1, pp. 10–20, 2011.
- [16] S. Sun, N. Liang, H. Piao, H. Yamamoto, Y. Kawashima, and F. Cui, "Insulin-S.O (sodium oleate) complex-loaded PLGA nanoparticles: formulation, characterization and in vivo evaluation," *Journal of Microencapsulation*, vol. 27, no. 6, pp. 471–478, 2010.
- [17] M. C. Manning, D. K. Chou, B. M. Murphy, R. W. Payne, and D. S. Katayama, "Stability of protein pharmaceuticals: an update," *Pharmaceutical Research*, vol. 27, no. 4, pp. 544–575, 2010.
- [18] G. Gao, Y. Yan, S. Pispas, and P. Yao, "Sustained and extended release with structural and activity recovery of lysozyme from complexes with sodium (sulfamate carboxylate) isoprene/ethylene oxide block copolymer," *Macromolecular Bioscience*, vol. 10, no. 2, pp. 139–146, 2010.
- [19] D. Stigter and K. A. Dill, "Charge effects on folded and unfolded proteins," *Biochemistry*, vol. 29, no. 5, pp. 1262–1271, 1990.
- [20] I. J. Castellanos, W. L. Cuadrado, and K. Griebenow, "Prevention of structural perturbations and aggregation upon encapsulation of bovine serum albumin into poly(lactide-co-glycolide) microspheres using the solid-in-oil-in-water technique," *Journal of Pharmacy and Pharmacology*, vol. 53, no. 8, pp. 1099–1107, 2001.
- [21] I. J. Castellanos, K. G. Carrasquillo, J. De Jesús López, M. Alvarez, and K. Griebenow, "Encapsulation of bovine serum albumin in poly(lactide-co-glycolide) microspheres by the solid-in-oil-in-water technique," *Journal of Pharmacy and Pharmacology*, vol. 53, no. 2, pp. 167–178, 2001.
- [22] L. Feng, A. De Dille, V. J. Jameson, L. Smith, W. S. Dernell, and M. C. Manning, "Improved potency of cisplatin by hydrophobic ion pairing," *Cancer Chemotherapy and Pharmacology*, vol. 54, no. 5, pp. 441–448, 2004.
- [23] J. R. Amrutkar and S. G. Gattani, "Chitosan-chondroitin sulfate based matrix tablets for colon specific delivery of indomethacin," *AAPS PharmSciTech*, vol. 10, no. 2, pp. 670–677, 2009.
- [24] W. Tiyaonchai and N. Limpeanchob, "Formulation and characterization of amphotericin B-chitosan-dextran sulfate nanoparticles," *International Journal of Pharmaceutics*, vol. 329, no. 1–2, pp. 142–149, 2007.
- [25] B. Sarmiento, S. Martins, A. Ribeiro, F. Veiga, R. Neufeld, and D. Ferreira, "Development and comparison of different nanoparticulate polyelectrolyte complexes as insulin carriers," *International Journal of Peptide Research and Therapeutics*, vol. 12, no. 2, pp. 131–138, 2006.
- [26] L. I. Shang, Y. Wang, J. Jiang, and S. Dong, "PH-dependent protein conformational changes in albumin:Gold nanoparticle bioconjugates: a spectroscopic study," *Langmuir*, vol. 23, no. 5, pp. 2714–2721, 2007.

Research Article

High-Resolution Imaging of Dendrimers Used in Drug Delivery via Scanning Probe Microscopy

Lifang Shi,¹ Christopher J. Fleming,¹ Shawn L. Riechers,¹ Nai-Ning Yin,¹ Juntao Luo,² Kit S. Lam,^{2,3} and Gang-yu Liu¹

¹Department of Chemistry, University of California, Davis, CA 95616, USA

²Department of Biochemistry and Molecular Medicine, UCD Cancer Center, University of California, Davis, Sacramento, CA 95817, USA

³Division of Hematology and Oncology, Internal Medicine, UCD Cancer Center, University of California, Davis, Sacramento, CA 95817, USA

Correspondence should be addressed to Gang-yu Liu, liu@chem.ucdavis.edu

Received 18 December 2010; Revised 7 March 2011; Accepted 30 March 2011

Academic Editor: Guru V. Betageri

Copyright © 2011 Lifang Shi et al. This is an open access article distributed under the Creative Commons Attribution License, which permits unrestricted use, distribution, and reproduction in any medium, provided the original work is properly cited.

Dendrimers and telodendrimer micelles represent two new classes of vehicles for drug delivery that have attracted much attention recently. Their structural characterization at the molecular and submolecular level remains a challenge due to the difficulties in reaching high resolution when imaging small particles in their native media. This investigation offers a new approach towards this challenge, using scanning tunneling microscopy (STM) and atomic force microscopy (AFM). By using new sample preparation protocols, this work demonstrates that (a) intramolecular features such as drug molecules and dendrimer termini can be resolved; and (b) telodendrimer micelles can be immobilized on the surface without compromising structural integrity, and as such, high resolution AFM imaging may be performed to attain 3D information. This high-resolution structural information should enhance our knowledge of the nanocarrier structure and nanocarrier-drug interaction and, therefore, facilitate design and optimization of the efficiency in drug delivery.

1. Introduction

Using nanoparticles composed of polymers or assemblies of amphiphilic molecules as drug delivery vehicles have attracted much attention in the recent quest for drug delivery [1–3]. Among them, many dendrimers have been synthesized with a great degree of control in the synthesis of the designed structure [4, 5]. Dendrimers exhibit great promise as nanocarriers for efficient drug delivery due to researchers' ability to control their size (e.g., 1 nm to 100 nm) through the variation of iteration cycles and to implement surface and intramolecular functionalities designed to carry or trap desired drug molecules through covalent, hydrophobic, ionic, or hydrogen-bonding interactions [1, 6–9]. Successful examples have been reported, such as the increase in solubility and *in vivo* compatibility of non-steroidal anti-inflammatory drugs (NSAIDs) using functionalized dendrimer carriers [10–14]. Specifically, the combination

of indomethacin with poly(amidoamine) (PAMAM) dendrimers resulted in enhanced *in vivo* pharmacokinetic performance over indomethacin alone [15].

Complimentary to the “hard” dendrimers discussed above, “soft” nanostructures, such as nanomicelles, made by assembly of biocompatible telodendrimers (e.g., a linear poly(ethylene glycol)- (PEG-) block-dendritic oligomers of cholic acid (CA)) in aqueous conditions were also developed recently [16–21]. These nanomicelles are highly flexible, and as such, they exhibit the advantage for *in vivo* movement. Since polymer molecules are the basic unit within micelles, multifunctionalities may be implemented for individual molecules, and size may be tuned (e.g., $d = 15\text{--}300\text{ nm}$) by varying the conditions of assembly. The amphiphilicity enables the incorporation of hydrophobic drugs such paclitaxel (PTX) enclosed inside the micelles, with a load capacity as high as 7.3 mg/mL [16]. The *in vitro* anticancer activity of PTX loaded PEG^{5k}-CA₈ micelles have been performed

on human ovarian clear cell carcinoma cells (ES-2) and firefly luciferase-expressing ovarian adenocarcinoma cell lines (SKOV3-luc-D3). PTX-loaded PEG^{5k}-CA₈ micelles exhibited equivalent cytotoxic activity *in vitro* compared with the clinical formulations of PTX, such as Taxol and Abraxane [17]. *In vivo* antitumor efficacy of PTX loaded PEG^{5k}-CA₈ micelles have been tested in nude mice bearing human SKOV3-luc ovarian cancer xenograft, where the results indicated that this vehicle could deliver PTX preferentially to tumor sites via enhanced permeation and retention (EPR) effect, and thus exhibits superior *in vivo* anticancer effect overall in animal models, compared to Taxol and Abraxane [16, 17].

To enhance the efficiency of drug delivery, knowledge of the nanocarrier structure and nanocarrier-drug interaction is critical for their design and optimization. In the case of dendrimer systems, the location and the binding of drug molecules to dendrimers are particularly important, as the outcome is directly related to loading capacity and release behavior. While macroscopic information such as solubility [12–14] and spectroscopy [22] are available, little is known at the molecular level. Despite the prediction by molecular dynamics simulations [23–25] that drug molecules may attach to both the exterior and interior of dendrimers, the direct evidence from experiments is still lacking due to difficulties in visualizing intramolecular structures of dendrimers. Scanning tunneling microscopy (STM), due to its high spatial resolution, offers a promising solution to this challenge [26]. The highest spatial resolution is typically reported for conductive and semiconductive systems, reaching the submolecular level [27]. Using metal ion coordination [28, 29], we extended the high-resolution capability of STM to dendrimers in this investigation, resolving individual indomethacin molecules at the dendrimer exterior.

In the case of telodendrimer micelles, dynamic light scattering (DLS) allows the average diameter and distribution to be determined in the solution phase [16, 17]. Individual micelles may be visualized using cryotransmission electron microscopy (cryo-TEM) upon freezing of the samples. The use of cryo-TEM is complicated, as the micelles are no longer in their natural environment [30]. A much simpler technique, atomic force microscopy (AFM), could offer some remedy to this pursuit. AFM offers high spatial resolution and versatility of imaging in various media, including micelle formation media and physiological buffers [31–33].

In this study, we have tested the feasibility and demonstrated the proof-of-concept of using scanning probe microscopy to image PTX-loaded thiol modified telodendrimer micelles, HS-PEG^{5k}-CA₈ (“5k” represents the molecular weight of PEG, and “8” indicates the number of CA subunits in the telodendrimer), in aqueous media where micelles form. The results are very encouraging: individual micelles are clearly visualized, from which we can extract the size and geometry of micelles in correlation with the conditions of assembly. The difference between native and drug carrying micelles is clearly visible under AFM, from which the drug carrying capacity can be estimated. In addition, the knowledge of the geometry and size of individual micelles facilitates our understanding of their efficacy and further optimization.

2. Materials and Methods

2.1. Materials. Paclitaxel was purchased from AK scientific Inc. 4th generation hydroxyl-terminated poly(amidoamine) dendrimers, G4 PAMAM-OH (98% purity, 10% by weight in methanol), and 1-(4-Chlorobenzoyl)-5-methoxy-2-methyl-3-indoleacetic acid, commonly known as indomethacin ($\geq 99.0\%$), were purchased from Sigma-Aldrich and used without further purification. 1-adamantanethiol (AD, 95% purity) and *n*-octanethiol (C₈, 98% purity) were purchased from Sigma-Aldrich and used as received. 200 proof ethanol (99.99% purity) was purchased from Gold Shield Chemical Co. K₂PtCl₄ (min. 42.4% Pt, Alfa Aesar) was used as received. Ultrapure water ($\geq 8 \text{ M}\Omega \cdot \text{cm}$) was obtained using a Millipore Milli-Q filtration system. Ultrapure N₂ ($\geq 98\%$, Air Gas Co.) and H₂ (99.99%, Praxair, Inc.) were used for drying and flaming, respectively. STM tips were made from W wire ($d = 0.010 \text{ in}$, 99.95%, California Fine Wire Co.). Epoxy glue (Epo-tek 377) was purchased from Epoxy Technology.

2.2. Synthesis of Thiol Functionalized Telodendrimer HS-PEG^{5k}-CA₈. BocNH-PEG^{5k}-CA₈ was synthesized following the established procedure [16]. The Boc protecting group was removed via the treatment with 50% of trifluoroacetic acid (TFA) in dichloromethane (DCM) for 30 min, and then, the majority of solvent was removed by blowing nitrogen. The polymer was precipitated by washing three times with cold ether. S-Triethyl-beta-mercaptopropionic acid (2 equ.) was coupled on the amino groups on the terminal end of telodendrimer using hydroxybenzotriazole (HOBt, 2 equ.) and diisopropylcarbodiimide (DIC, equ.) as coupling reagents overnight. The telodendrimer was precipitated and washed by cold ether and was treated with 50% TFA in DCM for 30 min, then the majority of solvent was removed by blowing nitrogen. The telodendrimer was precipitated and washed by cold ether and dissolved in water. The telodendrimer solution was filtered and then dialyzed against 4 L water in a dialysis tube with molecular weight cut-off (MWCO) of 3.5 KDa; reservoir water was refreshed completely four times in 24 h. Finally, the telodendrimer was lyophilized. The molecular weight of the telodendrimer was detected by matrix-assisted laser desorption ionization—time of flight mass spectrometry (MALDI-TOF MS) and nuclear magnetic resonance (NMR) spectrometry. The thiol group was detected by Ellman’s assay. The synthesized HS-PEG^{5k}-CA₈ telodendrimer was kept in desiccators before use.

2.3. Preparation of Gold Thin Films. Au(111) thin films were prepared via thermal evaporation of Au onto freshly cleaved mica (0001) in a high-vacuum evaporator (Denton Vacuum, Model 502-A) [34]. The substrate mica was heated via two quartz lamps to 350°C under a base pressure of 2×10^{-7} torr. The evaporation rate was 0.3 nm/sec and the final thickness of Au films was 150 nm. After evaporation, the Au was thermally annealed *in situ* at 375°C for 30–60 min to increase the size of the Au(111) terraces. After annealing, the Au film was allowed to cool for $\geq 5 \text{ hr}$. under vacuum. Upon removal, the Au films were stored in a sealed glass container.

2.4. Preparation of 1-Adamantanethiol Self-Assembled Monolayers (SAMs). The gold films described above were used to prepare ultraflat gold films on glass substrates following a method reported previously [35]. Briefly, the gold films were annealed in an H₂ flame in order to coalesce the gold grains on the mica. Then, the gold thin film was cooled in air to room temperature. A small droplet of epoxy glue was applied to each of the dry glass substrates (coverslips). The coverslips were then placed on the gold substrate with the glue attached side facing down. The glue was then cured at 150°C overnight. After removal from oven, the glass coverslip with gold thin film were peeled off from the mica substrate. The 1-adamantanethiol (AD) SAMs were prepared by immersing the gold films in a 10 mM ethanolic AD solution at room temperature for 24 hours [36]. The AD SAM on gold was rinsed first with ethanol, and then with Milli Q water, before the deposition of the loaded or unloaded micelles.

2.5. Loading of PTX into HS-PEG^{5k}-CA₈ Micelles and Characterization. 6 mg of PTX and 20 mg of HS-PEG^{5k}-CA₈ were dissolved in 3 mL of chloroform in a 10 mL single neck flask to form a homogeneous solution. The solvent was removed by rotavaporation, and the sample was further dried on high vacuum pump for 30 min. Then, 1 mL of phosphate buffered saline (PBS) was added into the flask to disperse the solid film via vortex and further sonication for 30 min to yield a homogenous micelle solution. The particle sizes of the micelles before and after PTX loading were measured with DLS Zetatract (Microtrac) to be 16 nm and 23 nm, respectively. The drug loading capacity was measured using high-performance liquid chromatography (HPLC) calibrated with PTX solutions in dimethyl sulfoxide (DMSO) with known concentrations.

2.6. AFM Imaging. AFM measurements of micelles and dendrimers were performed on a MFP3D AFM (Asylum Research Inc., Santa Barbara, Calif, USA). When imaging HS-PEG^{5k}-CA₈ and PTX-loaded HS-PEG^{5k}-CA₈ micelles in SAMs, tapping mode was utilized in aqueous solution. The probe is a MSNL-10 silicon cantilever (Veeco, Camarillo, Calif, USA) with a force constant of $k = 0.1$ N/m. During AFM tapping, the cantilever was modulated by a driving frequency of 68 kHz and an amplitude range from 0.30 to 0.71 V, with damping from 30 to 70%. When imaging PAMAM dendrimers, a silicon cantilever (AC-240, Olympus) was used. The probe has a force constant of $k = 1.0$ N/m as measured by thermal noise method. During tapping mode imaging, the cantilever was modulated by a driving frequency of 74 kHz and amplitude of 67.0 nm (0.63 V), with the damping set to 85%. For displacing adsorbates such as dendrimers or alkanethiolates, tips were placed in contact with the surface with increasing load beyond threshold [28, 29]. Data display and analysis were conducted using MFP-3D's software package written on Igor Pro platform (Wavemetrics). The surface coverage of micelle was calculated based on AFM topography images.

2.7. STM Imaging. The STM has a walker-type scanner (UHV 300, RHK Technologies, Inc.) and was used under

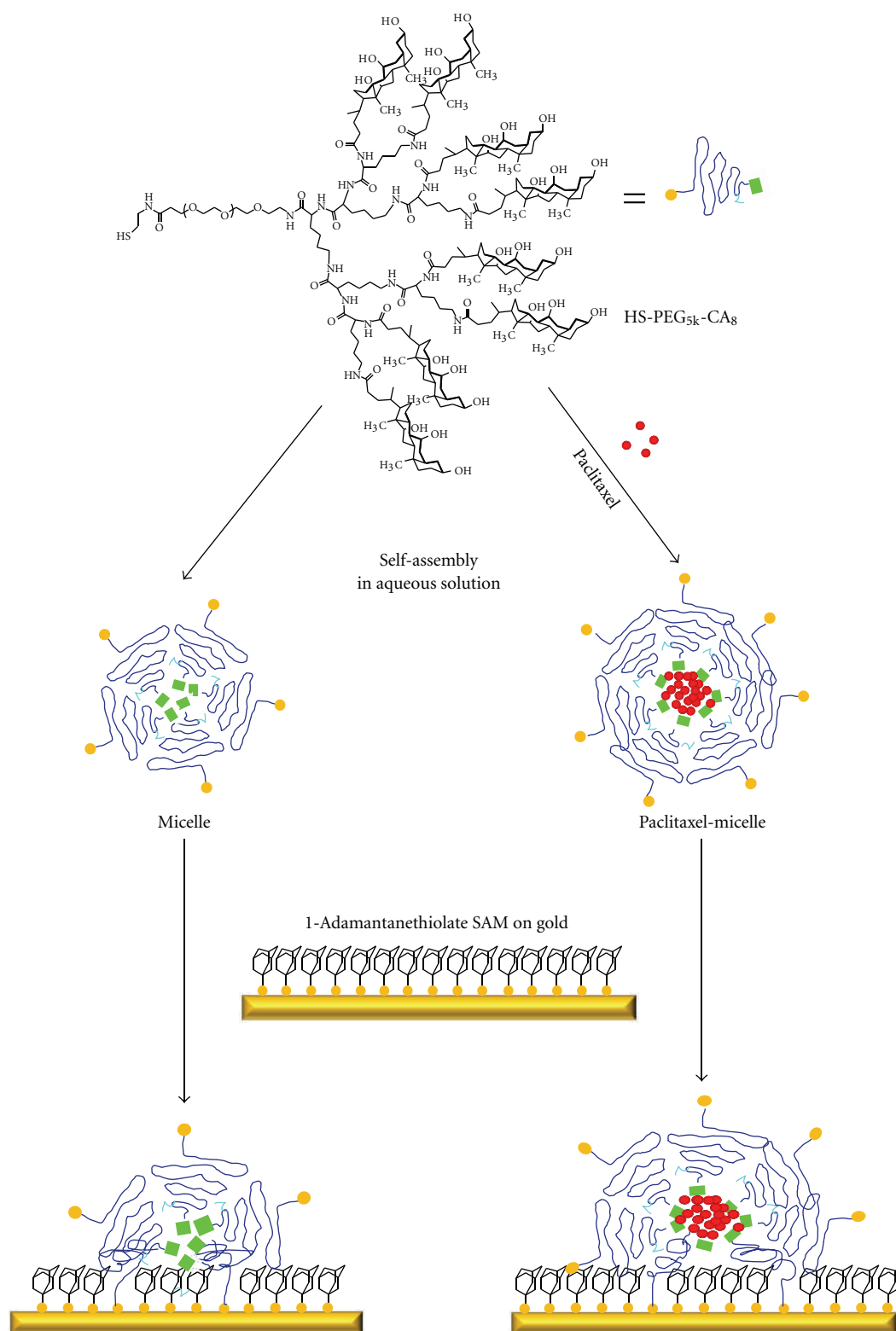
ambient conditions for this investigation. The STM tips were cut W wires which were electrochemically etched at 2.0 V in 3.0 M NaOH solutions. A homemade potentiostat monitored the etching process [34, 37]. All STM images were acquired in constant current mode with typical bias voltages ranging from 0.3 to 0.7 V and tunneling currents from 5 to 25 pA. The piezoelectric scanners were calibrated laterally using a decanethiol SAM (lattice constant = 0.50 nm) and vertically using a Au(111) single atomic step (0.235 nm).

3. Results and Discussion

3.1. Immobilization of Telodendrimer Micelles into SAMs for AFM Imaging. For structural characterization via AFM, micelles must be immobilized on surface supports. Immobilized drug delivery vehicles are the key component in therapies using patches [38]. A potential application of immobilized PTX-loaded micelles on surfaces is the development of a new type of PTX eluting stent [39]. The procedure of immobilization of micelles onto gold surfaces is shown in Scheme 1. HS-PEG^{5k}-CA₈ telodendrimer is soluble in water and self-assembles into micelles. PTX is loaded into the micelle via a procedure of solvent evaporation followed by the aqueous dispersion of micelles [40].

In order to maintain the integrity of micelles on solid surface, gold surfaces were covered by SAMs of AD. The use of AD is based mainly on two considerations: (a) SAMs provide a buffer to dampen collisions and allow full contact between micelles and gold surfaces and (b) AD can be exchanged by alkane thiol functionalities to enable micelles to anchor onto gold surfaces. As illustrated in Scheme 1, micelles are formed instantly via the self-assembly of telodendrimers dissolved in aqueous solution. The critical micelle concentration of micelles was 5.3 μM. The micelles have noncharged surfaces, the Zeta-potential was measured close to zero [21]. AD SAMs on gold were soaked in micelle solutions, 0.5 mg/mL, for 20 min. This short exposure resulted in 15.3% surface coverage of micelles on the gold surface. In the case of PTX-loaded micelles, a concentration of 26.4 mg/mL (weight ratio as 6.4 mg PTX: 20 mg HS-PEG^{5k}-CA₈) was used and the exposure time was typically 1 hour. This led to 29.0% surface coverage of PTX loaded micelle on the gold surface. After deposition, the samples were rinsed with Milli Q water and kept in the water solution before AFM measurement.

3.2. AFM Enables Visualization Telodendrimer Micelles in their Native Media and Detection of Changes upon Uptake of PTX. Upon immobilization, AFM imaging is carried out in water media. To attain accurate measurements in 3D without significant deformation, tapping mode is utilized, from which height is extracted from topographic images, and lateral boundaries are well defined from phase images. The AFM images in Figure 1 indicate that all micelles, PTX-loaded or unloaded, maintain the geometry of elliptical cap geometry. Figure 1(a) is a 300 × 300 nm² AFM topography image of PTX-loaded micelles on ultraflat Au. Each bright protrusion is a single PTX-loaded micelle. The height of a typical PTX-loaded micelle, as shown in cursor 1, is 4.0 nm,

SCHEME 1: Schematic of surface immobilization of unloaded and paclitaxel loaded HS-PEG^{5k}-CA₈ micelles on Au surfaces.

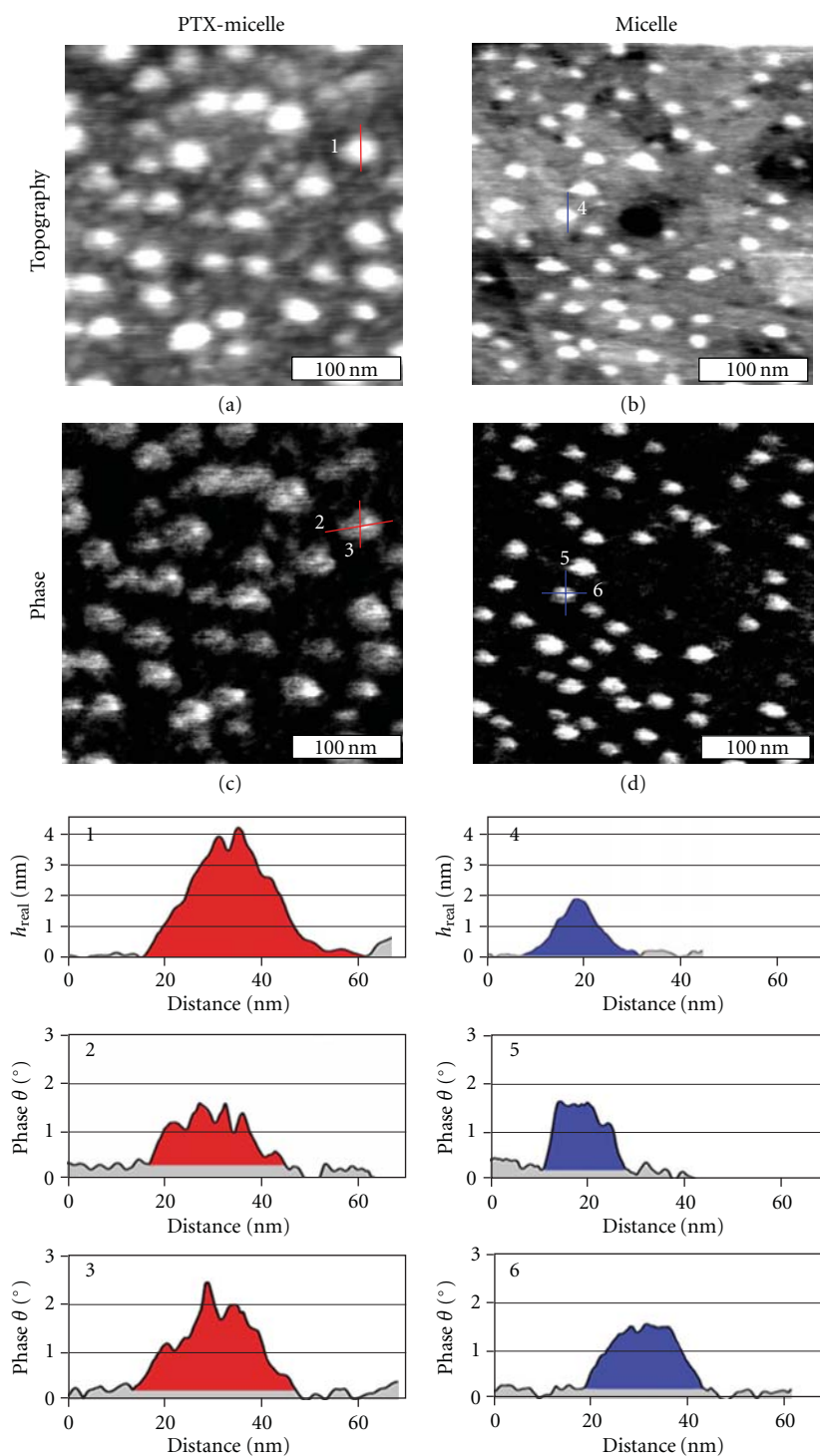


FIGURE 1: AFM characterization of paclitaxel- (PTX-) loaded HS-PEG^{5k}-CA₈ micelles and unloaded HS-PEG^{5k}-CA₈ micelle on gold substrate in aqueous solution. The first column is AFM topography (a), phase image (b) and corresponding cursors of PTX-loaded micelle. AFM topography (c), phase image (d), and corresponding cursors of unloaded micelle are shown in second column. In cursor profiles, areas indicated with red, blue, and grey are relative to PTX-loaded micelle, unloaded micelle and AD SAM, respectively. Height, short axis, and long axis of PTX-loaded micelle extracted from cursors profiles 1, 2, and 3. Height, short axis, and long axis of unloaded micelle extracted from cursors profiles 4, 5, and 6.

measured from the lowest point in the local surroundings to the apex of the micelle. Its lateral boundaries are clearly visible from the AFM phase image shown in Figure 1(c). The lateral dimensions are 28.1 nm and 33.0 nm for short axis and long axis, respectively, as shown in cursors 2 and 3. Among the 49 PTX-loaded micelles measured, the average 3D dimensions (long axis “a”, short axis “b”, and height “h”) are 31.8 ± 4.3 nm, 25.6 ± 3.2 nm, and 4.6 ± 0.7 nm, respectively. As a comparison, Figure 1(b) is a 300×300 nm² AFM topography image of original micelles on ultraflat Au. The measured height of the unloaded micelle is 1.9 nm, as shown in cursor 4. Figure 1(d) is the phase image of unloaded micelle, from which the lateral boundaries are clearly visible. The short and long axis of the unloaded micelle is 17.3 nm and 25.2 nm, respectively, as shown in cursors 5 and 6. Among the 50 unloaded micelles measured, the *a*, *b*, and *h* measure 23.7 ± 2.4 nm, 17.2 ± 2.3 nm, and 1.8 ± 0.2 nm, respectively.

The volume, *V*, of each micelle can be calculated using the simple geometric formula: $V = (1/6\pi h)(3/4ab+h^2)$ [28]. From Figures 1(a) and 1(c), the height of PTX-loaded micelle is 4.0 nm, the lateral dimensions are *a* = 33.0 nm, *b* = 28.1 nm, thus $V = 1490.1$ nm³. From Figures 1(b) and 1(d), the unloaded micelle, measures *a* = 25.2 nm, *b* = 17.3 nm, and *h* = 1.9 nm, which corresponds to $V = 328.9$ nm³. The average volume of PTX-loaded micelle and unloaded micelle is 1475.8 ± 396.2 nm³ and 295.1 ± 62.6 nm³, respectively. PTX-loaded micelle exhibits a larger volume than unloaded micelle. Our Investigations also reveal that the amounts of PTX uptake affect the volume of micelles.

By assuming that the micelle has a spherical shape in water solution, we can estimate the diameter of micelles in solution based on $V = 4/3\pi(D/2)^3$. Here, *V* is volume and *D* is the diameter. The volume of a typical PTX-loaded micelle in Figure 1(a) is 1490.1 nm³, the corresponding diameter is 14.2 nm. Among the 49 PTX-loaded micelles measured, the average diameter is 14.2 ± 1.2 nm. The volume of a typical unloaded micelle in Figure 1(b) is 328.9 nm³, the corresponding diameter is 8.6 nm. Among the 50 unloaded micelles measured, the average diameter is 8.2 ± 0.6 nm. The diameter of PTX-loaded and unloaded micelle obtained from the dynamic light scattering (DLS) measurement is 23 ± 8 and 16 ± 4 nm, respectively [16]. One notes that the size of adsorbed micelles as determined from AFM experiments is smaller than the corresponding diameter measured from the DLS in solution. While DLS gives the averaged hydrodynamic radius of the scattering particles, AFM provides true 3D measurements of individual micelle. The dimensions extracted from AFM measurements more truly reflect the true geometry of the micelles, In addition, it is difficult to reach high accuracy if the particle is very small and nonspherical, for example, <10 nm [41], while AFM does not have such a limitation.

As a bonus, we can estimate the number of PTX molecules based on the volume measurements from AFM. The numbers of PTX (N_{ptx}) and telodendrimers (N_{telo}) are estimated from two equations below, (a) assuming that the volume of individual components are conserved, based on

Connolly solvent-excluded volume [42] using Chem3D Software, using telodendrimer volume of 13.13 nm³, and PTX being 0.754 nm³; (b) the mixing follows 7.5: 2.1 = PTX: telodendrimers. Therefore, for a typical PTX loaded micelle in Figure 1(a), the volume is 1490.1 nm³

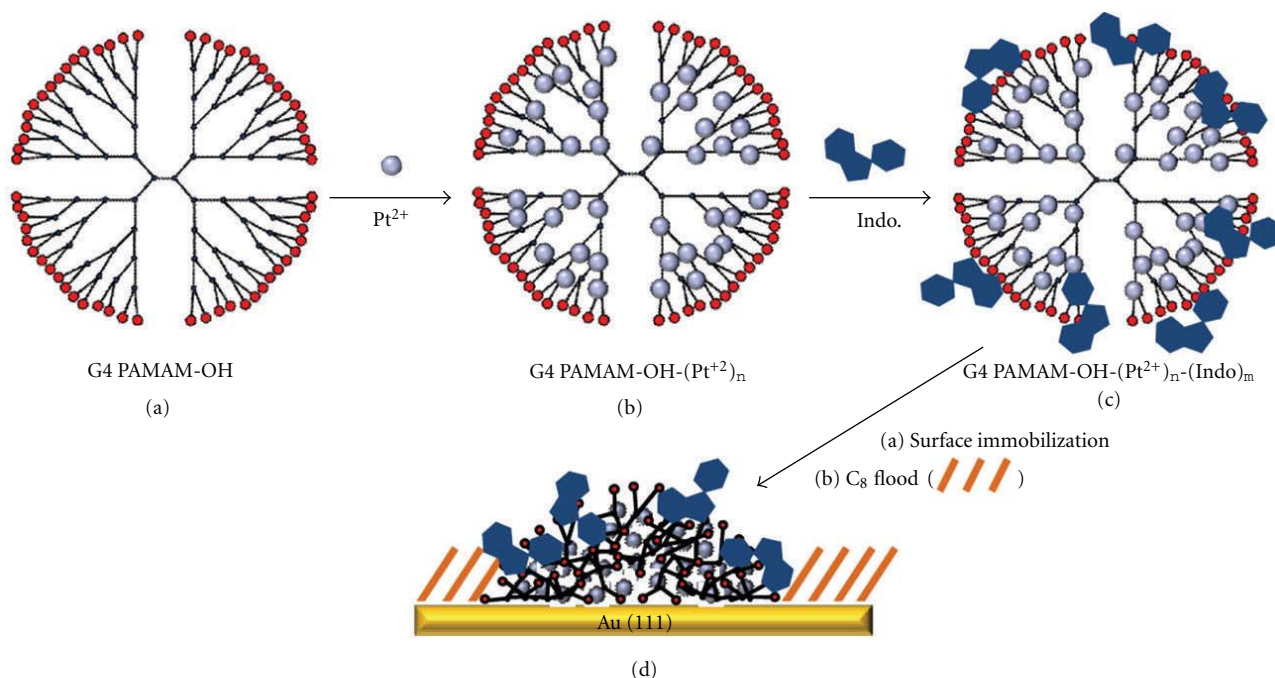
$$\frac{N_{\text{ptx}}}{N_{\text{telo}}} = \frac{7.5}{2.1}, \quad (1)$$

$$N_{\text{ptx}} \times 0.754 + N_{\text{telo}} \times 13.13 = 1490.1. \quad (2)$$

Solving (2) with (1), $N_{\text{ptx}} = 336$, while $N_{\text{telo}} = 94$. For a typical micelle indicated in Figure 1(b), there are 25 telodendrimer units. Within a typical PTX-loaded micelle as shown in Figure 1(a), there are 336 PTX molecules and 94 telodendrimers. The increase in overall size upon PTX loading is likely due to the increase in the number of the telodendrimer molecules within individual micelles. The hydrophobicity of PTX may require larger number of amphiphilic telodendrimers to enclose them inside micelles for overall reduced enthalpy [43].

Taken collectively, AFM provides an alternative and more accurate approach to measure the geometry and size of individual drug delivery vehicles. Even for soft systems such as HS-PEG^{5k}-CA₈ micelles, AFM images may be attained in their native media. This versatility of imaging in water media at a designed temperature allows direct comparison before and after loading or uptake of drugs. In addition, the accuracy enables quantification, such as the determination of height, lateral dimension, volume, and number of drugs enclosed. Therefore, we encourage researchers to consider the application of AFM in determination of the size and geometry of drug-carrying vehicles in the various synthetic and drug-loading steps.

3.3. Preparation and Immobilization of PAMAM Dendrimers for High-Resolution Imaging. To visualize intramolecular structure of PAMAM dendrimers using STM, two key steps are involved, surface immobilization and introduction of metal ions to enable the transport of STM current [28]. Detailed protocols for dendrimers have been discussed previously [28, 29]. For indomethacin carrying dendrimers, first, G4 PAMAM-OH dendrimer solutions were made by diluting aliquots of the methanol-based stock solutions to 12.5 μM aqueous solutions. Second, as illustrated in Scheme 2, K₂PtCl₄ was then added to achieve a molar ratio of 1:120, dendrimer: Pt²⁺. The ratios were guided by the number of tertiary amines (dendrimer branch points) within individual dendrimers, for example; G4 has 62 tertiary amines. Once mixed, the solution was kept at room temperature for 3–5 days, allowing sufficient time for Pt(II)-amine coordination within dendrimers [44]. Third, indomethacin was weighed and then directly added to reach a final stoichiometry of 1:120 dendrimer:indomethacin molar ratio to maximize the potential for interaction between the drug and the dendrimer –OH termini and available tertiary amines. Final dendrimer is represented by G4 PAMAM-OH-(Pt²⁺)_n-(Indo)_m, as represented in Scheme 2(c). The



SCHEME 2: Methodology for the metal ion coordination, drug loading, surface immobilization, and passivation of G4 PAMAM-OH dendrimers. Dendrimers in solution (a) are doped with Pt^{2+} ions (b). Indomethacin is then added to the solution (c). The conductive, drug-loaded dendrimers are then exposed to Au(111) (a) followed by C_8 flooding, (b), to obtain the surface-immobilized G4 PAMAM-OH- $(\text{Pt}^{2+})_n\text{-(Indo)}_m$.

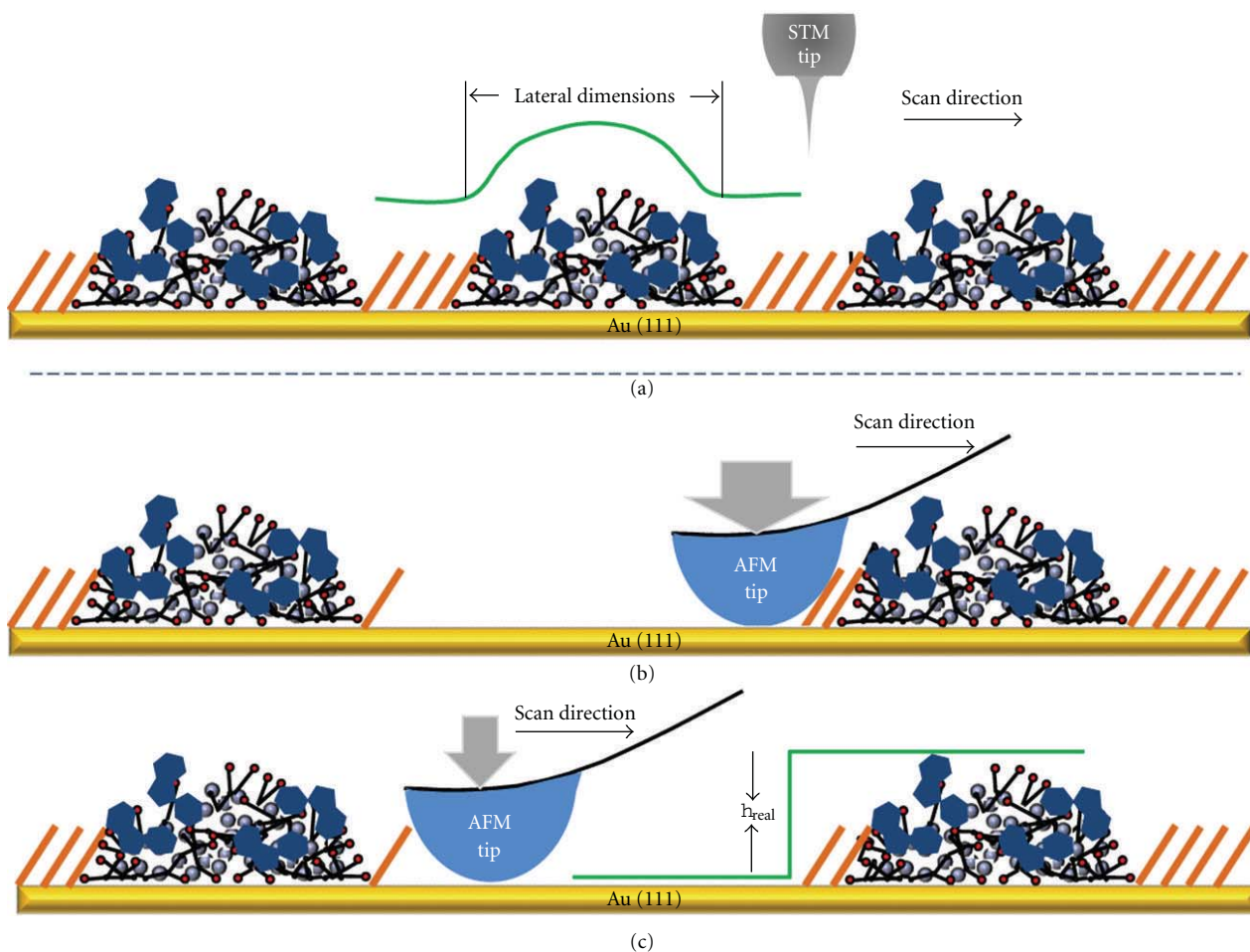
indomethacin-dendrimer mixture was vortexed for 30 min. and allowed to gestate for an additional 2-3 days [10].

For the surface deposition of dendrimers, as shown in Scheme 2(d), 1 cm^2 pieces of gold films were H_2 -flamed [34] and allowed 20 min cooling under clean ambient conditions. Then, a $\sim 75.0 \mu\text{L}$ drop of G4 PAMAM-OH- $(\text{Pt}^{2+})_n\text{-(Indo)}_m$ dendrimer solution was deposited onto the Au(111) surface and allowed to contact for 1.25 min. After washing with water and ethanol the surface was flooded with a 1.0 mM C_8 solution for 2 min. The surface was then washed again with ethanol and dried under N_2 before STM and AFM imaging. The formation of C_8 SAMs confines dendrimers laterally, thus maintaining the structural integrity, and prevents lateral movement during scanning [28]. SAMs also serves as an important internal reference standard for lateral calibration.

3.4. Combined AFM and STM Investigations Enable the Size and Geometry of Individual Dendrimers to be Determined. While STM enables high-resolution imaging and accurate determination of the lateral dimension of individual dendrimers [28], AFM allows for the height to be measured precisely [28, 45, 46]. Scheme 3 illustrates this combined approach. In STM imaging, the tip is located at a fraction of a nanometer above the surface (green tracking line). The current between the W-probe and Au surface is the feedback signal and very localized, and as such, the lateral dimension of the features (e.g., dendrimers) underneath are clearly defined from topographic images. The height in the STM topograph is influenced by the local structure as well as local density of states (LDOS). Although the STM height,

referred to as apparent height (h_{APP}), is a sensitive indicator of surface features, the accuracy is difficult to gauge due to the difficulties in determining the LDOS contribution. Therefore, AFM is frequently utilized for the same sample to determine the height of dendrimers [28]. As illustrated in Scheme 3, the true height of the PAMAM dendrimers is measured from the Au substrate to the apex of the dendrimer. For the cleanliness of the Au substrate, nanoshaving is exercised to remove adsorbates from the defined area to expose the Au as a reference of the origin [28]. Our previous studies have correlated the h_{APP} and true height with this combined approach [28, 29].

3.5. Uploading of Indomethacin Results in Increased Integrity and Size of PAMAM Dendrimers. Figure 2 shows STM images of dendrimers on surfaces. Upon immobilization, dendrimers deform and adopt elliptical cap geometry. Upon uptake of indomethacin, STM imaging reveals that G4 PAMAM-OH- $(\text{Pt}^{2+})_n\text{-(Indo)}_m$ dendrimers are taller than the bare G4 dendrimers. Figure 2(a) is a $20 \times 20 \text{ nm}^2$ STM topograph of G4 PAMAM-OH- $(\text{Pt}^{2+})_n\text{-(Indo)}_m$ dendrimers immobilized on a Au(111) surface. The bright protrusions correspond to individual G4 PAMAM-OH- $(\text{Pt}^{2+})_n\text{-(Indo)}_m$ dendrimer molecules. The STM apparent height, or h_{APP} , is obtained by measuring the height from the lowest point in the immediate surrounding matrix to the top of the dendrimer. These cursors indicate that dendrimers loaded with indomethacin adopt an elliptical dome shape similar to the base dendrimers reported previously [28, 29, 47, 48]. The h_{APP} in cursor profiles 1 and 2 is 0.43 and 0.48 nm,



SCHEME 3: Method of measuring the volume of PAMAM dendrimers using STM and AFM. The h_{APP} and lateral dimensions of single dendrimers are obtained through STM topographs (a). The removal of surface adsorbates under high force (b) allows for AFM height measurements during subsequent scans under normal imaging load (c).

respectively. In contrast, the h_{APP} of a typical G4 dendrimer, as shown in Figure 2(a), measures 0.35 nm and 0.33 nm, respectively. The uptake of indomethacin increases the h_{APP} by 0.08 nm. Among the 102 dendrimers we compared, drug-loaded G4 dendrimers appear 0.09 ± 0.02 nm taller than the dendrimers themselves. The true height is further investigated using AFM as described in the previous section. The typical real height (h_{REAL}) for G4 and indo-G4 complexes are 2.5 ± 0.3 nm and 3.4 ± 0.7 nm, respectively.

After measuring the lateral and vertical dimensions, the volume of dendrimers can be accurately determined and compared. Assuming an elliptical cap geometry for all dendrimers, the volume of individual molecules may be calculated using $V = (1/6\pi h_{\text{REAL}})(3/4ab + h_{\text{REAL}}^2)$, where a and b are the long and short lateral axes, respectively. In a typical case shown in Figure 2, the lateral dimensions are $a = 5.6$ nm, $b = 4.2$ nm for the indomethacin-loaded G4 and the height is 3.4 nm, thus $V = 52.3$ nm³. From Figure 2(b), the bare G4 dendrimers measure $a = 5.7$ nm, $b = 5.2$ nm, and $h_{\text{REAL}} = 2.2$ nm, which corresponds to a $V = 31.2$ nm³. Among the 102 dendrimers compared, drug-loaded

dendrimers are 54% more voluminous than base dendrimers. The average lateral dimensions are $a = 6.8 \pm 1.2$ nm and $b = 5.6 \pm 0.9$ nm for indomethacin-loaded G4 and $a = 6.2 \pm 0.8$ nm and $b = 5.1 \pm 0.7$ nm for unloaded G4. Since the lateral deformation of both loaded and unloaded G4 dendrimers are similar, the height, and thus volume, increases observed with the addition of indomethacin suggest that the addition of indomethacin to the exterior of dendrimers increases the overall structural integrity upon surface immobilization.

3.6. STM Imaging Enables Visualization of Individual Indomethacin Molecules Carried by Dendrimers.

The indomethacin is distinctly recognizable in STM topographs, because they appear taller and usually broader than the -OH termini of dendrimers. Figure 3 illustrates how to distinguish the two types of features. Since Figures 3(a) and 3(b) display with the same STM apparent height range, the contrast indicates the height and enables a direct comparison. It is clearly seen that the fine features at the surface of G4 PAMAM-OH-(Pt²⁺)_n-(Indo)_m dendrimers (Figure 3(a))

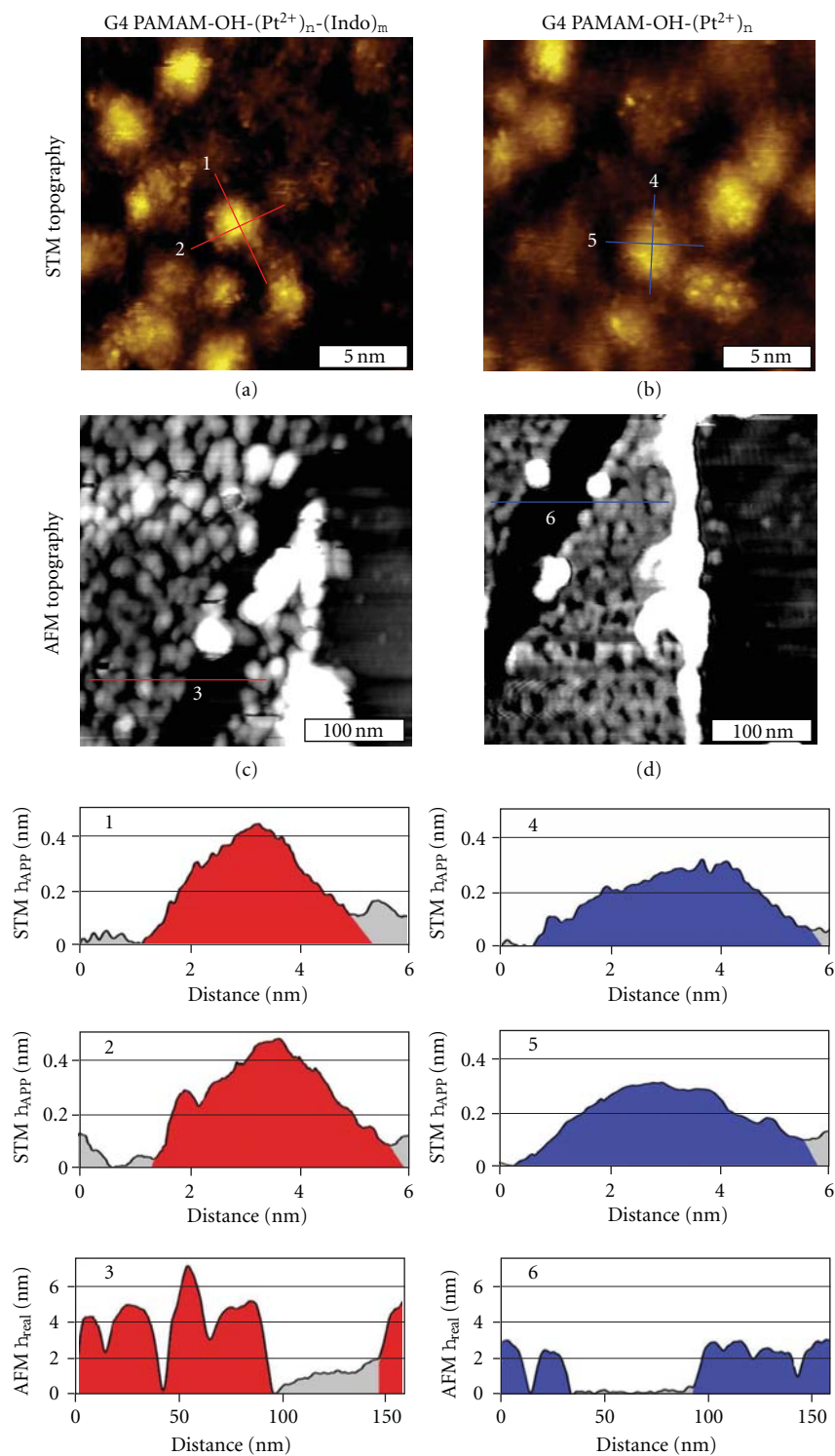


FIGURE 2: STM and AFM topographic lateral and height measurements determine the volume of single G4 PAMAM-OH-(Pt²⁺)_n-(Indo)_m and G4 PAMAM-OH-(Pt²⁺)_n dendrimers. (a) A 20 × 20 nm² STM topograph of G4 PAMAM-OH-(Pt²⁺)_n-(Indo)_m dendrimers immobilized on Au(111). Cursors 1 and 2 reflect the h_{APP} and lateral measurements. (b) A 20 × 20 nm² STM topograph of G4 PAMAM-OH-(Pt²⁺)_n dendrimers immobilized on Au(111). Cursors 4 and 5 reflect the STM height and lateral measures. STM images (a) and (b) were obtained using circa 0.3 V and 20 pA set points. (c) A 300 × 300 nm² AFM topograph of the same surface as (a). Cursor 3 is a representative of the cursors used to ascertain h_{REAL} from the bare Au surface to the dendrimer apex. (d) A 300 × 300 nm² AFM topograph of the same surface as (b). Cursor 6 serves the same purpose for G4 PAMAM-OH-(Pt²⁺)_n as cursor 3 does for drug-loaded dendrimers.

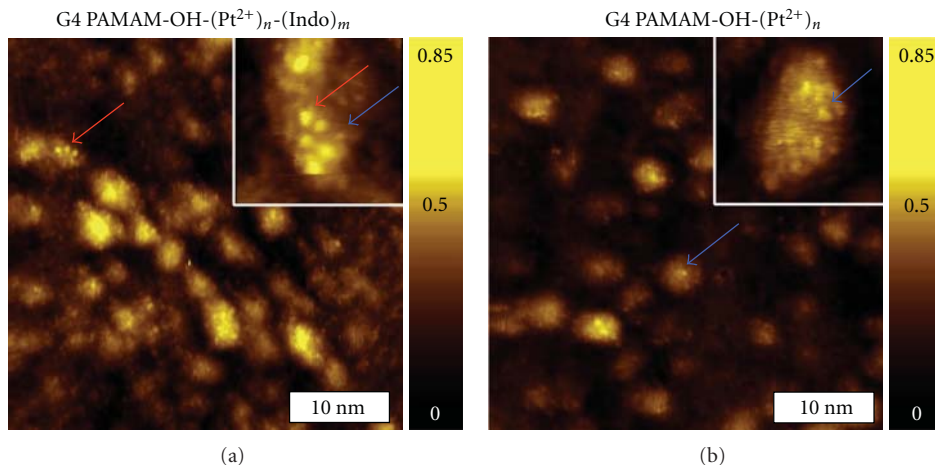


FIGURE 3: Visualization of indomethacin features from high-resolution STM images. (a) A $40 \times 40 \text{ nm}^2$ STM topographic image of G4 PAMAM-OH-(Pt²⁺)_n-(Indo)_m dendrimers immobilized on Au(111). The inset in (a) is a $5 \times 5 \text{ nm}^2$ high-resolution image of a single drug-loaded dendrimer from the same surface showing indomethacin features (red arrows) and a dendrimer intramolecular feature (blue arrow). (b) A $40 \times 40 \text{ nm}^2$ STM topographic image of G4 PAMAM-OH-(Pt²⁺)_n dendrimers immobilized on Au(111). The $6 \times 6 \text{ nm}^2$ inset is a bare dendrimer, where only intramolecular features are visible (blue arrows). All STM images were acquired at 0.3 V and 20 pA. The color scale is normalized to reflect the apparent height range of 0.00–0.85 nm.

appear brighter than the unloaded dendrimers which have only –OH at the termini (Figure 3(b)). Figure 3(a) is a STM topographic image of a G4 PAMAM-OH-(Pt²⁺)_n-(Indo)_m dendrimer surface and the inset is a high-resolution image of a single dendrimer in which the intramolecular features are clearly visible. At first glance, these intramolecular features fall into two types of contrast; that is, one appears brighter than the other. Both previous and present studies of G4-dendrimer reveal the apparent height of –OH termini to be below 0.11 nm [28, 29]. Therefore, we conclude that the bright and tall features identified in Figure 3(a) are new entities, that is, due to attachment by indomethacin. Among 20 G4 PAMAM-OH-(Pt²⁺)_n-(Indo)_m dendrimers analyzed, indomethacin features have a h_{APP} range = 0.12–0.25 nm with an average $h_{\text{APP}} = 0.16$ nm. In contrast, intramolecular feature h_{APP} measured on indomethacin-loaded and unloaded metal ion-doped G4 PAMAM-OH dendrimers ranged 0.03–0.10 nm, among 40 dendrimers measured previously [28] and in this study. Using the threshold of 0.12 nm, we were able to assign intramolecular and indomethacin features in the STM images, therefore, to count how many indomethacin each dendrimer could carry. Among all 19 intramolecular protrusions visible in Figure 3(a), 13 fall under 0.12 nm (0.03 to 0.11 nm), and 6 are above 0.12 nm (0.13 to 0.17 nm), thus assignment of 13 termini and 6 indomethacin molecules. Figure 3(b) is an STM topographic image of a base dendrimer molecule, G4 PAMAM-OH-(Pt²⁺)_n, where intramolecular features, or –OH termini, are clearly visible [28]. The number of indomethacin molecules carried by G4 PAMAM-OH varies from 2 to 14 among the 20 typical dendrimers analyzed in this investigation. This range is consistent with a previous report where each G4 PAMAM-OH dendrimer molecule could hold 12.5 indomethacin [11]. It is possible that indomethacin may reside in the dendrimer

interior void space; therefore, the observed number of indomethacin per dendrimer most likely represents the minimum uptake. Our investigations also reveal that the drug carrying capacity (load) increases with the generation, for example, G3, G4, and G5 PAMAM-OH-(Pt²⁺)_n-(Indo)_m dendrimers carry 5–7, 2–14, and 2–19 drugs, respectively [29]. The variations in height and geometry of dendrimer-immobilized indomethacin molecules suggest that drugs are nonspecifically bound to the dendrimer termini and exposed amidoamine moieties.

4. Conclusions

This study demonstrates the significance of using STM and AFM in the fundamental studies of new drug-delivery vehicles, telodendrimer micelles and PAMAM dendrimers. The preliminary results indicate that the exquisitely high-resolution images enable insightful and fundamental information be revealed in the context of molecular level location and load of drug molecules, as well as the stability of drug-carrier complex. The number of drug molecules per carrier can be directly extracted in the case of dendrimers and estimated in the case of telodendrimer micelles. Since those studies are at the individual carrier's level, the results can be directly linked to simulations which shall facilitate the prediction and design of new carriers.

Acknowledgments

The authors thank Dr. Thomas Mullen at UC Davis and Prof Paul Weiss at University of California, Los Angeles for their insightful information with respect to displacement in 1-adamantanethiol SAM. This work was supported by the University of California at Davis, NSF (CHE 0809977), an

NSF-MRSEC Grant through Stanford University's CPIMA program and RO1 (1R01CA140449, R01CA115483). L. Shi is recipient of the Institute for Complex Adaptive Matter (ICAM) postdoctoral fellowship. they thank Ms. Susan Stagner, Drs. Jie-Ren Li and Ming Zhang at UC Davis for their assistance in paper preparation. Lifang Shi and Christopher J. Fleming contributed equally to this work.

References

- [1] E. R. Gillies and J. M. J. Fréchet, "Dendrimers and dendritic polymers in drug delivery," *Drug Discovery Today*, vol. 10, no. 1, pp. 35–43, 2005.
- [2] M. Yokoyama, "Polymeric micelles as a new drug carrier system and their required considerations for clinical trials," *Expert Opinion on Drug Delivery*, vol. 7, no. 2, pp. 145–158, 2010.
- [3] J. Zhang, S. Li, and X. Li, "Polymeric nano-assemblies as emerging delivery carriers for therapeutic applications: a review of recent patents," *Recent Patents on Nanotechnology*, vol. 3, no. 3, pp. 225–231, 2009.
- [4] B. K. Nanjwade, H. M. Bechra, G. K. Derkar, F. V. Manvi, and V. K. Nanjwade, "Dendrimers: emerging polymers for drug-delivery systems," *European Journal of Pharmaceutical Sciences*, vol. 38, no. 3, pp. 185–196, 2009.
- [5] A. Samad, M. I. Alam, and K. Saxena, "Dendrimers: a class of polymers in the nanotechnology for the delivery of active pharmaceuticals," *Current Pharmaceutical Design*, vol. 15, no. 25, pp. 2958–2969, 2009.
- [6] O. L. Padilla De Jesús, H. R. Ihre, L. Gagne, J. M. J. Fréchet, and F. C. Szoka Jr., "Polyester dendritic systems for drug delivery applications: in vitro and in vivo evaluation," *Bioconjugate Chemistry*, vol. 13, no. 3, pp. 453–461, 2002.
- [7] C. M. Henry, "Drug delivery," *Chemical and Engineering News*, vol. 80, no. 34, pp. 39–47, 2002.
- [8] L. M. Kaminskas, J. Kota, V. M. McLeod, B. D. Kelly, P. Karellas, and C. J. H. Porter, "PEGylation of polylysine dendrimers improves absorption and lymphatic targeting following SC administration in rats," *Journal of Controlled Release*, vol. 140, no. 2, pp. 108–116, 2009.
- [9] C. C. Lee, J. A. MacKay, J. M. J. Fréchet, and F. C. Szoka, "Designing dendrimers for biological applications," *Nature Biotechnology*, vol. 23, no. 12, pp. 1517–1526, 2005.
- [10] A. S. Chauhan, N. K. Jain, P. V. Diwan, and A. J. Khopade, "Solubility enhancement of indomethacin with poly(amidoamine) dendrimers and targeting to inflammatory regions of arthritic rats," *Journal of Drug Targeting*, vol. 12, no. 9-10, pp. 575–583, 2004.
- [11] A. S. Chauhan, S. Sridevi, K. B. Chalasani et al., "Dendrimer-mediated transdermal delivery: enhanced bioavailability of indomethacin," *Journal of Controlled Release*, vol. 90, no. 3, pp. 335–343, 2003.
- [12] C. Yiyun, X. Tongwen, and F. Rongqiang, "Polyamidoamine dendrimers used as solubility enhancers of ketoprofen," *European Journal of Medicinal Chemistry*, vol. 40, no. 12, pp. 1390–1393, 2005.
- [13] B. Devarakonda, R. A. Hill, W. Liebenberg, M. Brits, and M. M. De Villiers, "Comparison of the aqueous solubilization of practically insoluble niclosamide by polyamidoamine (PAMAM) dendrimers and cyclodextrins," *International Journal of Pharmaceutics*, vol. 304, no. 1-2, pp. 193–209, 2005.
- [14] U. Gupta, H. B. Agashe, A. Asthana, and N. K. Jain, "Dendrimers: novel polymeric nanoarchitectures for solubility enhancement," *Biomacromolecules*, vol. 7, no. 3, pp. 649–658, 2006.
- [15] S. Kannan, P. Kolhe, V. Raykova et al., "Dynamics of cellular entry and drug delivery by dendritic polymers into human lung epithelial carcinoma cells," *Journal of Biomaterials Science, Polymer Edition*, vol. 15, no. 3, pp. 311–330, 2004.
- [16] J. T. Luo, K. Xiao, Y. P. Li et al., "Well-defined, size-tunable, multifunctional micelles for efficient paclitaxel delivery for cancer treatment," *Bioconjugate Chemistry*, vol. 21, no. 7, pp. 1216–1224, 2010.
- [17] K. Xiao, J. Luo, W. L. Fowler et al., "A self-assembling nanoparticle for paclitaxel delivery in ovarian cancer," *Biomaterials*, vol. 30, no. 30, pp. 6006–6016, 2009.
- [18] Y. Li, K. Xiao, J. Luo, J. Lee, S. Pan, and K. S. Lam, "A novel size-tunable nanocarrier system for targeted anticancer drug delivery," *Journal of Controlled Release*, vol. 144, no. 3, pp. 314–323, 2010.
- [19] X. L. Wu, J. H. Kim, H. Koo et al., "Tumor-targeting peptide conjugated pH-responsive micelles as a potential drug carrier for cancer therapy," *Bioconjugate Chemistry*, vol. 21, no. 2, pp. 208–213, 2010.
- [20] Y. Li, S. Pan, W. Zhang, and Z. Du, "Novel thermo-sensitive core-shell nanoparticles for targeted paclitaxel delivery," *Nanotechnology*, vol. 20, no. 6, Article ID 065104, 2009.
- [21] K. Xiao, Y. Li, J. Luo et al., "The effect of surface charge on in vivo biodistribution of peg-oligocholic acid based micellar nanoparticles," *Biomaterials*, vol. 32, no. 13, pp. 3435–3446, 2011.
- [22] A. M. Caminade, R. Laurent, and J. P. Majoral, "Characterization of dendrimers," *Advanced Drug Delivery Reviews*, vol. 57, no. 15, pp. 2130–2146, 2005.
- [23] A. D'Emanuele and D. Attwood, "Dendrimer-drug interactions," *Advanced Drug Delivery Reviews*, vol. 57, no. 15, pp. 2147–2162, 2005.
- [24] J. Hu, Y. Cheng, Y. Ma, Q. Wu, and T. Xu, "Host-guest chemistry and physicochemical properties of the dendrimer-mycophenolic acid complex," *Journal of Physical Chemistry B*, vol. 113, no. 1, pp. 64–74, 2009.
- [25] L. Zhao, Y. Cheng, J. Hu, Q. Wu, and T. Xu, "Host-guest chemistry of dendrimer-drug complexes. 3. Competitive binding of multiple drugs by a single dendrimer for combination therapy," *Journal of Physical Chemistry B*, vol. 113, no. 43, pp. 14172–14179, 2009.
- [26] P. Guaino, A. A. Cafolla, D. Carty, G. Sheerin, and G. Hughes, "An STM investigation of the interaction and ordering of pentacene molecules on the Ag/Si(111)-(√3 × √3)R30 degrees surface," *Surface Science*, vol. 540, no. 1, pp. 107–116, 2003.
- [27] D. M. Eigler and E. K. Schweizer, "Positioning single atoms with a scanning tunnelling microscope," *Nature*, vol. 344, no. 6266, pp. 524–526, 1990.
- [28] C. J. Fleming, Y. X. Liu, Z. Deng, and G. Y. Liu, "Deformation and hyperfine structures of dendrimers investigated by scanning tunneling microscopy," *Journal of Physical Chemistry A*, vol. 113, no. 16, pp. 4168–4174, 2009.
- [29] C. J. Fleming, N. N. Yin, S. L. Riechers, G. Chu, and G. Y. Liu, "High-resolution imaging of the intramolecular structure of indomethacin-carrying dendrimers by scanning tunneling microscopy," *ACS Nano*, vol. 5, no. 3, pp. 1685–1692, 2011.
- [30] H. Cui, T. K. Hodgdon, E. W. Kaler et al., "Elucidating the assembled structure of amphiphiles in solution via cryogenic

- transmission electron microscopy,” *Soft Matter*, vol. 3, no. 8, pp. 945–955, 2007.
- [31] Z. Deng, V. Lulevich, F. T. Liu, and G. Y. Liu, “Applications of atomic force microscopy in biophysical chemistry of cells,” *Journal of Physical Chemistry B*, vol. 114, no. 18, pp. 5971–5982, 2010.
- [32] I. W. Hamley, S. D. Connell, and S. Collins, “In situ atomic force microscopy imaging of adsorbed block copolymer micelles,” *Macromolecules*, vol. 37, no. 14, pp. 5337–5351, 2004.
- [33] S. Li and A. F. Palmer, “Structure and mechanical response of self-assembled poly(butadiene)-b-poly(ethylene oxide) colloids probed by atomic force microscopy,” *Macromolecules*, vol. 38, no. 13, pp. 5686–5698, 2005.
- [34] A. Ripoșan, Y. Li, Y. H. Tan, G. Galli, and G. Y. Liu, “Structural characterization of aldehyde-terminated self-assembled monolayers,” *Journal of Physical Chemistry A*, vol. 111, no. 49, pp. 12727–12739, 2007.
- [35] M. Hegner, P. Wagner, and G. Semenza, “Ultralarge atomically flat template-stripped Au surfaces for scanning probe microscopy,” *Surface Science*, vol. 291, no. 1-2, pp. 39–46, 1993.
- [36] A. A. Dameron, L. F. Charles, and P. S. Weiss, “Structures and displacement of 1-Adamantanethiol self-assembled monolayers on Au(111),” *Journal of the American Chemical Society*, vol. 127, no. 24, pp. 8697–8704, 2005.
- [37] G. Yang and G. Y. Liu, “New insights for self-assembled monolayers of organothiols on Au(111) revealed by scanning tunneling microscopy,” *Journal of Physical Chemistry B*, vol. 107, no. 34, pp. 8746–8759, 2003.
- [38] M. E. Napier and J. M. DeSimone, “Nanoparticle drug delivery platform,” *Polymer Reviews*, vol. 47, no. 3, pp. 321–327, 2007.
- [39] J. Greenhalgh, J. Hockenhull, N. Rao, Y. Dundar, R. C. Dickson, and A. Bagust, “Drug-eluting stents versus bare metal stents for angina or acute coronary syndromes,” *Cochrane Database of Systematic Reviews*, vol. 2010, no. 5, Article ID CD004587, 2010.
- [40] J. Liu, H. Lee, and C. Allen, “Formulation of drugs in block copolymer micelles: drug loading and release,” *Current Pharmaceutical Design*, vol. 12, no. 36, pp. 4685–4701, 2006.
- [41] A. Garg and E. Kokkoli, “Characterizing particulate drug-delivery carriers with atomic force microscopy,” *IEEE Engineering in Medicine and Biology Magazine*, vol. 24, no. 1, pp. 87–95, 2005.
- [42] M. Cazacu, C. Racles, M. Alexandru, A. Ioanid, and A. Vlad, “Morphology and surface properties of some siloxane-organic copolymers,” *Polymer International*, vol. 58, no. 6, pp. 697–702, 2009.
- [43] I. Akiba, N. Terada, S. Hashida et al., “Encapsulation of a hydrophobic drug into a polymer-micelle core explored with synchrotron SAXS,” *Langmuir*, vol. 26, no. 10, pp. 7544–7551, 2010.
- [44] P. J. Pellechia, J. Gao, Y. Gu, H. J. Ploehn, and C. J. Murphy, “Platinum Ion uptake by dendrimers: an NMR and AFM study,” *Inorganic Chemistry*, vol. 43, no. 4, pp. 1421–1428, 2004.
- [45] Y. Gu, H. Xie, J. Gao et al., “AFM characterization of dendrimer-stabilized platinum nanoparticles,” *Langmuir*, vol. 21, no. 7, pp. 3122–3131, 2005.
- [46] A. Hierlemann, J. K. Campbell, L. A. Baker, R. M. Crooks, and A. J. Ricco, “Structural distortion of dendrimers on gold surfaces: a tapping-mode AFM investigation [5],” *Journal of the American Chemical Society*, vol. 120, no. 21, pp. 5323–5324, 1998.
- [47] R. W. J. Scott, O. M. Wilson, and R. M. Crooks, “Synthesis, characterization, and applications of dendrimer-encapsulated nanoparticles,” *Journal of Physical Chemistry B*, vol. 109, no. 2, pp. 692–704, 2005.
- [48] D. A. Tomalia, A. M. Naylor, and W. A. Goddard, “Starburst dendrimers: molecular-level control of size, shape, surface chemistry, topology, and flexibility from atoms to macroscopic matter,” *Angewandte Chemie International Edition in English*, vol. 29, no. 2, pp. 138–175, 1990.

Research Article

Poly(amidoamine)-Cholesterol Conjugate Nanoparticles Obtained by Electrospraying as Novel Tamoxifen Delivery System

R. Cavalli,¹ A. Bisazza,¹ R. Bussano,¹ M. Trotta,¹ A. Civra,² D. Lembo,² E. Ranucci,³ and P. Ferruti³

¹Dipartimento di Scienza e Tecnologia del Farmaco, Università di Torino, Via P. Giuria 9, 10125 Torino, Italy

²Department of Clinical and Biological Sciences, University of Torino, Orbassano, 10043 Torino, Italy

³Dipartimento di Chimica Organica e Industriale, Università degli Studi di Milano, Via Venezian 21, 20133 Milano, Italy

Correspondence should be addressed to R. Cavalli, roberta.cavalli@unito.it

Received 10 January 2011; Accepted 1 April 2011

Academic Editor: Guru V. Betageri

Copyright © 2011 R. Cavalli et al. This is an open access article distributed under the Creative Commons Attribution License, which permits unrestricted use, distribution, and reproduction in any medium, provided the original work is properly cited.

A new poly(amidoamine)-cholesterol (PAA-cholesterol) conjugate was synthesized, characterized and used to produce nanoparticles by the electrospraying technique. The electrospraying is a method of liquid atomization that consists in the dispersion of a solution into small charged droplets by an electric field. Tuning the electrospraying process parameters spherical PAA-chol nanoparticles formed. The PAA-cholesterol nanoparticles showed sizes lower than 500 nm and spherical shape. The drug incorporation capacity was investigated using tamoxifen, a lipophilic anticancer drug, as model drug. The incorporation of the tamoxifen did not affect the shape and sizes of nanoparticles showing a drug loading of 40%. Tamoxifen-loaded nanoparticles exhibited a higher dose-dependent cytotoxicity than free tamoxifen, while blank nanoparticles did not show any cytotoxic effect at the same concentrations. The electrospray technique might be proposed to produce tamoxifen-loaded PAA-chol nanoparticle in powder form without any excipient in a single step.

1. Introduction

Polymeric nanoparticles focused a great attention in the biomedical field as delivery systems for active molecules. These nanoparticles have the potential to act as a reservoir of drugs, protecting them from the environments and controlling their release rates, thereby enhancing the biological activity and decreasing the adverse side effects [1–4].

Various procedures have been proposed in the literature for the fabrication of polymeric nanoparticles and the most used are based on emulsion techniques. However novel methods are attracting increasing attention. One of such is electrohydrodynamic atomization (EHDA), a process with many applications, such as manufacturing nanoscale polymer fibres or thin film and particulate systems [5, 6]. Particularly, EHDA in the cone jet mode (electrospraying) has been previously studied to produce polymeric particles which can be used as drug delivery systems [7, 8]. The electrospray is a method of liquid atomization that consists

in the dispersion of a solution into small charged droplets by an electric field.

Electrospraying is a one-step technique with the potential to ensure particle with reproducible sizes and morphology with a narrow size distribution in the micro- and nanometer range by selecting the proper process conditions.

The principle of electrospraying is based on the capacity of an electric field to deform the interface of a droplet as reported by Jaworek [9]. Particularly, when an electric field is applied on a droplet, it generates an electrostatic force inside the droplets able to overcome the cohesive force of the droplet. Thus the droplet will undergo break-up into smaller droplets in the micro-nanoscale range. Depending on the spraying mode, droplets can be smaller than 100 nm with low standard deviation. This charged aerosol is self-dispersing preventing the droplets from coalescence. This phenomenon is known as Taylor Cone and consists in the progressive shrinking of the charged droplet into a cone from which smaller charged droplets will be ejected [10].

The electro spraying process is simple; it consists in the loading of a polymer solution in a syringe which is infused at constant rate by a pump through a highly charged capillary, forming a droplet at the tip. A droplet formed at the capillary tip and after the droplet detached from the Taylor cone the solvent evaporates generating solid particles. During the electro spraying process there are several parameters which can affect particle sizes, size distribution, encapsulation efficiency, and *in vitro* release profiles. These include voltage, flow rate, distance from the collector, solvent, and needle gauge. Consequently the number of parameters to be considered to obtain a reproducible process is several and the optimization is complex.

Previously we have tuned the electro spraying process parameters for producing lipid-based micro-nanoparticles [11]. Narrowly dispersed spherical particles with sizes lower than $1\ \mu\text{m}$ were obtained using stearic acid and ethylcellulose in a 4.5:0.5 ratio (w/w).

The aim of this work was to investigate the feasibility of obtaining solid polymeric nanoparticles using a cholesterol polyamidoamines (PAAs) conjugate by electro spraying.

PAAs are synthetic degradable polymers obtained by Micheal-type polyaddition of primary or bis-secondary amines to bis-acrylamides [12]. All PAAs contain amide and tertiary amine groups along the main chain.

In PAA-cholesterol conjugates an active substituent was bound to the polymer chain through a disulfide linkage that is known to be stable in the bloodstream but amenable to reductive cleavage inside cells. Preliminary cytocompatibility tests demonstrated that all prepared PAA-cholesterol samples are cytocompatible and thus show potential for biotechnological and pharmaceutical applications [13]. In this work a new PAA conjugate was used to prepare solid nanoparticles by electro spraying as potential drug delivery systems. The goal of the work was to develop a reproducible one-step process to obtain spherical solid PAA-cholesterol nanoparticles with homogeneous size distribution by electro spraying. Moreover cytotoxicity of nanoparticles was assessed in order to avoid the possibility of toxic residues after the electro spraying process.

Tamoxifen, a lipophilic anticancer drug, was used as model drug to study the encapsulation capacity of the PAA conjugate. Tamoxifen is a selective estrogen receptor modulator widely used in breast cancer therapy. The drug can produce serious side effects, as thrombosis, pulmonary embolism, and modification in liver enzyme levels. In addition cancer cells can develop resistance against tamoxifen, and it may initiate endometrial cancer. The encapsulation of tamoxifen in a drug delivery system might provide a better drug release profile potentially preventing the development of cell resistance [14].

2. Material and Methods

2.1. Material. n-Pentanol was from Merck (Darmstadt, Germany). Tamoxifen, sodium citrate, Rhodamine B, and citric acid were from Sigma Aldrich (St. Louis, USA).

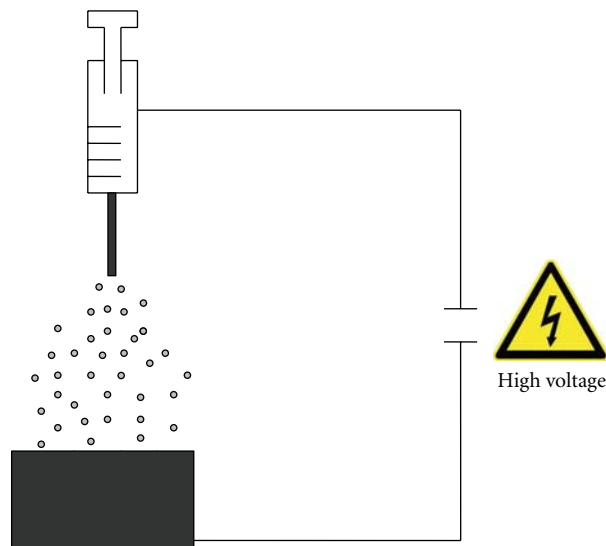


FIGURE 1: Scheme of the apparatus for electro spraying.

Cellulose dialysis membrane (Spectra/Por dialysis membrane) was from Spectrum Laboratories, Inc (Canada). 2,2-bis(acrylamido)acetic acid and 1,4-bis(acryloil)piperazine were synthesized as previously described [15, 16]. All reagents are of analytical grade.

2.2. Cells. Both MCF-7 (a human breast adenocarcinoma cell line) and Vero (an African green monkey kidney cell line) were maintained in Minimum Essential Medium (PAA, 4061 Pasching, Austria) with 10% Fetal Calf Serum (Gibco/BRL) and 1% Zell Shield (Minerva Biolabs GmbH, Berlin). Subculturing of cells was carried out by trypsinization and by diluting cells with fresh medium. Cells were grown in the presence of 5% CO_2 at 37°C .

2.3. Electro spraying Setup. The apparatus for electro spraying comprises a 2.5 mL syringe connected to an infusion pump (KDS 100, Biological Instruments, VA, Italy). A Teflon pipe connects the syringe to the tip of a metal capillary (ID: 0.6 mm) (Figure 1). An aluminium foil collector is placed opposite the capillary as counter electrode. A strong electric field was applied between the tip and the collector. The distance from metal tip to collecting plate varied from 20 to 15 cm.

The solution contained in the syringe is supplied to the nozzle at a flow rate forming a droplet. The electric field induces charges on the droplet surface. A liquid jet occurs that can break up in droplets with a narrow size distribution. Solid particles formed by solvent evaporation from the droplets which travel through the electric field.

2.4. Preparation and Characterization of PAA-Cholesterol Conjugate. A PAA-cholesterol conjugate derived from two different bis-acrylamides, namely 2,2-bis(acrylamido)acetic acid and 1,4-bis(acryloil)piperazine, with a cholesterol content of 8.1% w/w and $M_w = 13000$ was obtained (Figure 2).

The reaction pathway consisted of three steps: (1) the synthesis of a PAA-based hydrogel containing cystamine as cross-linker, (2) a disulfide-exchange reaction with 2,2'-dipyridyl disulfide that leads to soluble linear polymers containing ethyldithiopyridine moieties, and (3) a thiol-exchange reaction between thiocholesterol and the dithiopyridine moieties [13].

The solubility of the PAA-cholesterol conjugate was determined in water and in n-pentanol the solvent selected for the electrospaying. The surface tension of the polymer solutions in water was measured using a Kruss Ring platinum tensiometer K10 (Hamburg).

The zeta potential (ZP) values of the conjugate were determined in aqueous solutions at increasing pH values, ranging from 4.0 to 7.0, to verify the polymer charge distribution as function of the pH. A 90 Plus instrument (Brookhaven, NY, USA) was used to determine the electrophoretic mobility and the zeta potential of the polymer. For the determinations, the aqueous solutions of the polymer were placed in the electrophoretic cell, where an electric field of about 14 V/cm was applied. Each value reported is the average of ten measurements. The electrophoretic mobility measured was converted into Zeta Potential using the Smoluchowski equation [17].

The PAA-solution conductivity in water was determined using a conductometer (Orion, Boston, USA).

2.5. Hemolytic Activity Determination of PAA-Cholesterol Conjugate. The haemolytic activity of the PAA-cholesterol conjugate was evaluated on human blood. Different percentages (2%, 4%, 7%, 10%, and 15% w/v) of polymer were added in a erythrocytes suspension (30% v/v) phosphate buffer, pH 7.4. A sample containing only a suspension of erythrocytes (30% v/v) in phosphate buffer pH 7.4 was used as blank. In addition a blank sample containing an excess of ammonium chloride was prepared to obtain complete erythrocyte hemolysis as hemolytic control.

After 90 minutes of incubation at 37°C the samples were centrifuged at 1500 rpm for 10 minutes and the supernatant was analyzed using a Lambda 2 Perkin-Elmer spectrophotometer at a wavelength of 543 nm. The percentage of hemolysis was calculated versus the 100% hemolysis control.

2.6. Preparation of PAA-Cholesterol Nanoparticles. To prepare PAA-cholesterol nanoparticles the electrospaying apparatus previously described was used. Preliminary experiments were carried out to select the process parameters suitable to obtain spherical nanoparticles with the PAA-cholesterol conjugate. Different parameters were varied to tune the process; flow rate of 15, 10, and 5 $\mu\text{L min}^{-1}$ and electric field of 20, 25, and 30 KV were mainly investigated. The experimental conditions selected were a flow rate of 5 $\mu\text{L min}^{-1}$ and an electric field of 20 KV applied between the capillary tip and an aluminum plate. The selected distance from metal tip to collecting plate was 15 cm. A solution of PAA-cholesterol conjugate in n-pentanol (1% w/w) was prepared and supplied to the capillary nozzle with a 5 $\mu\text{L min}^{-1}$ flow. During free flight the organic solvent evaporated

and solid nanoparticles collected on the plate. To obtain fluorescent-labelled nanoparticles Rhodamine B was added in the polymer pentanol solution (0.05% w/v). The same process parameters were applied during electrospaying.

2.7. Preparation of Tamoxifen-Loaded PAA-Cholesterol Nanoparticles. Tamoxifen-loaded PAA-cholesterol nanoparticles were prepared by dissolving the drug (5 mg/mL) in the conjugate n-pentanol solution (10 mg/mL) under stirring. The solution was then electrospayed to obtain the drug loaded PAA-cholesterol nanoparticles using the same process parameters selected to obtain blank nanoparticles.

2.8. Quantitative Determination of Tamoxifen. The amount of tamoxifen-loaded into the nanoparticles was determined after addition of 2.0 mL of phosphate buffer pH 7.4 containing 20 mg of citric acid to a weighed amount of drug-loaded nanoparticles (2 mg). After vortex and centrifuge for 5 minutes at 5000 rpm, 2 mL of ethanol and 0.5 mL of water were added to the precipitate. After stirring and separation the supernatant was analyzed by HPLC.

Tamoxifen content was determined using an HPLC system consisting of Shimadzu liquid chromatograph (Shimadzu, Kyoto, Japan) equipped with an SDP 10A variable wavelength ultraviolet detector and a CR6A integrator. A Lichrospher C-18, 5 μm (Merck, Darmstadt, Germany), 25 cm \times 4.6 mm ID reversed-phase column was used. The column was eluted with a mobile phase containing methanol/water/triethylamine (89/11/1, v/v). The eluent was run at rate of 1 mL/min and monitored at 265 nm following injected volumes of 20 μL of tamoxifen standard solutions and samples. The calibration curve was found to be linear in the range 0.05–30 $\mu\text{g/mL}$. Each sample was analyzed in triplicate.

2.9. Characterization of the PAA-Cholesterol Nanoparticles. The average diameters and polydispersity indices of the three nanoparticle formulations were determined after dispersion of the samples in filtered water by photocorrelation spectroscopy (PCS) using a 90 Plus instrument (Brookhaven, NY, USA) at a fixed angle of 90° and a temperature of 25°C. The polydispersity index indicates the size distribution within a nanoparticles population. The electrophoretic mobility and zeta potential of the formulations were determined using a 90 Plus instrument (Brookhaven, NY, USA). For zeta potential determination, samples of the formulation were placed in the electrophoretic cell, where an electric field of about 15 V/cm was applied. Each sample was analyzed at least in triplicate. The electrophoretic mobility measured was converted into zeta potential using the Smoluchowski equation [17].

The nanoparticles morphology was evaluated by Scanning Electron Microscopy (SEM) (Leica Stereoscan 410, Wetzlar, Germany) and fluorescent microscopy. To perform SEM a thin layer of particles was mounted on a copper stud, which was then sputter coated with gold (SCD 050, Lewica, Wetzlar, Germany) for 60 seconds under vacuum at a current intensity of 60 mA. The gold-coated particle layer was scanned using the accelerating voltage scanning of 20 kV.

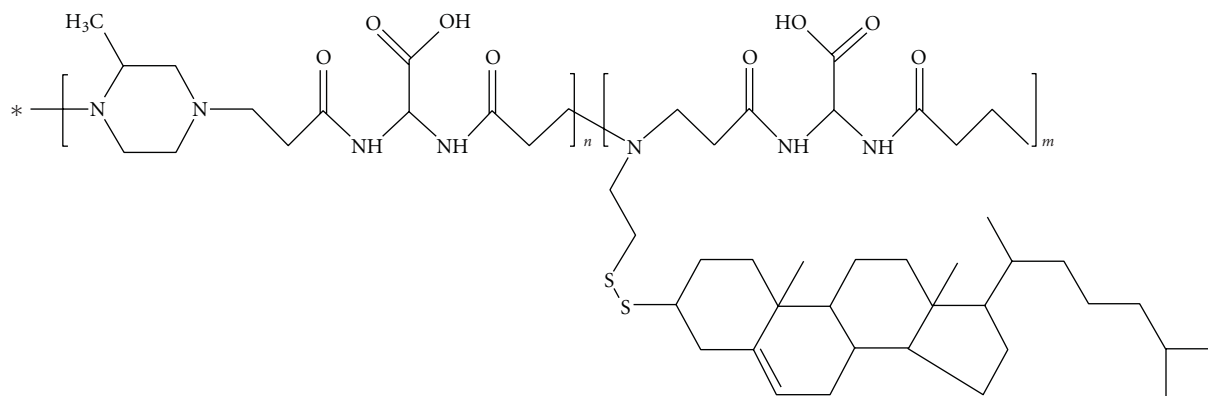


FIGURE 2: Chemical structure of the PAA-cholesterol conjugate.

2.10. Thermal Analysis of Nanoparticles. Differential scanning calorimetry (DSC) analysis was carried out using a DSC7 differential scanning calorimeter (Perkin-Elmer, Conn, USA) equipped with a TAC7/DX instrument controller. The instrument was calibrated with indium for melting point and heat of fusion. A heating rate of 10°C/min was employed in the 30–120°C temperature range. Standard aluminium sample pans (Perkin-Elmer) were used; an empty pan was used as reference standard. Blank nanoparticles, tamoxifen-loaded nanoparticles, and tamoxifen powder (3–4 mg) were weighed in conventional aluminium pans, and analyses were performed under nitrogen purge; triple runs were carried out for each sample.

2.11. In Vitro Release Kinetics of Tamoxifen. A multicompartmental rotating cell was used to evaluate the *in vitro* release profile of tamoxifen. A tamoxifen aqueous suspension 1.17 mM as control and tamoxifen-loaded nanoparticles at the same concentration dispersed in water were prepared, and 1 mL of each was placed in the donor compartment. A cellulose dialysis membrane with cutoff at 12,000–14,000 was chosen to separate the compartments. The receptor compartment was filled with 1 mL of pH 5.5 0.1 M citrate buffer. Each experiment lasted 24 h. At fixed times, the receptor buffer was completely withdrawn and replaced with fresh citrate buffer. The withdrawn samples were then analyzed by HPLC. The experiment was performed in triplicate.

2.12. Internalization Study of PAA-Cholesterol Nanoparticles. The cellular uptake of PAA-cholesterol fluorescent nanoparticles was evaluated through confocal laser scanning microscopy on Vero cell. Exponentially growing cells were plated and cultured overnight in 24-well plates on glass coverslips; the cell monolayers were incubated with appropriated dilutions of PAA-cholesterol fluorescent nanoparticle suspension for 1 h and then extensively washed with PBS for observation of live cells. Confocal sections were taken on an inverted Zeiss LSM510 fluorescence microscope.

2.13. Cytotoxicity Assay. To test the cytotoxic effect of tamoxifen-loaded nanoparticles, MCF-7 cells were seeded in a 96-well plate at a density of 1.2×10^4 /well; the next day they were treated with increasing concentrations, ranging from 1 to 40 μ M, of free tamoxifen and tamoxifen-loaded nanoparticles. Treatment with equal concentrations of blank nanoparticles was made in order to rule out the possibility of any cytotoxic effect ascribable to the delivery system.

After 24, 48, and 72 hours of incubation, cell viability was determined by the CellTiter 96 Proliferation Assay Kit (Promega, Madison, WIs, USA) according to the manufacturer's instructions. Absorbances were measured using a Microplate Reader (Model 680, BIORAD) at 490 nm. The effect on cell viability of the formulation at different concentrations was expressed as a percentage, by comparing treated cells with cells incubated with culture medium alone. The 50% cytotoxic concentration (CC_{50}) values and the 95% confidence intervals (CIs) were determined using the Prism software (GraphPad Software, San Diego, CA).

3. Results

Firstly the new PAA-cholesterol conjugate was *in vitro* characterized. The percentage of cholesterol was determined by NMR resulting in 8% w/w.

For the electrospaying process is necessary an organic solvent in which the PAA-Cholesterol conjugate is very soluble. For this purpose 1-pentanol (b.p. = 137.5°C) in which the conjugate is soluble more than 2% w/v was selected.

The conjugate is amphiphilic for the presence of cholesterol in the structure. The surface tension of the PAA-cholesterol conjugate in water at pH 6.0 was determined, and it is reported in Figure 3. PAA-cholesterol showed a CMC in water of about 2 mg/mL.

Zeta potential measurements demonstrated that PAA-cholesterol is positively charged in aqueous solution with a value of +21 mV at pH 7.0 and the positive charge increase lowering the pH value to 4.0. The conjugate conductivity in water was 74.8 μ S.

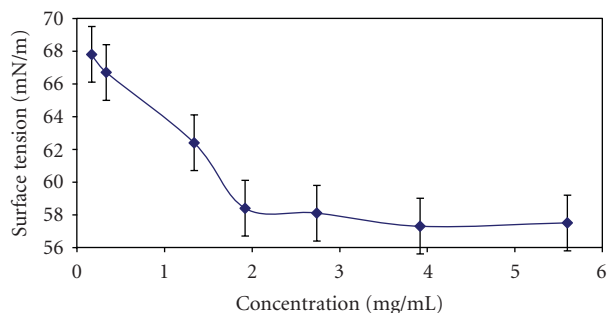


FIGURE 3: Surface tension of PAA-cholesterol conjugate in water.

TABLE 1: Characteristics of PAA-cholesterol nanoparticles.

Formulation	d ± SD (nm)	Poly-index	PZ ± SD (mV)
PAA-cholesterol nanoparticles	223.2 ± 10.0	0.29	21.28 ± 2.76
PAA-cholesterol fluorescent nanoparticles	362.8 ± 23.8	0.15	17.89 ± 1.32
PAA-cholesterol tamoxifen nanoparticles	247.0 ± 17.7	0.26	14.86 ± 0.99

No significant haemolytic activity was observed for PAA-cholesterol conjugate after 90 minutes of incubation in blood at pH 7.4 up to a concentration of 15% w/v.

Spherical solid PAA-cholesterol nanoparticles formed easily using an electric field of 20 KV and a flow of $5 \mu\text{L min}^{-1}$. The nanoparticle sizes were mainly tuned by the control of electrospaying flow rate and polymer concentration.

The physicochemical characteristics of PAA-cholesterol nanoparticles are reported in Table 1.

All the PAA-cholesterol conjugate nanoparticles showed sizes lower than 500 nm with a quite narrow size distribution and a positive Zeta Potential. The loaded nanoparticles had sensible greater sizes and a decrease of the Zeta potential values demonstrating the presence of incorporated molecules in the nanoparticle structure.

SEM analyses showed that PAA-cholesterol nanoparticles are spherical with smooth surfaces and confirmed their sizes. The blank PAA-cholesterol nanoparticles image is reported in Figure 4.

A fluorescent PAA-cholesterol formulation was also prepared by the electrospaying process using Rhodamine B as fluorescent marker to evaluate the nanoparticle cell internalization. The morphology of the fluorescent formulation is reported in Figure 5. The fluorescent nanoparticles were easily internalized in Vero cells (Figure 6).

SEM analysis confirmed sizes and shape of tamoxifen-loaded PAA-cholesterol nanoparticles.

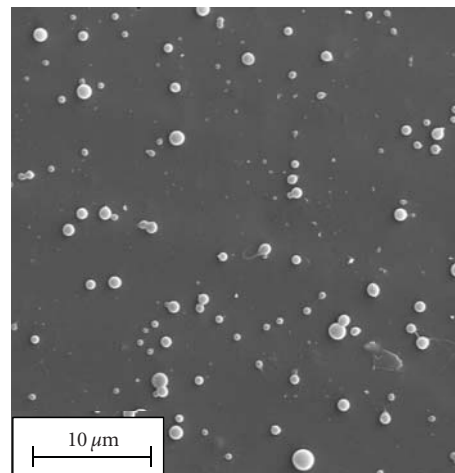


FIGURE 4: SEM image of blank PAA-cholesterol nanoparticles.

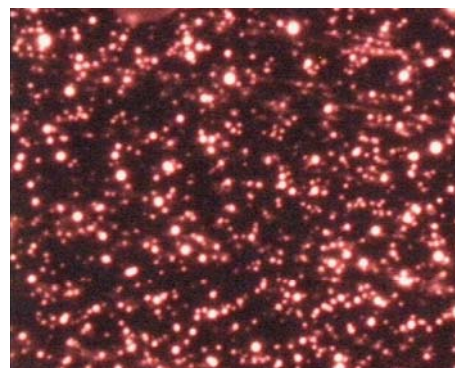


FIGURE 5: Fluorescent PAA-cholesterol nanoparticles containing Rhodamine B (fluorescent microscopy).

The incorporation of the drug did not affect the shape and the smooth surface of nanoparticles as shown in Figure 7.

As it is possible to note in the figure the presence of the drug could affect the physicochemical characteristics of the PAA-cholesterol solution favouring a partial coalescence of the droplet. Decreasing the amount of tamoxifen, well-separated nanoparticles were obtained (data not shown).

Tamoxifen-loaded PAA-cholesterol nanoparticles showed a drug loading of about 40% w/w and the encapsulation efficiency of about 90%.

Thermal analysis of tamoxifen-loaded nanoparticles did not show the endothermic peak at about 97°C related to the drug melting. The disappearance of the melting peak in the DSC profile indicates that the drug can be dispersed in the polymer matrix. The PAA-cholesterol conjugate did not show thermal change in this temperature range. The DSC thermograms of the tamoxifen-loaded nanoparticles and of tamoxifen are reported in Figure 8.

The *in vitro* release profile of tamoxifen from the drug-loaded nanoparticle showed a slow release over time without initial burst effect indicating that the drug is mainly incorporated in the PAA-cholesterol matrix and not adsorbed

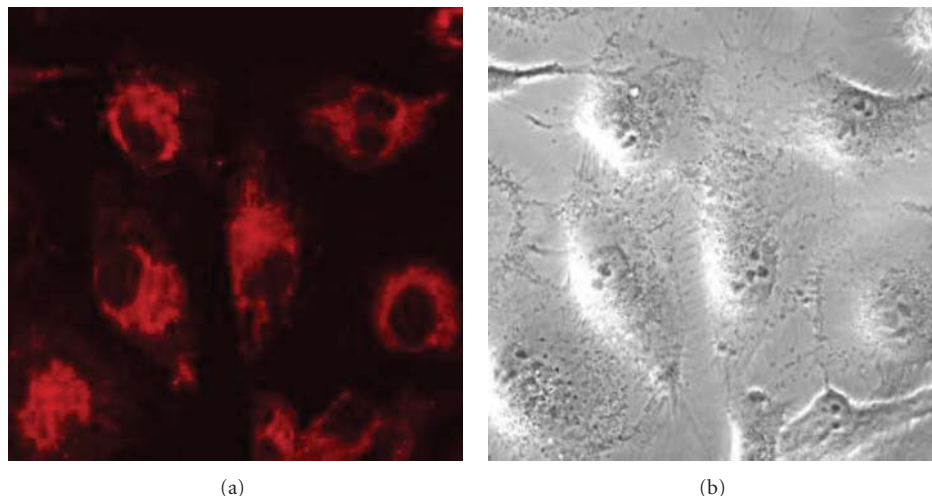


FIGURE 6: Internalization of fluorescent PAA-cholesterol nanoparticles on Vero cells analysed by confocal laser scanning microscopy.

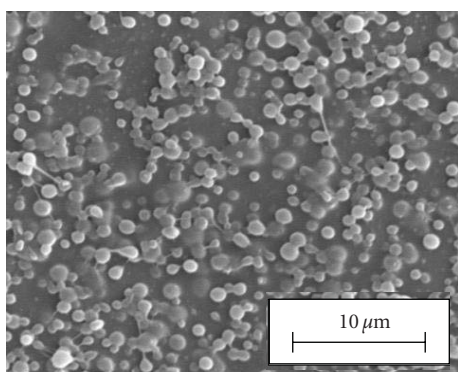


FIGURE 7: SEM image of *In vitro* release of the formulations.

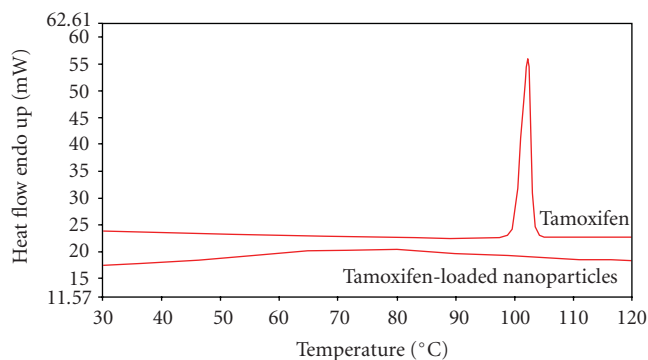


FIGURE 8: Thermal analysis of tamoxifen and tamoxifen-loaded nanoparticles.

on particle surface. After 6 h about 26% of tamoxifen was released from the PAA-cholesterol nanoparticles. On the contrary about 15% of tamoxifen from aqueous drug suspension diffused after 6 h (Figure 9).

3.1. Cytotoxicity Assay. To assess the activity of the formulation, MCF-7 cells were incubated with solutions containing blank nanoparticles or tamoxifen-loaded nanoparticles,

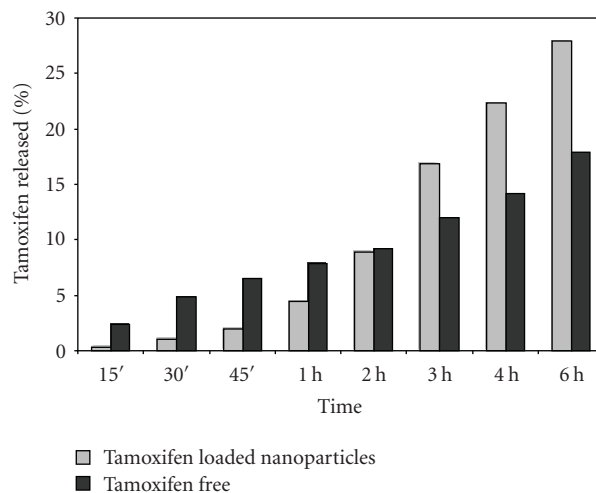


FIGURE 9: *In vitro* release of tamoxifen from the formulations.

having the same nanoparticle concentration. Free tamoxifen was used as positive control. As free tamoxifen was diluted in DMSO, corresponding volumes of DMSO were also added for comparison. After 24, 48, and 72 hours from the beginning of treatment, cells were analyzed by MTS colorimetric assay to test cell viability.

As shown in Figures 10(a), 10(b), and 10(c), tamoxifen-loaded nanoparticles exhibited a more pronounced concentration-dependent cytotoxicity than free tamoxifen at each time point analyzed. The finding that blank nanoparticles did not show any cytotoxic effect even at high concentrations rules out their contribution to the increased activity of the formulation and confirmed the absence of residues.

Notably, cytotoxic effect measured for those samples that received volumes of tamoxifen greater than $2 \mu\text{L}$ (2% v/v) seems mostly ascribable to the presence of DMSO, as indicated by the treatment with this solvent alone.

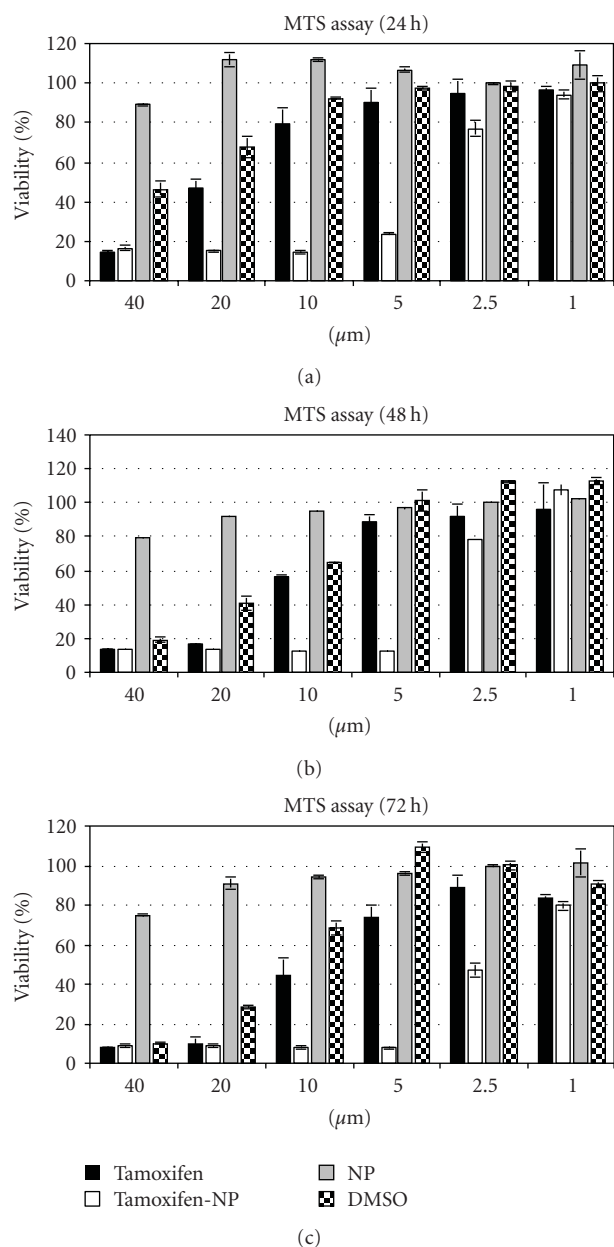


FIGURE 10: Cell viability of MCF-7 breast cancer cells incubated for 24, 48, and 72 h (a, b, and c panels, resp.) with free tamoxifen (Tamoxifen), tamoxifen-loaded nanoparticles (tamoxifen-NP), empty nanoparticles (NP), or DMSO. Each bar represents the mean of three samples \pm SD.

4. Discussion

Electrospraying (electrohydrodynamic spraying) is a process of simultaneous droplet generation and charging by means of electric field [9]. Production of particles of uniform size can be accomplished by generation of cone-jet mode. This mode of spraying is very sensitive to any change in liquid properties, and the droplet size can vary unexpectedly with parameter changes. By the selection of suitable process parameters the production in a single step

of solid nanoparticles using a PAA-cholesterol conjugate as matrix was possible. The new PAA conjugate containing 8% of cholesterol is soluble either in water or in organic solvents with a CMC of about 2 mg/mL. Because of its amphiphilic nature it is particularly suitable to produce nanoparticles by electrospraying [13]. The surface tension of the solution can affect the nanoparticle formation; generally it was shown that, decreasing the surface tension of a solution, there is a decrease in the particle sizes with a corresponding increase in standard deviation of the particle sizes distribution [18]. Surface charge density and surface tension play important roles in the process. When the surface charge density is low, the Rayleigh limit, the maximum limit of surface charge density when the electrostatic forces exceed surface tension, is never reached. Another possibility is that the surface charge density of the droplets is high, so the Rayleigh limit is reached immediately or after solvent evaporation and droplets disintegrate (Coulomb fission), forming small charged droplets. In the process the Coulomb fission should be avoided because droplets of uniform size are required [11, 19]. The PAA-cholesterol nanoparticles are positive charged showing that during the droplet shrinking the hydrophilic region remains on the surface, while the cholesterol molecules can be oriented inside the droplets.

Reproducible PAA-cholesterol nanoparticles with sizes lower than 300 nm and spherical shape from pentanol solution were obtained in one single step.

The effect of conductivity on particle formation has also been investigated [20]. The increase of a solution conductivity from μ S/cm to mS/cm resulted in a marked reduction of the particle size due to the Coulomb fission.

Tamoxifen is a hydrophobic molecule with a low water solubility (0.4 mg/mL), a high hygroscopicity and UV light sensitivity. Its solubility in pentanol reached 2 mg/mL. Tamoxifen-loaded PAA-cholesterol nanoparticles formed by electrospray maintaining a mean diameter lower than 300 nm. The drug is incorporated in the polymer matrix as DSC and *in vitro* release studies showed. The absence of an initial burst effect confirmed the incorporation of tamoxifen inside the polymer matrix. Hydrophobic interaction between cholesterol and hydrophobic portion of tamoxifen molecules could favour the incorporation of the drug in the internal lipophilic region. The drug probably remains molecularly dispersed in the PAA-cholesterol conjugate matrix without crystallizing. The disappearance of the melting peak of the drug in the DSC profile can confirm this hypothesis.

The electrospraying process tuned employs n-pentanol, an organic solvent with boiling point of 137.5°C in which the conjugate is soluble. It is important to assess that this solvent is completely removed otherwise the electrosprayed nanoparticles might be toxic to cells.

Therefore we tested the blank nanoparticles and the results showed no cytotoxicity up to a concentration of 20 μ M. This behaviour indicates that the conjugate nanoparticles are not toxic as previously reported [13] and that no n-pentanol remains incorporated in the polymer matrix but it evaporates during the flight and nanoparticle formation. The data are in agreement with pentanol residues determined previously by gas chromatography in the stearic

acid:ethylcellulose particles (4.5:0.5 w/w). The pentanol content was 0.2 milligrams per gram of lipid based particles [11].

According to previous report [21], we found that MCF7 cells are highly sensitive towards DMSO. Indeed, volumes equal to or higher than 2 μ L (2% v/v) result in a cytotoxic effect that partially overlaps the one observed in cells treated with free tamoxifen diluted in DMSO. Therefore, this “background” cytotoxicity leads to an overestimation of the free tamoxifen activity, although the CC₅₀ value we measured is comparable to the ones presented in the literature for free tamoxifen diluted in DMSO [22]. By contrast, tamoxifen-loaded PAA-cholesterol nanoparticles showed a clear dose-dependent cytotoxic activity, completely ascribable to the drug. Considering that the CC₅₀ value of free tamoxifen is overestimated, the cytotoxic potency of the tamoxifen nanoparticle formulation is even more attractive.

5. Conclusion

Solid polymeric nanoparticles with spherical shape and smooth surface were obtained using a new PAA-cholesterol conjugate by electro spraying, a cost effective technique.

In this work electro spraying parameters were tuned to obtain PAA-cholesterol nanoparticles avoiding fiber formation, particularly varying flow rate and voltage applied to the nozzle.

The new PAA-cholesterol conjugate is suitable to produce nanoparticles by electro spraying in the absence of excipients and in powder form in a single step. The PAA-cholesterol nanoparticles show small size, spherical shape, and good drug loading. Tamoxifen-loaded in PAA-cholesterol nanoparticles showed a slow release over time due to the incorporation in the conjugate matrix.

The PAA-cholesterol nanoparticles did not show any toxic effects. The tamoxifen-loaded nanoparticles showed an enhanced cytotoxicity in comparison to the free drug.

Acknowledgment

The authors would like to acknowledge the support of Ricerca sanitaria finalizzata bando 2008/bis and 2009 to D. Lembo. Blood was purchased from Blood Bank of Molinette hospital (Turin).

References

- [1] L. Cismaru and M. Popa, “Polymeric nanoparticles with biomedical applications,” *Revue Roumaine de Chimie*, vol. 55, no. 8, pp. 433–442, 2010.
- [2] J. M. Chan, P. M. Valencia, L. Zhang, R. Langer, and O. C. Farokhzad, “Polymeric nanoparticles for drug delivery,” *Methods in Molecular Biology*, vol. 624, pp. 163–175, 2010.
- [3] C. Chauvierre, C. Vauthier, D. Labarre, P. Couvreur, M. C. Marden, and L. Leclerc, “A new generation of polymer nanoparticles for drug delivery,” *Cellular and Molecular Biology*, vol. 50, no. 3, pp. 233–239, 2004.
- [4] R. Singh, S. Singh, and J. W. Lillard, “Past, present, and future technologies for oral delivery of therapeutic proteins,” *Journal of Pharmaceutical Sciences*, vol. 97, no. 7, pp. 2497–2523, 2008.
- [5] S. N. Jayasinghe and A. C. Sullivan, “Electrohydrodynamic atomization: an approach to growing continuous self-supporting polymeric fibers,” *Journal of Physical Chemistry B*, vol. 110, no. 6, pp. 2522–2528, 2006.
- [6] C. J. Hogan, K. M. Yun, D. R. Chen, I. W. Lenggoro, P. Biswas, and K. Okuyama, “Controlled size polymer particle production via electrohydrodynamic atomization,” *Colloids and Surfaces A*, vol. 311, no. 1–3, pp. 67–76, 2007.
- [7] L. Ding, T. Lee, and C. H. Wang, “Fabrication of monodispersed Taxol-loaded particles using electrohydrodynamic atomization,” *Journal of Controlled Release*, vol. 102, no. 2, pp. 395–413, 2005.
- [8] D. Fantini, M. Zanetti, and L. Costa, “Polystyrene microspheres and nanospheres produced by electro spray,” *Macromolecular Rapid Communications*, vol. 27, no. 23, pp. 2038–2042, 2006.
- [9] A. Jaworek, “Electrostatic micro- and nanoencapsulation and electroemulsification: a brief review,” *Journal of Microencapsulation*, vol. 25, no. 7, pp. 443–468, 2008.
- [10] M. S. Wilm and M. Mann, “Electrospray and Taylor-Cone theory, Dole’s beam of macromolecules at last?” *International Journal of Mass Spectrometry and Ion Processes*, vol. 136, no. 2-3, pp. 167–180, 1994.
- [11] M. Trotta, R. Cavalli, C. Trotta, R. Bussano, and L. Costa, “Electrospray technique for solid lipid-based particle production,” *Drug Development and Industrial Pharmacy*, vol. 36, no. 4, pp. 431–438, 2010.
- [12] P. Ferruti, M. A. Marchisio, and R. Duncan, “Poly(amidoamine)s: biomedical applications,” *Macromolecular Rapid Communications*, vol. 23, no. 5-6, pp. 332–355, 2002.
- [13] E. Ranucci, M. A. Suardi, R. Annunziata, P. Ferruti, F. Chiellini, and C. Bartoli, “Poly(amidoamine) conjugates with disulfide-linked cholesterol pendants self-assembling into redox-sensitive nanoparticles,” *Biomacromolecules*, vol. 9, no. 10, pp. 2693–2704, 2008.
- [14] R. R. Barakat, T. A. Gilewski, L. Almadrones et al., “Effect of adjuvant tamoxifen on the endometrium in women with breast cancer: a prospective study using office endometrial biopsy,” *Journal of Clinical Oncology*, vol. 18, no. 20, pp. 3459–3463, 2000.
- [15] P. Ferruti, E. Ranucci, F. Trotta et al., “Synthesis, characterisation and antitumour activity of platinum(II) complexes of novel functionalised poly(amidoamine)s,” *Macromolecular Chemistry and Physics*, vol. 200, no. 7, pp. 1644–1654, 1999.
- [16] P. Ferruti, M. A. Marchisio, and R. Barbucci, “Synthesis, physico-chemical properties and biomedical applications of poly(amidoamine)s,” *Polymer*, vol. 26, no. 9, pp. 1336–1348, 1985.
- [17] A. Sze, D. Erickson, L. Ren, and D. Li, “Zeta-potential measurement using the Smoluchowski equation and the slope of the current-time relationship in electroosmotic flow,” *Journal of Colloid and Interface Science*, vol. 261, no. 2, pp. 402–410, 2003.
- [18] J. Doshi and D. H. Reneker, “Electrospinning process and applications of electrospun fibers,” *Journal of Electrostatics*, vol. 35, no. 2-3, pp. 151–160, 1995.
- [19] R. P. A. Hartman, D. J. Brunner, D. M. A. Camelot, J. C. M. Marijnissen, and B. Scarlett, “Electrohydrodynamic atomization in the cone-jet mode physical modeling of the liquid cone and jet,” *Journal of Aerosol Science*, vol. 30, no. 7, pp. 823–849, 1999.
- [20] A. M. Gañán-Calvo, J. Dávila, and A. Barrero, “Current and droplet size in the electro spraying of liquids. Scaling laws,” *Journal of Aerosol Science*, vol. 28, no. 2, pp. 249–275, 1997.

- [21] M. Licciardi, G. Cavallaro, M. Di Stefano et al., "New self-assembling polyaspartylhydrazide copolymer micelles for anticancer drug delivery," *International Journal of Pharmaceutics*, vol. 396, pp. 219–228, 2010.
- [22] A. Bhatia, S. Bhushan, B. Singh, and O. P. Katare, "Studies on tamoxifen encapsulated in lipid vesicles: effect on the growth of human breast cancer MCF-7 cells," *Journal of Liposome Research*, vol. 19, no. 3, pp. 169–172, 2009.